Effect of Bedding and Drilling-Induced Stresses on Borehole Sonic Logging

A Thesis

Submitted to the College of Graduate and

Postdoctoral Studies in Partial Fulfillment of the

Requirements

for the

Degree of Master of Science

in the

Department of Civil, Geological and Environmental Engineering:

University of Saskatchewan

Saskatoon

by

Sepidehalsadat Hendi

PERMISSION TO USE

ABSTRACT

Advancements in the design of sonic logging tools have made it possible to characterize rock formations more extensively. This achievement has had a great impact on the design of effective drilling, completion and production practices. However, interpretation of advanced sonic logging tools is complex, and the relative contributions of intrinsic and stress-induced elastic property anisotropy on tool response are not well understood. This thesis presents a methodology for predicting sonic logging tool response accounting for the effects of bedding and drilling-induced stresses, based on anisotropic and stress-dependent dynamic and static elastic properties.

In this project, boreholes from two areas were studied: Northeast British Columbia (Montney Formation) and Southeast Saskatchewan (Deadwood Formation). Samples provided from these boreholes were tested by laboratory technical staff under hydrostatic and uniaxial loads, and these results were used to predict the stress dependence of all five dynamic and static elastic moduli comprising the transversely isotropic stiffness tensor.

The static elastic properties as a function of stress (acquired from lab testing results) were utilized to define the static elastic stiffness tensor, and static stress analysis was conducted to predict the stress alteration around the borehole. The results of this static stress analysis were then used in conjunction with dynamic elastic properties (defined as a function of stress) to determine dynamic elastic stiffness properties of the rock around the borehole. These dynamic properties were used as inputs for dynamic (wave propagation) modeling.

The modeled acoustic waveforms were recorded for each simulation. The results were used as input for a codes written in Matlab to generate dispersion curves. Simulation outputs were compared to field-based logging results, in terms of dispersion curve appearance and shear wave velocity anisotropy.

The results of comparison between simulated and field results showed a similarity in the general form of the results, but differences in the absolute values of velocities. Because the modeling tools (for simplified scenarios) were tested against analytical solutions, and favourable comparisons were observed between predicted velocities based on simulation results and values taken directly from experimental results, the difference between field and simulated results are believed to result from differences between lab testing conditions and in-situ conditions such as temperature, frequency, size (dimensions), pore fluid properties, pore pressure, and rock property heterogeneity.

ACKNOWLEDGEMENT

The last three years at University of Saskatchewan have been one of the most important, exciting and enjoyable phases in my life. There are many people who made this journey a unique experience.

First of all, I would like to extend my deepest gratitude to my advisor, Professor Christopher Hawkes for his guidance, encouragement, and support. This dissertation was inspired by Professor Hawkes, and was enriched by his ideas and insights. The many scientific discussions with him were always gratifying for me. I feel honored and privileged to be one of his students.

I also thank Professor Samuel Butler for his teachings, feedback, encouragement, and providing us with an analytical solution. This dissertation would not be possible without his advice on many of the technical details. Thanks also to Donna Beneteau for her guidance on writing which was extremely valuable to me.

Finally, thank you to my other committee member, Professor Jim Merriam, for his constructive comments and excellent suggestions. And thanks to the Rock Mechanics laboratory technician, Zig Szczepanik, for providing me with experimental results.

Special thanks to Weatherford, Petroleum Technology Research Center (PTRC), Mitacs, and their industrial affiliates for financial support. Thanks also to Don White for showing me the practical application of my research during my internship.

I would like to dedicate this thesis to my parents, Morteza and Mina, both of whom have helped me through all the good times and the bad. They have always supported and encouraged my work and have nurtured my curiosity through my life. I would also like to dedicate this work to my wonderful sister, Saeideh, who puts up with all of my quirks and is always willing to listen to gripes and rants while offering sound advice.

At the end, I am grateful to my husband Mostafa for his unwavering encouragement and unconditional love throughout my life.

TABLE OF CONTENTS

LIST OF FIGURES

LIST OF TABLES

LIST OF SYMBOLS AND ABBREVIATIONS

SYMBOLS:

$a_{1_{ij}}$ – *slope of the line fitted on the experimental data.*

$a_{2_{ij}}$ – *intercept of the line fitted on the experimental data (GPa)*

$a(t)$ – *Change in sphere radius in time*

$\dot{a}$– *Fluid velocity at the sphere surface*

A_{ijkl} – *The unstressed fourth-order stiffness tensor (second-order elastic constants* C_{ij}^{0}*)*

A_{ijklmn} – *The six-order elastic constants (or third-order elastic constants* C_{ijk} *in Voigt notation)*

C_0 – *Compressional velocity of fluid (drilling mud velocity)*

C – *Stiffness tensor*

E – *Young's modulus*

E_1 – *Young's modulus parallel to the axis of symmetry in VTI material*

E_3 – *Young's modulus parallel to the bedding in VTI material*

f_1 – *Low-cut frequency*

f_2 – *Low-pass frequency*

f_3 – *High-pass frequency*

f_4 – *High-cut frequency*

f_c – *Central frequency*

F – *Stress function*

G – *Shear modulus*

G_{12} – *Shear modulus of bedding in VTI material*

G_{23} – *Shear modulus of the plane parallel to the axis of symmetry in VTI material*

k – *Wavenumber*

K – *Bulk modulus*

m – *Mass moving across the sphere of* a_0.

$\overline{m}$ – *The average of mass moving across the sphere of* a_0.

M – *Mass*

P – *Pressure*

r – *Radius*

S_{ijkl} – *Compliance tensor*

t – *Time*

u – *Displacement*

$\widehat{u'}$ – *Velocity matrix in 3D*

$\overrightarrow{u'}$ – *Velocity vector in 1D*

$\widehat{u'_0}$ – *Background velocity*

$\widehat{u'_1}$ – *Velocity change with time*

$V_{P_{0^\circ}}$ – *Compressional velocity in the direction perpendicular to the bedding.*

$V_{P_{45^\circ}}$ – *Compressional velocity in the direction 45° to the bedding.*

$V_{P_{90^\circ}}$ – *Compressional velocity in the direction parallel to the bedding.*

$V_{S_{0^\circ}}$ – *Shear velocity in the direction perpendicular to the bedding.*

$V_{SH_{90^\circ}}$ – *Shear velocity in the direction parallel to the bedding.*

V – *Bulk volume*

$\bar{V}$ – *Amplitude of the pulsation velocity*

V_P – *Compressional velocity*

V_m – *Mud velocity*

V_s – *Shear velocity*

$X_1, X_2,$ *and* X_3 – *Cartesian coordinate axis direction*

δ – *Kronecker delta*

∇ – *Gradient operator*

∇^2 – *Laplace operator*

ε – *Strain tensor*

ε_{mn} – *Principal strains.*

ε_x – *Strain in x direction*

ε_y – *Strain in y direction*

ε_z – *Strain in z direction*

θ – *Angle (cylindrical coordinate system)*

λ – *Wavelength*

ϑ – *Poisson's ratio*

ϑ_{12} – *Poisson's ratio of bedding in VTI material*

ϑ_{13} – *Poisson's ratio in the plane parallel to axis of symmetry in VTI material*

ϑ_{31} – *Poisson's ratio in the plane parallel to axis of symmetry in VTI material*

ρ – *Density*

ρ' – *Density change in time*

ρ_b – *Background Density*

σ_{hmin} – *Minimum horizontal stress*

σ_{Hmax} – *Maximum horizontal stress*

σ_v – *Vertical stress*

$\sigma_{x,0}, \sigma_{y,0}, \sigma_{z,0}, \tau_{xy,0}, \tau_{xz,0},$ *and* $\tau_{yz,0}$ – *Virgin in-situ stress field.*

σ – *Normal stress*

τ – *Shear stress*

φ – *Potential function*

ψ – *Stress function*

ω – *Angular frequency*

ABBREVIATIONS:

BH – Borehole

CXD – Cross-dipole sonic tool

DFIT – Diagnostic Fracture Injection Test

DISECA – Dispersion Seismogram Calculation

FCP- Fracture Closure Pressure

FD3D– Finite Difference 3 Dimensional

FDTD – Finite Difference Time Domain

FM - Formation

HTI – Horizontal Transverse Isotropic

Inf – Infinite Domain

NEV – North-East-Vertical

PML – Perfectly Matched Layer

QC – Quality Control

RAI – The real axis integration method

RR – Spacing between Receivers

TOH – Top of Borehole

TR – Distance from Transmitter to First Receiver

VTI – Vertical Transverse Isotropic

RMSE – Root-Mean-Square Error

1. Introduction

1.1 Background

A new generation of specialized sonic logging tools has provided the capability of obtaining a multitude of formation properties more accurately, including acoustic anisotropy, in-situ stress magnitude and directions, permeability, and pore fluid type. These properties assist in the design of effective drilling, completion and production operations

The factors affecting a tool's response can be quite complex. Among these factors, the most relevant to this research are the following:

- Sedimentary rocks are intrinsically anisotropic in terms of their elastic properties and sonic velocities because of preferential orientations of sediment grains, pores and layering.
- Elastic properties and sonic velocities tend to be stress-dependent (e.g., due to opening/closure of pores and micro-fractures).
- The principal in-situ stresses in the earth's crust tend to be unequal in magnitude, hence induced stress magnitudes are generally variable around the perimeter of a borehole. This gives rise to a component of stress-induced anisotropy of elastic properties and sonic velocities in the rock around a borehole, which is superimposed upon the afore-noted intrinsic anisotropy.
- Near-well stresses are controlled by static elastic properties while velocities are affected by dynamic elastic properties, and static properties generally differ from dynamic properties.

This project was aimed at developing a methodology for predicting sonic logging tool response accounting for intrinsic and stress-induced anisotropy of both static and dynamic elastic properties.

1.2 Research Objective

The primary objective of this research was to develop a workflow that enables quantitative prediction of sonic logging tool response as a function of intrinsic and stress-induced anisotropy of elastic properties. The secondary objective was to assess how bedding-related anisotropy and stress-induced anisotropy affect borehole sonic logging.

These objectives were achieved by undertaking the following tasks:

- Laboratory testing on rocks at representative field conditions (conducted by technical staff in the Rock Mechanics Laboratory) in order to establish relationships between elastic properties, orientation (intrinsic anisotropy), and stress (induced anisotropy);
- Development of a numerical modeling workflow, used with the laboratory data to simulate the stress state around a borehole and predict sonic logging results;
- Assessment of the numerical modeling workflow by comparing the results of simulations to the field data.

1.3 Significance of the Study

The results of this study provide a better understanding of the geomechanical and acoustic properties of the Montney Formation and the Deadwood Formation in the Western Canada Sedimentary Basin. The modeling workflow developed in this research provide an enhanced capability to interpret advanced sonic logging tool response.

1.4 Thesis Structure

This dissertation is organized with the following structure:

Chapter 2 begins with a general description of different borehole sonic logging tools. It also describes intrinsic anisotropy and stress-dependent behavior of rock because these affect the sonic tool's response. Also, different methods of stress analysis as well as borehole wave propagation modeling are explained. Finally, the study areas are characterized in terms of geology and geomechanical properties. Chapter 3 describes the methodology that was applied to achieve the objectives of this research. Results are presented in Chapter 4, and in Chapter 5 they are compared to field data. In Chapter 6, the conclusions of this research are summarized, limitations of this research are listed, and recommendations for future studies are presented.

2. Literature Review and Study Area Background

2.1 Borehole Sonic Logging

Various types of logging tools, such as sonic, are typically run down a hole after drilling is completed in order to provide a better understanding of the formations penetrated by the borehole. Most sonic logging tools are similar in terms of their basic operating principle. A sound pulse is transmitted into the formation using the tool's transmitter, and this sound is detected at other locations along the length of the tool by its receivers. By recording the arrival time of the acoustic energy at successive receivers at known, fixed locations, the sound wave velocity (or inverse velocity; i.e., "slowness" or interval transit time) of the rock can be calculated.

The arrival time and character of acoustic waves recorded by sonic logging tools depends on the energy source (transmitter), the path the wave follows, and the properties of the formation and the borehole. The main factor distinguishing between sonic logging tools is the nature of the energy source. Two primary types of transmitters used in wireline sonic logging are monopole and dipole. Monopole transmitters generate energy uniformly around the tool, while dipole transmitters emit energy in a preferred direction (Figure 2-1) (Xiang & Gaoyang, 2012; Petrowiki, 2015). Monopole, dipole and crossed dipole logging tools are described in this section.

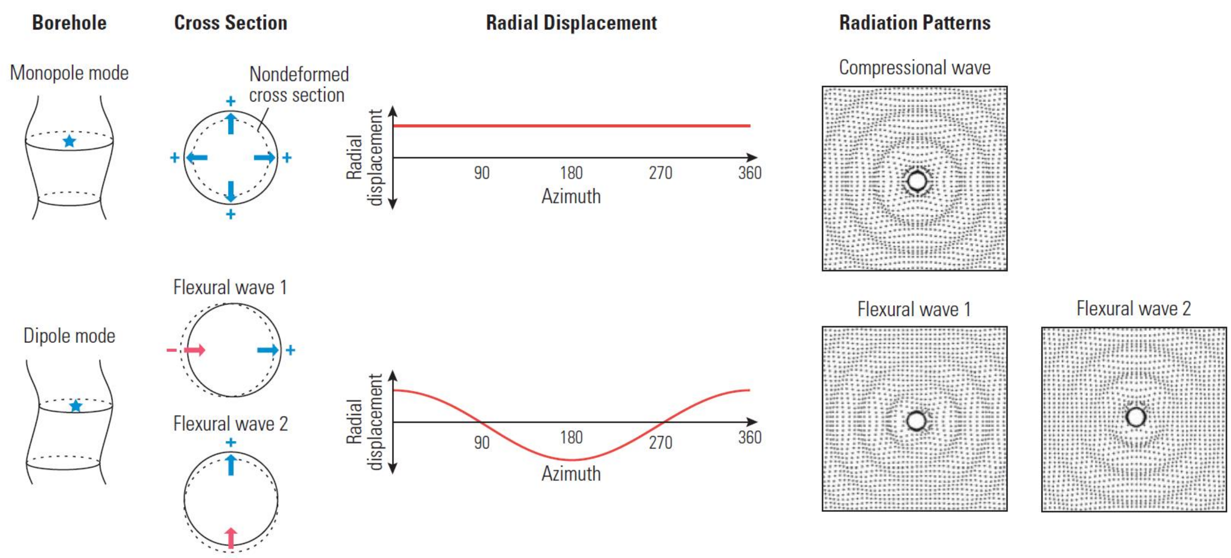

Figure 2-1: Two types of sonic sources (Alford et al., 2012).

2.1.1 Monopole Transmitter

The monopole transmitter is the most basic transmitter type and it is common across nearly all forms of sonic tools. The typical frequency range for monopole transmitters is from 0.5 to 40 kHz. When a monopole transmitter is activated, it generates a spherical wavefront which propagates through the mud-filled borehole, and eventually encounters the borehole wall. According to Snell's law, depending on the angle at which the wavefront meets the wall, part of the energy is reflected back into the borehole and part is refracted and propagates into the formation (Figure 2-2). The reflected part of energy creates a wavefront traveling toward the borehole center with a velocity (V_m) dictated by the properties of the drilling mud; this energy is generally not useful. The refracted part generates compressional or "primary" (P) and shear (S) wavefronts which travel through the formation with velocities V_P and V_s, respectively.

The critically refracted P-wave propagates parallel to the borehole-formation interface at a velocity faster than the reflected borehole-fluid wave. Moreover, every point on the interface, excited by the critically refracted P-wave, acts as a secondary source of P-waves in the drilling mud. These secondary sources create a new wavefront in the borehole known as a head wave, which is non-dispersive (i.e., the slowness of non-dispersive waveforms is independent of frequency) (Figure 2-3). The first sonic energy recorded at each receiver is the head wave generated by the P-wave propagating along the borehole wall. This is called the P arrival. The refracted P-waves that do not travel parallel to the borehole wall propagate through the formation as a body wave. Although these body waves could provide additional information about the formation, standard sonic logging tools are not able to record them.

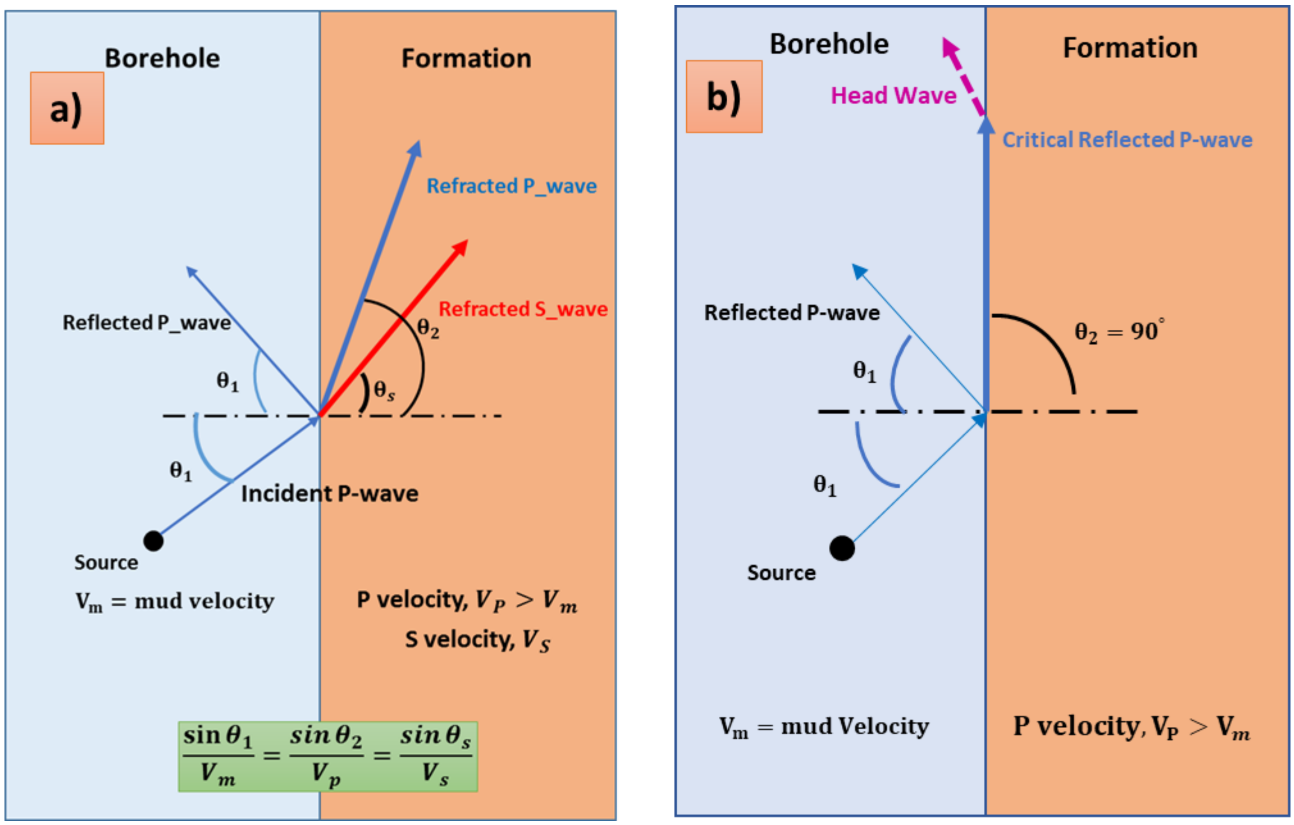

Figure 2-2: Wavefront refraction and reflection at borehole-formation interface, and Snell's law (after Haldorsen et al., 2006). a) General scenario, showing refracted waves. b) Critically refracted P-wave which propagates through the rock parallel to the borehole wall and makes a head wave which propagates back into the borehole.

The refracted S-wave follows a similar scenario to the refracted P-wave. The critically-refracted S-wave propagates parallel to the borehole wall at velocity V_S, and generates its own head wave (Figure 2-3). This headwave (termed the S-wave arrival) arrives at each receiver later than the P-wave arrival because V_S is less than V_P. It is worth noting that monopole receivers are only able to record the S-wave arrival in fast formations; i.e., formations in which V_S is greater than the borehole drilling mud fluid velocity. In slow formations, the shear wave does not produce an identifiable head wave, since critical angle of refraction does not occur due to slower shear formation velocity compared to the drilling mud velocity.

The Stoneley wave is the last arrival when using a monopole source. It is a surface wave that propagates along the borehole-formation interface with a velocity less than the mud wave and shear wave velocities. Compressional and Stoneley waves are always recorded by the receivers when using a monopole transmitter, even in slow formations. The Stoneley wave is slightly dispersive, so it shows frequency-dependent behavior and its amplitude decays with distance from the borehole wall (Figure 2-3). In other words, Stoneley-wave amplitude attenuates significantly at high frequencies and modern tools utilize low frequency transmitters (1-12 kHz) to ensure the acquisition of a Stoneley arrival in slow formations. Since the Stoneley-wave is sensitive to formation permeability, its dispersion data over a wide bandwidth of frequencies can be inverted to estimate formation permeability (Xiang & Gaoyang, 2012; Petrowiki, 2015; Haldorsen et al., 2006; Alford et al., 2012).

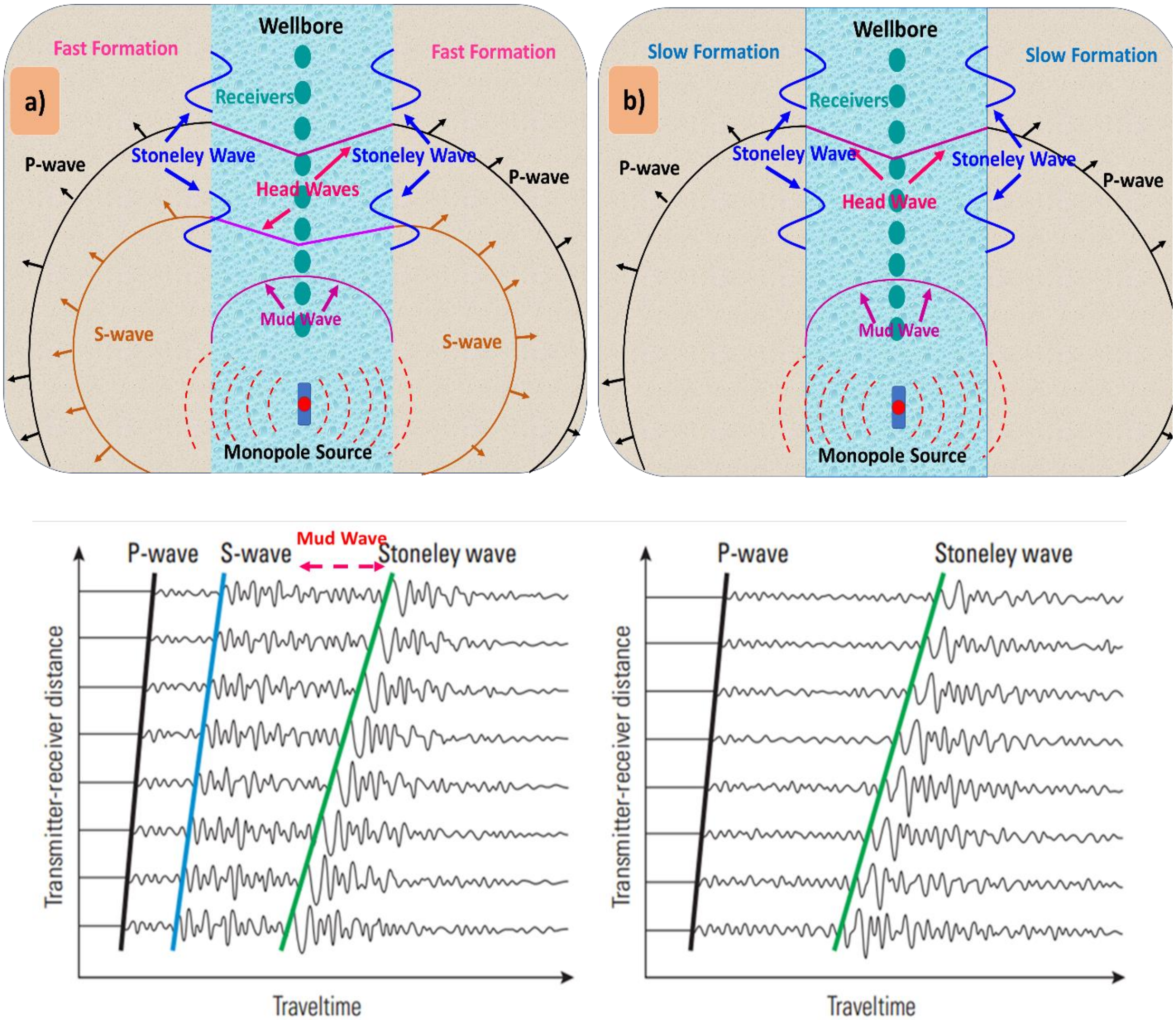

Figure 2-3: Different wave modes generated by a monopole source and recorded by an array of receivers in (a) fast and (b) slow formations (after Alford et al., 2012).

2.1.2 Dipole Transmitter

To enable shear wave velocity measurement in slow formations, the dipole sonic tool was invented. In such a tool, a low frequency (300 Hz to 8 kHz) dipole transmitter is used. The dipole transmitter generates a wave front that propagates in a linear fashion (Figure 2-4) towards the borehole wall, which in turn creates a flexural wave when it encounters the borehole wall (Petrowiki, 2015; Haldorsen et al., 2006; Alford et al., 2012).

The flexural wave generated by a dipole transmitter propagating along the borehole wall in the plane of the source. Particle motion in such a wave is perpendicular to the direction of wave propagation, in a similar fashion to an S-wave. Moreover, the shear wave slowness of the rock formation is estimated using the low-frequency components of the flexural wave slowness. This relationship provides a capability to interpret S-wave slowness from flexural-wave data (Alford et al., 2012).

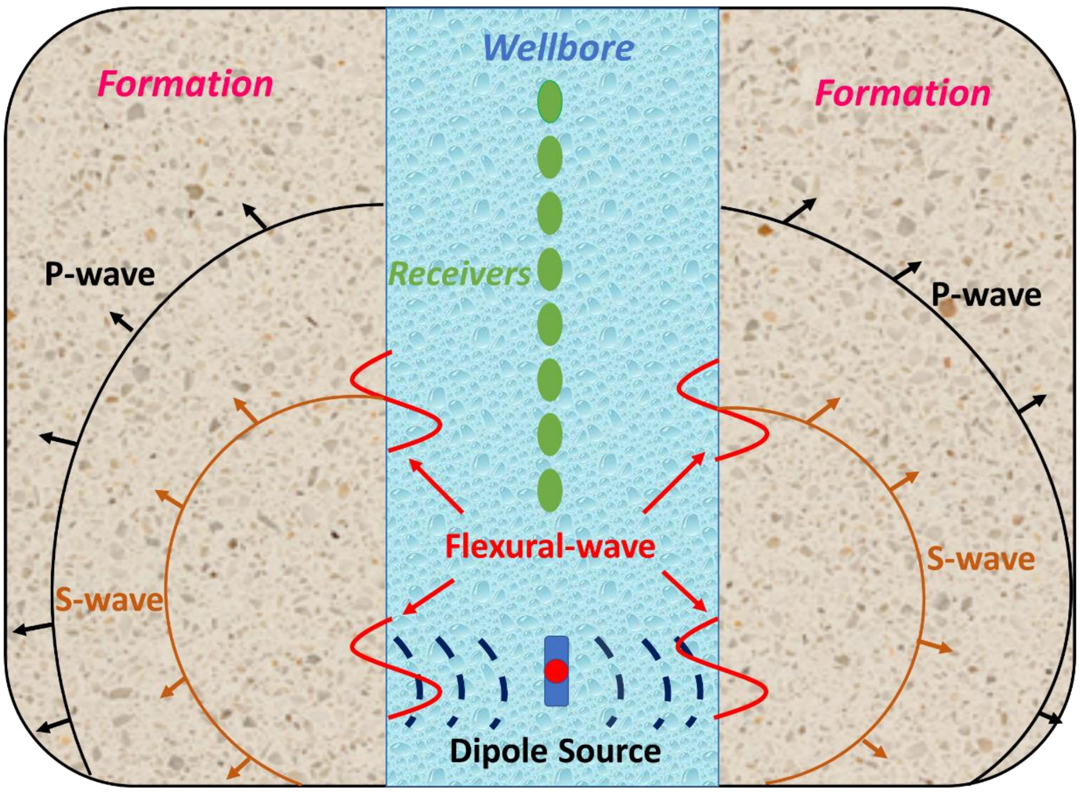

Figure 2-4: Acoustic wavetrain in a slow formation logged using a dipole transmitter (after Avila-Carrera et al., 2011).

2.1.3 Crossed-Dipole Transmitters

Crossed- dipole sonic logging tools typically integrate multipole transmitters (monopole and dipole) and one or more arrays of monopole and dipole receivers (Figure 2-5). Two adjacent dipole sources, of the same frequency and strength, are oriented orthogonally along the tool's X- and Y-axes. The dipole transmitters are fired separately; i.e., the X-dipole is first fired, and after recording its waveform at the receiver array, the Y-dipole is fired. Similarly, the monopole transmitter is fired separately, either before or after the dipole transmitters.

This combination of transmitters results in measuring compressional wave velocities (and shear wave velocities in fast formations) using the monopole sources, and measuring oriented shear wave velocities using the dipole sources. When a shear wave goes through an anisotropic medium, it is split into fast and slow components. One of the most significant achievements of crossed-dipole tools is their ability to provide data that can be used to interpret orientation (and in some cases magnitudes) of in-situ stresses by measuring stress-induced S-wave velocity anisotropy around and near a borehole. This is possible because the difference between two shear-wave velocities is proportional to the stress difference in the two directions of particle motion, and the direction of the fast shear wave is coincidentally aligned with the maximum stress orientation of the geologic formation (Sinha et al., 2000; Franco et al., 2006).

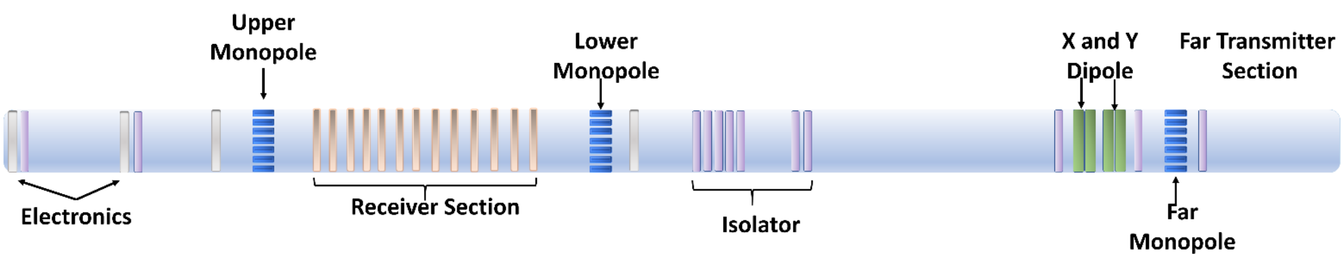

Figure 2-5: Sonic Scanner tool with three monopole transmitters and two orthogonal dipole transmitters (after Franco et al., 2006). Each receiver station typically has a monopole receiver and dipole receiver in the X and Y directions, respectively.

2.2 Elastic Property Anisotropy

The theory of elasticity is generally applied to explain the relationships between applied stress and strain for small deformations in linear elastic materials. Elastic behavior is relevant to this research because it controls the stress distributions around boreholes (static elastic properties) and wave propagation velocities (dynamic elastic properties).

The following relationship exists between applied stress and strain in elastic materials:

$$\sigma_{ij} = C_{ijkl}\varepsilon_{kl} \tag{2.1}$$

Where,

σ = Stress

ε = Strain

C = Stiffness tensor

C has 81 components but these reduce to 21 terms for the general case of an anisotropic medium with intrinsic symmetry and with other considerations, such as conservation of energy:

$$C_{ijkl} = C_{klij} \tag{2.2}$$

Depending upon the nature of a medium's anisotropy, even fewer elastic constants may be required to fully define C. An isotropic material is fully defined by two constants (C_{33} and C_{44}), while a material with cubic symmetry is described by 3 constants. A transversely anisotropic material is characterized by 5 constants (Zoback, 2010).

2.3 Anisotropic and Stress-dependent Rock Properties

Rocks are generally anisotropic in nature. This intrinsic characteristic of rocks results from layering of mineral grains, fractures, and/or differential stresses. A reasonable approximation for many rocks is transverse anisotropy in which the medium has an axis of rotational symmetry. As shown in Figure 2-6, the alignment of clay minerals and horizontal fine-scale layering in sedimentary rocks can result in vertical transverse isotropy (VTI) with a vertical axis of rotational symmetry, while horizontal transverse isotropy (HTI) with a horizontal axis of rotational symmetry can result in some rock masses containing vertical fractures, micro cracks or horizontal stress anisotropy (Sayers, 2010).

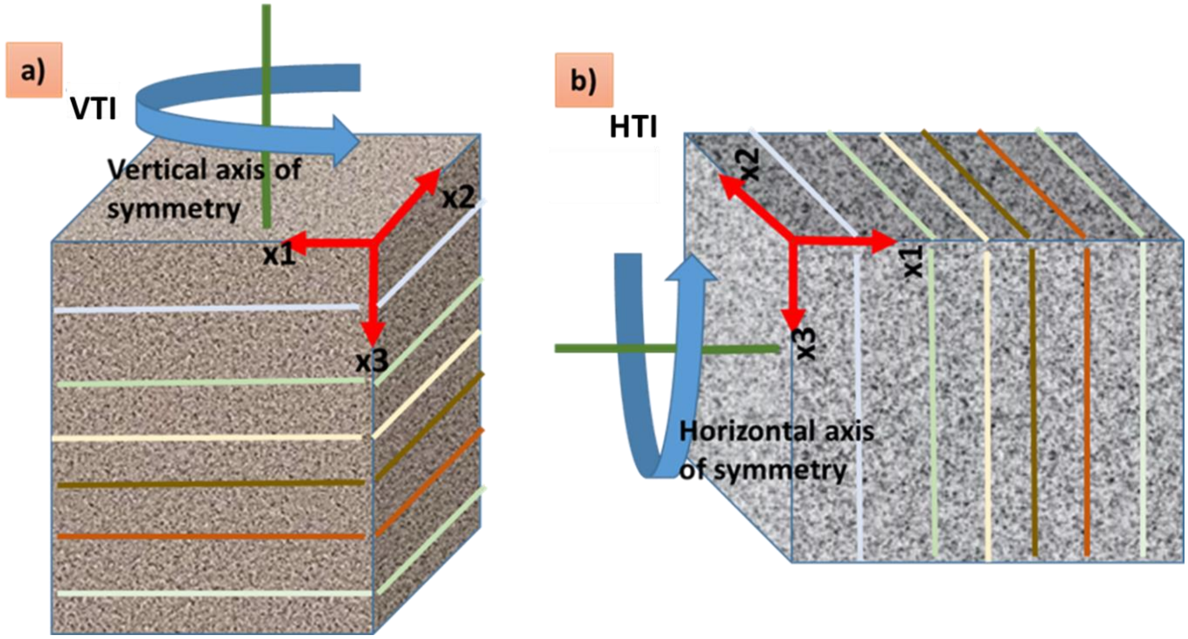

Figure 2-6: Illustration of transverse isotropy illustration for two simple cases: a) VTI anisotropy b) HTI anisotropy (after Haldorsen et al., 2006).

C_{11},C_{33}, C_{44}, C_{66} and C_{13} are the 5 elastic constants required to fully describe a body with vertical transverse isotropy, as follows:

$$C_{ij} = \begin{pmatrix} C_{11} & C_{12}(= C_{11} - 2C_{66}) & C_{13} & 0 & 0 & 0 \\ C_{12} & C_{11} & C_{13} & 0 & 0 & 0 \\ C_{13} & C_{13} & C_{33} & 0 & 0 & 0 \\ 0 & 0 & 0 & C_{44} & 0 & 0 \\ 0 & 0 & 0 & 0 & C_{44} & 0 \\ 0 & 0 & 0 & 0 & 0 & C_{66} \end{pmatrix} \tag{2.3}$$

Commonly used elastic properties such as Young's modulus (E), Poisson's ratio (ϑ) and shear modulus (G) can be defined in terms of elastic constants as follows:

$$E_1(= E_2) = \frac{(C_{11} - C_{12})[C_{33}(C_{11} + C_{12}) - 2C_{13}^2]}{C_{11}C_{33} - C_{13}^2} \tag{2.4}$$

$$E_3 = \frac{C_{33}(C_{11} + C_{12}) - 2C_{13}^2}{C_{11} + C_{12}} \tag{2.5}$$

$$\vartheta_{12} = \frac{C_{33}C_{12} - C_{13}^2}{C_{11}C_{33} - C_{13}^2} \tag{2.6}$$

$$\vartheta_{31} = \frac{C_{13}}{C_{11} + C_{12}} \tag{2.7}$$

$$G_{23} = C_{44} \tag{2.8}$$

Where the subscripts 1, 2 and 3 refer to the coordinate axis directions indicated in Figure 2-6 and:

ϑ_{12}= Ratio of ε_{22} to ε_{11} due to σ_{11}

ϑ_{13}= Ratio of ε_{33} to ε_{11} due to σ_{11}

ϑ_{31}= Ratio of ε_{11} to ε_{33} due to σ_{33}

G_{23}= Contribution of ε_{23} to τ_{23}

The work of previous investigators has resulted in the following equations which relate phase velocities to dynamic elastic constants in a medium with vertical transverse isotropic symmetry (VTI) (Melendez, 2014):

$$C_{11} = \rho V_{P_{90^\circ}}^2 \tag{2.9}$$

$$C_{33} = \rho V_{P_{0^\circ}}^2 \tag{2.10}$$

$$C_{44} = \rho V_{S_{0^\circ}}^2 \tag{2.11}$$

$$C_{66} = \rho V_{SH_{90^\circ}}^2 \tag{2.12}$$

$$C_{13} = -C_{44} + \left[\frac{\left(4\rho V_{P_{45^\circ}}^2 - C_{11} - C_{33} - 2C_{44}\right)^2 - (C_{11} - C_{33})^2}{4}\right]^{1/2} \tag{2.13}$$

Where

$V_{P_{90^\circ}}$ = Compressional velocity in the direction parallel to the bedding

$V_{P_{45^\circ}}$ = Compressional velocity in the direction 45° to the bedding

$V_{P_{0^\circ}}$ = Compressional velocity in the direction perpendicular to the bedding

$V_{SH_{90^\circ}}$ = Shear velocity in the direction parallel to the bedding

$V_{S_{0^\circ}}$ = Shear velocity in the direction perpendicular to the bedding

In recent decades, a significant amount of laboratory research has been conducted to investigate the effects of confining pressure on both dynamic and static elastic constants. By definition, the dynamic moduli of rock are those calculated from the elastic wave velocity and density, while the static moduli are those directly measured in a deformational experiment. Figure 2-7 illustrates how that acoustic velocities in rocks are generally sensitive to stress; i.e., acoustic velocities tend to increase with stress. This is generally attributed to the closing of compliant, crack-like pore space, including microcracks and compliant grain boundaries. As confining pressure is raised, the most compliant pores are closed, followed by the next most compliant, and so on. Closing pores results in an increase of the mechanical stiffness of rocks, and corresponding increase in acoustic velocities of rock (Melendez, 2014; Sone & Zoback, 2013; Hawkes et al., 2015; Mavko & Godfrey, 1995; Wang, 2002). The same processes also account for the increase is static stiffness that is generally observed with increasing stress in rocks.

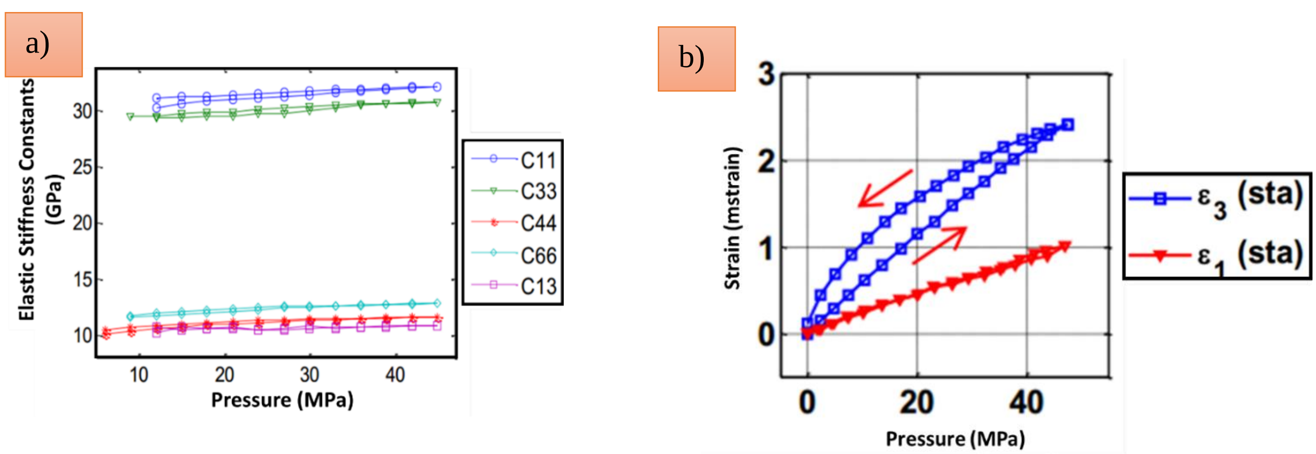

Figure 2-7: Effect of confining pressure on (a) dynamic and (b) static elastic constants (Melendez, 2014).

2.4 Borehole Stress Analysis

Variations in the origin, magnitude, and direction of the stresses acting on formations could stem from characteristics of the formation such as lithology, pore pressure and temperature and from processes such as burial, uplift, erosion and tectonic events. Over geological time, in-situ reservoir stresses generally reach an equilibrium. In an unstressed state, reservoir rocks may show varying degrees of intrinsic anisotropy (e.g., limited anisotropy in a massive sandstone reservoir; significant anisotropy in a shale gas reservoir). Regardless, by excavating a borehole, the local stress distribution is significantly altered since rock stresses in the vicinity of the borehole are redistributed. The support that was originally offered by the drilled-out rock is replaced by the hydraulic pressure of the mud. This process gives rise to altering grain contact stresses and may open or close cracks in the surrounding rocks, thus causing an additional component of stress-induced anisotropy. Both components of anisotropy must be considered in the estimation of rock properties and in-situ stresses. This section introduces analytical and numerical approaches for estimating stress magnitudes.

2.4.1 Analytical Method

Equations for calculating induced stresses around a circular hole were initially derived by Kirsch and have been adapted for boreholes in porous media (e.g., Zoback, 2010). These equations are based on linear elasticity and assume isotropic rock properties.This scenario may be acceptable for shallow rock engineering and for sedimentary rocks with massive bedding structures; however, with increase in drilling depth and prevalence of fine bedding, the anisotropic properties of the rock mass become more pronounced.

Aadnoy (1987) developed a mathematical model to the calculate elastic stresses around an inclined borehole in a medium that behaves as a transverse isotropic body. Aadnoy’s model is based on linear elasticity and it neglects plastic or time-dependent effects. Also, his model is limited to the boreholes greater than 2000 ft (610 m) deep (in order to have infinity assumption). This model is based on a generalized plain strain assumption. As shown in Figure 2.8, the stress state around the perimeter of a borehole can be notably different for a rock with transversely-isotropic elastic properties compared to isotropic properties.

Although solutions of this type are commonly used in industry, the stress-dependent elastic properties of formations are not taken into account. This results in less representative estimation of stresses around a borehole.

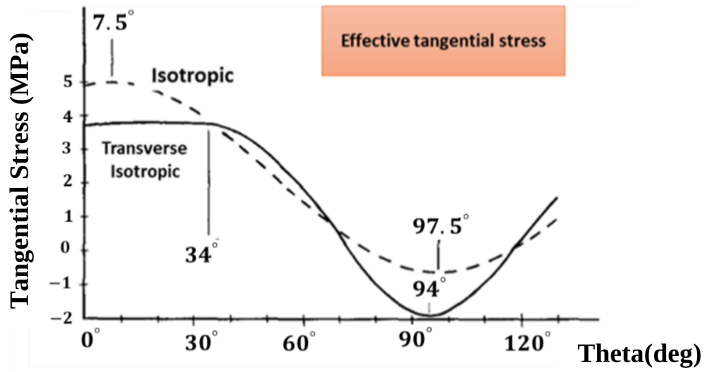

Figure 2-8: This figure represents the stress distribution around borehole (theta) based on scenario of transverse isotropic rock properties as per Aadnoy (1987). The magnitudes and angular positions of stress peaks and troughs are different for the isotropic case compared to the case with transverse isotropy.

2.4.2 Numerical Method

Numerical modelling is a powerful method of borehole stress analysis which can be used to analyze stress-induced anisotropy with any degree of isotropic, vertical, horizontal transverse or, orthorhombic anisotropy at any depth. In particular, the finite element method (FEM) has been used many times as an approach to calculate the stress field around a borehole (Figure 2-9) (e.g., Fang et al., 2013; Liu & Sinha, 2003).

In drilling operations, borehole breakouts (i.e., borehole enlargements that develop in a preferential direction due to failure and spalling of rock fragments in zones of peak stress around the perimeter of a borehole) may develop in rocks that are relatively weak and/or subjected to relatively high in-situ stresses. These features are useful for geomechanical site characterization because they grow in a direction parallel to the minimum horizontal stress (σ_{hmin}), however they cannot be analyzed using analytical methods, since the stress state becomes complex as the borehole geometry becomes non-circular. Numerical modeling can be used to analyze borehole breakouts, by defining an appropriate failure criterion. For example, an elasto-plastic material model may be assumed, with anisotropic yield characteristics where applicable, in order to simulate the development of a failed zone (Zoback et al., 1985; Zou et al, 1996; Frydman & Sergio, 1997), which effectively serves as an estimate of the size and shape of the borehole breakouts.

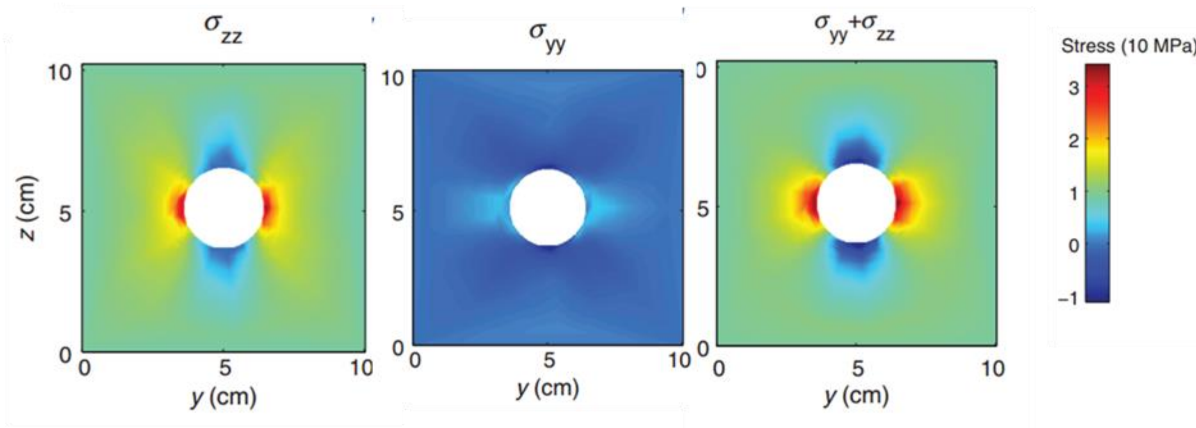

Figure 2-9: Distribution of normal stresses around a borehole (in zz and yy directions) as modeled by a FEM software (Fang et al., 2013).

2.5 Borehole Wave Propagation Modeling

There has been significant attention towards the study of variations in velocities based on formation stresses and pressures, since characterization of these variations is required to estimate in-situ stress magnitudes. Over recent decades, significant effort has been allocated to developing approaches to analyze synthetic waveforms of monopole or dipole sources in a borehole containing pressurized fluid (Fang et al., 2013; Liu & Sinha, 2003; Cheng, 1994; Winkler et al., 1998; Sinha et al., 1996; Liu & Sinha, 2000). Three methods have been developed for this purpose: (1) analytical, (2) semi-analytical, and (3) numerical. Methods 1 and 2 will not be used in this research, other than to validate numerical modeling outputs. Regardless, all these methods are described in sections 2.5.1 to 2.5.3.

2.5.1 Analytical Solution

In this method, a borehole of radius a is considered, filled with nonviscous fluid with density ρ_1 . A cylindrical coordinate system (r, θ, z) is used that extends to infinity in the z direction. The borehole is embedded in an infinite homogeneous and perfectly elastic medium and a point source is located (r_0, θ_0, z_0) in the borehole fluid.

This model can be implemented for different types of acoustic sources including monopole, dipole, quadrupole. Helmholtz's theorem is applied as a general solution to solve the problem in an elastic formation. According to this theorem, the displacement vector with radial, azimuthal, and vertical components (u, v, w) satisfies a vector wave equation. From the displacements, the elements of the strain tensor in the cylindrical coordinate system are calculated which results in obtaining stress elements based on Hooke's law (Figure 2-10) (Tang & Cheng, 2004).

By calculating the stress field and applying a boundary condition, wave motion in such a borehole is related to the wave motion of the formation. Mathematically, the reflected wave field in the borehole is obtained which, together with the direct wave field radiated from the source, results in obtaining the acoustic wave field in the borehole (Figure 2-11). To simulate logging with an acoustic tool, the wave field on the axis of the borehole is studied (Tang & Cheng, 2004).

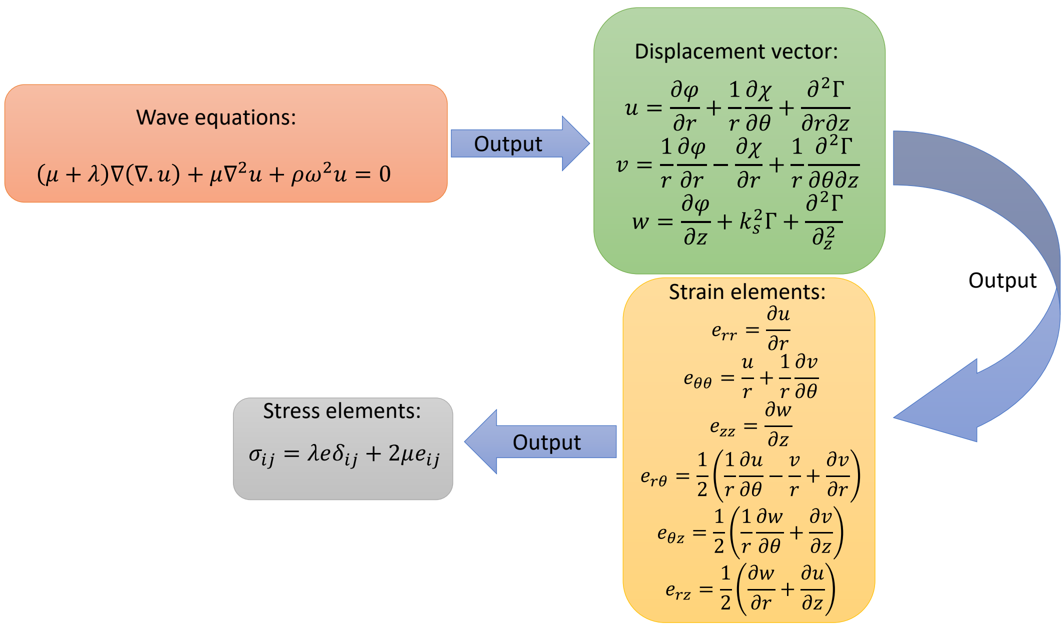

Figure 2-10: Workflow of analytical solution to calculate the dynamic stress field during wave propagation.

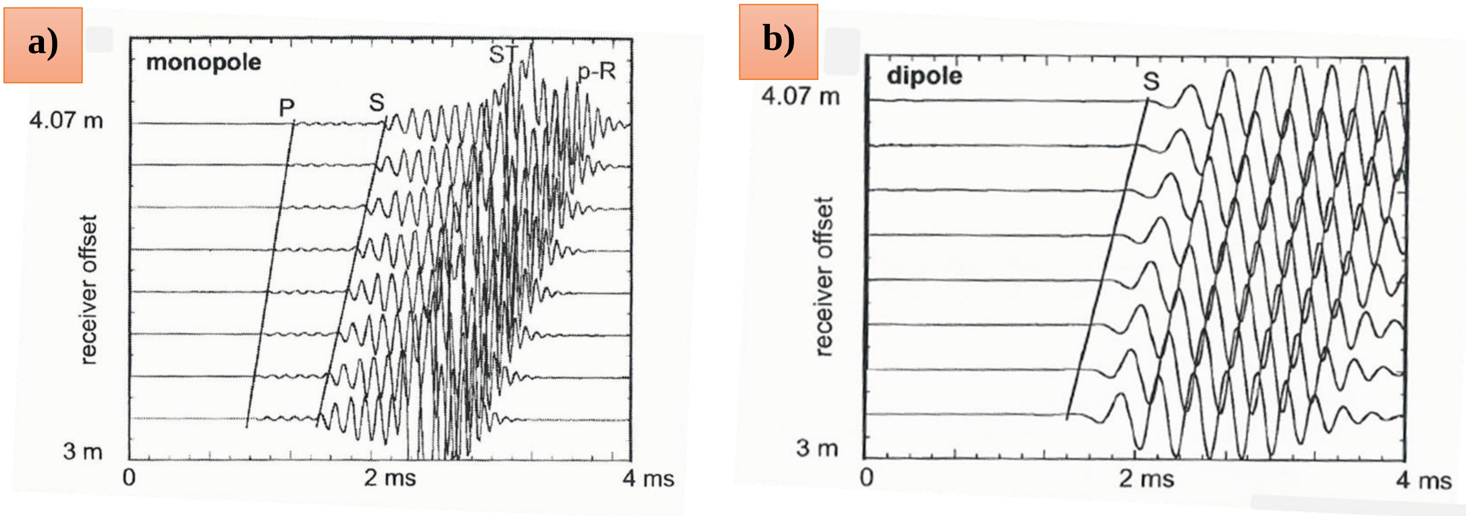

Figure 2-11: Simulated sonic logging wave-forms generated using an analytical solution (Tang & Cheng, 2004).

The analytical solution is only applicable for the condition that the formation around the borehole is a homogenous isotropic medium. In analyzing complex problems, the analytical solution is not considered as an appropriate choice to quantify the cause of variation in velocities in different formations and directions, since it cannot simply filter out the existing overlap between S-wave arrival times. Moreover, the effect of stress concentration around the borehole is not included in analytical approaches.

2.5.2 Semi-Analytical Approach

In more complex cases such as fast and slow formations, or an anisotropic formation, a semi-analytical method would be preferred to analytical solutions to evaluate the response of static media to excitation by transient point sources. Consider a fluid-filled cylindrical borehole of radius a_0 embedded in a radially stratified transversely isotropic medium (Figure 2-12). Each layer of stratification is characterized by five elastic constants $C_{11}^{(j)}$, $C_{12}^{(j)}$, $C_{13}^{(j)}$, $C_{33}^{(j)}$ and $C_{44}^{(j)}$ and the densityρ^j of the formation.

A multilayered elastic media assumption about the surrounding media has given rise to applying Thomson-Haskell transfer matrices to derive stiffness matrices for such media to propagate displacement-stress vectors through the formation. In this approach, a scalar potential φ is defined which satisfies the wave equation. The gradient of the scalar potential φ gives rise to the displacement of the particles in the fluid $u = \nabla\varphi(r,t)$ at a point defined by position vector r and at time t. Semi-analytical solutions vary in terms of numerical integration methods. Two typical solutions are real axis integration and branch-cut integration (Schmitt, 1988; Roever et al., 1974; Bouchon, 2003; Kurkjian, 1985; Schmitt, 1989; Chan & Tsang, 1983).

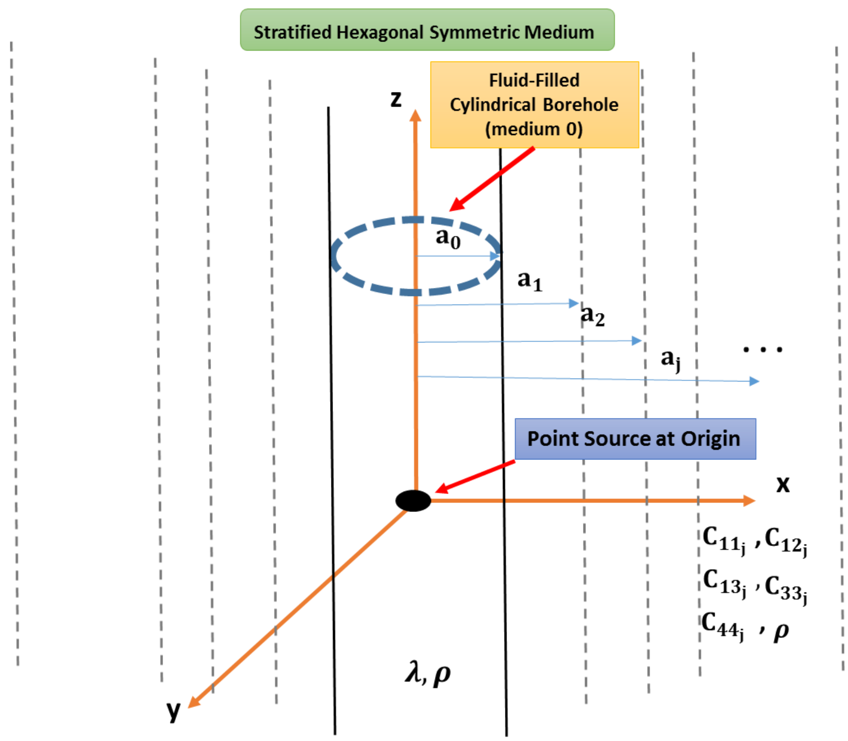

Figure 2-12: Schematic of semi-analytical solution for simulating wave propagation around a borehole (Chan & Tsang, 1983).

The real axis integration (RAI) method consists of integration along the Laplace contour in the complex frequency wave-number plane. This method yields the complete transient waveform including all arrivals, but it requires extensive computation time (Che et al., 2005; Chan & Tsang, 1983; Muga et al., 2015). A full waveform is shown in Figure 2-13.

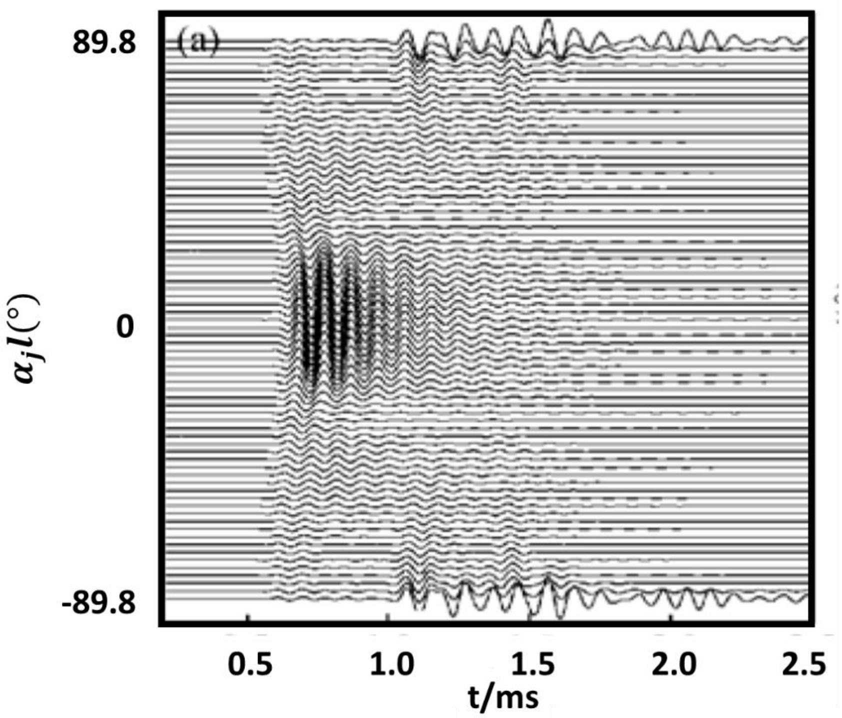

Figure 2-13: Full waveforms calculated based on real axis integration, where $\alpha_j l$ stands for radial wave number(RAI) (Che et al., 2005).

In Branch-cut Integration the compressional and shear wave arrivals are studied individually by using branch cuts which are chosen to coincide with the paths of steepest descent. This method results in a substantial reduction of computation time. It also allows for study of the frequency spectrum of the impulse response of compressional and shear head waves by branch-cut integration. Since branch-cut integration studies use individual arrivals, the problem of S-wave overlap in the full waveform analysis is solved. As well, this technique enables examination of the sensitivities of each arrival to various factors (Figure 2-14) (Schmitt, 1988; Roever et al. 1974; Bouchon, 2003; Kurkjian, 1985; Schmitt, 1989).

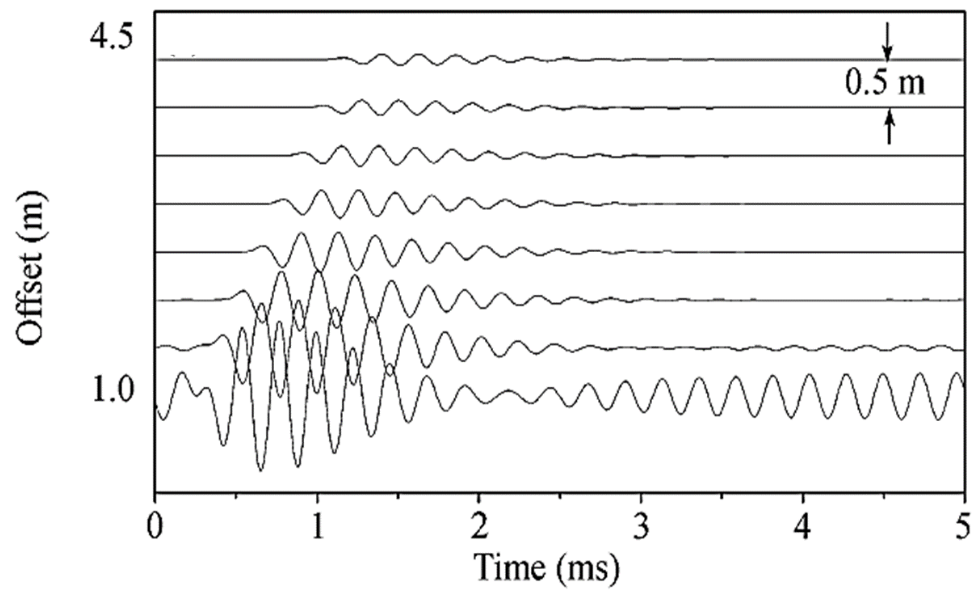

Figure 2-14: Simulated dipole waveforms by branch-cut integration approach (Zhang et al., 2009).

Analytical and semi-analytical solutions are restricted to a condition in which the borehole axis is parallel to the symmetry axis of the TI formation. Hence, these solutions of the wave field cannot be used when the borehole axis is deviated. Moreover, in both the semi-analytical and analytical methods, the influence of stress concentration around a borehole is not taken into account. In addition, in more complex studies, the semi-analytical solution provides approximate solutions, giving rise to less accuracy in the results.

2.5.3 Numerical Approach

Numerical solutions of wave propagation problems in and around boreholes can overcome the limiting assumptions common to analytical and semi-analytical solutions. In a prestressed formation, a finite difference formulation of the equations of motion for elastic waves is generally utilized to calculate synthetic waveforms at an array of receivers in a liquid-filled borehole (Fang et al., 2013; Liu & Sinha, 2003). These formulations have been developed to investigate the effect of borehole hydrostatic (mud) pressure as well as formation stresses on acoustic waves emitted by either a monopole or dipole transmitter located on the borehole axis. They are suitable to model waves in deviated boreholes penetrating transversely isotropic formations (Lin & Liu, 2015; Liu & Liu, 2014).

A specific version of the finite difference method widely used in simulating fluid-filled boreholes is the finite-difference time-domain (FDTD) method. This method has proven to be a highly efficient technique for numerous applications in wave propagation around a borehole because it consideres both intrinsic and stress-induced anisotropy in the interpretation of the data (Figure 2-15). Comprehensive references on this topic can be found in a number of papers (Liu & Sinha, 2003; Cheng, 1994; Lin & Liu, 2015; Liu & Lin, 2014).

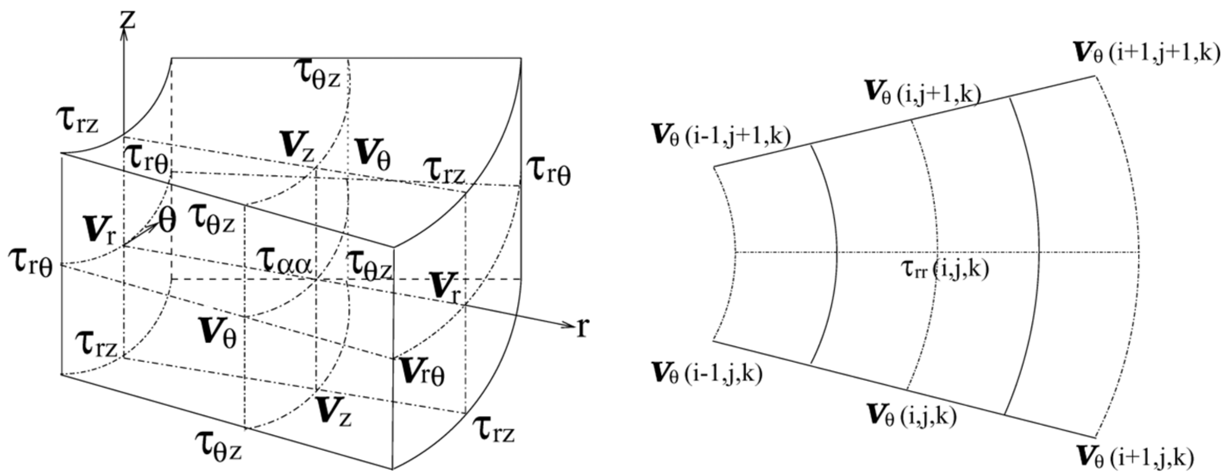

Figure 2-15: A unit cell of the finite-difference staggered grid for prestressed media (Liu & Sinha, 2003).

There are two general types of FDTD which vary in terms of dimension. They are exclusively applied to simulate wave propagation around the borehole in a cylindrical system to determine the stress coefficients of velocities as a function of frequency, as follows:

1. 2.5-dimensional finite difference time domain (2.5D FDTD).
2. 3-dimensional finite difference time domain (3D FDTD).

Liu et al. (2014) developed a 2.5-dimensional method to investigate the mode waves in a deviated borehole embedded in a transversely isotropic formation. The phase velocity dispersion curves of the fast and slow flexural mode waves excited by a dipole source are computed accurately at different deviation angles for both hard and soft formations. The sensitivity of flexural mode waves to all five elastic constants are calculated (Figure 2-17) (Lin & Liu, 2014; Liu & Lin, 2015).

It is worth nothing that the 3D version of FDTD has several advantages over the 2.5D version, which makes it more effective for analyzing elastic waves in fluid-filled boreholes in triaxially stressed formations. These advantages are listed as follows (Figure 2-16) (Liu & Sinha, 2003; Liu & Sinha, 2000) and a comparison of results is shown in Figure 2-16:

1. 3D FDTD can consider 3D heterogeneities, while 2.5D FDTD only considers heterogeneities in the plane transverse to the borehole axis.
2. Static wellbore pressure and the vertical overburden are accounted in 3D FDTD, whereas the 2.5D method only accounts for transvers stresses.
3. The PML boundary condition (discussed below) can be used in 3D FDTD, which is more accurate and stable than the Liu et al (2014). boundary condition in 2.5D FDTD.

In 2011, a new version of finite difference code was introduced known as FD3D. In this new version, the absorbing boundary condition (Convolution Perfectly-Matched-Layer) and the grid of finite difference grid (the standard-staggered-grid) was improved to solve the velocity-stress hyperbolic system of wave propagation with higher accuracy in time and space (Figure 2-18). Moreover, this version is capable of simulating wave propagation in both elastic and viscoelastic media. Another advantage of this version is its capability of simulating in one, two and three dimensions (Zhang, 2011).

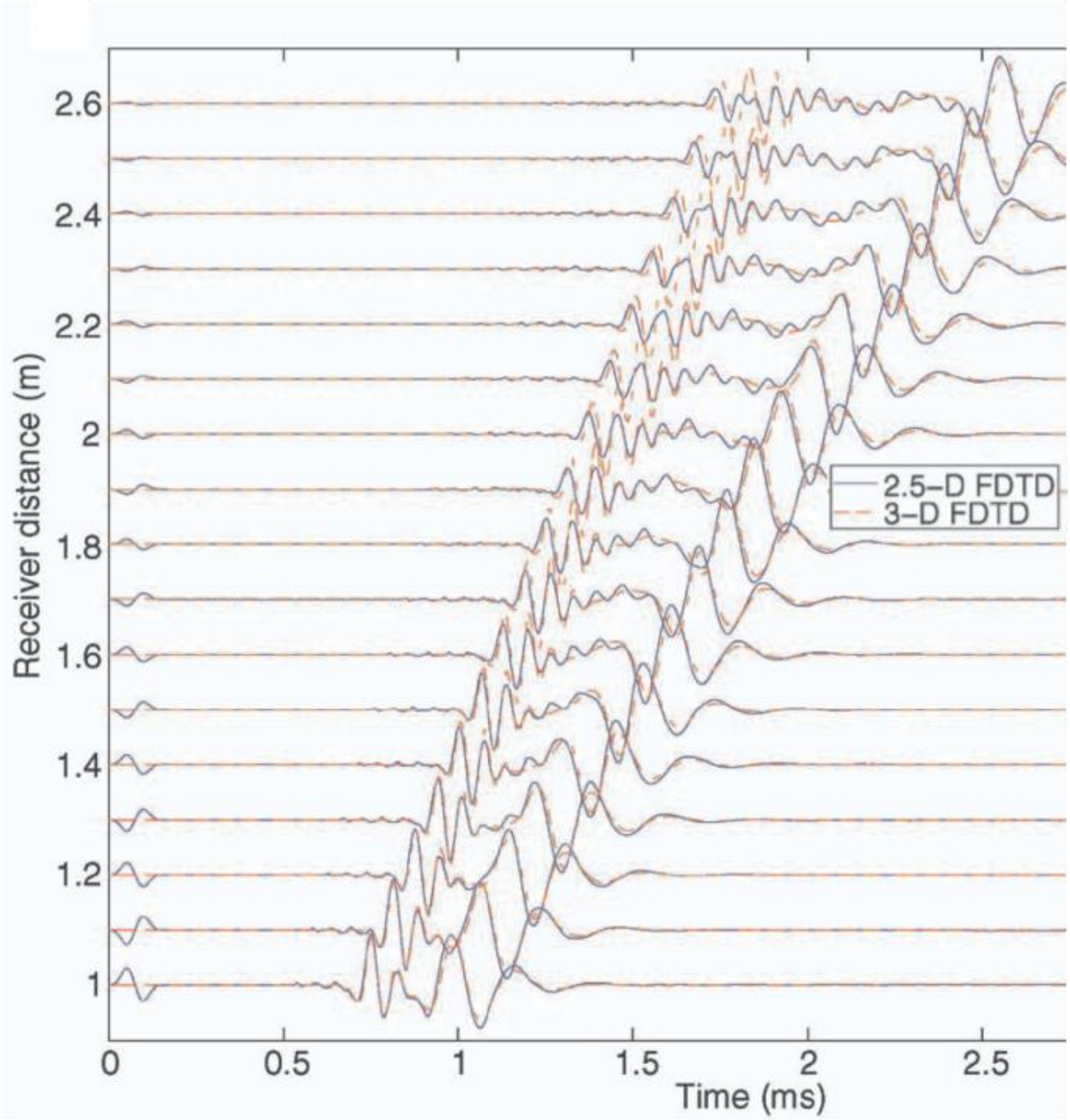

Figure 2-16: Comparison of simulated dipole waveforms (2.5 D vs. 3D) for a formation under biaxial prestress for a center frequency of 10 kHz (Liu & Sinha, 2003).

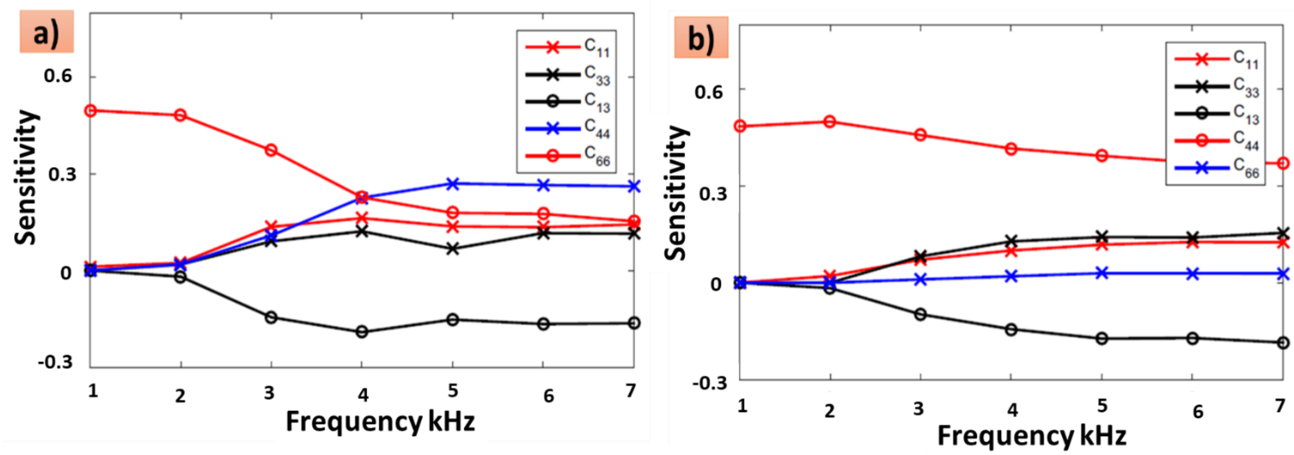

Figure 2-17: Sensitivity of elastic constants to frequency for $\alpha = 90^{\circ}$ for a) a fast flexural wave b) and a slow flexural wave (Lin & Liu, 2015).

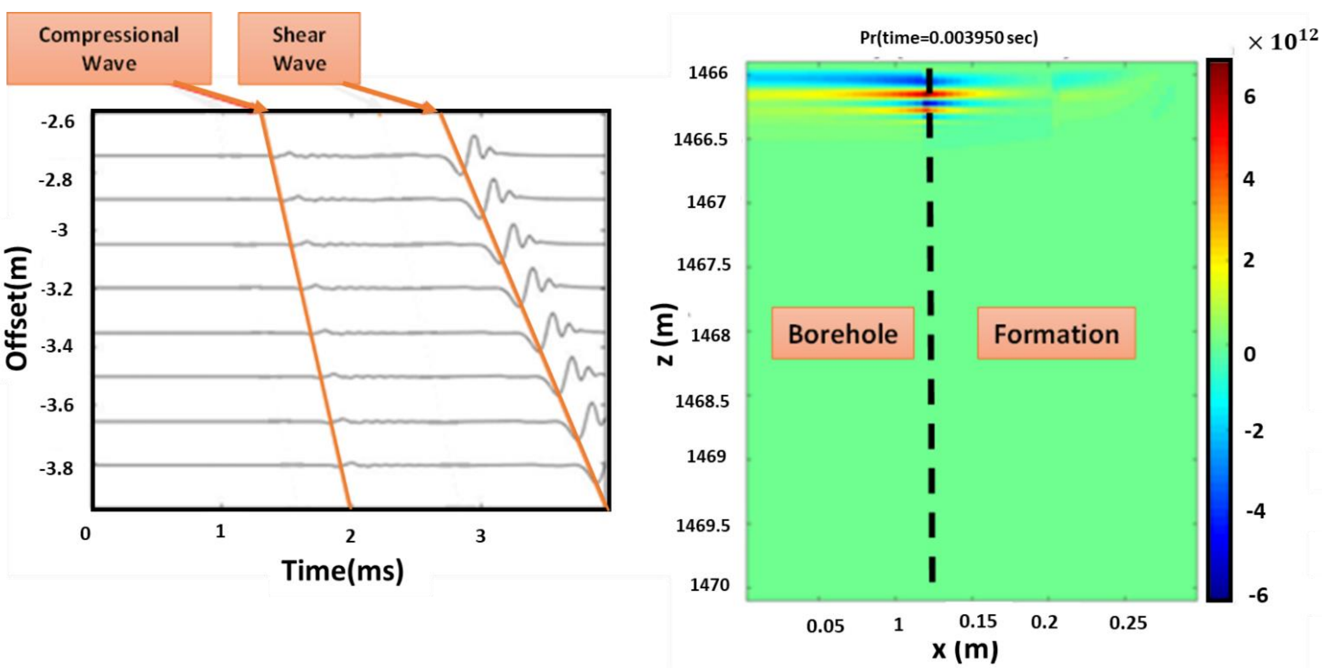

Figure 2-18: Wave propagation traces generated by the author using FD3D a) monopole waveforms simulated using the FD3D code, and b) snapshot of pressure generated inside formation surrounding a borehole by a point source located close to the bottom of the borehole.

2.6 Dispersion Analysis

As noted in section 2.1.1, the flexural waves induced by dipole transmitters are dispersive; i.e., the slowness of flexural waves is dependent on frequency (or dispersive waves). Analysis of flexural-wave dispersion curves generated from dipole sonic logging helps to classify formations according to anisotropy type (i.e., intrinsic anisotropy or stress-induced anisotropy) by comparing observed dispersion curves to those modeled assuming a homogenous isotropic formation. In a homogeneous isotropic formation, shear waves do not split into fast and slow components, so the two observed flexural-wave dispersion curves have identical slowness-versus- frequency signatures, and will overlie one another (Figure 2-19.a) (Franco et al., 2006).

In a vertical borehole scenario through a VTI layered formation (or horizontal borehole scenario through an HTI layered formation), there is no azimuth variation of shear slowness around the borehole (by assuming no stress differential) (Figure 2-19.a). In this condition, the shape of dispersion curves is the same as homogenous isotropic condition. It does not mean that there is no intrinsic anisotropy, there would be anisotropy but because of the study direction it would not be seen.

In cases of intrinsic anisotropy, when a dipole transmitter is fired inside the anisotropic formation, a fast shear wave is polarized in the fast direction (i.e., particle motion within bedding) and slow shear is polarized in slow direction (i.e., particle motion normal to bedding). As such the two dispersion curves remain offset at all frequencies and tend to true slowness at low frequency (e.g., horizontal borehole through VTI layered formation / vertical borehole through an HTI formation) (Figure 2-19.b).

In a formation with stress-induced anisotropy, the fast and slow shear-wave dispersion curves cross. This characteristics feature is caused by near-wellbore stress concentration (Figure 2-19.c). By drilling a borehole, the stress regime around the borehole is reorganized with compressive hoop stress, which is maximum in the direction of minimum far-field stress and minimum in the direction of maximum far-field stress (Figure 2-20). This reorganization results in having fast shear waves in the direction of minimum stress and slow shear wave in the direction of maximum stress at high frequency (near the borehole), while fast shear waves are recorded in the direction of maximum stress and slow shear waves in the direction of minimum stress at low frequency (further from the borehole) (Figure 2-20).

These simplified relationships between dispersion curves are valid when only one physical mechanism controls wave behavior. When multiple mechanisms are involved (e.g., both stress-induced and intrinsic anisotropy), the curves can be different.

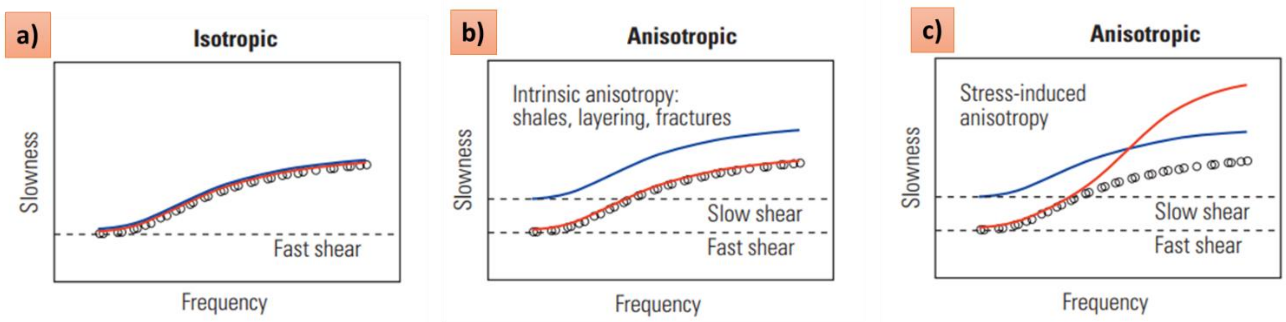

Figure 2-19: Flexural wave dispersion curves for classifying formation anisotropy based on recorded flexural waves on orthogonal dipole receivers (red and blue curves); black circles represent flexural-wave dispersion curves based on a homogenous isotropic model. : a) Borehole drilled through an isotropic formation or vertical borehole drilled through a VTI anisotropic formation / horizontal borehole drilled through an HTI anisotropic formation; b) Horizontal borehole drilled through a VTI anisotropic formation / vertical borehole drilled through an HTI anisotropic formation; c) Stress-induced anisotropy plot (Franco et al., 2006).

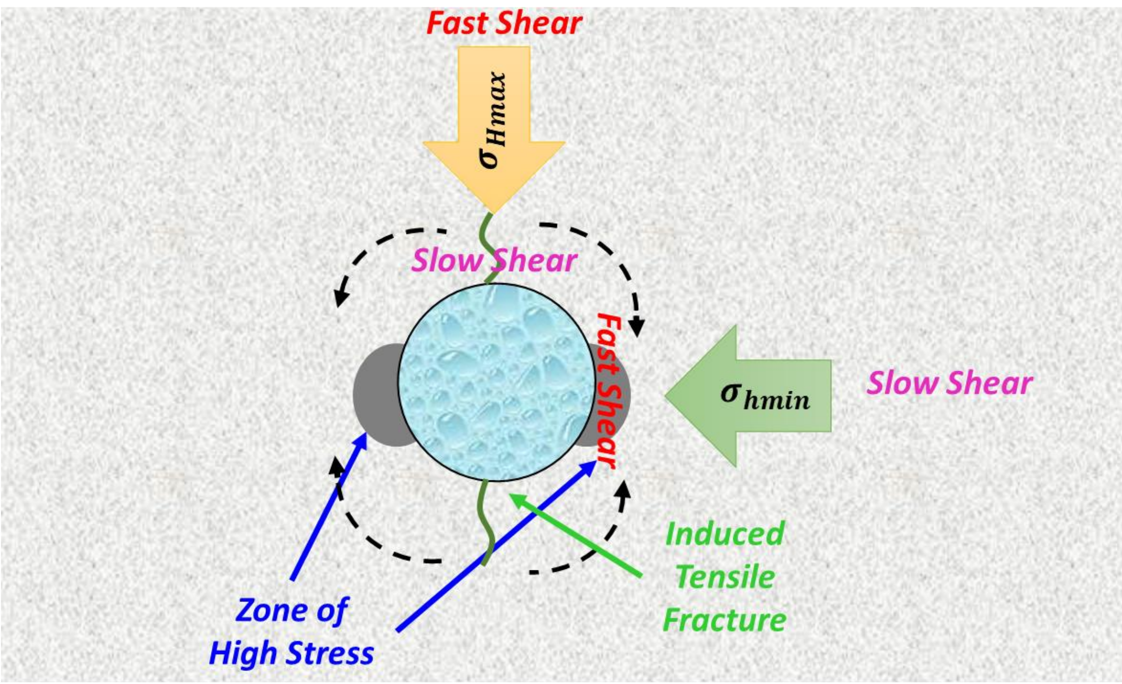

Figure 2-20: Reorganization of stress regime around a borehole, and impacts of stress on shear wave velocities. Note that zones of low stress occur near the borehole in the direction parallel to σ_{Hmax}. In some cases, induced tensile fractures (as shown in the figure) may develop in these zones; however, fracturing (and fracture-related stress changes) are not considered in this work. Similarly, borehole breakouts may develop in the zones of high stress, but these features are not considered in this work.

2.7 Study Areas

2.7.1 Farrell Creek (Montney Formation)

The Montney Formation is an aerially extensive unconventional resource in northeastern British Columbia and northwestern Alberta with significant natural gas and natural gas liquids in place. Development of the Montney began in the 1950's, targeting conventional sandstone and dolostone reservoirs predominantly in the east. The unconventional part of this reservoir remained undeveloped until 2005. After 2005, advances in horizontal drilling and multi-stage hydraulic fracturing made it possible to economically develop this resource. More recently, the exploration interest has focused on fine-grained (tight gas/shale) intervals in both the Lower and Upper members of the Montney.

2.7.1.1 Geological Characterization

The Lower Triassic aged Montney Formation of the Western Canadian Sedimentary Basin has been the focus of a large number of studies since the 1950s, including those by Markhasin (1998), Kendall (1999), Moslow (1997), Zonneveld et al. (2010).

The 143,000 km^2 area covered by Montney Formation stretches from northeastern British Columbia to northwestern Alberta (Figure 2-21). The thickness of this formation varies from less than 1 m in the east to over 350 m in the west. Stratigraphically, the Montney Formation is unconformably underlain by Permian Belloy Formation and is overlain by the Middle Triassic Doig Formation (Rogers et al., 2014; Davey, 2012; Walesh et al., 2006; Note, 2013; Egbobawaye., 2013; Yang, 2018). Figure 2-21 shows the stratigraphic chart.

The deposition of the Montney Formation occurred in a ramp setting, and a ramp edge or slope break defines the updip depositional limit of the turbidite facies. The other facies are conventional sandstone in the east through shelf siltstone and sandstones to shale facies in the west. The boundary between the Lower and Upper Montney Formation is a retrogradational shoreface succession and consists of laterally discontinuous dolomite coquina beds. The Lower Montney contains reservoir-quality, upward-coarsening shoreface and coarse siltstones. The Upper Montney consists of multicyclic coarsening-upward shoreface siltstones and interbedded very fine sandstones with hummocky cross-stratification and local developments of thin dolomitized coquina facies (Duenas, 2014; Davey, 2012). In terms of the reservoir property characteristics, the

Montney Formation has: low matrix permeability (0.01-0.02 mD) and low porosity (6-10%), which is formally defined as tight gas. Compared to other shale reservoirs, the Montney Formation shows a higher percentage of quartz and dolomite minerals in general.

In this study, the area of interest is the Farrell Creek Field (also reffered to as Altares) (Figure 2-23). The Farrell Creek Field produces from distal facies of the Montney Formation, which formed in a basinal setting. Farrell Creek is actively being developed for its unconventional shale assets and produces entirely dry gas hydrocarbons (Davey, 2012).

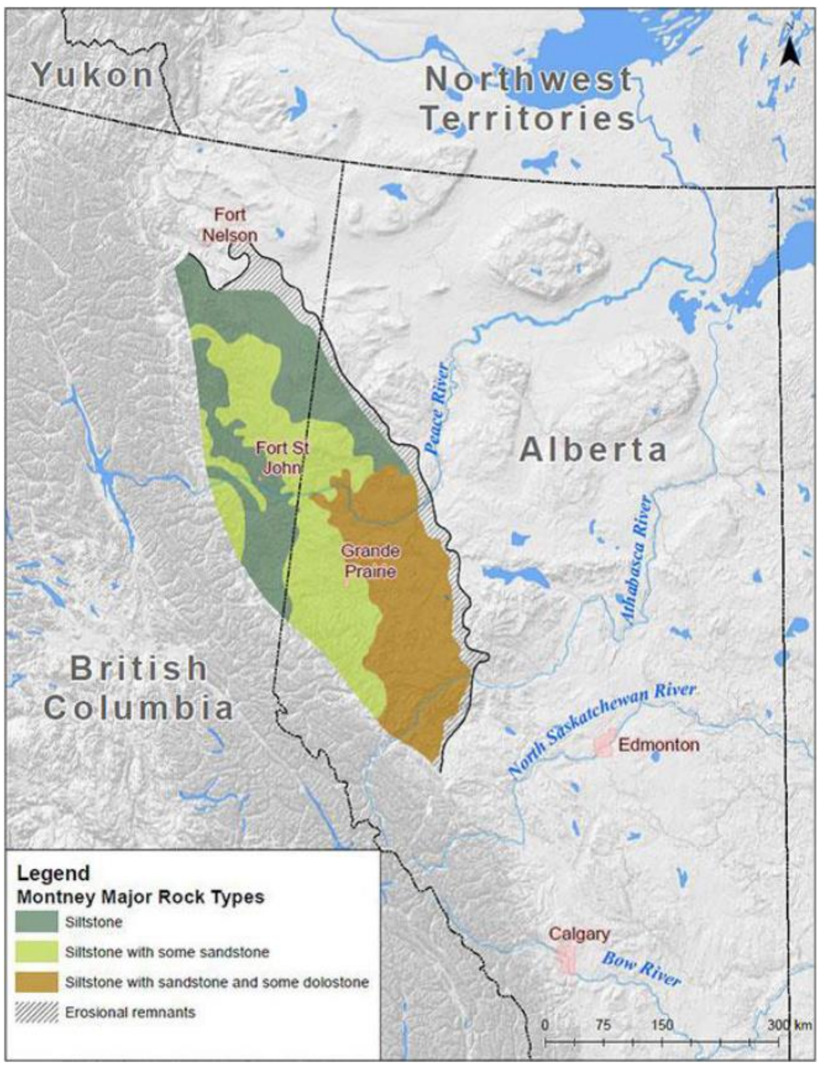

Figure 2-21: Generalized map showing the location and rock types of the Montney Formation (NEB, 2013).

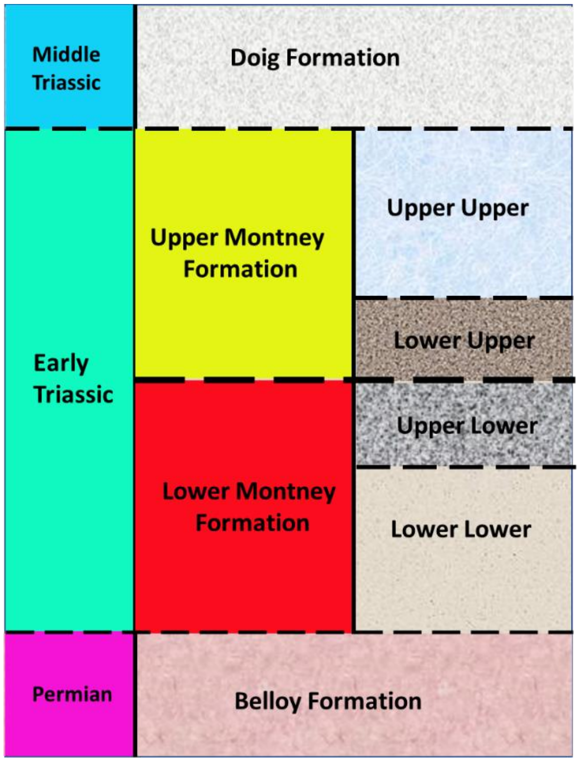

Figure 2-22: Stratigraphic chart for the Montney Formation , which has commonly been subdivided into two major unconformity-bounded members by earlier studies (after Rogers et al., 2014).

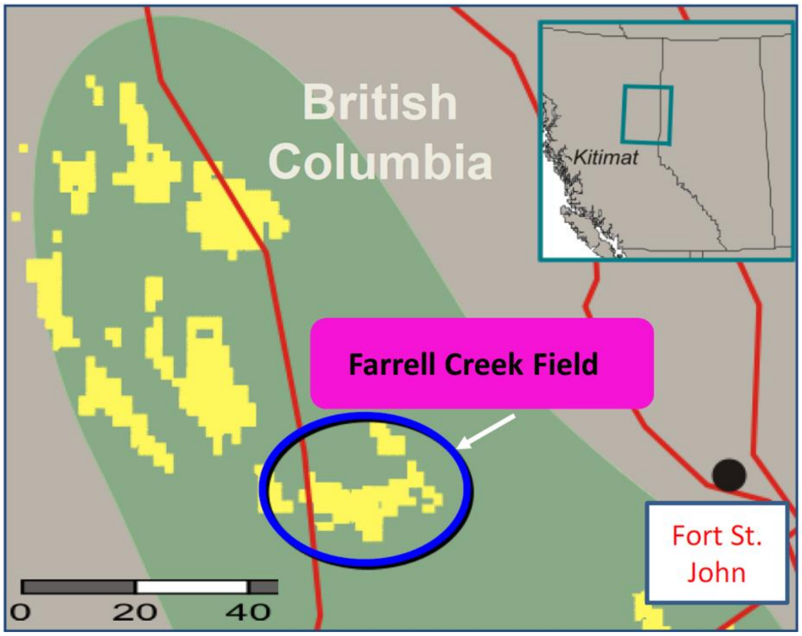

Figure 2-23: Location of the Farrell Creek Field (Rogers et al., 2014)

2.7.1.2 In-Situ Stresses in the Montney Formation

Extensive work has been completed to determine mechanical parameters and the stress regime in the Montney Formation because these play a key role in hydraulic fracture simulation of unconventional reservoirs. Stress magnitudes can be measured or estimated using a variety of methods, such as mini-frac tests, leak-off tests, overcoring methods, or by calculating from density logs. The conventional method (mini-frac) and Diagnostic Fractures Injection Test (DFIT) are the main methods that have been used in the Montney Formation to determine minimum horizontal stress magnitude.

Based on the integrated density log and DFIT's in the Farrell Creek Field, the minimum horizontal (σ_{Hmin}) and vertical stress gradients (σ_v) are interpreted to be 21.1 kPa/m and 25.3 kPa/m, respectively (McLellan et al., 2014; Song & Hareland, 2012; Hawkes et al., 2013). Minimal data is published about maximum horizontal stress, as reliable estimation of σ_{Hmax} is difficult and numerous assumptions result in high uncertainties in estimation. However, McLellan et al. (2014) suggested 27.4 (kPa/m) for maximum horizontal stress in the Farrell Creek Field. As such, the stress regime at Farrell Creek is strike slip with high horizontal stress anisotropy.

Pore pressure is another contributing factor in stress calculation. As the Montney Formation has low permeability, it would be difficult to measure pore pressure directly. Sonic velocity is a good indication for pore pressure prediction. The pore pressure gradient has been estimated as 16.6 kPa/m (Song & Hareland, 2012; McLellan et al., 2014). The in-situ stress magnitudes and pore pressure for different units of the Montney Formation at Farrell Creek are shown in Figure 2-24.

Regional data for Alberta suggests a maximum horizontal in-situ stress in the Montney formation that is oriented roughly perpendicular to the Rocky Mountain orogenic belt (Reiter et al., 2014). Horizontal in-situ stress orientations of Farrell Creek Field have been determined through examination of drilling-induced tensile fractures (which propagate in the direction of maximum horizontal stress (σ_{Hmax}), as shown in Figure 2-20) and borehole break-outs in image logs. Results have shown that maximum horizontal stress (σ_{Hmax}) is oriented approximately NE-SW(N42°E) (Figure 2-25). This orientation is in consistent with results obtained from seismic anisotropy studies (Tak et al., 2017; Reiter et al., 2014; McLellan et al., 2014).

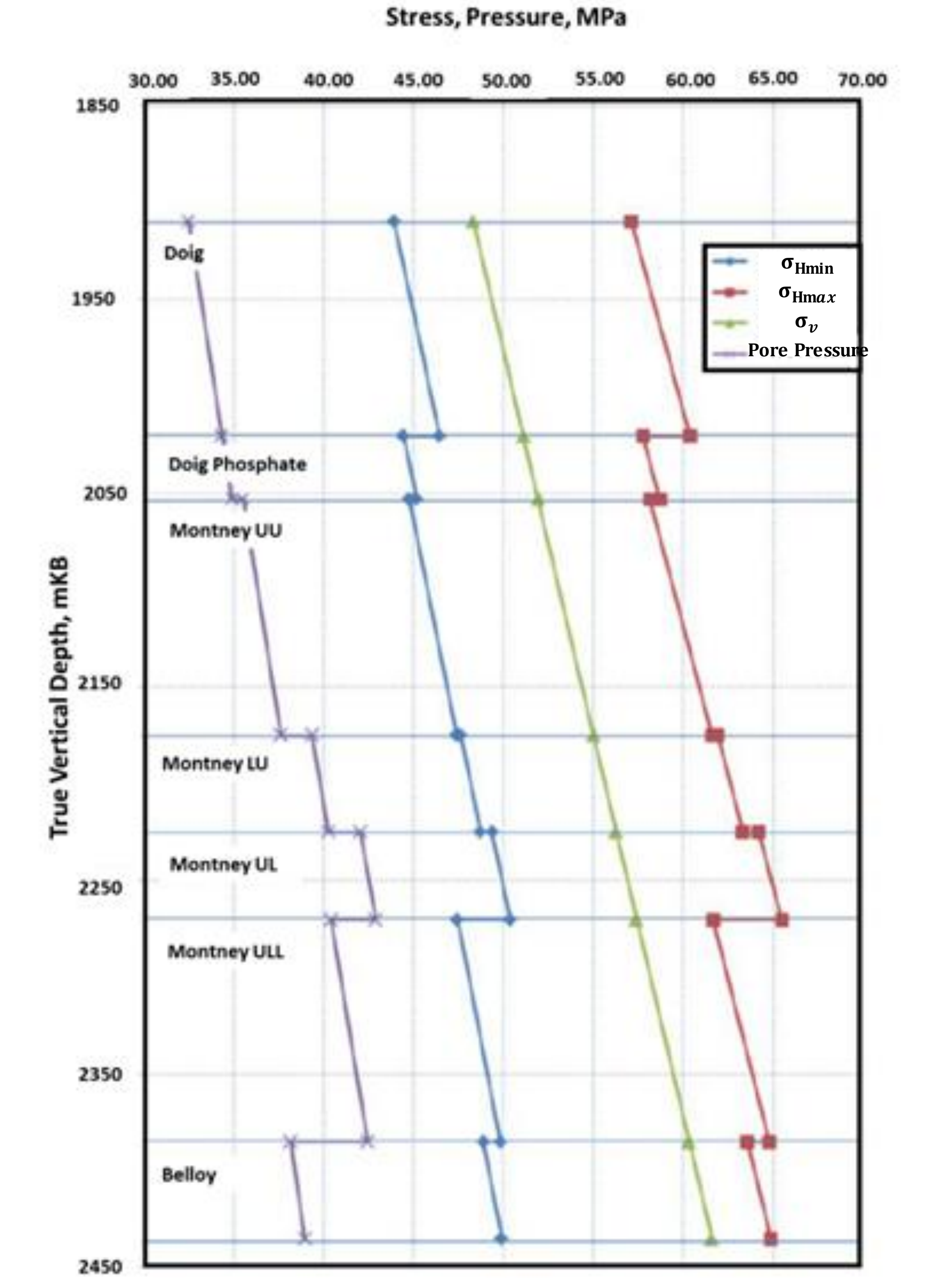

Figure 2-24: Example profile of pore pressures and in-situ stresses in the Montney Formation. These data are derived from DFIT's and borehole breakout inversion and bulk density logs (McLellan et al., 2014).

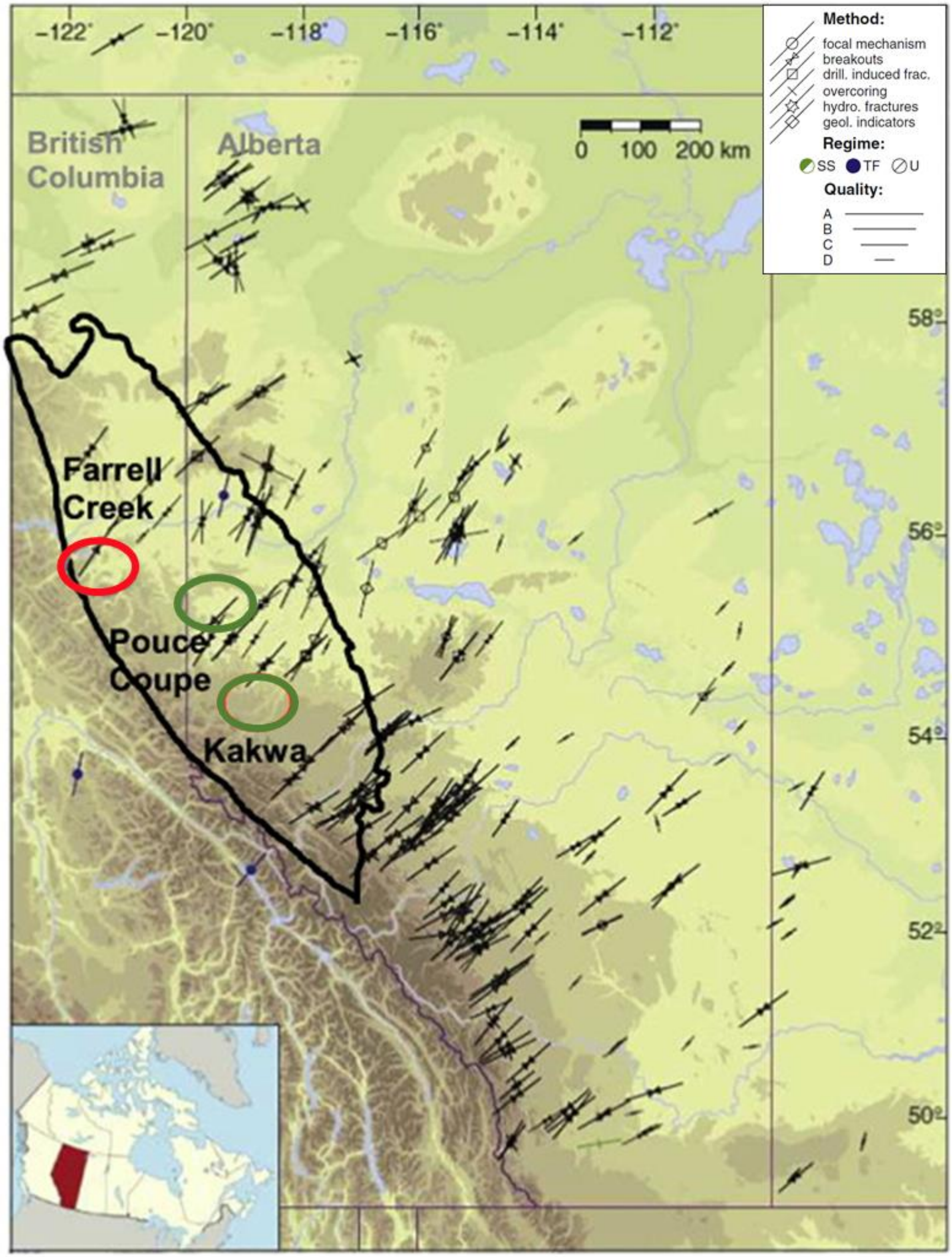

Figure 2-25: In-situ stress orientation map of Alberta and northeast British Columbia. Lines represent orientations of the maximum horizontal compressional stress (σ_{Hmax}) northeast British Columbia. The red ellipse shows the location of the Farrell Creek Field (Reiter et al., 2014).

2.7.2 Aquistore Project (Deadwood Formation)

The northern portion of the Williston Basin has been identified as an excellent geological area to permanently store CO_2, specifically in the Deadwood and Winnipeg Formations because they are the deepest sedimentary units (about 3,200 m deep) and are composed of thick clastic sequences of Cambro-Ordovician sandstones. In 2012, an extensive drilling and logging program was conducted at the Aquistore site which is located near Estevan, Saskatchewan (Figure 2-26). The results have been used to evaluate the geological suitability of the Deadwood and Winnipeg Formations for long-term storage of carbon dioxide (CO_2). Since April 2015, this site has served as a storage site for the world's first commercial post-combustion carbon capture, storage project from a coal-fired power generation facility. It is claimed that this site has the capability of receiving 250–300 ktonnes of CO_2 at variable rates of up to 800 tonnes per day. This study is focussed on the Deadwood Formation, and laboratory testing was done on samples from this formation (White et al., 2016; Fyson, 1961).

2.7.2.1 Geological Characterization

The Deadwood and Winnipeg Formations are present in the Williston Basin and Western Canada Sedimentary Basin. The Williston Basin is present in parts of North Dakota and South Dakota, and Montana in the United States, and in parts of Alberta, Saskatchewan, and Manitoba in Canada (Figure 2-26). The Deadwood Formation is considered to be of Upper Cambrian to Lower Ordovician age, while the Winnipeg Formation is of Middle to Upper Ordovician (Kurz et al., 2014).

In the Williston Basin, the Deadwood Formation is overlain by the Winnipeg Formation in the basin center and by the Red River Formation near the basin margins. In the central and southern Black Hills, it is overlain by the Mississippian Englewood Formation. In Alberta and Saskatchewan, it is overlain by the Devonian Elk Point Group. The Winnipeg Formation is conformably overlain by Ordovician age carbonates (Fyson, 1961; McLean, 1960; Stork et al., 2018; Rostron et al., 2014; White et al., 2016; Jiang et al., 2017).

In most areas, the deposition of the Deadwood and Winnipeg Formations occurred in near shore, shallow water environments as an ancient sea advanced across the exposed and weathered landscape of Precambrian rocks. Most of the conglomerates appear to be matrix-supported debris flow deposits. The thickness of the Deadwood Formation varies from 0 m in northeastern Dakota and most of eastern Saskatchewan to 270 m in the northern Black Hills (Fyson, 1961; McLean, 1960; Stork et al., 2018).

The Deadwood Formation is a regionally extensive sandstone of variable grain-size that contains intervals of silty-to-shaly interbeds. The overlying Winnipeg Formation comprises a lower sandstone called the Black Island member and upper shale, the Icebox Member, which would form the primary seal to the storage complex, owing to its low permeability. It is reported that Aquistore site porosity varies between 10% to 15%, which is consistent with experimental results which show porosities ranging from 2.7% to as high as 15.9%. Experimental results have shown that permeability range from 0.002 mD to 137 mD (Stork et al., 2018; Rostron et al., 2014).

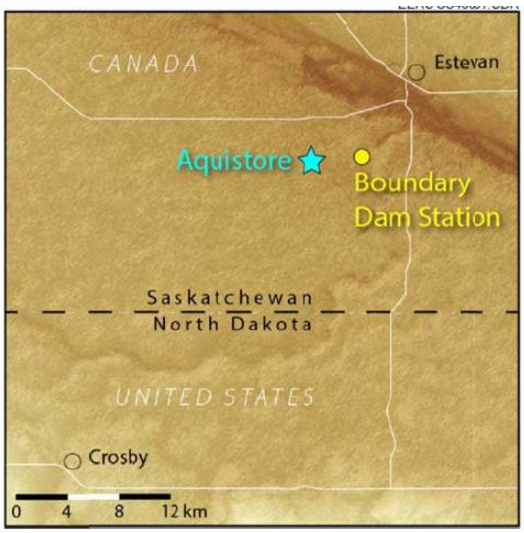

Figure 2-26: Location map of the Aquistore CO_2 injection well (PTRC_INJ_5-6-2-8 W2M) that was drilled in 2012 (Kurz et al., 2014).

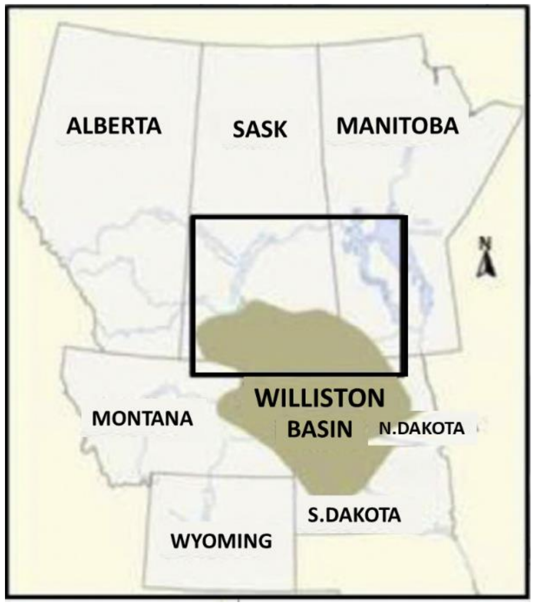

Figure 2-27: Area of extent of the Deadwood and Winnipeg Formations (White et al., 2016).

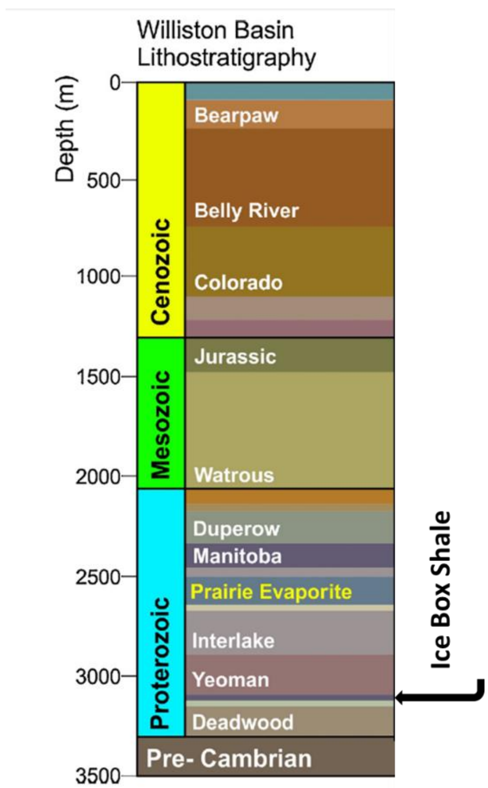

Figure 2-28: Different sedimentary units in the Williston Basin (Stork et al., 2018).

2.7.2.2 In-Situ Stresses in the Deadwood Formation

The regional stress regime of the Aquistore site is transitional between normal and strike-slip, meaning that the overburden stress is similar in magnitude to the maximum horizontal (White et al., 2016). The presence of drilling-induced tensile fractures and borehole breakouts in ultrasonic borehole image logs indicate anisotropic horizontal stresses.

Based on integration of bulk density logs, the vertical stress gradient has been estimated as 24.7 kPa/m. Based on well tests, the pore pressure gradient has been estimated 10.7 kPa/m. Based on a microfrac test and calculations using log-derived rock mechanical properties, horizontal stress magnitudes have been calculated as shown in Figure 2-29a. The orientation of maximum horizontal stress (σ_{Hmax}) at Aquistore site was determined based on the analysis of borehole breakouts and drilling induced tensile fractures. Observations suggests maximum horizontal stress (σ_{Hmax}) trends ENE-WSW at $65^{\circ} \pm 5^{\circ}$ (Figure 2-29.b) (Stork et al., 2018).

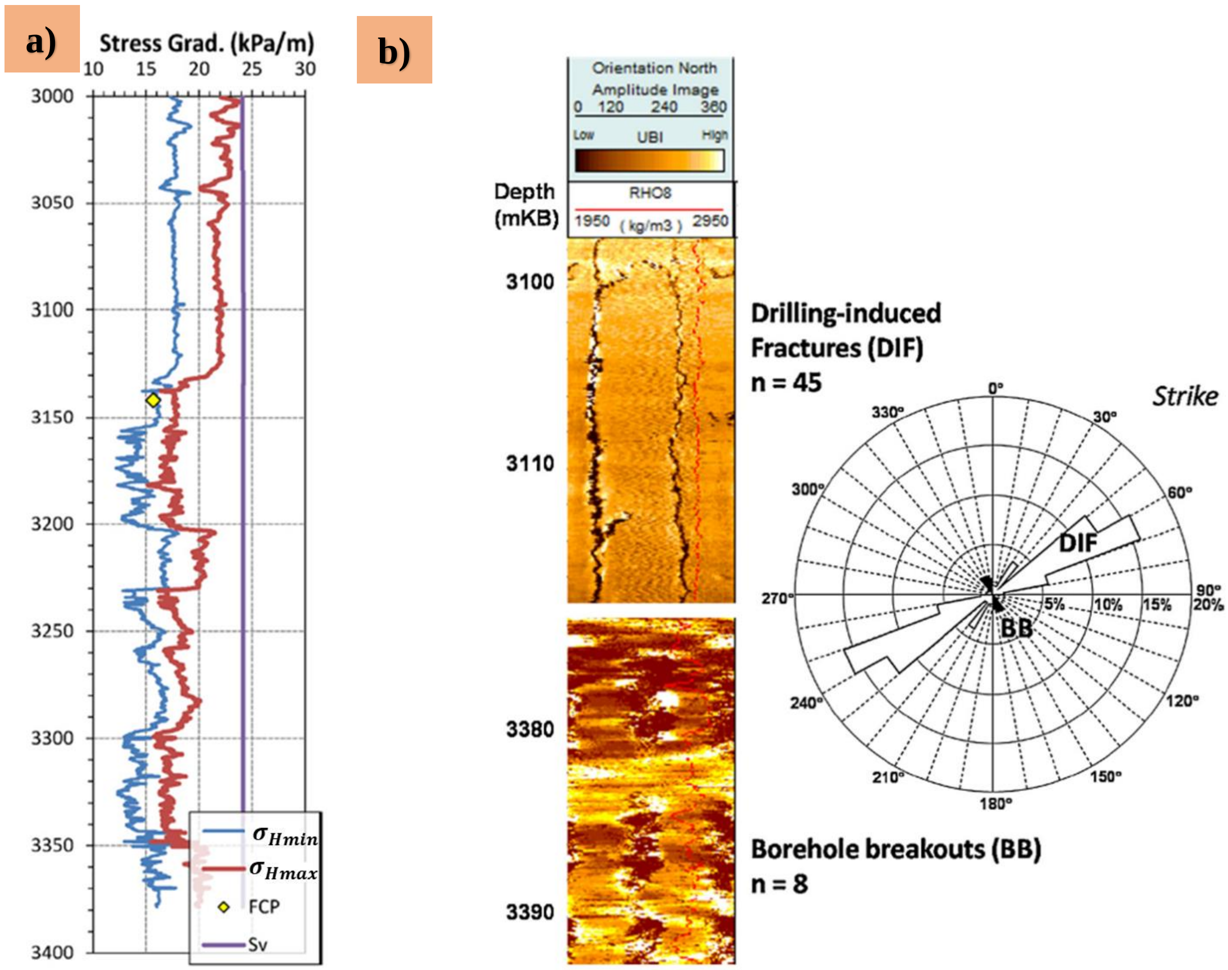

Figure 2-29: a) Sample profile of in-situ stresses and fracture closure pressure (denoted by FCP) at the Aquistore site. b) Static Ultrasonic Borehole Imager (UBI) images from the Aquistore site observation well, illustrating drilling-induced tensile fractures (denoted by DIF and shown by thin black line around 3110 m) and borehole breakouts (denoted by BB and shown by thick brown area around 3380 m) the Deadwood Formation extends from approximately 3200 to 3330 m depth (after Stork et al., 2018). Density (denoted by RHOB) is shown by red dashed line, as well.

3. Methodology

3.1 Experimental Approach

3.1.1 Montney Formation

3.1.1.1 Sample Description and Preparation

The Montney Formation was selected for study because it is an important resource (shale gas production), it is intrinsically anisotropic and located a setting with significant horizontal stress anisotropy. The specific well chosen for study was selected because core samples were available, and because the cored well (and another well nearby) had been logged with cross-dipole sonic logging tools. The samples obtained were dark grey shaly siltstone, taken from Talisman Altares 12-36-83-25W6 ST1. Eight samples were obtained, but only three (samples #1, #6, #8) were tested, due in part to damage incurred during transportation and handling, and also due to due date. Table 3-1 lists the samples used for the testing program and Table 3-2 lists their dimensions.

Note: This testing program was conducted by technical staff in the University of Saskatchewan Rock Mechanics Laboratory, and the results were provided to the author for use in this research.

Table 3-1: Mid-point depths of Montney Formation samples.

Sample	***Driller's Depth (m)***	***Corrected Depth (m)***
1	2357.85	2359.25
6	2363.44	2364.84
8	2363.98	2365.38

Table 3-2: Montney Formation sample dimensions (averaged, based on multiple reading). See Figure 3-1 for definitions of a, b, c and d.

Sample No	***a(mm)***	***b(mm)***	***c(mm)***	***d(mm)***	$\boldsymbol{\rho(kg/m^3)}$
1	38.0	19.5	33.0	49.0	2600
6	40.0	29.0	33.5	45.0	2600
8	37.0	19.0	38.5	49.0	2600

The specialized testing technique of Melendez et al. (2014) was undertaken in this test with a minor modification; i.e., utilizing a triaxial load cell instead of a hydrostatic load cell. The advantage of this method is that it overcomes heterogeneity problems, which are inherent to conventional methods that use independent measurements on multiple core samples from adjacent locations (but drilled at different locations) (Melendez, 2014; Melendez et al., 2013).

According to the coordinate axes shown in Figure 3-1, the vertical direction X_3 is perpendicular to bedding, and the horizontal directions X_2 and X_1 are parallel to bedding. The X1 and X2 directions are interchangeable given the assumption of vertical transverse isotropy.

Samples were cut using a rock saw into a prismatic shape. Representative photographs of samples 1 and 8, taken prior to instrumentation and testing, are shown in Figure 3-2. These images reveal that some of the samples contained bedding-parallel fractures that were likely enhanced while preparing the samples. The existence of these fractures would impact velocity measurements in the vertical and diagonal directions, especially at low stress levels.

The technique of Melendez et al.(2014) enables simultaneous measurement of compressional and shear wave velocities in three directions; i.e., normal to bedding, parallel to bedding, and at 45° to bedding (Figure 3-1).

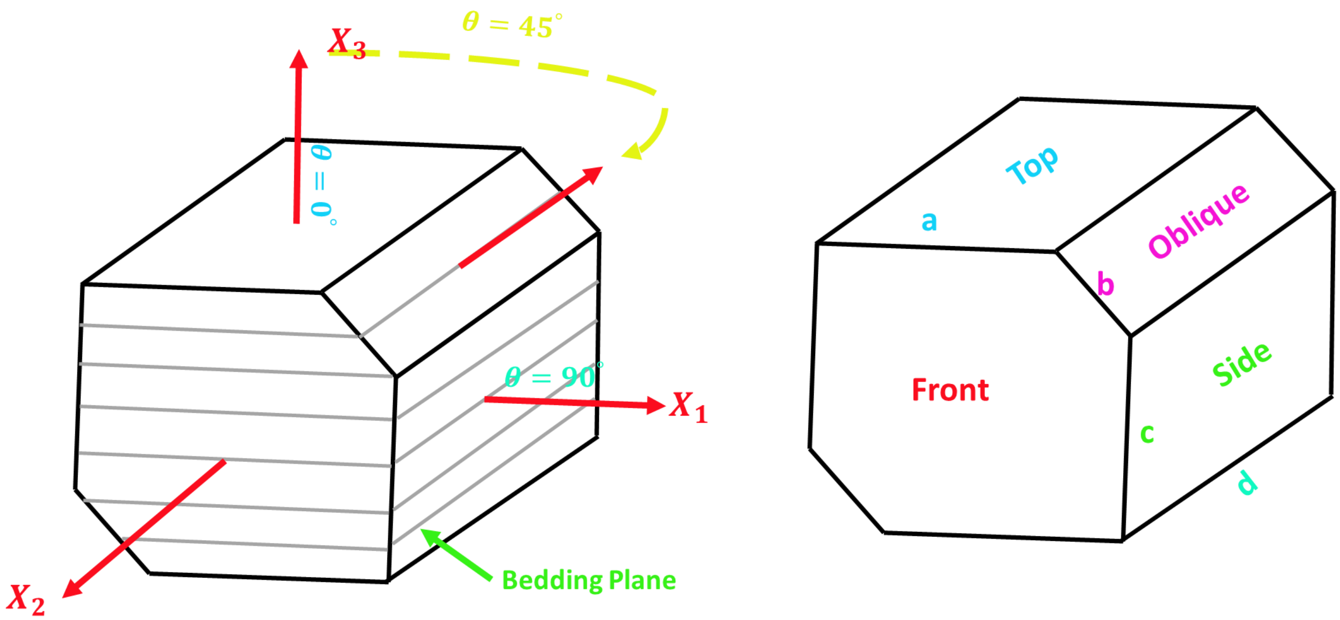

Figure 3-1: Sample geometry (after Melendez, 2014).

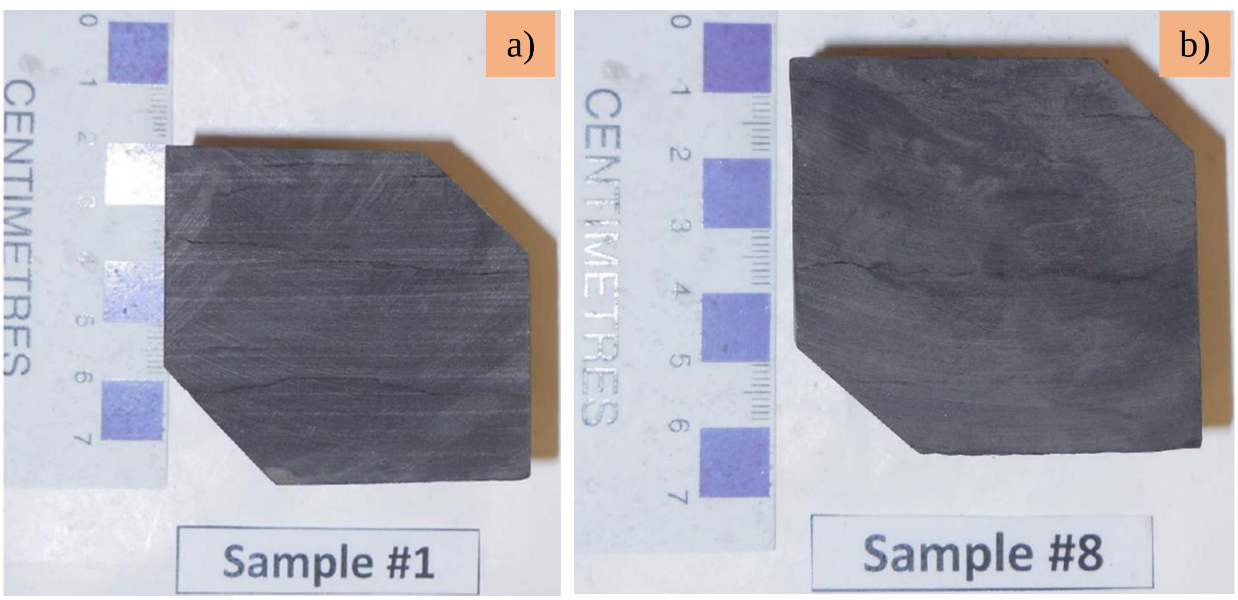

Figure 3-2: View of front surface prior to instrumentation and testing of samples 1 and 8 on the front surfaces shown. The fractures shown are orientated parallel to the bedding.

3.1.1.2 Laboratory Testing Procedure

3.1.1.2.1 Sample instrumentation

Figure 3-3 illustrates the typical instrumentation used for the Montney Formation samples. For measuring the compressional and shear velocities in the horizontal and diagonal directions, transducers were attached directly on the sample surfaces. Vertical load was applied to the samples, using platens with transducers embedded within them, thus enabling measurement of compressional and shear velocities in the vertical direction.

The transducers were purchased from Boston Piezo-Optics and had a frequency of 1 MHz. A copper foil of thickness of 0.064 mm (0.0025 inch) was attached to the front and oblique surfaces of the sample using Micro-Measurement epoxy type AE-10, while Kurt J. Lesker KL-325K Silver Epoxy was used to attach the transducer to the outter side of the copper foil. Moreover, Kurt J. Lesker KL-325K Silver Epoxy was applied on the outer surface of each transducer to attach wires.

To enable measurement of static and dynamic parameters simultaneously, two strain gauges (type EA-06-250BG-120) were attached to one side face of each sample at 90-degree orientations, in order to measure horizontal and vertical strains (Figure 3-3).

In one case (sample #1), after completing two test sequences (sequences #1 and #2) according to the standard instrumentation configuration as shown in Figure 3-3, the transducers were cut off of the front and back faces of the sample and new transducers were glued onto the top and bottom faces. The sample was then loaded uniaxially parallel to the bedding (sequence #3). In this configuration (shown in Figure 3-4), the transducers embedded within the loading platens were utilized to measure horizontal (or bedding-parallel) velocities.

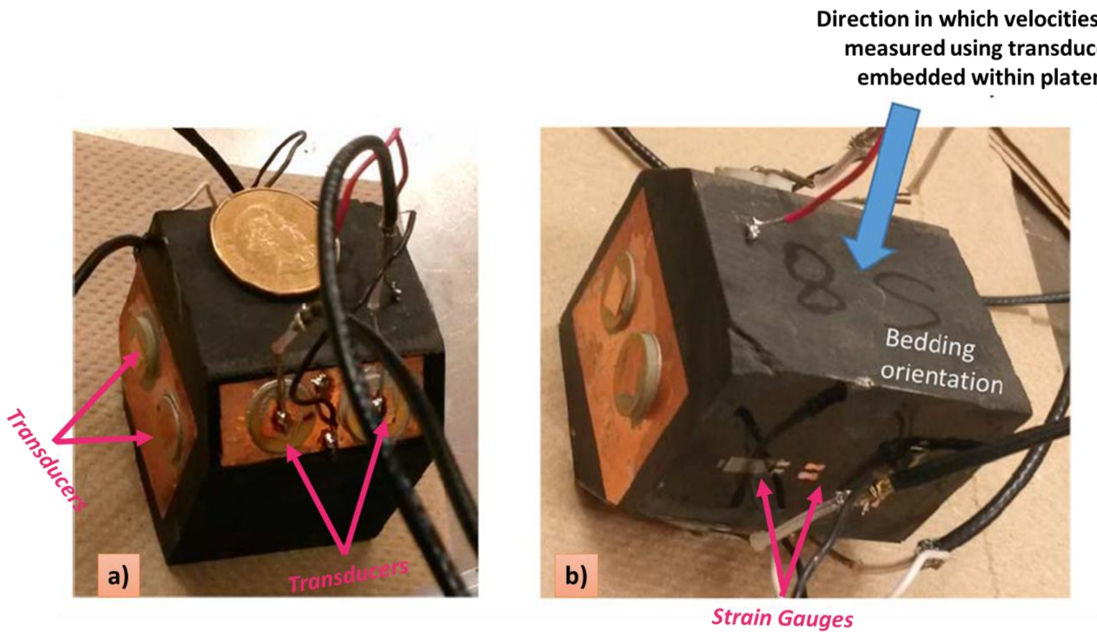

Figure 3-3: Sample #8, illustrating standard instrumentation configuration. a) Compressional and shear transducers mounted on the front face and oblique face of the sample. In this figure, the matching transducers on the back and opposing oblique face are not visible. A Canadian $1 coin is used as a scale on top of the sample. b) Horizontal and vertical (partially hidden behind black wire) strain gauges that were mounted on one side face of the sample.

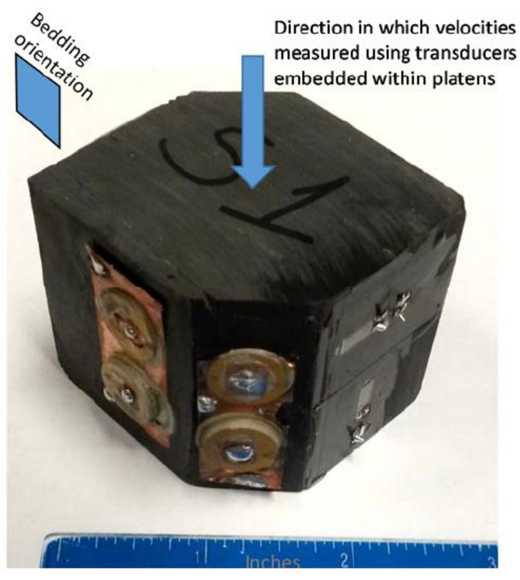

Figure 3-4: Sample #1, illustrating the alternate instrumentation configuration that was used for sample #1 test sequence #3.

3.1.1.2.2 Test Procedures

Each sample was inserted into an elastomer jacket in order to protect the sample from hydraulic oil penetration during loading. The following procedure was followed:

- Wires were attached to the transducers and strain gauges
- The sample was sandwiched between platens, held in place using c-clamp
- The sample and platens were placed in a cylindrical mould
- Liquid Skinflex was poured into the mould, then allowed to set for 24 hours.

Figure 3-5 shows an example of a Skinflex mould after testing was completed. It was removed by cutting it with a knife.

Figure 3-5: Top half of elastomer (Skinflex) sample jacket, shown after test completion and removal of sample.

The jacketed sample was placed into a Soiltest CT 710 triaxial cell, wires were connected to electrical feed-throughs, and the cell was closed and filled with confining fluid (hydraulic oil). It is significant to note that the cell lacked sufficient electrical feed-throughs to simultaneously accommodate all of the instrumentation, hence it was necessary to run each experiment with either strain gauge measurements or horizontal velocity measurements disabled. By controlling confining pressure and axial load, a series of load paths was applied to each sample.

For each pair of sample faces, one face had transducers that acted as a transmitter and on the opposite face was a receiver. The arrival times for P-waves and S-waves were picked manually by viewing the received waveforms using an oscilloscope. To obtain the true travel time between the opposing faces of each sample, transducer zero times were obtained. To obtain these zero times, the transducers were placed in direct contact (via copper foil), depending on the instrumentation configuration used for the sample faces of interest. P-wave and S-wave velocities were calculated based on the distance between the opposing sample faces and the corrected travel time.

A Wheatstone bridge circuit was used to connect the strain gauges to the data acquisition system. Strains were calculated based on the change in recorded voltage.

In order to measure velocities of sample #1 under sequence #1 with hydrostatic loading, the sample was initially tested in the triaxial cell with electrical feed-throughs configured such that all velocity transducers were active, but the strain gauges were inactive. First the hydrostatic load was incrementally increased from 0 to 40 MPa, then incrementally decreased from 40 to 0 MPa.

To conduct test sequence #2, after completing test sequence #1, the triaxial cell was drained and opened, and the electrical feed-throughs were reconfigured to deactivate the horizontal transducers. This enabled the activation of the strain gauges. During this sequence, hydrostatic load was incrementally increased from 0 to 20 MPa and then incrementally decreased from 20 to 0 MPa. Pore pressure was 0 MPa during all testing sequences in this program.

Based on the assumption that horizontal velocities will be effectively constant for sample #8, to a similar extent as observed for sample #1, sample #8 was tested with the horizontal transducers deactivated. Similar to sample #1, test sequence #2, this enabled the measurement of strains, which in turn can be used to calculated static elastic properties. (Note: Horizontal velocities were measured on sample #8 prior to filling the triaxial cell.)

In order to assess the static response of sample #1, test sequence #3, uniaxial compression load was applied parallel to the bedding. Strains were measured parallel and perpendicular to bedding.

Hydrostatic compression was applied on sample #1, test sequence #2, while strains were measured parallel and perpendicular to bedding.

3.1.2 Deadwood Formation

3.1.2.1 Sample Description and Preparation

The Deadwood Formation is of interest because of its use for CO_2 sequestration (Aquistore Project), brine disposal (various potash mines) and its potential for geothermal resource development (Marcia, 2019). It was selected for study because of availability of core samples and a comprehensive logging suite, including a cross-dipole tool, in the Aquistore injection well. Furthermore, the selection of Deadwood samples enabled study across a broader range of lithology (Montney-shale, Deadwood-sandstone) in a setting with less horizontal stress anisotropy than Farrell Creek. The Deadwood Formation samples studied in this work are sandstones dominated by well-compacted quartz sand with glauconite clay and varying stages of dissolution. Sub-horizontal bedding lamination were weakly visible in these samples. They were taken from the Aquistore injection well (PTRC_INJ_5-6-2-8 W2M) located near Estevan, Saskatchewan. Six samples were selected for this testing program, but due to due date, only five were tested. Four out of five samples ($Tx1, Tx2, Tx3$ and $Tx4$) were cut in the vertical direction to characterize shear and compressional velocities as well as static elastic properties in the direction parallel to the axis of anisotropy symmetry. The other sample (H1) was prepared in the direction parallel to the bedding to characterize static properties in the plane of symmetry. Table 3-3 lists samples used for the testing program. The average sample dimensions are presented in Table 3-4.

Note: This testing program was conducted by technical staff in the University of Saskatchewan Rock Mechanics Laboratory, and the results were provided to the author for use in this research.

Table 3-3: Mid-point depths of Deadwood Formation samples.

Sample	***Driller's Depth (m)***	***Corrected Depth (m)***
$\boldsymbol{Tx1}$	3302.08	3308.88
$\boldsymbol{Tx2}$	3302.42	3309.22
$\boldsymbol{Tx3}$	3303.85	3310.65
$\boldsymbol{Tx4}$	3303.85	3310.65
$\boldsymbol{H1}$	3300.13	3306.93

Table 3-4: Deadwood Formation Sample dimensions (averaged, based on multiple reading).

Sample No	***D (mm)***	***L (mm)***	$\boldsymbol{\rho}\ ({}^{\boldsymbol{kg}}/_{\boldsymbol{m^3}})$
$\boldsymbol{Tx1}$	38.2	88.2	2334
$\boldsymbol{Tx2}$	38.0	89.6	2328
$\boldsymbol{Tx3}$	38.0	88.2	2406
$\boldsymbol{Tx4}$	38.0	86.2	2423
$\boldsymbol{H1}$	38.0	77.3	2553

In order to fully determine the elastic moduli of an ideal transverse isotropic media, velocities must be measured in three different directions (see Figures 3-6). The directions generally used are perpendicular, parallel and oblique to the material's layering, based on the assumption that the perpendicular direction aligns with the axis of symmetry. For this work, core plugs were drilled by technical staff of University of Saskatchewan Rock Mechanics Laboratory (RML) from the sample in only two directions: perpendicular to the bedding (along X_3, $\theta = 0^{\circ}$) , and parallel to the bedding (along X_1 or X_2, $\theta = 90^{\circ}$). Two of the samples are shown in Figure 3-7. Properties in the oblique direction were estimated based on symmetry relationships (Prioul et al., 2004):

$$C_{12} = C_{11} - 2C_{66} \qquad and \qquad C_{13} = C_{33} - 2C_{44} \tag{3.1}$$

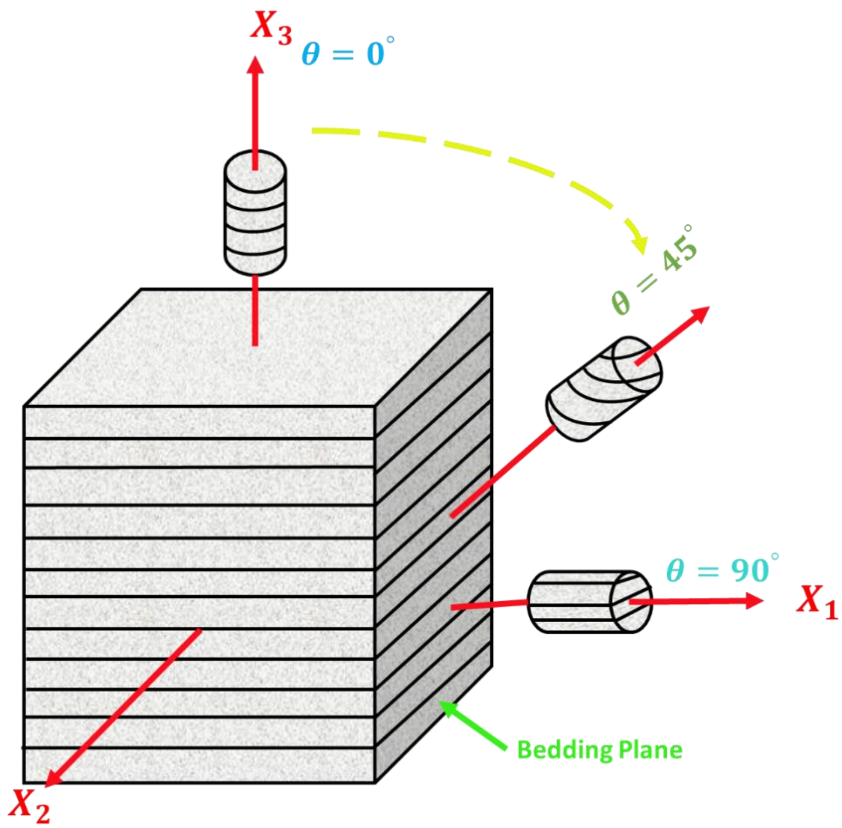

Figure 3-6: Schematic of the three core plugs needed to estimate the elastic constants that define a VTI symmetry (after Melendez et al., 2013).

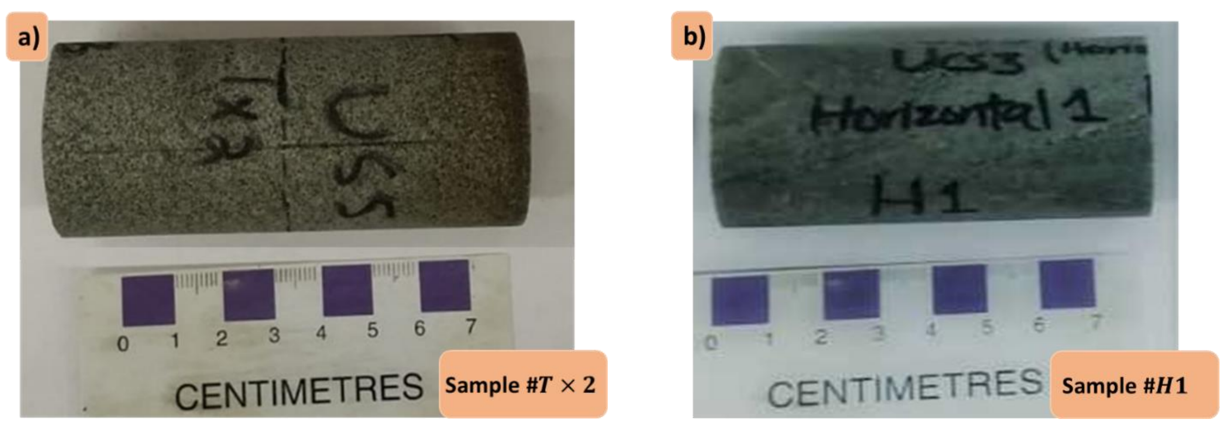

Figure 3-7: a) Sample #Tx2, drilled vertical to the bedding (vertical sample) ; and b) Sample H1, drilled parallel to the bedding (horizontal sample), prior to instrumentation and testing.

3.1.2.2 Laboratory Testing Procedure

3.1.2.2.1 Sample Instrumentation

To fully characterize dynamic properties both parallel and normal to the bedding, separate tests were conducted on samples drilled in the horizontal direction (sample $H1$) and in the vertical direction (samples $Tx1 - Tx4$). For measuring the compressional and shear velocities in the parallel to the sample axis direction, load was applied on the sample through platens having transducers embedded within them. Four strain gauges were attached to each sample using epoxy; two oriented vertically and two oriented horizontally. This enabled the measurement of axial and lateral strains, which were then used to calculate static elastic moduli.

3.1.2.2.2 Test Procedure

Each sample was jacketed according to procedures described in section 3.1.2.2, then inserted into a triaxial cell and tested according to standard procedures. Axial stress and confining pressure were controlled independently. For the velocity tests, hydrostatic conditions were imposed. For the strain (static elastic property) tests, confining pressure was maintained constant at 5 MPa, while axial stress was increased steadily. Some samples were loaded until failure occurred. Others were tested before failure to avoid damage to the ultrasonic transducers. Given that this study was concerned with elastic properties, failure stresses are not reported here.

Testing was performed following standard triaxial testing procedures, using loading platens containing embedded compressional and shear wave transducers which enabled measurement of V_P and V_S parallel to the sample axis.

3.1.3 Relationship Between Static Elastic Constants and Applied Stress

This section explains how five static elastic moduli were extracted for the Montney Formation in order to fully characterize this vertical transverse isotropic (VTI) medium using the available lab data.

In the current experiments, we made measurements using both strain gauges for static values and ceramic transducers for dynamic values. Existing relationships between elastic stiffness constants and elastic properties make it possible to characterize the anisotropic body. As a first step, in a body with hexagonal symmetry or transverse isotropic symmetry (TI), the following compliance tensor in terms of Young's modulus (E), shear modulus (G) and the Poisson ratios (ϑ) is utilized to define the anisotropic body:

$$S_{ij} = \begin{pmatrix} \frac{1}{E_1} & -\frac{\vartheta_{12}}{E_1} & -\frac{\vartheta_{31}}{E_3} & 0 & 0 & 0 \\ -\frac{\vartheta_{12}}{E_1} & \frac{1}{E_1} & -\frac{\vartheta_{31}}{E_3} & 0 & 0 & 0 \\ -\frac{\vartheta_{13}}{E_1} & -\frac{\vartheta_{13}}{E_1} & \frac{1}{E_3} & 0 & 0 & 0 \\ 0 & 0 & 0 & \frac{1}{G_{23}} & 0 & 0 \\ 0 & 0 & 0 & 0 & \frac{1}{G_{23}} & 0 \\ 0 & 0 & 0 & 0 & 0 & \frac{2(1+\vartheta_{12})}{E_1} \end{pmatrix} \tag{3.2}$$

The corresponding stiffness matrix, which is the inverse of the compliance matrix, in a TI medium is given by:

$$C_{ij} = \begin{pmatrix} C_{11} & C_{12} & C_{13} & 0 & 0 & 0 \\ C_{12} & C_{22} & C_{23} & 0 & 0 & 0 \\ C_{13} & C_{23} & C_{33} & 0 & 0 & 0 \\ 0 & 0 & 0 & C_{44} & 0 & 0 \\ 0 & 0 & 0 & 0 & C_{55} & 0 \\ 0 & 0 & 0 & 0 & 0 & C_{66} \end{pmatrix} \tag{3.3}$$

Where C_{11}, C_{22}, C_{33}, C_{44}, C_{55}, C_{66}, C_{12} and $C_{13}$are elastic stiffness constants. To find elastic stiffness constants as function of elastic properties, it is required to calculate the inverse of the compliance matrix. For the sake of simplicity, the following substitutions are made:

$$a = \frac{1}{E_1}, \quad b = -\frac{\vartheta_{12}}{E_1}, \quad c = -\frac{\vartheta_{31}}{E_3}, \quad d = -\frac{\vartheta_{13}}{E_1}, \quad e = \frac{1}{E_3}, \tag{3.4}$$
$$f = \frac{1}{G_{23}}, \quad g = \frac{2(1+\vartheta_{12})}{E_1}$$

Thus:

$$C_{ij} = \begin{pmatrix} \frac{(a*e-c*d)}{((a-b)*(a*e-(2*c*d)+b*e)))} & \frac{(c*d-b*e)}{((a-b)*(a*e-(2*c*d)+b*e)))} & \frac{-c}{(a*e-(2*c*d)+b*e)} & 0 & 0 & 0 \\ \frac{(c*d-b*e)}{((a-b)*(a*e-(2*c*d)+b*e)))} & \frac{(a*e-c*d)}{((a-b)*(a*e-(2*c*d)+b*e))} & \frac{-c}{(a*e-(2*c*d)+b*e)} & 0 & 0 & 0 \\ \frac{-d}{(a*e-(2*c*d)+b*e)} & \frac{-d}{(a*e-(2*c*d)+b*e)} & \frac{(b+a)}{(a*e-(2*c*d)+b*e)} & 0 & 0 & 0 \\ 0 & 0 & 0 & \frac{1}{f} & 0 & 0 \\ 0 & 0 & 0 & 0 & \frac{1}{f} & 0 \\ 0 & 0 & 0 & 0 & 0 & \frac{1}{g} \end{pmatrix} \tag{3.5}$$

As such, we have:

$$C_{11} = C_{22} = \frac{(a * e \; - \; c * d)}{((a \; - \; b) * (a * e \; - \; 2 * c * d \; + \; b * e)} \tag{3.6}$$

$$C_{12} = C_{21} = \frac{(c * d \; - \; b * e)}{((a \; - \; b) * (a * e \; - \; 2 * c * d \; + \; b * e))} \tag{3.7}$$

$$C_{13} = C_{23} = \frac{-c}{(a * e \; - \; 2 * c * d \; + \; b * e)} \tag{3.8}$$

$$C_{31} = C_{32} = \frac{-d}{(a * e \; - \; 2 * c * d \; + \; b * e)} \tag{3.9}$$

$$C_{33} = \frac{(a \; + \; b)}{(a * e \; - \; 2 * c * d \; + \; b * e)} \tag{3.10}$$

$$\mathrm{C}_{55} = \mathrm{C}_{44} = \frac{1}{\mathrm{f}} \tag{3.11}$$

$$C_{66} = \frac{1}{g} \tag{3.12}$$

By substituting the actual values of (a, b, c, d, e, f, g), we find:

$$C_{11} = C_{22} = \frac{E_1[1 - \vartheta_{13}\vartheta_{31}]}{(1 + \vartheta_{12})[1 - (2\vartheta_{31}\vartheta_{13} + \vartheta_{12})]} \tag{3.13}$$

$$C_{12} = C_{21} = \frac{E_1[\vartheta_{12} + \vartheta_{13}\vartheta_{31}]}{(1 + \vartheta_{12})[1 - (2\vartheta_{31}\vartheta_{13} + \vartheta_{12})]} \tag{3.14}$$

$$C_{13} = C_{23} = \frac{E_1\vartheta_{31}}{[1 - (2\vartheta_{31}\vartheta_{13} + \vartheta_{12})]} \tag{3.15}$$

$$C_{31} = C_{32} = \frac{E_3\vartheta_{13}}{[1 - (2\vartheta_{31}\vartheta_{13} + \vartheta_{12})]} \tag{3.16}$$

$$C_{33} = \frac{E_3(1 - \vartheta_{12})}{[1 - (2\vartheta_{31}\vartheta_{13} + \vartheta_{12})]} \tag{3.17}$$

$$C_{55} = C_{44} = G_{23} \tag{3.18}$$

$$C_{66} = \frac{E_1}{2(1 + \vartheta_{12})} \tag{3.19}$$

Based on the relationships presented in equations 3.13-3.19, it can be concluded that:

$$C_{12} = C_{11} - 2C_{66} \tag{3.20}$$

In a body with a hexagonal symmetry (or transverse isotropic symmetry (TI)) the elastic stiffness can be reduced to 5 elastic constants which are necessary to fully characterize the TI medium:

$$C_{13} = C_{31} \quad \rightarrow \quad \frac{E_1\vartheta_{31}}{[1-(2\vartheta_{31}\vartheta_{13}+\vartheta_{12})]} = \frac{E_3\vartheta_{13}}{[1-(2\vartheta_{31}\vartheta_{13}+\vartheta_{12})]} \quad \rightarrow \quad E_1\vartheta_{31} = E_3\vartheta_{13} \tag{3.21}$$

It can be concluded, by symmetry constraints that $E_1\vartheta_{31} = E_3\vartheta_{13}$.

Figure 3-8 shows the three measurements that would ideally be conducted to determine the elastic properties. The bulk modulus (K) requires hydrostatic compression, which is shown in Figure 3-8.c, and can be described simply as the change in pressure divided by the change in volume.

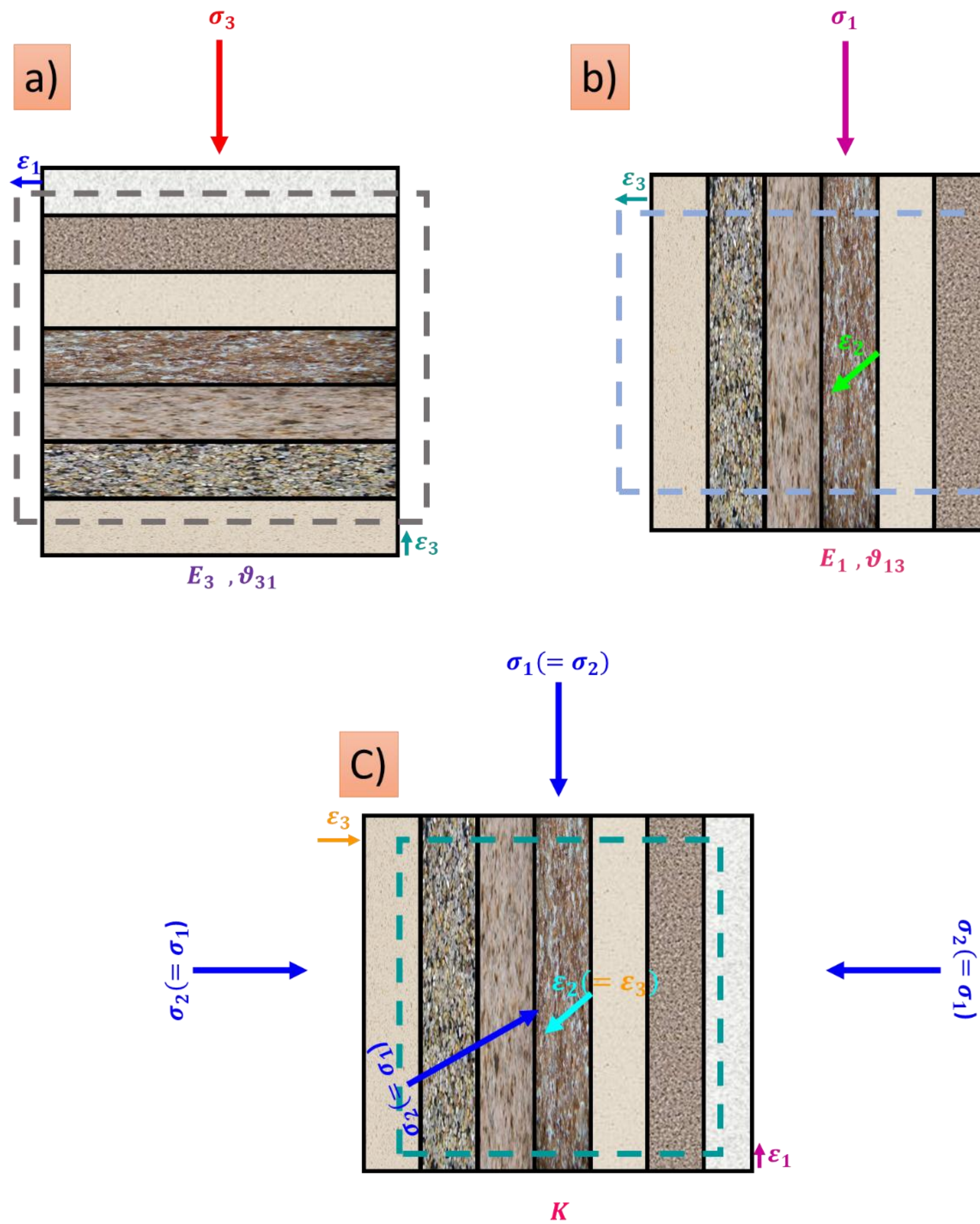

Figure 3-8: The three experiments that would ideally be conducted to recover all the Young's moduli and Poisson's ratios (after Havens, 2012). Strain measurement devices are not shown; in practice sensors would be attached to the samples to enable measurement of ε_1, ε_2 and ε_3 in these experiments. a) Uniaxial compression normal to bedding, b) uniaxial compression parallel to bedding, and 3) hydrostatic compression.

In this work on the Montney Formation, only measurements of the type presented in Figure 3-3.b and 3-8.c are conducted. Under uniaxial conditions only E_1 and ϑ_{13} were measured, and under hydrostatic loading bulk modulus (K) was measured. By assuming vertical transverse isotropy

(VTI) behaviour for our samples, with a vertical axis of rotational symmetry, we could fully characterize the bedding properties using existing relationships between elastic properties (Hudson et al., 2000).

$$\vartheta_{12} = \frac{3K - E_1}{6K} \tag{3.22}$$

$$G_{12} = \frac{3KE_1}{9K - E_1} \tag{3.23}$$

It is still necessary to find a way to characterize properties in the direction of the axis of symmetry. It is claimed by Melendez (2014) that the following relationship exists between bulk modulus and elastic stiffness constants:

$$K = \frac{C_{33}(C_{11} + C_{12}) - 2C_{13}^2}{C_{11} + 2C_{33} + C_{12} - 4C_{13}} \tag{3.24}$$

By substituting the derived equations for C_{ij} as a function of elastic properties (3.13-3.19) and the symmetry equation given in equation (3.21), the following equation can be obtained for bulk modulus in a TI medium:

$$K = \frac{E_1\vartheta_{31}}{2\vartheta_{31}\big(1 - (\vartheta_{12} + 2\vartheta_{13})\big) + \vartheta_{13}} = \frac{E_3E_1}{E_1 + 2E_3(1 - (\vartheta_{12} + 2\vartheta_{13}))} \tag{3.25}$$

The following equation is derived for Poisson's ratio (ϑ_{31}) in the plane of $X_3 - X_1$; i.e., the plane parallel containing the axis of symmetry:

$$\vartheta_{31} = \frac{\vartheta_{13}K}{E_1 - 2K[1 - (\vartheta_{12} + 2\vartheta_{13})]} \tag{3.26}$$

By substituting for ϑ_{12} using equation (3.22), equation (3.26) becomes:

$$\vartheta_{31} = \frac{3\vartheta_{13}K}{2E_1 - 3K[1 - (4\vartheta_{13})]} \tag{3.27}$$

Also, the following equation can be deduced for Young's modulus in the planes parallel to the axis of symmetry:

$$E_3 = \frac{KE_1}{E_1 - 2K(1 - (\vartheta_{12} + 2\vartheta_{13}))} \tag{3.28}$$

Nonlinear elasticity theory provides relationships between the effective elastic stiffness tensor C_{ijkl} and the principal stresses σ_{ik} and strains ε_{mn}, which can be written as following (Prioul et al., 2004):

$$C_{ijkl} = A_{ijkl} + A_{ijklmn}\varepsilon_{mn} \tag{3.29}$$

Where:

A_{ijkl}= The unstressed fourth-order stiffness tensor (second-order elastic constants C_{ij}^0)

A_{ijklmn}= The six-order elastic constants (or third-order elastic constants C_{ijk}in Voigt notation)

ε_{mn}= Principal strains.

According to Prioul et al. (2004), equation 3.29 can be expressed as follows:

$$\begin{aligned}
C_{11} &= C_{33}^0 + C_{111}\varepsilon_{11} + C_{112}\varepsilon_{22} + C_{112}\varepsilon_{33} \\
C_{22} &= C_{33}^0 + C_{112}\varepsilon_{11} + C_{111}\varepsilon_{22} + C_{112}\varepsilon_{33} \\
C_{33} &= C_{33}^0 + C_{112}\varepsilon_{11} + C_{112}\varepsilon_{22} + C_{111}\varepsilon_{33} \\
C_{23} &= C_{12}^0 + C_{123}\varepsilon_{11} + C_{112}\varepsilon_{22} + C_{112}\varepsilon_{33} \\
C_{13} &= C_{12}^0 + C_{112}\varepsilon_{11} + C_{123}\varepsilon_{22} + C_{112}\varepsilon_{33} \\
C_{12} &= C_{12}^0 + C_{112}\varepsilon_{11} + C_{112}\varepsilon_{22} + C_{123}\varepsilon_{33} \\
C_{44} &= C_{55}^0 + C_{144}\varepsilon_{11} + C_{155}\varepsilon_{22} + C_{155}\varepsilon_{33} \\
C_{55} &= C_{55}^0 + C_{155}\varepsilon_{11} + C_{144}\varepsilon_{22} + C_{155}\varepsilon_{33} \\
C_{66} &= C_{55}^0 + C_{155}\varepsilon_{11} + C_{155}\varepsilon_{22} + C_{144}\varepsilon_{33}
\end{aligned} \tag{3.30}$$

Where C_{111}, C_{112} and C_{123} are the three independent parameters with $C_{114} = {}^{(C_{112} - C_{123})}/_{2}$ and $C_{115} = {}^{(C_{111} - C_{112})}/_{4}$.

From nonlinear elastic equations 3.30 and 3.20, it is concluded that:

$$C_{11} + C_{33} = 2(C_{13} + 2C_{55}) \tag{3.31}$$

By substituting equations (3.13, 3.15, 3.17 and 3.18) into equation 3.31, the following equation for shear modulus (G_{23}) is obtained:

$$G_{23} = C_{55}(= C_{44}) = \frac{E_1(\vartheta_{13} - \vartheta_{31}\big((\vartheta_{12} + \vartheta_{13})^2 - (1 - 2\vartheta_{13})\big))}{4\vartheta_{13}((1 + \vartheta_{12})\big(1 - (\vartheta_{12} + 2\vartheta_{13}\vartheta_{31})\big))} \tag{3.32}$$

As such, using equations 3.21, 3.22, 3.25, 3.27 and 3.30, we can fully characterize a VTI medium based on conducting experiment presented in Figure 3.8.b and 3-8.c. Elastic stiffness constants could be calculated based on equations 3.13 to 3.19.

3.2 Numerical Approach

3.2.1 COMSOL Software

COMSOL Multiphysics is a powerful software which has the capability of simulating multiple physical processes in any dimension (1D, 2D, 3D). COMSOL Multiphysics is based on the Finite Element (FEM) method, in which the spatial domain is divided into small parts (mesh elements) to achieve accurate representation of complex geometries.

To conduct dynamic and static analysis, three different modules of COMSOL Multiphysics were used; i.e., the acoustic, solid mechanics and geomechanics modules.

The acoustic module was used in conjunction with the solid mechanics module to combine pressure waves in the fluid with elastic waves in the solid to simulate wave propagation around a fluid-filled borehole.

The solid mechanics and geomechanics modules were used in conjunction for simulation of static stress analysis around a fluid-filled borehole.

There were several reasons for choosing COMSOL Multiphysics as a tool to conduct the dynamic and static studies in this work. First of all, the most important factor was to facilitate a direct import of the results from static analysis into the dynamic simulation, hence enabling the use of stress-dependent dynamic elastic properties. Secondly, the acoustic module supports time-harmonic (frequency domain) and transient studies for fluid pressure analyses. Time-harmonic study was selected over transient study because it is less time consuming and requires less computer memory. The time-harmonic equation is a Fourier transform of the original time-dependent equations and its solution as a function of frequency (ω) is the Fourier transform of a full transient solution. It is therefore possible to synthesize a time-dependent solution from a frequency-domain simulation by applying an inverse Fourier transform of the results. Finally, it provides an opportunity to define different types of point source (Monopole, Dipole and Quadrupole) with the desired point source function (e.g., Ricker, Sinc, Square, Ormsby).

3.2.2 Modeling Process

The workflow for doing simulation with COMSOL Multiphysics is given in Figure 3-9.

A static analysis was performed in step 1, in order to calculate the static stresses around the borehole. Initially, the in-situ stress state of the formation was computed before the excavation of the borehole. Next, the stress concentration around the borehole was computed after excavation of the borehole.

The dynamic analysis was conducted in step 2. The static analysis results were imported directly into the dynamic model to help to define dynamic elastic stiffness parameters as a function of stresses.

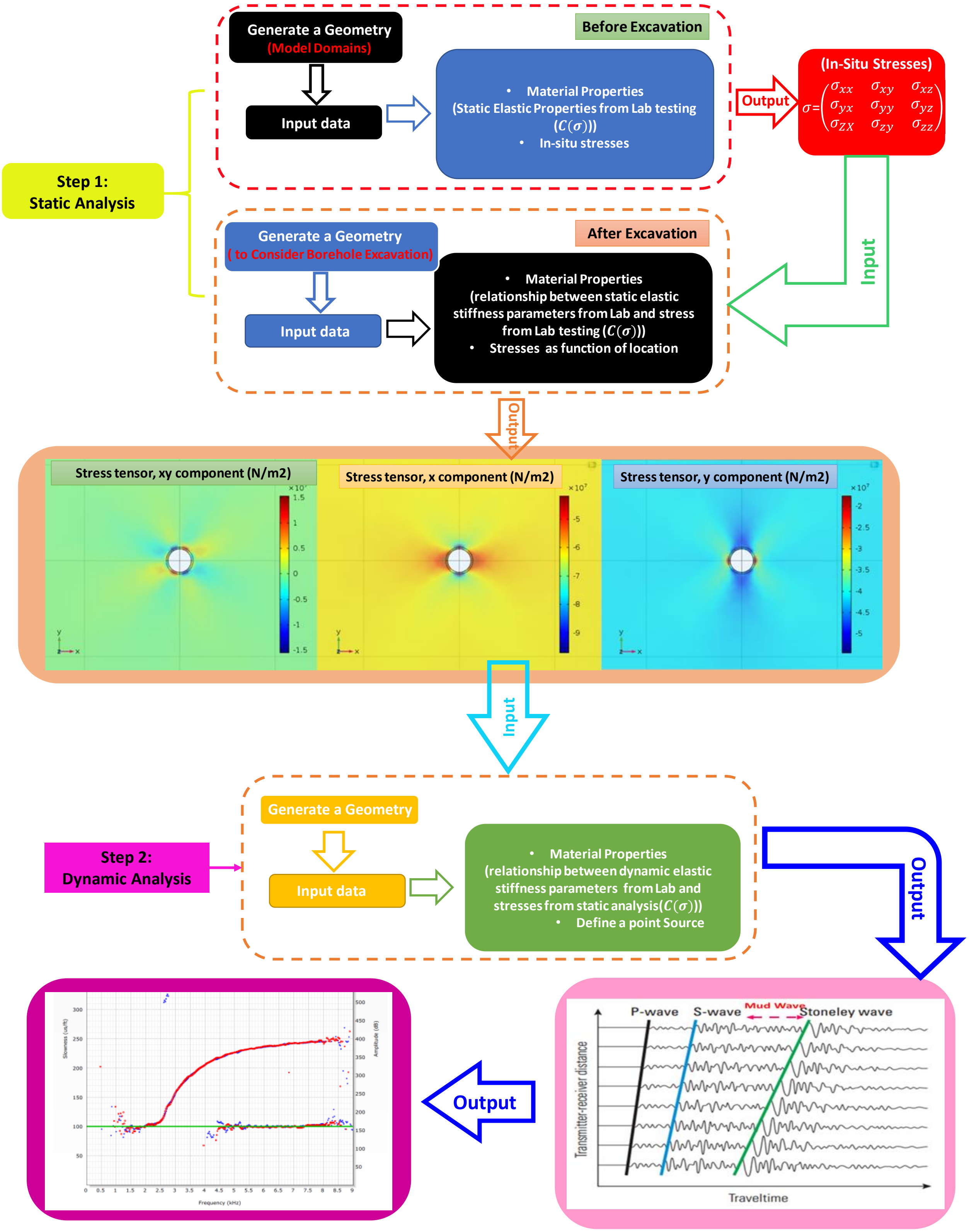

Figure 3-9: Workflow for simulating static stresses, wave propagation and flexural wave dispersion around a borehole using COMSOL Multiphysics.

3.2.3 Static Stress Analysis

In order to calculate the stress-induced anisotropy in homogenous rocks, the redistribution in stresses around the borehole resulting from drilling must be estimated. In static stress analysis, we consider an infinite formation of arbitrary anisotropy which is homogenous and continuous in all directions. Internally this body is bounded by a cylindrical borehole of radius a located in the center of the formation. In the far field an in-situ stress field is applied where the principal stress tensor takes the form:

$$\sigma = \begin{pmatrix} \sigma_1 & 0 & 0 \\ 0 & \sigma_2 & 0 \\ 0 & 0 & \sigma_3 \end{pmatrix} \tag{3.33}$$

For the sake of the simplicity, but without loss of generality, in simulating the stress concentration and displacement around the borehole some assumptions were made, as follows:

- one of the principal stresses is aligned parallel to the axis of anisotropy (Figure 3-10).
- The borehole is semi infinite and homogenous in the axial direction; this is referred to as a generalized plane strain formulation. The generalized plane strain assumption used at the top of the model domain requires the displacement components to be functions of x and y, and the only strain which is zero is ε_{zz}. The assumption of being infinite was made, in order to make sure that the solution inside the region of interest is not affected by the presence of artificial boundaries. This objective was accomplished by applying a coordinate scaling factor to a layer of virtual domain at the bottom of the borehole and formation. This virtual domain was stretched out toward infinity, giving rise to infinite elements. In COMSOL Multiphysics, this virtual domain is predefined as an infinite domain, which is applied on the bottom of the borehole and formation, as shown in Figure 3-11. It is strongly recommended by COMSOL to use swept meshing in the infinite element domain to prevent poor mesh element quality, giving rise to poor or slow convergence for iterative solvers and making the problem ill-conditioned in general.
- The size of the model in the radial direction is sufficiently large to avoid significant influence of model size on stress concentrations.

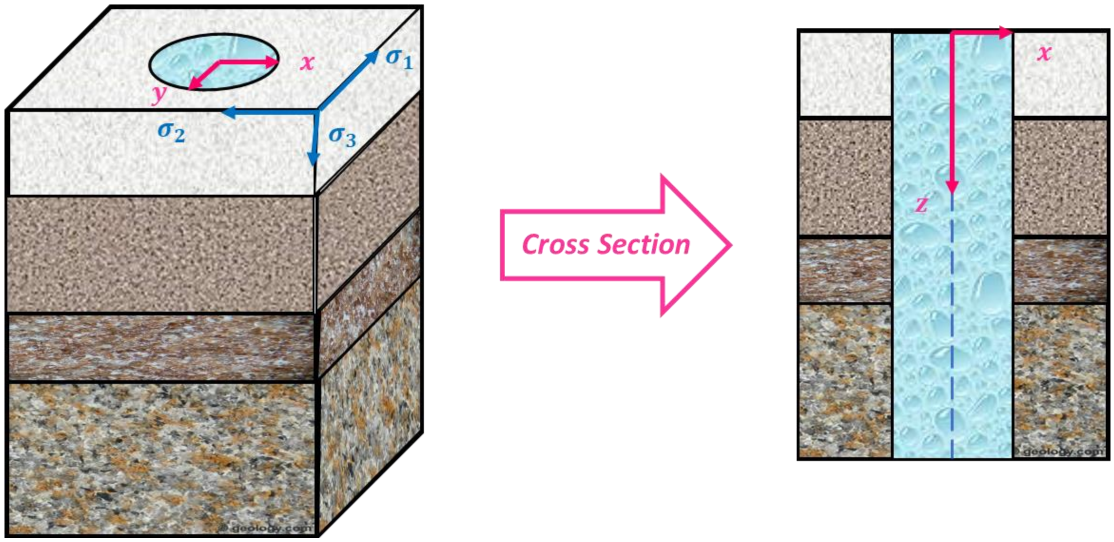

Figure 3-10: Alignment of the principal stresses in the direction of axis of anisotropy.

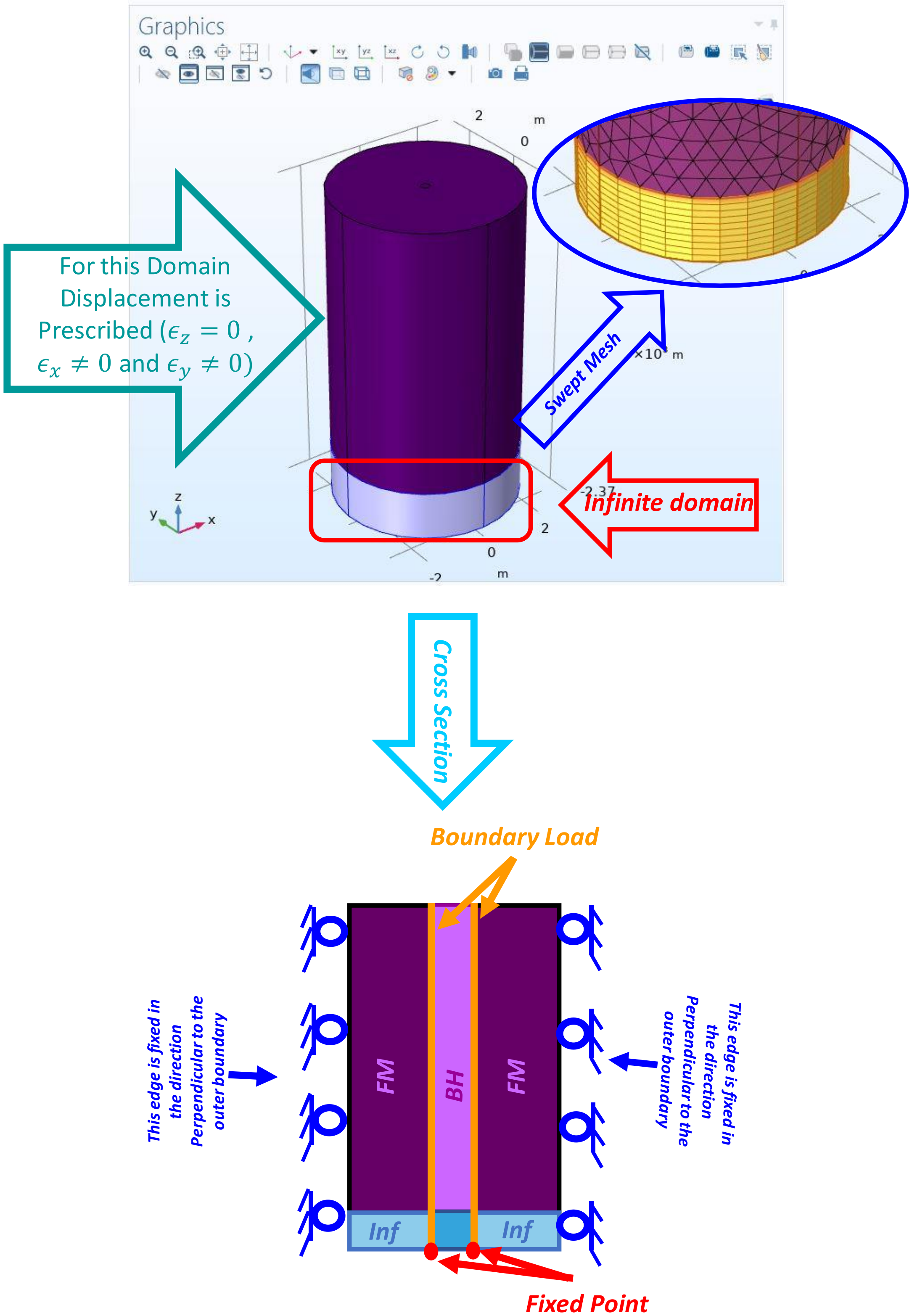

Figure 3-11: Model geometry for static stress analysis. An infinite domain, shown in blue, is used to eliminate boundary effects at the base of the model. The upper surface is a free surface.

The modelling of the stress field through the model domain consists of solving Navier's equations of motion for displacements and strain, and stress components through Hooke's law. In order to calculate stresses, two steps are required (see Figures 3-12). In the first step, the stress state of the formation before the excavation of the borehole is computed. In the second step, the response of formation to redistribution of stresses by excavating a borehole is computed. Because only a static solution of the Navier's equations is considered, the deformation of the borehole is assumed to happen "instantaneously" after the application of appropriate forces on the borehole wall.

In order to obtain a stable solution, boundary conditions must be imposed. The outer edges were considered fixed in the direction perpendicular to the outer boundary of the model. The bottom of the hole is fixed to prevent any rotation that would be caused by external loads. The only boundary condition applied on borehole /formation interface is a boundary load, which simulates the uniform pressure applied by the drilling mud pressure inside the borehole.

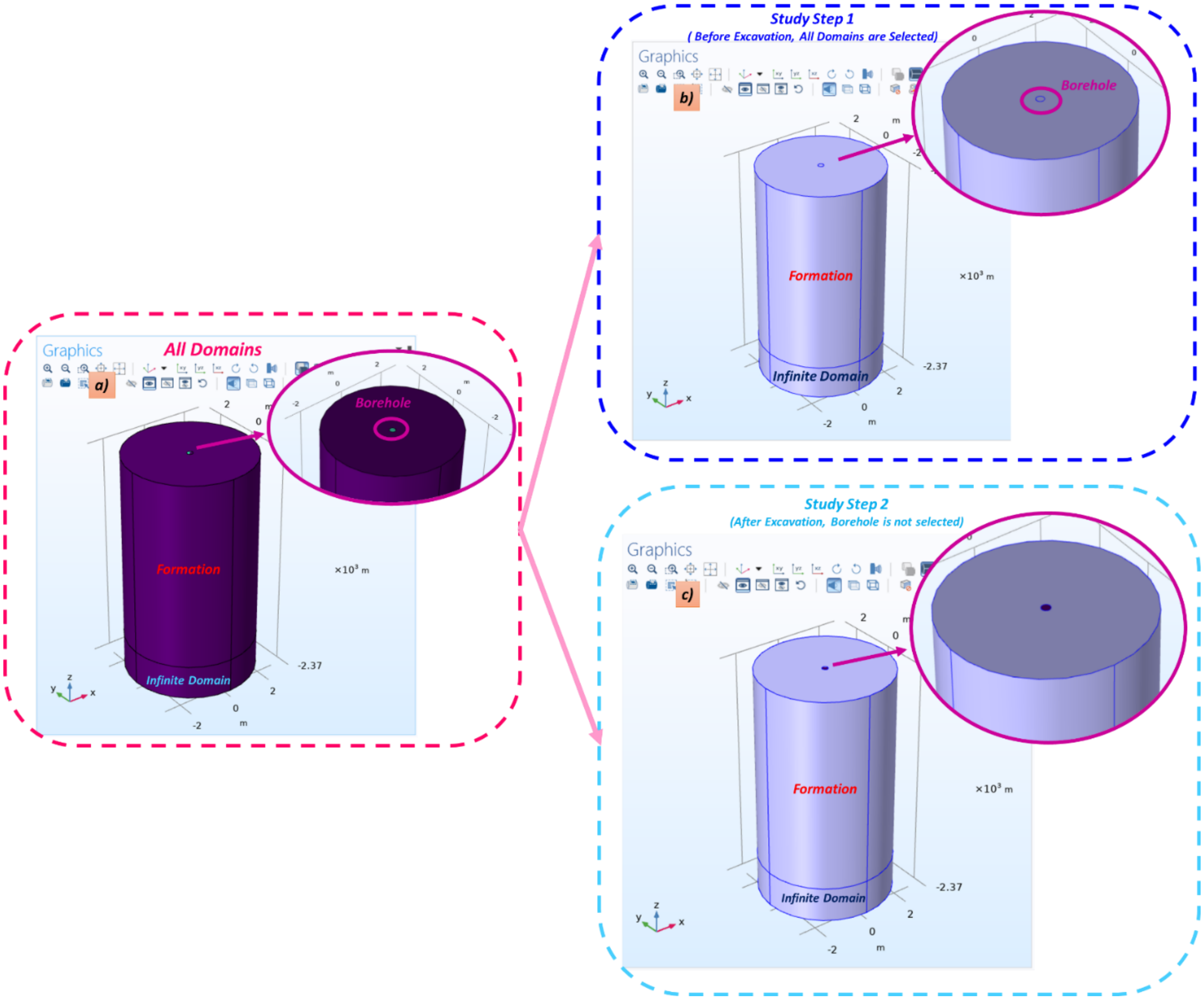

Figure 3-12: a) Domains defined for simulating static stress analysis; b) selected domains in modelling step 1 (before excavation); and, c) selected domains in modeling step 2 (after excavation).

3.2.3.1 Model Assessment

Assessment of the static numerical modeling was conducted by comparison against Aadnoy's analytical solution (presented in Appendix A) for stress concentration around an arbitrarily oriented borehole in a general anisotropic elastic model. The input data used were taken from Gaede et al. (2012).

Three different scenarios were modeled: vertical, horizontal and deviated boreholes (Figure 3-13). A cylindrical model with a radius of 5 m was used. The borehole was placed in the center of the model with radius of 0.1 m. As stated before, it was assumed that the coordinate system of the model is aligned with the in-situ stresses. For convenience, the compliance tensor was rotated into the top of borehole (TOH) coordinate frame. The formulation for transformation of the compliance tensor is presented in Appendix B. The value of the elastic parameters and in-situ stresses are presented in Tables 3-5 and 3-6. Results of the model assessment are shown in section 4.3.1.1.

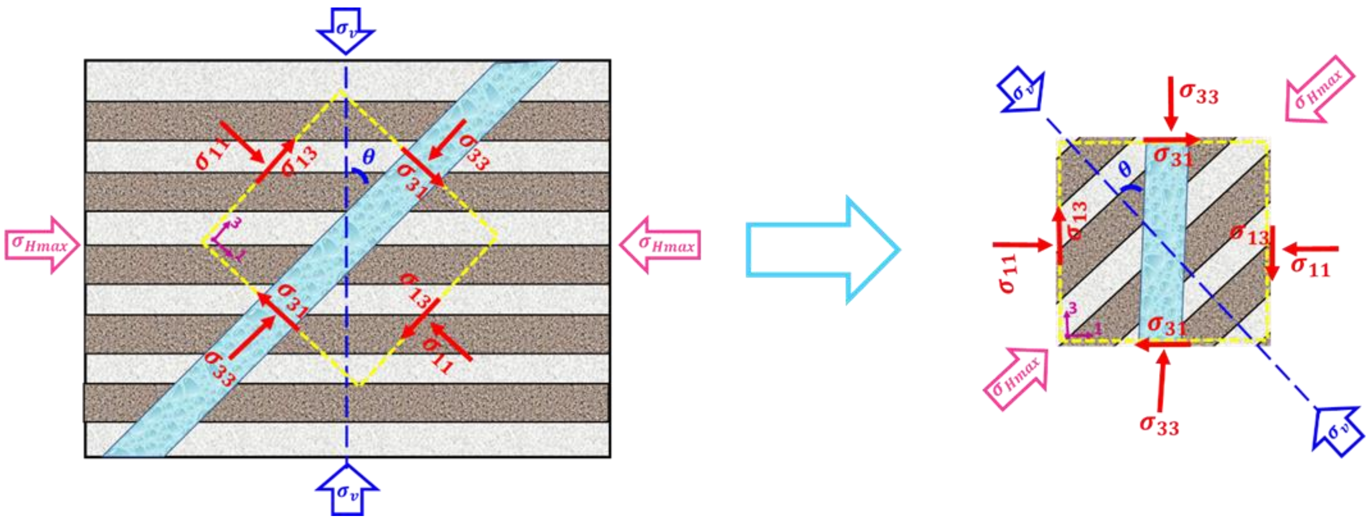

Figure 3-13: a) Schematic of the stress and elastic tensor transformations required to set up the boundary conditions at a borehole. Three different scenarios $\theta = 0$ (vertical borehole), $\theta = 90°$(horizontal borehole) and $\theta = 45°$ (deviated borehole); b) Rotated 'top of borehole" coordinate system used in COMSOL (after Karpfinger et al., 2011).

Table 3-5: Anisotropic elastic properties for vertical transverse isotropy (VTI), where the rock density is 2535 kg/m^3.

Elastic Properties		***Elastic Constants***	
$\boldsymbol{E_h}$	31.17 (GPa)	C_{11}	45.20 (GPa)
$\boldsymbol{E_v}$	15.42 (GPa)	C_{33}	28.00 (GPa)
$\boldsymbol{\vartheta_h}$	0.08	C_{44}	7.05 (GPa)
$\boldsymbol{\vartheta_v}$	0.32	C_{66}	14.40 (GPa)
$\boldsymbol{G_v}$	7.05 (GPa)	C_{13}	19.76 (GPa)

Table 3-6: In-situ stress field and mud pressure.

$\boldsymbol{\sigma_v}$	$\boldsymbol{\sigma_{Hmax}}$	$\boldsymbol{\sigma_{hmin}}$	$\boldsymbol{P_m}$
30 (MPa)	20 (MPa)	10 (MPa)	5 (MPa)

3.2.3.2 Montney Formation

The numerical model was used to simulate the stress concentration around the borehole in the Montney Formation at Farrell Creek for two scenarios: i.e., a vertical borehole and a horizontal borehole (parallel to the minimum horizontal stress). The following input parameters were required (values are presented in Table 3-7):

- The diameter of the undeformed borehole coincides with the bit size in well.
- The in-situ stresses and pore pressure were defined based on the literature review conducted in Chapter 2.
- The mud density was calculated as a function of temperature and pressure based on the equation presented by Carcione & Poletto (2000). Based on the completion report, Invert and Polymer based muds were used in the horizontal and vertical wells in the Montney Formation, respectively. Mud pressures inside the boreholes were defined based on calculated mud densities and the average depth of samples.
- Stress-dependent static elastic stiffness properties were defined based on the lab testing results presented in section 4.1.1.4.

Table 3-7: Input parameters for static analysis (Montney Formation).

		Vertical Borehole	Horizontal Borehole
Geometry	Borehole Diameter	$0.171(m)$	$0.171(m)$
	Formation Diameter	$7.60(m)$	$7.60(m)$
	Height	$12.83(m)$	$12.83(m)$
In-Situ Stresses	Maximum Horizontal Stress	$64.82(MPa)$	$64.82(MPa)$
	Minimum Horizontal Stress	$49.86(MPa)$	$49.86(MPa)$
	Vertical Stress	$59.83(MPa)$	$59.83(MPa)$
Drilling Mud	Pressure	$42.42(MPa)$	$36.32(MPa)$
Pore Pressure		$39.23(MPa)$	$39.23(MPa)$

3.2.3.3 Deadwood Formation

The model was used to simulate the stress concentration around a vertical borehole in the Deadwood Formation at the Aquistore Site. The model input parameters are listed in Table 3-8.

- The diameter of the undeformed borehole coincides with the bit size in the well.
- The in-situ stresses and pore pressure were defined based on the literature review conducted in Chapter 2.
- The mud density was calculated based on the equation used for calculating Montney boreholes. According to the completion report, the type of mud filling the vertical borehole in Deadwood Formation was Invert. Based on the presented volume fraction of components, the mud density was calculated. Mud pressure inside the borehole was defined based on the calculated mud density and the average depth of the samples.
- Stress-dependent static elastic stiffness properties were defined based on the lab testing results presented in section 4.2.1.4.

Table 3-8: Input parameters for static analysis (Deadwood Formation).

		Vertical Borehole
Geometry	Borehole Diameter	$0.251(m)$
	Formation Diameter	$7.60(m)$
	Height	$12.83(m)$
In-Situ Stresses	Maximum Horizontal Stress	$59.90(MPa)$
	Minimum Horizontal Stress	$51.96(MPa)$
	Vertical Stress	$81.74(MPa)$
Drilling Mud	Pressure	$41.03(MPa)$
Pore Pressure		$35.41(MPa)$

3.2.4 Dynamic Analysis

The acoustic module of COMSOL Multiphysics was utilized to simulate acoustic wave propagation around a fluid-filled borehole. The numerical model comprises two main domains: 1) the borehole, and 2) the formation surrounding the borehole, as shown in Figure 3-14. Acoustic energy is emitted by a point source located close to the bottom of borehole. Depending on the type of point source, different types of energy can be emitted into the borehole. Simulations using a monopole source were conducted during this work; however, these simulations were not the main focus of this work (interested readers are referred to Appendix C for monopole simulation results). The results of simulations using a dipole source are presented in Chapter 4, as the main focus of this research was to investigate fast/slow shear waves and flexural wave dispersion.

A number of virtual points, at which acoustic energy was recorded, were designated to represent an array of receivers. The number of virtual point receivers and their positions relative to the transmitter were based on the specific tool used to log the boreholes of interest for this work.

Modeling of wave propagation requires high resolution meshing of the borehole and the formation immediately surrounding the borehole in the vicinity of the logging tool. However, it is also necessary to model the borehole (in the axial direction) and formation (in the axial and radial directions) in the regions extending further away from the logging tool. Unfortunately, the boundaries between the inner and outer parts of the model domain will result in the occurrence of apparent reflected waves which are not representative of in-situ behaviour. In order to minimize these artifacts, a specially designed layer, widely known as a Perfectly Matched Layer (PML) is used for the outer parts of the model domain. In COMSOL Multiphysics, PML domains are a predefined option. PML domains were used surrounding the formation and borehole. It was found to be important to define separate PML domains for the formation and the borehole (as shown in Figure 3-14), since the predefined PML coordinate stretching functions are controlled by the typical wavelength (representing the longest wavelength of propagating waves in an infinite medium) provided by the physics interface, and two distinct physics were used for the formation (Solid Mechanics physics) and the borehole (Acoustic physics) and each of these domains have different compressional wave velocities (hence wavelengths). Also in the infinite element domain, it is strongly recommended by COMSOL to use swept meshing in the PML domains to prevent poor mesh element quality, giving rise to poor or slow convergence for iterative solvers and making the problem ill-conditioned in general.

It is believed that acoustic waves do not penetrate the surrounding media for distances exceeding a few dominant wave lengths, which is estimated to be between 0.5 and 0.7 m. Thus, it is natural to truncate the simulation area to 6 to 7 times the borehole radius (Pissarenko et al., 2009). However, initial dynamic simulation results (Appendix D) revealed that this radius would be better determined based on the static stress analysis results because dynamic elastic properties are defined as a function of stress, and the zone of induced stress change can extend beyond 7 borehole radii. In this research, formation radius during dynamic analysis was defined based on static stress analysis results.

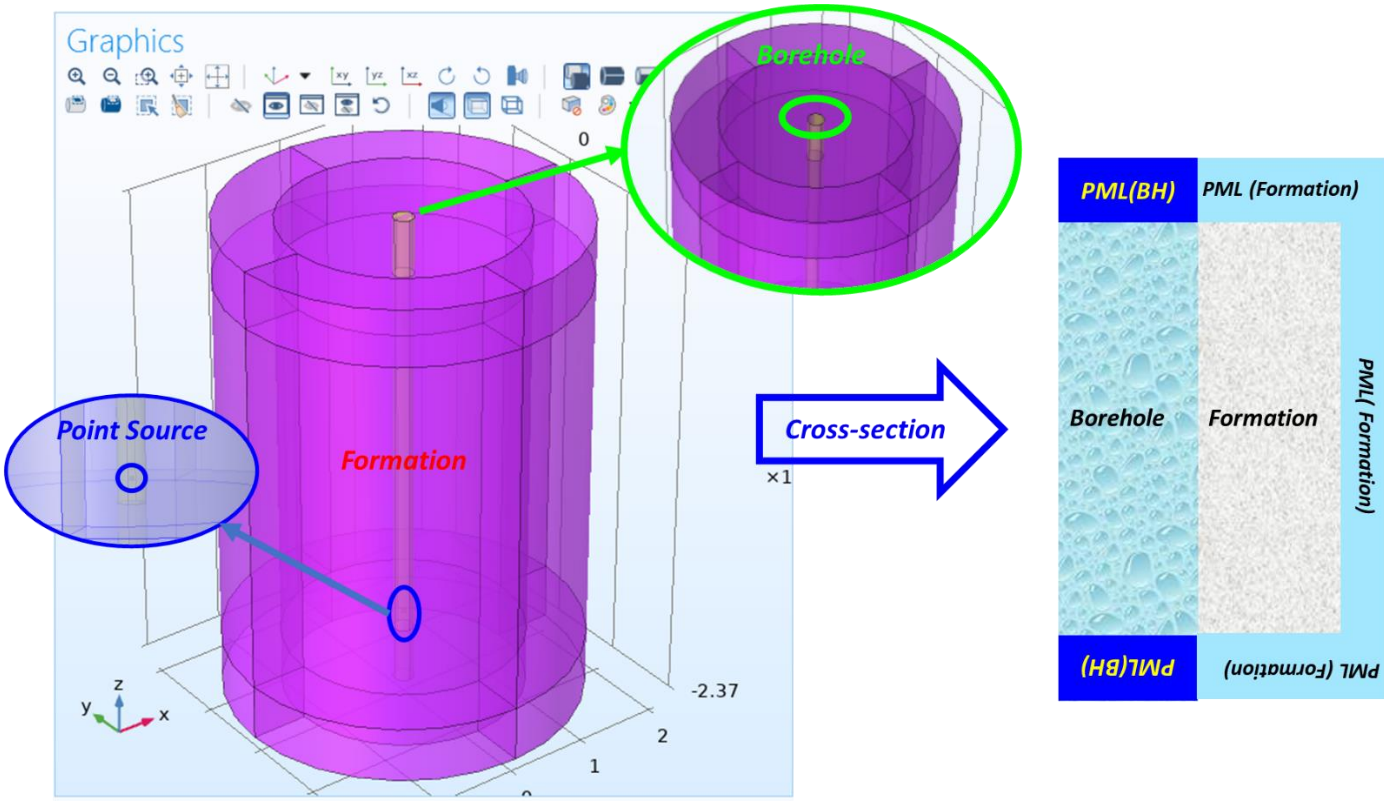

Figure 3-14: Graph showing the position of an acoustic point source and also illustrating the two PML domains used to simulate wave propagation during sonic logging using the acoustics module in COMSOL.

3.2.4.1 Model Assessment

To assess that the numerical model was functioning properly, simulation results were compared against the analytical solution proposed in section 3.4. To achieve this, a 3D finite element model was developed, which only contains an acoustic domain (known as the borehole) surrounded by a PML domain. In this model the transmitter was 3.5 m apart from the receiver array (according to sonic scanner tool specification) as shown in Figure 3-15. Two types of source wavelet were modeled; i.e., the Ricker wavelet and the Ormsby wavelet. Appendix E presents the methods used to derive frequency domain functions from time domain equations for these wavelets. Table 3-9 presents the properties assigned to the model for simulations using the Ricker wavelet, which is used in Weatherford's CXD logging tool. Since this model is in the low frequency range, the PML thickness was assigned one-quarter of a wavelength ($^1/_4\,\lambda$).

The Ormsby wavelet was chosen with the goal of generating a frequency sweep that simulates the Sonic Scanner tool used by Schlumberger. Table 3-10 presents the properties used for the Ormsby wavelet. Frequencies were chosen to be close to the frequency range generated by the Sonic Scanner tool, which is claimed to be flat from 300 HZ to 8 kHz (Franco et al., 2006). The results of the model assessment are presented in section 4.3.21.

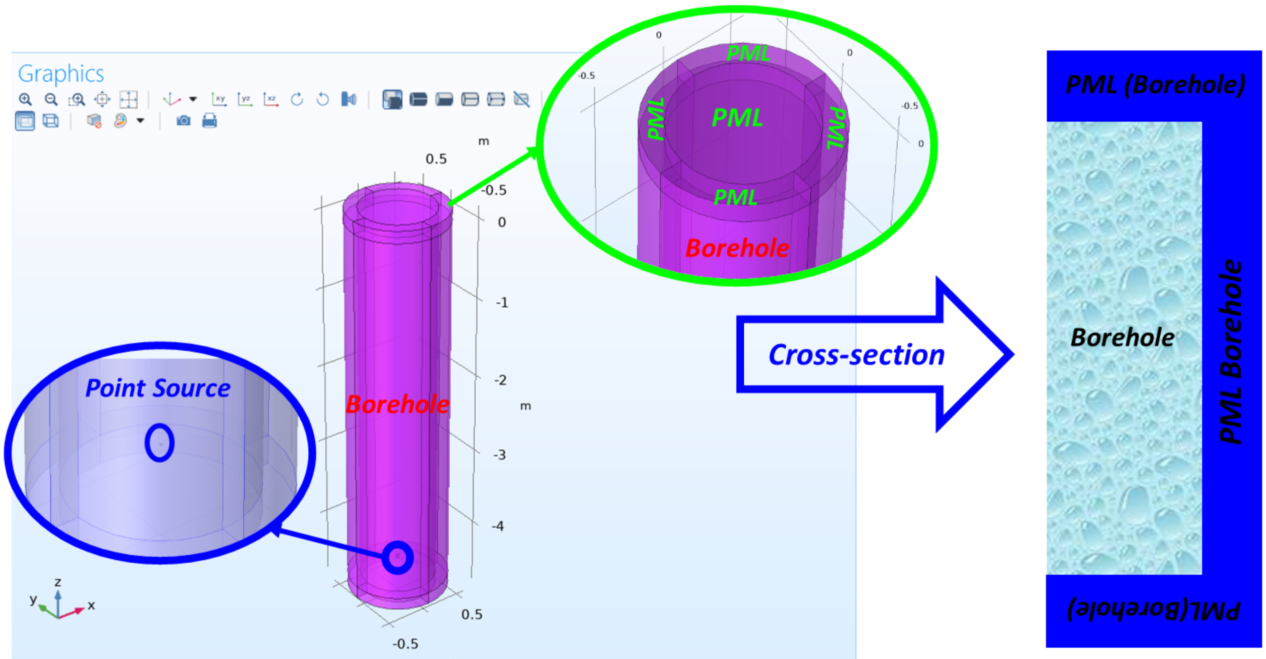

Figure 3-15: Graph showing the position of the point source and the two main domains used in the model assessment simulation; i.e., the borehole and the PML.

Table 3-9: Characteristics assigned to the model in order to assess the dynamic simulation using the Ricker wavelet source function.

	Acoustic velocity (km/s)	*Density of fluid (kg/m^3)*	*Maximum Frequency (Hz)*	*Central frequency (Hz)*	*PML velocity (km/s)*	*PML Thickness (m)*
Acoustic Domain Characteristics (Borehole)	1500	1000	1000	500	1500	0.375

Table 3-10: Characteristics assigned to the model in order to assess the dynamic simulation using the Ormsby wavelet source function.

	Acoustic velocity (km/s)	*Density of fluid (kg/m^3)*	$f_1(Hz)$	$f_2(Hz)$	$f_3(Hz)$	$f_4(Hz)$	*PML Thickness (m)*
Acoustic Domain Characteristics (Borehole)	1500	1000	0	300	8000	11000	1.25

3.2.4.2 Montney Formation

The model was used to simulate wave propagation during sonic logging of boreholes in the Montney Formation in Farrell Creek. For a horizontal borehole available data provided by Weatherford Inc were used for comparison against the simulation results. As such, the configuration of the Compact Cross-Dipole Sonic (CXD) tool was used as the basis for the model. The CXD tool uses a Ricker wavelet with frequency range between 2-10 kHz as its source. The following tool specifications were also used:

- Array of receivers is composed of 8 receivers.
- Spacing between adjacent receivers (RR) is 0.20 m
- The distance from the transmitter to first receiver (TR) is 2.6 m

For a vertical borehole, available data provided by Schlumberger Inc were used for comparison. As such, the configuration of the Sonic Scanner tool was used as the basis for the model. Based on the frequency response of the Sonic Scanner tool, it was concluded that this tool uses an Ormsby wavelet with frequency range between 2-10 kHz as its source. The following tool specifications were also used:

- Array of receivers is composed of 13 receivers.
- Spacing between two receivers (RR) is 0.1524 m
- The distance from the transmitter to first receiver (TR) is 3.5 m

Additional modeling parameters were as follows:

- Dynamic elastic properties were defined as a function of stress as mentioned in section 4.1.1.2, and stresses were imported from the static stress analysis described in section 4.2.1.2.
- The thickness of the PML domain was modified according to the minimum frequency in the practical frequency range of the tool ($thickness_{PMl} = {}^{1}/_{4}\,\lambda = {}^{fluid\ velocity}/_{4f_{min}}$).
- Mud velocities were calculated based on the equation presented in Carcione & Poletto (2000), to be close to the real field conditions. Based on the calculation, mud velocities for the horizontal well (Invert mud) and vertical well (Polymer based mud) were estimated to be 1540 m/s and 2350 m/s, respectively.

Table 3-11: Input parameters for dynamic analysis (Montney Formation).

		Vertical Borehole	Horizontal Borehole
Geometry	Borehole Diameter	$0.171(m)$	$0.171(m)$
	Formation Diameter	$2.052(m)$	$2.052(m)$
	Height	$8.33(m)$	$8.33(m)$
	PML Thickness	$2(m)$	$2(m)$
Point Source	Type of Point Source	Dipole	Dipole
	Type of Wavelet	Ormsby	Ricker
	Frequency Range	$300-8000(Hz)$	$2000-10000(Hz)$
Drilling Mud	Density	$1830(^{kg}/_{m^3})$	$1570(^{kg}/_{m^3})$
	Velocity	$2350(^{m}/_{s})$	$1540(^{m}/_{s})$

3.2.4.3 Deadwood Formation

The model was used to simulate wave propagation during sonic logging in the Deadwood Formation at the Aquistore site. For the vertical borehole logged at this site, available data provided by Schlumberger Inc were used for comparison. As such, the configuration of the Sonic Scanner tool was used as the basis for the model. Based on the frequency response of Sonic Scanner tool, it was concluded that this tool uses an Ormsby wavelet with a frequency range between 2-10 kHz as its source. The following tool specifications were also used:

- Array of receivers is composed of 13 receivers.
- Spacing between two receivers (RR) is 0.1524 m
- The distance from the transmitter to first receiver (TR) is 3.5 m

Additional modeling parameters were as follows:

- Dynamic elastic properties were defined as a function of stress as mentioned in section 4.2.1.2 and stresses were imported based on the conducted static stress analysis in section 4.2.1.3.
- The thickness of the PML domain was modified according to the minimum frequency in the practical frequency range of the tool ($thickness_{PMl} = {}^{1}/_{4}\lambda = {}^{fluid\ velocity}/_{4f_{min}}$).
- For the inverted mud used mud velocity was calculated as 842 m/s based on the equation presented in Carcione & Poletto (2000).

Table 3-12: Input parameters for dynamic analysis (Deadwood Formation).

		Vertical Borehole
Geometry	Borehole Diameter	$0.251(m)$
	Formation Diameter	$2.259(m)$
	Height	$8.33(m)$
	PML Thickness	$2(m)$
Point Source	Type of Point Source	Dipole
	Type of Wavelet	Ormsby
	Frequency Range	$300 - 8000(Hz)$
Drilling Mud	Density	$1260({}^{kg}/_{m^3})$
	Velocity	$842({}^{m}/_{s})$

3.2.5 Dispersion Analysis

In this project, dispersion analysis was conducted as a primary quality control (QC) method to verify numerical simulation and to estimate the dispersive character of the waves to quantify anisotropy behaviour of the formation. Two different methods were used to write MATLAB codes to calculate dispersion curves: 1) Dispersion Imaging Seismogram Calculation (DISECA)

(Gaždová & Vilhelm, 2011) and 2) the Phase Moveout method (Assous et al., 2014). Consistency between the results of these codes was used as means to validate the dispersion codes. (Raw waveforms could not be extracted from the field data provided by Schlumberger and Weatherford; hence it was not possible to validate these algorithms by comparison against dispersion curves provided by these service companies.)

The DISECA method is based on picking peak amplitude. In this method, time windows with different slope (phase velocity) are applied on an array of normalized sinusoids curves. If the curves are summed together within a finite time length along each slope, they will give new sinusoid curves of finite length whose amplitudes are between 0 to 1. The slope that gives the maximum amplitude will be the correct value of phase velocity being sought.

The Phase Moveout method is based on measuring the change in phase between the signal at each receiver, then converting the phase change to time delay and hence to a slowness by knowing spacing between receivers.

3.3 Additional Input Data

In addition to the input data properties presented previously (e.g., borehole diameter, in-situ stresses, pore pressure, mud properties and acoustic source properties), the following input parameters were required to run the COMSOL Multiphysics simulations conducted in this research:

- Rock dynamic and static elastic properties.
- Relationships between dynamic and static elastic stiffness parameters as a function of stress.

3.3.1 Rock Physical Properties

The results of lab testing were used to calculate the rock physical properties. Rock dynamic elastic properties were calculated according to equations 2.9 to 2.13. Static elastic properties were calculated based on the established relations presented in section 4.1.2.4.

3.3.2 Relationship between dynamic elastic stiffness parameters with stresses

The relationships between dynamic elastic stiffness parameters and stresses were established based on the hydrostatic experimental results for both the Montney Formation and the Deadwood Formation.

3.4 Analytical Solution Used for Assessment of Numerical Model

To assess a numerical model's accuracy, it is common to simulate a basic scenario for which an analytical solution is available. Sections 3.4.1 to 3.4.4 describe an analytical solution used in this research to assess the numerical model used for wave propagation simulation.

Note: This derivation was developed based on Yoshida (2018), with the assistance of Professor Samuel Butler.

3.4.1 Acoustic Wave Propagation in Fluid

The Navier-Stokes equation is a potential differential equation that describes the motion of viscous fluids. With this equation, the velocity can be calculated at many points within a region of space and an interval of time. Once the velocity field is calculated, other quantities of interest such as pressure or temperature may be found using additional equations and relations.

The general form of the Navier-Stokes equation is as follows:

$$\rho\left(\frac{\partial u}{\partial t} + u.\nabla u\right) = -\nabla\rho + \lambda\nabla^2 u \tag{3.34}$$

Where,

ρ = Density

u = Velocity

t =Time

λ = Volume viscosity

In equation 3.34, we assume that the fluid is incompressible. For the sake of simplicity, the role of viscosity is neglected in this work ($\lambda\nabla^2 u = 0$). To solve for the velocity of waves using the Navier-Stokes equation, the conservation of mass and a linear relation between pressure and density is applied. The general form of the mass conservation equation for an arbitrary domain can be defined as follows:

$$\frac{\partial\rho}{\partial t} + \nabla.(\rho\, u) = 0 \tag{3.35}$$

3.4.1.1 Relation between Density and Pressure

To achieve the relation between pressure and density, the compressibility equation is utilized:

$$K = -\frac{1}{V}\frac{\partial V}{\partial P} \tag{3.36}$$

Where,

K = Compressibility

V = Bulk volume

P = Pressure

The basic equation for density (equation 3.5) is combined with equation 3. 36, as follows:

$$\rho = \frac{M}{V} \tag{3.37}$$

Where,

M = mass

V = volume

$$\frac{dV}{d\rho} = \frac{M}{\rho}\frac{\partial V}{\partial \rho} = -\frac{M}{\rho^2}\frac{\partial \rho}{\partial P} \tag{3.38}$$

$$K = -\frac{\rho}{M}\left(\frac{-M}{\rho^2}\right)\frac{\partial \rho}{\partial P} \tag{3.39}$$

$$K = \frac{1}{\rho}\frac{\partial \rho}{\partial P} \tag{3.40}$$

Thus, the change in density is defined as follows:

$$\partial \rho = \rho K \partial P \tag{3.41}$$

The substitution of equation 3.41 into equation 3.35 gives Navier-Stokes equation in terms of pressure:

$$\rho K \frac{\partial P}{\partial t} + \nabla^2(\rho\ u) = 0 \tag{3.42}$$

The density change caused by acoustic pressure at each point is expressed by the background density (ρ_b) and its change in time (ρ'):

$$\rho = \rho_b + \rho' \tag{3.43}$$

$$\rho u = \rho_b u + \rho' u \tag{3.44}$$

In equation 3.44, the change in density in time is assumed to be small enough to be ignored. By having this assumption, equation 3.42 can be changed to the following equation:

$$\rho K \frac{\partial P}{\partial t} + \nabla . (\rho_b\, u) = 0 \tag{3.45}$$

3.4.1.2 Simplified Navier-Stokes Equation to 1D

For a one-dimensional problem, equation 3.45 can be expressed as follows:

$$\rho_b K \frac{\partial P}{\partial t} + \frac{\partial}{\partial x} (\rho_b\, \vec{u}) = 0 \tag{3.46}$$

Taking the partial derivative with respect to t, we find:

$$\rho_b K \frac{\partial^2 P}{\partial t^2} + \frac{\partial^2}{\partial x\, \partial t} (\rho_b\, \vec{u}) = 0 \tag{3.47}$$

Based on the conservation of momentum, the following relationship exists between pressure and velocity:

$$\rho_b \frac{\partial \vec{u}}{\partial t} = -\frac{\partial P}{\partial x} \tag{3.48}$$

By deriving from x:

$$\rho \frac{\partial^2 \vec{u}}{\partial x\, \partial t} = -\frac{\partial^2 P}{\partial x^2} \tag{3.49}$$

By replacing equation (3.49) into equation (3.47), the following equation is obtained:

$$\rho_b K \frac{\partial^2 P}{\partial t^2} - \frac{\partial^2 P}{\partial x^2} = 0 \tag{3.50}$$

By simplifying equation 3.50, the following equation is obtained:

$$K \frac{\partial^2 P}{\partial t^2} - \frac{1}{\rho_b} \frac{\partial^2 P}{\partial x^2} = 0 \tag{3.51}$$

We can then generalize the 1D equation 3.50 to a 3D wave equation, as follows:

$$K\frac{\partial^2 P}{\partial t^2}-\frac{1}{\rho_b}\nabla^2 P=0 \quad (3.52)$$

3.4.2 Potential Function

As mentioned in Chapter 2, logging tools are generally made up of two or more transmitters and an array of receivers. A transmitter is a point source that radiates a wavefront. Depending on the type of source, this wavefront can be symmetrical as with the monopole sensor, or the wave front can be asymmetrical with respect to the source as per the dipole sensor (as illustrated in Figure 2-1). In this work, the transmitter is considered as the origin of the coordinate system.

To simulate the wave propagation analytically as function of time and location, a potential function is required to determine the pattern or the phase variation of the wave. In the following section, the derivation of the potential function for different types of transmitters is shown.

3.4.2.1 General Type of Potential Function

To achieve a general form of the potential function, a mass balance and force balance are applied, as follows:

$$\frac{\partial\rho}{\partial t}+\nabla.(\rho u)=0 \quad (3.53)$$

$$\rho=\rho_b+\rho' \quad (3.54)$$

$$\hat{u}=\widehat{u_0}+\widehat{u_1} \quad (3.55)$$

Where:

ρ_b = Background density

ρ' ≔ Density change with time

$\widehat{u_0}$= Background velocity

$\widehat{u_1}$= Velocity change with time

The background state of velocity is zero, as follows:

$$\widehat{u} = \widehat{u_1} \tag{3.56}$$

$$\frac{\partial(\rho_b + \rho')}{\partial t} + \nabla.\left((\rho_b + \rho')\widehat{u_1}\right) = 0 \tag{3.57}$$

Zero orders are constant with time:

$$\frac{\partial(\rho_b)}{\partial t} + O(0) = 0 \quad \xRightarrow[0th\ order\ are\ constant\ with\ time]{} \quad \frac{\partial(\rho_b)}{\partial t} = 0 \tag{3.58}$$

Then the first order equation is as follows:

$$\frac{\partial\rho}{\partial t} + \nabla.(\rho_b u) + O(2) = 0 \quad \xRightarrow[1th\ order]{} \quad \frac{\partial\rho'}{\partial t} + \rho_b \nabla.(u) = 0 \tag{3.59}$$

By substituting equation 3.40 into equation 3.59, the following equation is derived:

$$\rho_b K \frac{\partial P}{\partial t} + \rho_b \nabla.(u) = 0 \tag{3.60}$$

Based on a force balance:

$$\rho \frac{\partial u}{\partial t} + \rho u.\nabla^2 u = -\nabla p \tag{3.61}$$

$$(\rho_b + \rho'\ ) \frac{\partial u_1}{\partial t} + (\rho_b + \rho'\ ) u_1.\nabla^2 u_1 = -\nabla p \tag{3.62}$$

The first order derivative accounts for the change of background state; here we neglect the second order, and the zero order is constant in space.

$$\rho_b \frac{\partial \widehat{u_1}}{\partial t} + O(0) = -\nabla p \tag{3.63}$$

Next equation 3.58 and equation 3.62 are used, and equation 3.63 is derived with respect to time and gradient from equation 3.62. Moreover, we assume that $= \nabla\varphi$, where φ is a potential function. Then equation 3.58 becomes:

$$-K\rho_b \frac{\partial^2\varphi}{\partial t^2} + \nabla^2\varphi = 0 \tag{3.64}$$

By the spherical Laplacian, it is concluded that it is required to define a new variable to simplify the above equation $\emptyset = \varphi r$:

$$\frac{\partial^2 \nabla \emptyset}{\partial t^2} - C_0^2 \frac{\partial}{\partial r} \emptyset = 0 \tag{3.65}$$

In equation 3.66, $C_0 (= {}^{1}\!/\!_{\sqrt{K\,\rho_b}})$ is the compressional wave velocity of the fluid.

To determine the pattern or the phase variation of the wave, it is required to define $\emptyset$ as the combination of the two arbitrary functions showing the wave going outwardly from the source at the speed C_0 (f) and inwardly to the source at the speed $C_0(g)$:

$$\emptyset = f\left(t - \frac{r}{C_0}\right) + g(t + \frac{r}{C_0}) \tag{3.66}$$

Acoustic waves are radiated in an outward direction, so the g function can be ignored in simulating the acoustic waves:

$$\emptyset = f\left(t - \frac{r}{C_0}\right) = r\varphi \tag{3.67}$$

$$\varphi = \frac{f\left(t - \frac{r}{C_0}\right)}{r} \tag{3.68}$$

On the other hand, the same relation holds between the general velocity vector $\hat{u}$ and φ :

$$\hat{u} = \nabla\varphi \ .$$

By substituting this relation into equation 3.63 (, the following equation is derived:

$$\rho_b \frac{\partial^2}{\partial t^2} \nabla\varphi = -\frac{\partial}{\partial t} \nabla P_1 \tag{3.69}$$

By integrating equation 3.69, the following equation is achieved:

$$\rho_b \frac{\partial \varphi}{\partial t} = -P_1 \tag{3.70}$$

Next, considering a sphere centered at the origin and having a small pulsating motion, the equation of its surface is:

$$r = a_0 + a(t) \tag{3.71}$$

Where:

a_0= Initial radius of sphere

$a(t)$= Change in sphere radius in time

If it is considered that the velocity in the radial direction is V_r , the following relation exists for fluid velocity at the sphere surface (Yoshida,2018):

$$V_r = \frac{\partial \varphi}{\partial r} = \frac{dr}{dt} = a'(t) \tag{3.72}$$

So, from equations 3.68 and equation 3.72, the following relation is obtained for arbitrary function (f):

$$f(t) = -a_0 c_0 \int_{-\infty}^{\infty} a'(t + \frac{a_0}{c_0}) e^{-\frac{c_0}{a_0}(t-t')} dt \tag{3.73}$$

The wavelength (λ) is assumed to be much greater than the sphere radius (a_0), then the following holds trues:

$$if\ a_0 \ll \lambda \qquad \lambda = C_0 T \qquad \rightarrow \qquad f(t) = -a_0^2\, a' \tag{3.74}$$

It is thus concluded for φ:

$$\varphi = \frac{f(t - {}^{r}/_{C_0})}{r} = -\frac{a_0^2 a'(t - {}^{r}/_{C_0})}{r} \tag{3.75}$$

Moreover, according to the mass flow rate, the mass moving across the sphere of $a_0$is given by:

$$m(t) = 4\pi a_0^2 \rho_b a' \tag{3.76}$$

3.4.3 Harmonic Motion in Frequency Domain (Monopole)

For a harmonic motion:

$$\dot{a} = \bar{V} e^{-i\omega t} \tag{3.77}$$

In equation 3.77, $\dot{a}$ represents the fluid velocity at the sphere surface, and $\bar{V}$ represents the amplitude of the pulsation velocity.

By substituting equation 3.77 into equation 3.73, the following relation can be derived for an arbitrary function (f):

$$f(t) = \frac{-a_0 C_0 \bar{V} e^{-i\omega(t+{}^{a_0}/_{C_0})}}{{}^{C_0}/_{a_0} - i\omega} \tag{3.78}$$

From equation 3.77, the following equation is derived for φ:

$$\varphi = \frac{f(t-{}^{r}/_{C_0})}{r} = \frac{-a_0 C_0 \bar{V} (\frac{C_0}{a_0} + i\omega) e^{-i\omega(t-{}^{r}/_{C_0}+{}^{a_0}/_{C_0})}}{\left[\left({}^{C_0}/_{a_0}\right)^2 + \omega^2\right] r} \tag{3.79}$$

By substituting equation 3.77 into equation 3.75 for a frequency domain condition, the following equation is obtained for $\bar{m}$:

$$\bar{m} = 4\pi a_0^2 \bar{V} \rho_b \tag{3.80}$$

The following equation can be concluded for $\bar{V}$:

$$\bar{V} = \frac{\bar{m}}{4\pi a_0^2 \rho_b} \tag{3.81}$$

The following relation exists for wave number K:

$$K = \frac{\omega}{C_0} \tag{3.82}$$

Now, a new variable ($\widetilde{\omega}$) is defined for frequency:

$$\widetilde{\omega} = \frac{\omega a_0}{C_0} \tag{3.83}$$

By substituting the variable in equation 3.83 into equation 3.79, the following relation is derived for φ:

$$\varphi = \frac{-\bar{m}\sqrt{1+\widetilde{\omega}^2} e^{-i(\omega t - \emptyset - K(r-a_0))}}{4\pi\rho[1+\widetilde{\omega}^2]^{1/2}} \tag{3.84}$$

This provides the following relations for pressure (P) and radial velocity:

$$V_r = \frac{\partial\varphi}{\partial r} = \frac{-\bar{m}}{4\pi\rho_0}\left(\frac{-e^{i(Kr-\omega t)}}{r^2} + \frac{iKe^{i(Kr-\omega t)}}{r}\right) \tag{3.85}$$

$$P = -\rho_b \frac{\partial \varphi}{\partial t} = -\rho_b \frac{i\omega \overline{m} e^{i(K-\omega t)}}{4\pi \rho_0 r} \tag{3.86}$$

By simplification of equations 3.85 and 3.86, the following relations exist for pressure and radial velocity in a harmonic condition like the monopole configuration:

$$V_r = \frac{\partial \varphi}{\partial r} = \frac{-\overline{m}}{4\pi \rho_b}\left(\frac{\cos Kr}{r^2} + \frac{K \sin Kr}{r}\right) + i\left(\frac{\sin Kr}{r^2} - \frac{K \cos Kr}{r}\right) \tag{3.87}$$

$$P = -\rho_b \frac{\partial \varphi}{\partial t} = \frac{\omega \overline{m}(\sin Kr + i \cos Kr)}{4\pi r} \tag{3.88}$$

3.4.4 Dipole

A dipole is composed of two parts; i.e., a positive transmitter on one side and a negative transmitter on the other side. These two sources are separated by a very short distance. Finding the potential function of a dipole is more difficult than a monopole configuration, so this section provides an approximation for this type of transmitter.

The potential function of the dipole can be defined as follows:

$$\varphi_d = \frac{-me^{ikr}}{4\pi \rho_b}\left(\frac{iKr - 1}{r^2}\right) d cos\theta \tag{3.89}$$

Where d stands for distance between two sources.

To find the potential function of a dipole, the total work must be done by this source. The total work can be calculated as follows:

$$Power_t = \int_0^{2\pi}\int_0^{\pi} V \rho_b r^2 \sin\theta \, d\theta \, d\varphi \tag{3.90}$$

Using equation 3.90, a surface integral is performed. By substituting equation 3.89 into equation 3.90, the following result can be obtained for dipole power:

$$Power_t = \frac{m^2 \omega d^2 i K^3 e^{i2Kr}}{8\pi \rho_b} \int_0^{\pi} \sin\theta \cos^2\theta \; d\theta \tag{3.91}$$

By doing the integral, the total power of dipole source is calculated as:

$$Power_t = \frac{m^2 \omega d^2 i K^3 e^{i2Kr}}{24\pi\rho_b} \tag{3.92}$$

It can be concluded that:

$$m = \sqrt{\frac{12\pi Power_t \rho_b}{\omega d^2 K^3}} \tag{3.93}$$

In these equations, it can be assumed that:

$$d^2 \cong 0 \qquad \& \qquad e^{i2kr} \cong 1 \tag{3.94}$$

The following equations are obtained for pressure P and radial velocity (V_r) generated by a dipole source:

$$V_r = \frac{\partial\varphi}{\partial r} = \frac{-\overline{m}}{4\pi\rho_b} \cos\theta \; e^{ikr}(ik\left(\frac{ikr-1}{r^2}\right) + \frac{ik}{r^2} - \frac{2(ikr-1)}{r^3}) \tag{3.95}$$

$$P = \frac{-i\omega\overline{m}}{4\pi} e^{ikr} \frac{(ikr-1)}{r^2} \tag{3.96}$$

4. Results

This chapter presents the results of study on the effect of intrinsic and stress-induced anisotropy on borehole sonic logging of both the Montney Formation (at Farrell Creek) and the Deadwood Formation (at Aquistore project site). Laboratory experiments in conjunction with numerical modelling were utilized to fulfill this objective. Sections 4.1 and 4.2 present the physical properties of the samples that were obtained in order to advance the understanding of the relationship between stresses and physical properties of rocks. Section 4.3.1 describes static analysis to determine the stress field around boreholes. Results of the modeling in section 4.3.1 were used to define dynamic elastic properties that were used for dynamic wave propagation modeling described in section 4.3.2.

4.1 Laboratory Results (Montney Formation)

Dynamic and static properties of sample #1, #6 and #8 were measured under hydrostatic, uniaxial and deviatoric loading conditions. The most measurements selected for dynamic analysis were those calculated under hydrostatic loading conditions, because the lab data were of better data quality acquisition for the hydrostatically loaded samples. For static analysis, to define elastic properties as a function of stresses, uniaxial and hydrostatic loading data were used. Although sample #6 was tested under hydrostatic load, results from the experiment are not presented in this section since this sample was instrumented exclusively with compressional-wave transducers, in order to simplify (and expedite) testing while evaluating testing procedures and equipment. The results for this sample, being partial in nature, were not useful in elastic properties calculations presented in this chapter.

4.1.1 Experimental Results for Dynamic Analysis

4.1.1.1 Sample #1, Test sequence #1, Hydrostatic Loading

Velocities measured during hydrostatic loading/unloading are presented in Figure 4-1. Following are some general observations:

- Horizontal velocities are consistently greater than vertical velocities.
- Diagonal velocities are intermediate between vertical and horizontal; roughly midway between the two for compressional waves, but only slightly greater than the vertical velocities through the mid and upper range of hydrostatic stresses for shear waves.

- Horizontal velocities are relatively insensitive to hydrostatic stress change. This is consistence with expectations, given that waves propagating within bedding laminations do not have to cross stress-sensitive, bedding parallel fractures.
- Vertical and diagonal velocities show a trend of increasing velocity with increasing hydrostatic stress, with stress sensitivity being greatest at low stress (below approximately 7 MPa). This stress sensitivity is likely due to closure of bedding-parallel fractures for both vertical and diagonal velocity measurements, and additionally due to closure of platen-sample interfaces for vertical velocities.
- Velocities measured during loading and unloading were generally similar for stresses greater than 7 MPa, but notably different in some cases at lower stress levels.

Elastic constants for sample #1 calculated using the data collected data during sequence #1 are shown in Figure 4-2. The elastic constants show varying degrees of hysteresis effects as a consequence of the hysteresis observed in the velocities during unloading versus loading. C_{13} shows the highest degree of hysteresis due to the more complex form of equation 2.13 (i.e., it is influenced by a large number of velocity components than the other elastic constants). From Figure 4-2, an increase in the stiffness of the samples as a function of hydrostatic load can be observed as a consequence of closure of microcracks and pores, though the stress dependence of C_{11} and C_{66} (which are functions of the velocities of waves propagating parallel to bedding)appear to be negligible.

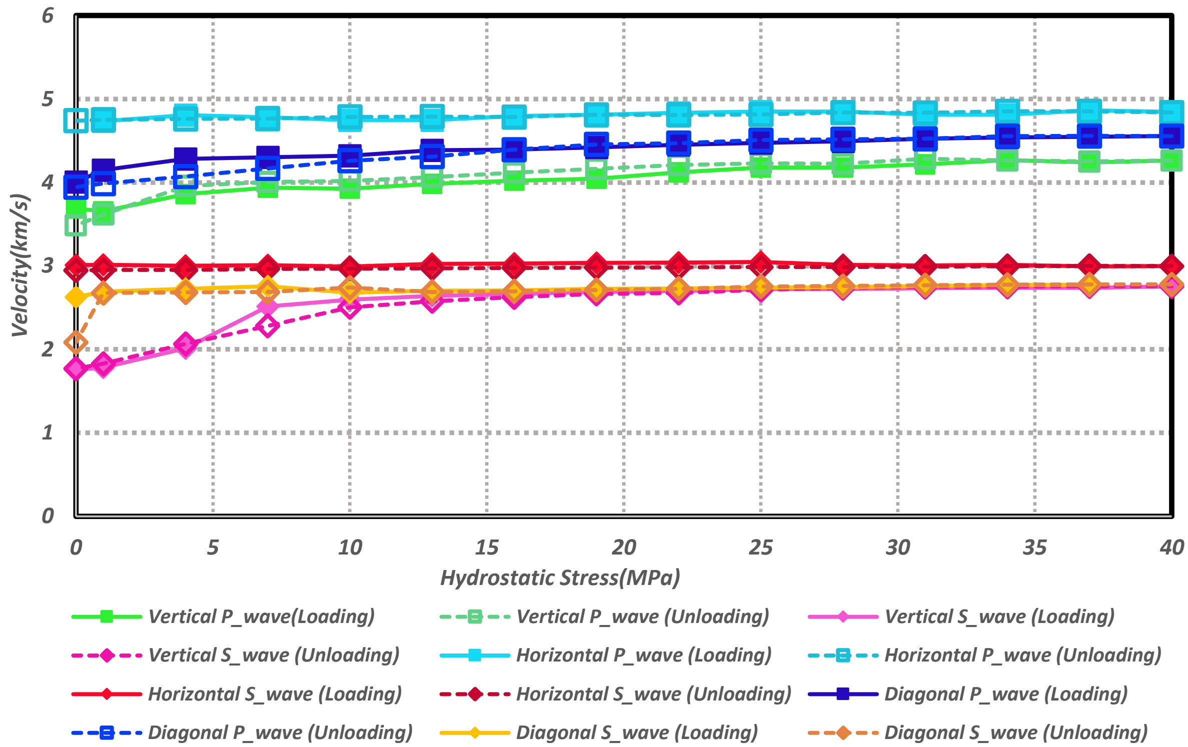

Figure 4-1: Graphical compilation of velocities measured on sample #1 during hydrostatic loading, test sequence #1. "Vertical" denotes the bedding-normal direction; "Horizontal" denotes the bedding parallel direction; "Diagonal" denotes the direction rotated 45° from the bedding normal; "Loading" denotes velocities measured while confining pressure was being increased incrementally to its maximum value; and "Unloading" denotes velocities measured while confining pressure was being decreased incrementally from its maximum values.

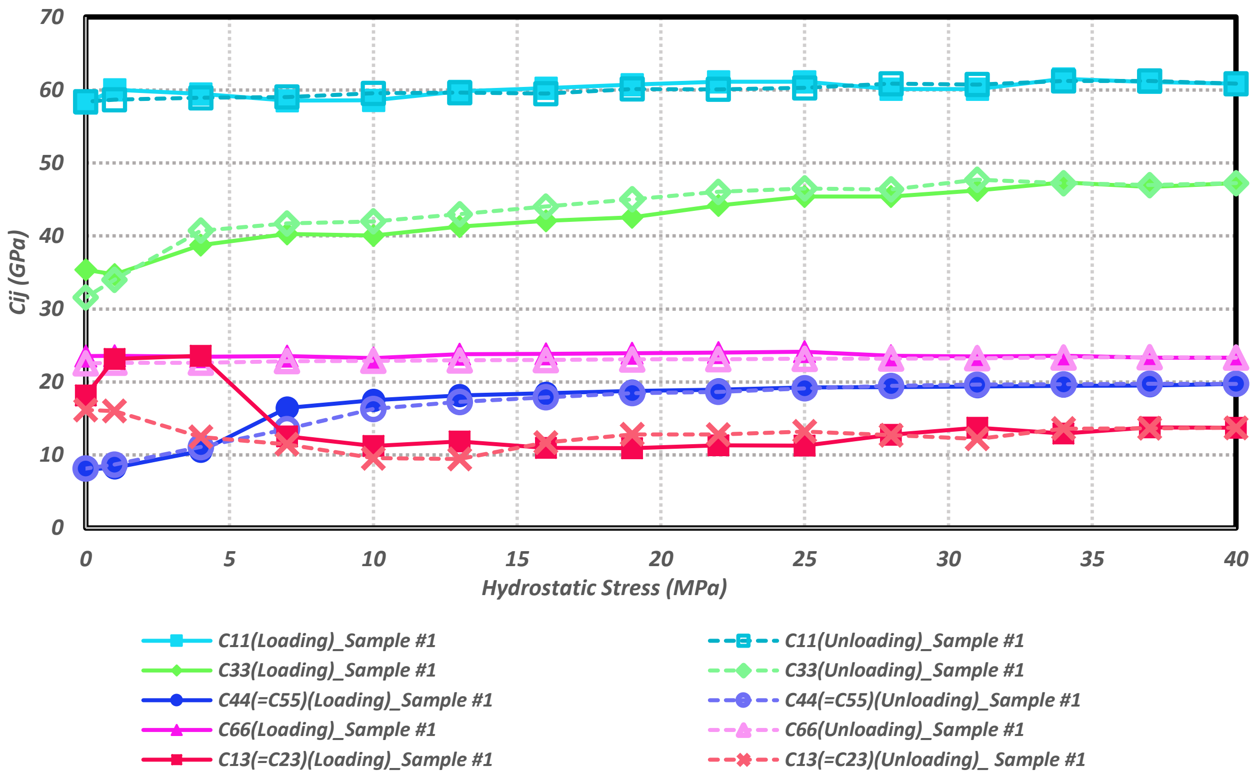

Figure 4-2: Graphical compilation of elastic constants on sample #1 during hydrostatic loading, test sequence #1. "Vertical" denotes the bedding-normal direction; "Horizontal" denotes the bedding parallel direction; "Diagonal" denotes the direction rotated 45° from the bedding normal; "Loading" denotes velocities measured while confining pressure was being increased incrementally to its maximum value; and "Unloading" denotes velocities measured while confining pressure was being decreased incrementally from its maximum values.

4.1.1.2 Sample #1, Test Sequence #2, Hydrostatic Loading

Measured loading/unloading velocities are presented in Figure 4-3. Comparing these results to test sequence #1, bearing mind the difference in peak hydrostatic stress for these sequences (40 MPa vs. 20 MPa) and disregarding some of the more variable results obtained at low stresses, the results for both test sequences compare favourably.

Estimated elastic constants for sample #1 while conducting sequence 2 are shown in Figure 4-4. C_{11}, C_{33}, C_{44} and C_{66} show the same behaviour as velocities, since there are direct relationships between each of these elastic constants and each of the measured velocities. C_{13} shows more complex behaviour compared to other elastic constants, owing to its dependence on several of the velocities. From Figure 4-4, an increase in the stiffness of the samples as a function of hydrostatic load can be observed as a consequence of closure of microcracks and pores, expcept for $C_{11}$and C_{66} which were assumed to be constant in testing sequence #2.

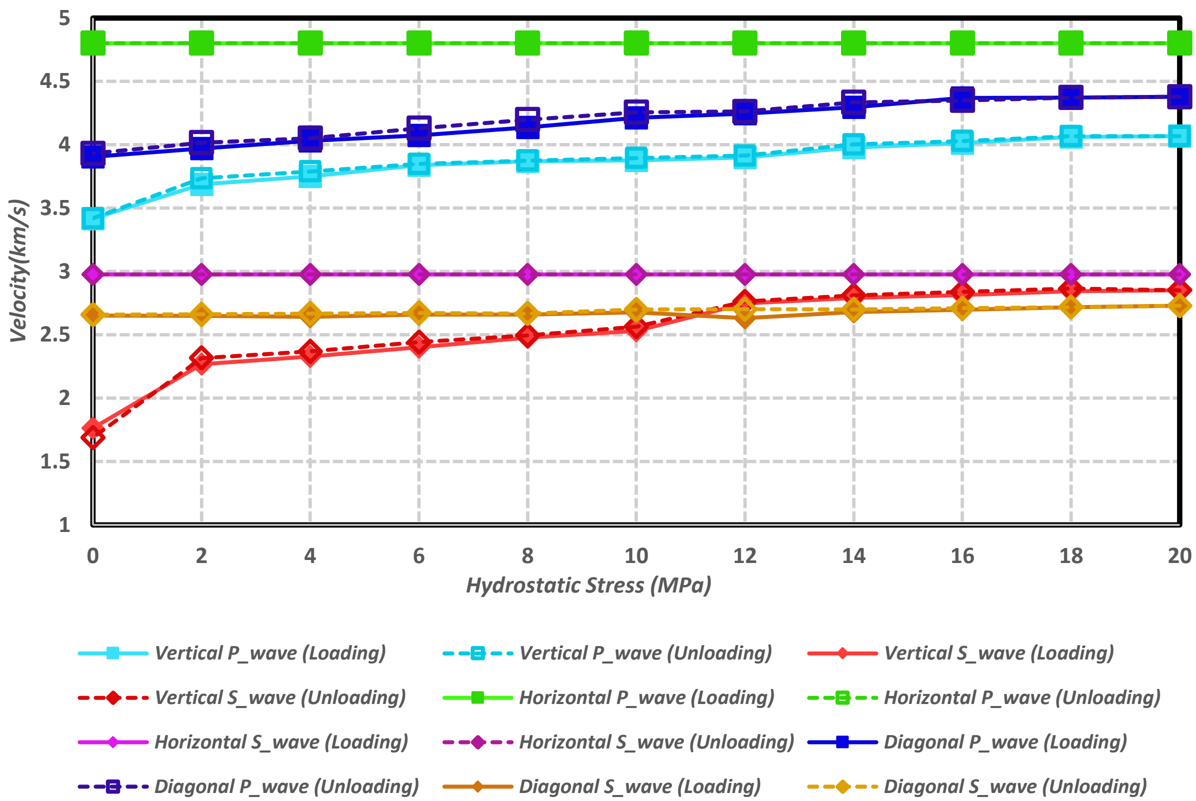

Figure 4-3: Graphical compilation of velocities measured on sample #1 during hydrostatic loading, test sequence #2. Horizontal velocities were assumed constant ($V_p = 4.80 \ ^{km}/_{s}$; $V_s = 2.98 \ ^{km}/_{s}$) based on an average of results obtained during test sequence #1.

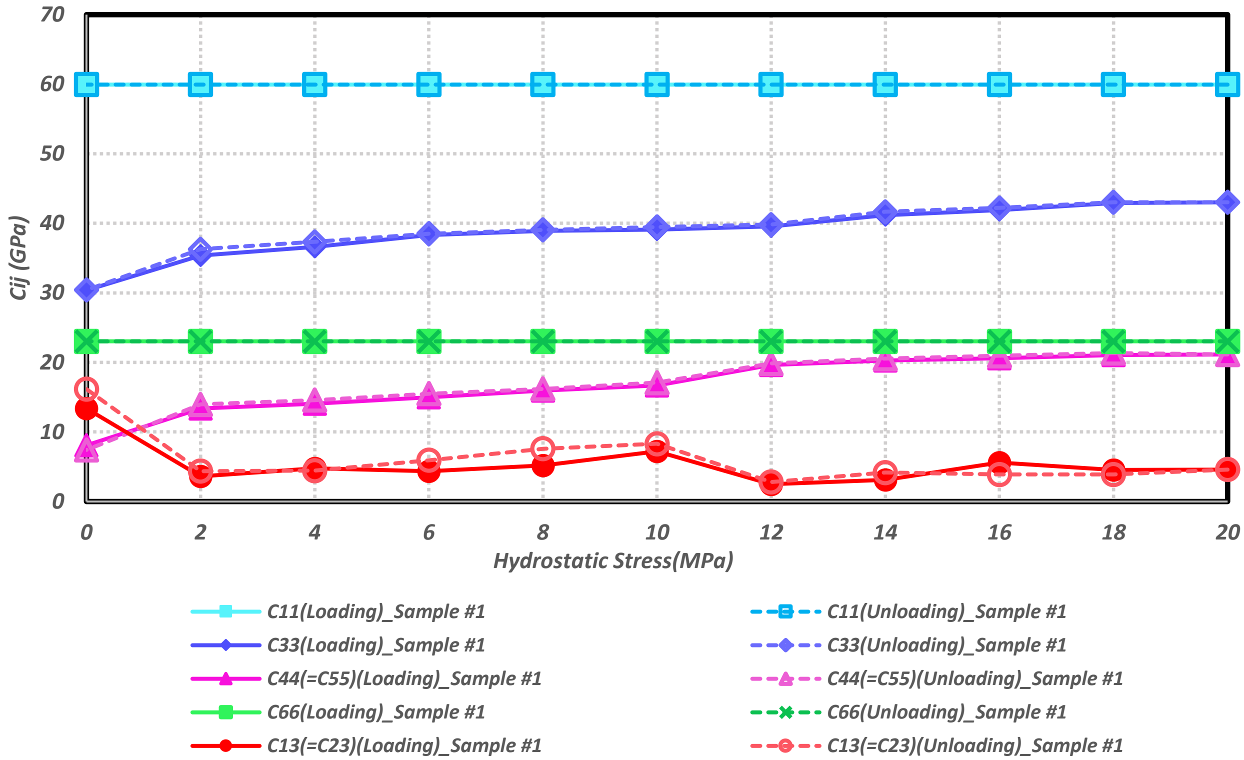

Figure 4-4: Graphical compilation of elastic constants estimated on sample #1 during hydrostatic loading, test sequence #2. Horizontal velocities were assumed constant ($V_p = 4.80\ {}^{km}/_{s}$; $V_s = 2.98\ {}^{km}/_{s}$) based on an average of results obtained during test sequence #1.

4.1.1.3 Sample #8, Hydrostatic Loading

Figure 4-5 shows the velocities measured during hydrostatic loading and unloading of sample #8 to a maximum hydrostatic stress of 40 MPa. The general trends observed for velocities and elastic constants for sample #1 also hold true for sample #8, though the values are slightly lower.

Elastic constants for sample #8 calculated using these velocities, are shown in Figure 4-6.

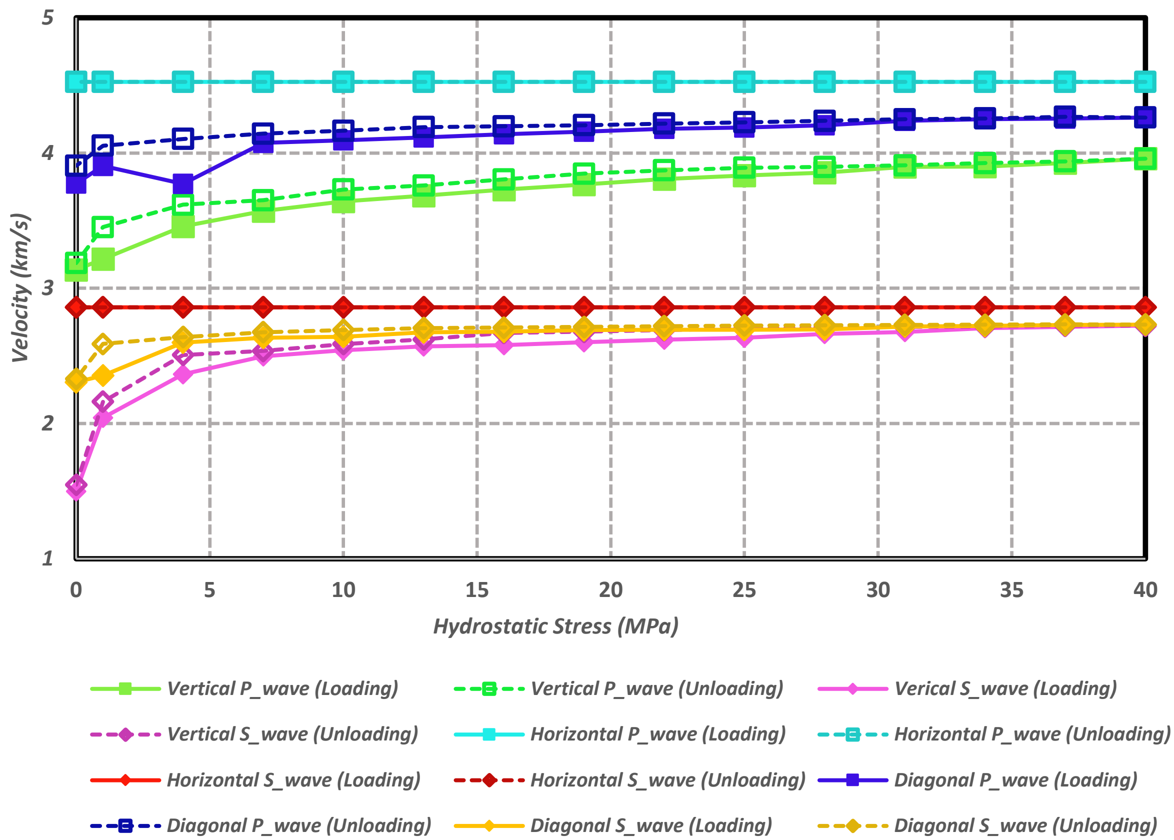

Figure 4-5: Graphical compilation of velocities measured on sample #8 during hydrostatic loading. Horizontal velocities assumed constant ($V_P = 4.526\ {km}/{s}$; $V_S = 2.859\ {km}/{s}$) based on results obtained before filling the triaxial cell.

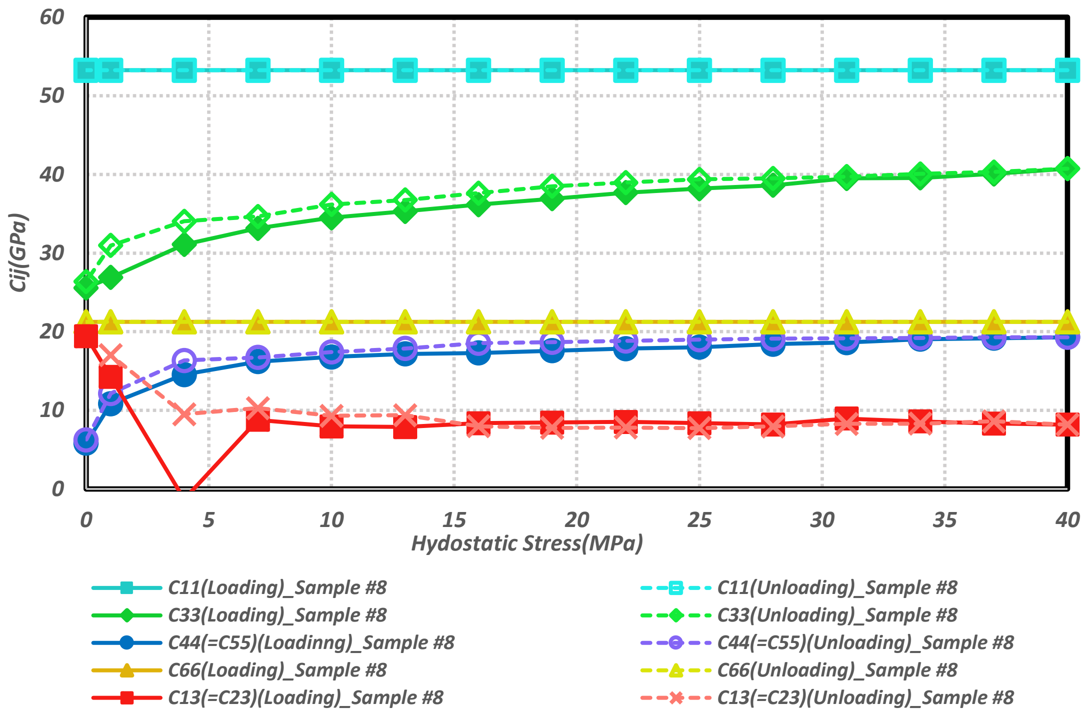

Figure 4-6: Graphical compilation of elastic constants estimated on sample #8 during hydrostatic loading. Horizontal velocities assumed constant ($V_P = 4.526\ {}^{km}/_{s}; V_S = 2.859\ {}^{km}/_{s}$) based on results obtained before filling the triaxial cell. The negative value calculated for C_{13} at $4MPa$ during loading is deemed unrealistic and has been ignored in this work.

4.1.1.4 Relationship Between Dynamic Elastic Constants and Hydrostatic Stress

To develop a rock physics model based on nonlinear elasticity that describes the dependence of the effective stiffness tensor as a function of a 3D stress field in intrinsically anisotropic formations, the hydrostatic testing results were used as an input in dynamic analysis in COMSOL.

The COMSOL model developed in this research for dynamic analysis requires the specification of C_{ij_Dyn}values as functions of stress. There are different ways that this could be done. For example, given that all three principal stresses at any given point around a borehole will generally be unequal in magnitude, it would be most rigorous to relate elastic constants to parameters that characterize both mean and deviatoric components of stress. It is suggested that the development of these relationships would serve as the basis of a stand-alone research project, involving extensive laboratory study under a wide range of stress states. For the sake of simplicity, and because the most comprehensive dataset available for the Montney and Deadwood Formation samples studied in this work were acquired under hydrostatic loading conditions, the numerical modeling was conducted assuming a linear relationship between effective dynamic elastic stiffnesses (ΔC_{ij}) and mean effective stress. This is represented mathematically as follows;

$$C_{ij} = a_{1_{ij}}(\sigma_1 + \sigma_2 + \sigma_3) + a_{2_{ij}} \quad (4.1)$$

Where

C_{ij}= effective elastic stiffness parameters (GPa).

σ_1, σ_2, σ_3= applied effective stresses (converted to GPa for this calculation).

$a_{1_{ij}}$ = slope of the line fitted on the experimental data.

$a_{2_{ij}}$= intercept of the line fitted on the experimental data (GPa)

Note: In the experiments conducted for this research, total stresses were equal to effective stresses, since pore pressures were zero.

Figure 4-7 shows each elastic constant plotted against mean stress for sample #1, as well as linear trendlines fit through the data points. These trendlines are based on the data for hydrostatic stresses greater than 7 MPa; i.e., they ignore the data at low stresses, where stress-dependence is more acute and – in some cases – erratic. The unloading data are deemed more representative of in-situ conditions, on the assumption that microcracks induced by coring and handling will have most impact during the loading cycle. Table 4-1 lists the linear trendline parameters for each elastic constant, measured during the unloading cycle of test sequence #1.

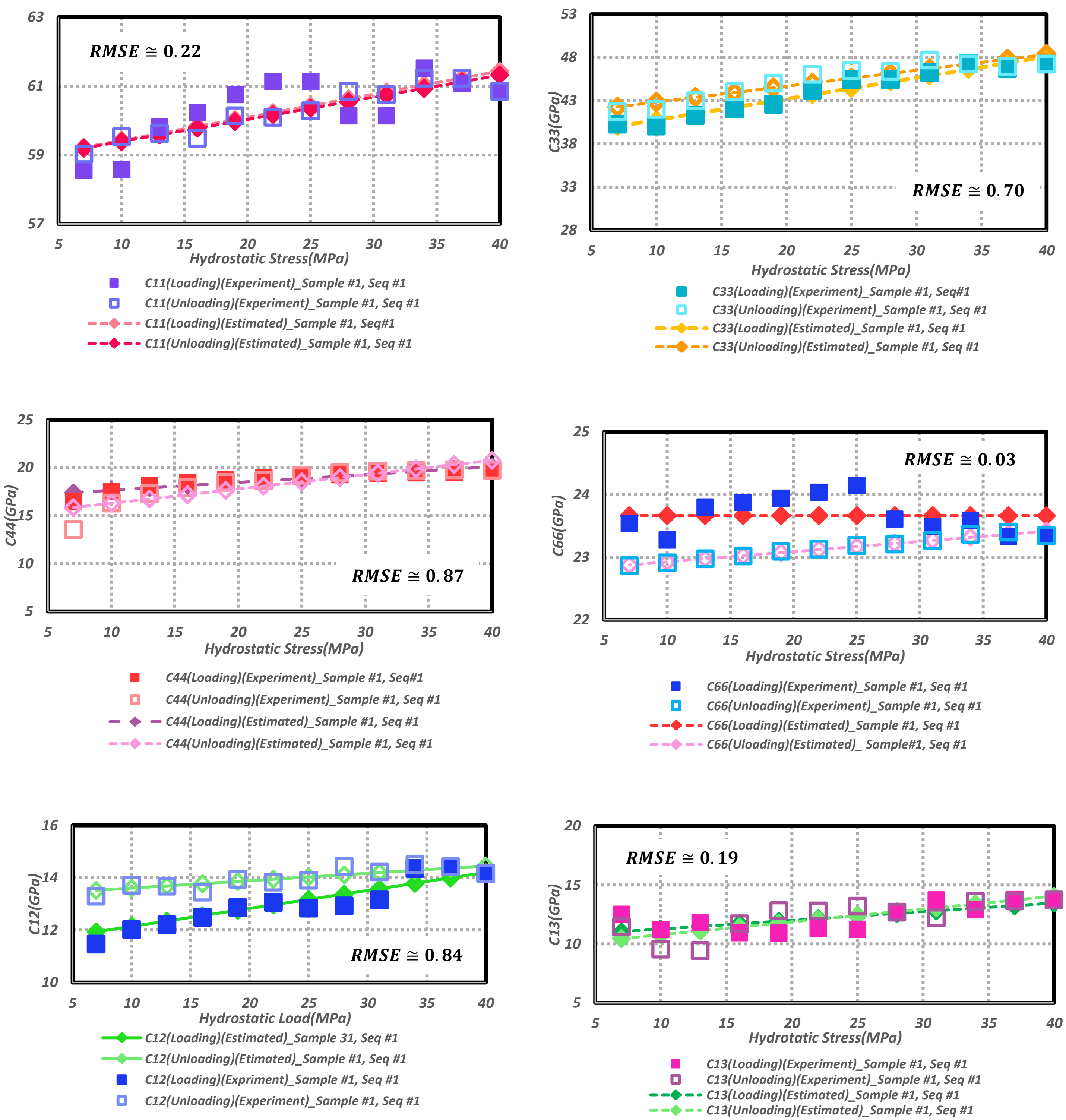

Figure 4-7: Dynamic elastic constants and linear trendlines plotted versus hydrostatic stress for Montney Formation sample #1, sequence #1. The root mean square error (*RMSE*) shown in each graph was calculated for the trendline fit to the unloading data.

Table 4-1: Trendline parameters (see equation 4.1) for stress-dependent dynamic elastic stiffness constants of the Montney Formation (sample #1) during unloading.

	$a_{1_{Dyn}}$(-)	$a_{2_{Dyn}}$(GPa)
$C_{11_{Dyn}}$	64.30	58.75
$C_{33_{Dyn}}$	245.43	32.48
$C_{44_{Dyn}}(= C_{55_{Dyn}})$	228.55	19.84
$C_{66_{Dyn}}$	16.41	22.76
$C_{12_{Dyn}}(= C_{21_{Dyn}})$	28.22	13.33
$C_{13_{Dyn}}(= C_{23_{Dyn}})$	108.86	9.70

4.1.2 Experimental Data for Static Analysis

4.1.2.1 Static Elastic Properties of Sample #1, Sequence #3, Uniaxial Loading

In order to assess the static response of sample #1 to deviatoric loading, the sample instrumentation was modified as described in section 3.1.2, and the sample was subjected to uniaxial loading parallel to bedding (on the front and back faces of the sample).

Figure 4-8 represents the calculated static elastic properties based on the vertical and horizontal strains measured during uniaxial loading of sample #1. As shown in this figure, Young's modulus increases with uniaxial stress with values in the 8-9 GPa range occurring at the low end of the stress range, increasing to 12-13 GPa at the high end of the stress range. Poisson's ratio shows a weak positive trend during loading, increasing from roughly 0.26 to 0.29 across the axial stress range investigated in this test. During unloading, Poisson's ratio shows variable results, first decreasing to 0.14, then gradually increases to 0.23 at lowest axial stress.

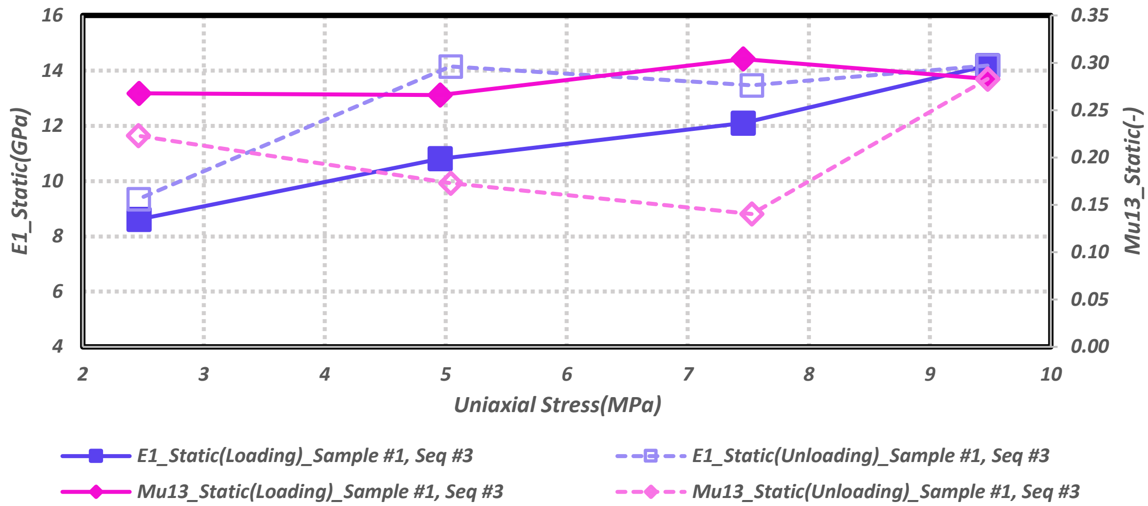

Figure 4-8: Graphs of Static Young's modulus and Poisson's ratio parallel to bedding, calculated for sample #1 during uniaxial loading (test sequence #3).

4.1.2.2 Static Elastic Properties of Sample #1, Sequence #2, Hydrostatic

Figure 4-9 shows the static bulk modulus calculated for sample #1 during hydrostatic loading, test sequence #2. Values are close to 10 GPa at hydrostatic confinement of 7 MPa, increasing to 15-20 GPa at maximum confinement.

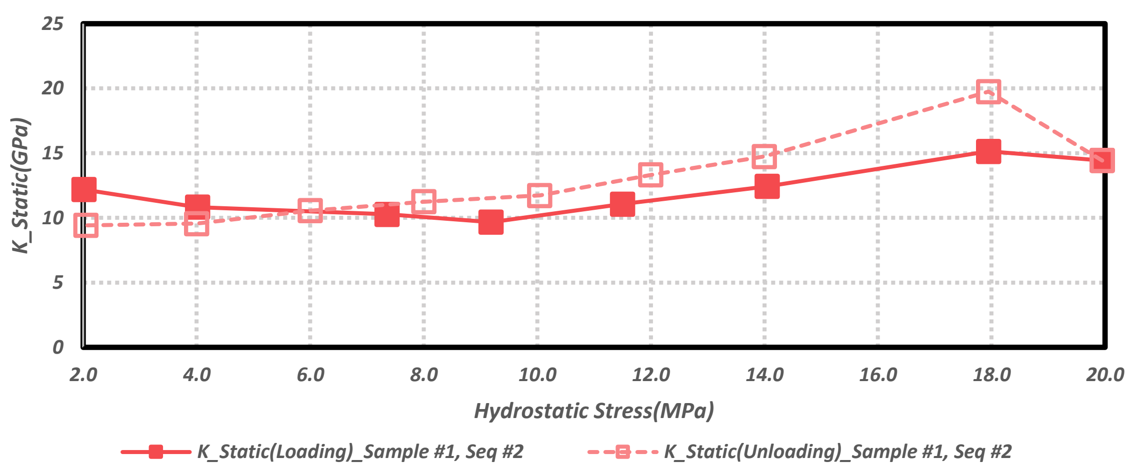

Figure 4-9: Graph of static bulk modulus calculated for sample #1 during hydrostatic loading, test sequence #2.

4.1.3 Static-Dynamic Property Constants

In the study of dynamic properties, linear relations between applied stresses and elastic stiffness constants were assumed (equation 4.1). To define static elastic stiffness constants as a function of stress, the approach chosen was to develop a correlation between static and dynamic elastic stiffness constants. Previous studies on different types of rocks have suggested that linear relationships between static and dynamic elastic properties are generally observed (King, 1980; Eissa & Kazi, 1988; Mokovciakova, 2003). For this reason, and for model simplicity, linear relationships were assumed in this work; investigation of possible non-linear relationships suggested by some of the data (e.g., for C_{44}) was flagged as a topic of future research. As such, in this study we assumed a linear relationship between effective static and dynamic elastic properties, as follows.

$$C_{ij_{Static}} = a_{ij}\left(C_{ij_{Dynamic}}\right) + b_{ij} \tag{4.2}$$

Correlation between static elastic stiffness constants and dynamic elastic stiffness constants, are shown in Figure 4.10. The average values for a_{ij} and b_{ij} are presented in Table 4-2. Based on the correlations, the constants presented in Table 4-3, are obtained to define static elastic stiffness constants as function of stresses**.**

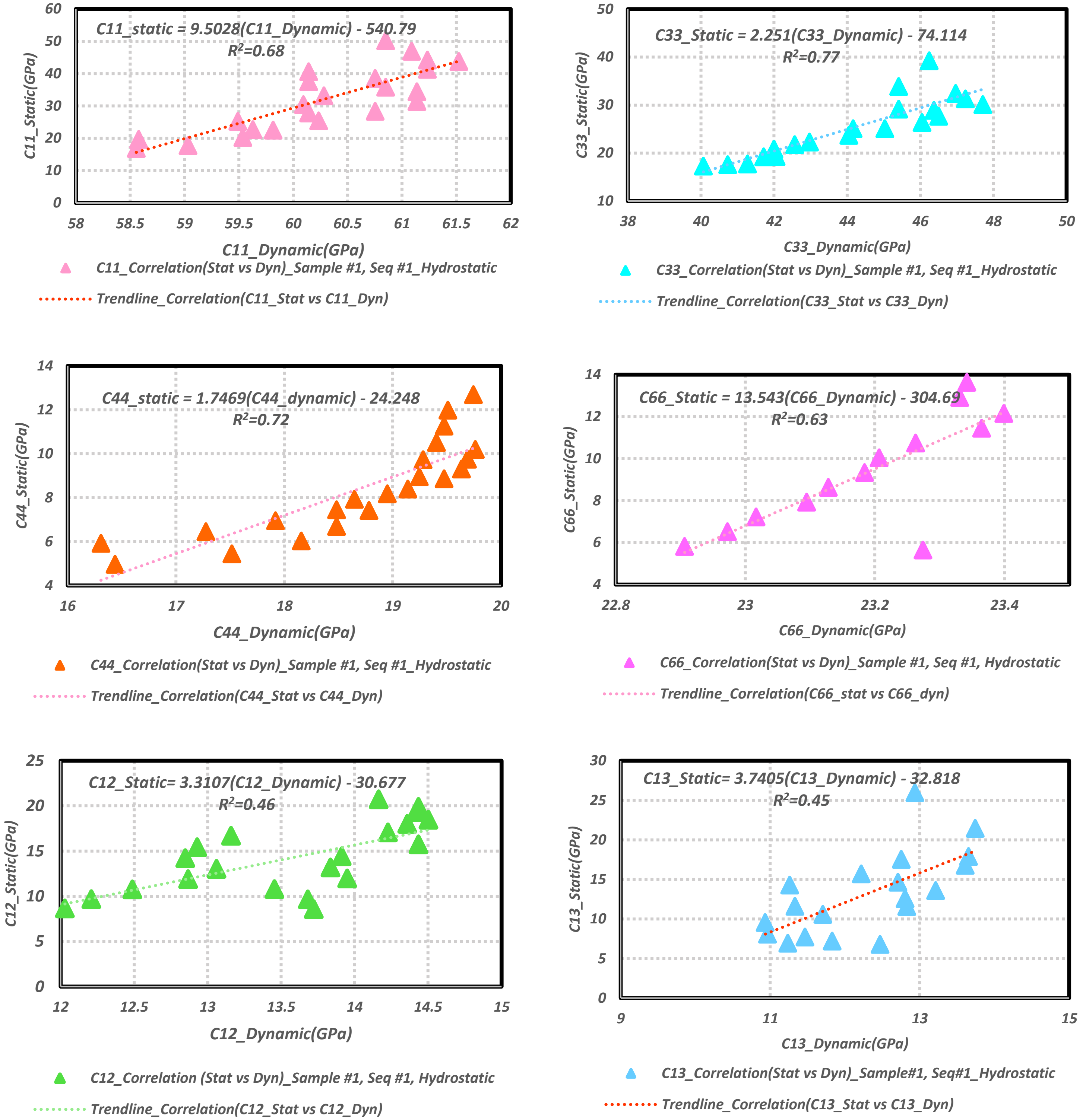

Figure 4-10: Correlation between static and dynamic elastic stiffness constants for sample #1, sequence #1, under hydrostatic stress.

Table 4-2: Averaged values of linear trendline coefficients relating effective static and dynamic elastic stiffness constants (Montney Formation).
($C_{ij} = a_{1_{ij}}(\sigma_1 + \sigma_2 + \sigma_3) + a_{2_{ij}}$)

a_{ij}(-)		b_{ij}(GPa)	
a_{11}	9.50	b_{11}	-540.79
a_{33}	2.11	b_{33}	-66.16
a_{44}	1.19	b_{44}	-14.47
a_{66}	9.28	b_{66}	-206.06
a_{12}	3.31	b_{12}	-30.68
a_{13}	1.66	b_{13}	-6.95

Table 4-3: Derived trendline parameters for stress-dependent between effective static elastic stiffness constants of the Montney Formation.

	$\mathbf{a}_{1_{Stat}}$**(-)**	$\mathbf{a}_{2_{Stat}}$**(GPa)**
$\boldsymbol{C_{11_{Stat}}}$	610.98	17.49
$\boldsymbol{C_{33_{Stat}}}$	319.14	6.02
$\boldsymbol{C_{44_{Stat}}}(= \boldsymbol{C_{55_{Stat}}})$	296.02	9.20
$\boldsymbol{C_{66_{Stat}}}$	222.25	3.48
$\boldsymbol{C_{12_{Stat}}}(= \boldsymbol{C_{21_{Stat}}})$	93.43	13.44
$\boldsymbol{C_{13_{Stat}}}(= \boldsymbol{C_{23_{Stat}}})$	230.10	0.80

4.2 Laboratory Results (Deadwood Formation)

4.2.1 Experimental Results for Dynamic Analysis

4.2.1.1 Vertical Samples

Measured compressional wave velocities during hydrostatic loading of the vertical cores are presented in Figure 4-12. Following are some observations based on these results:

- Vertical velocities show a trend of increasing velocity with increasing hydrostatic stress, with stress sensitivity being greatest at low stress (below approximately 5 MPa). This stress sensitivity is likely due to closure of bedding-parallel fractures and additionally due to closure of platen-sample interfaces.
- Estimated elastic constants for vertical samples are shown in Figure 4.13. Elastic constants show the same trend as velocities. Elastic constants calculated based on the sample Tx4 have the highest values, while calculated elastic constants based on the sample Tx2 show the lowest values. This is consistent with the fact that velocities were highest and lowest for these samples, respectively.

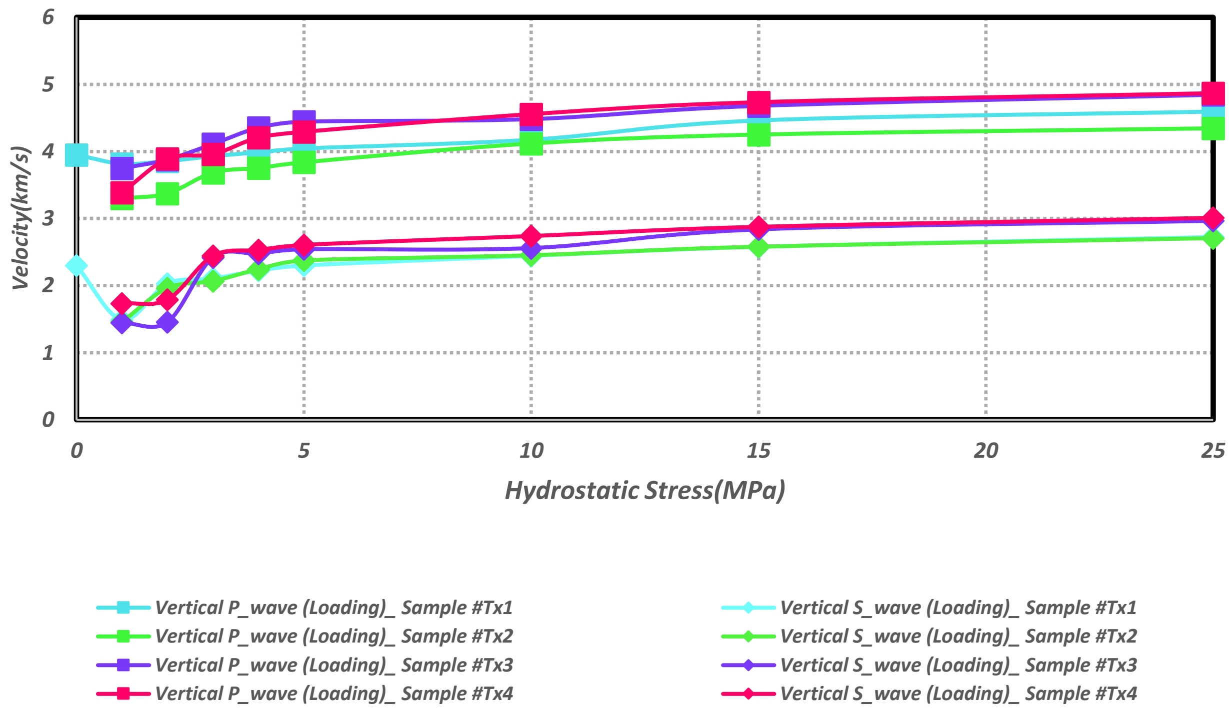

Figure 4-11: Graphical compilation of vertical velocities measured on samples $Tx1, Tx2, Tx3$ and $Tx4$ during hydrostatic loading.

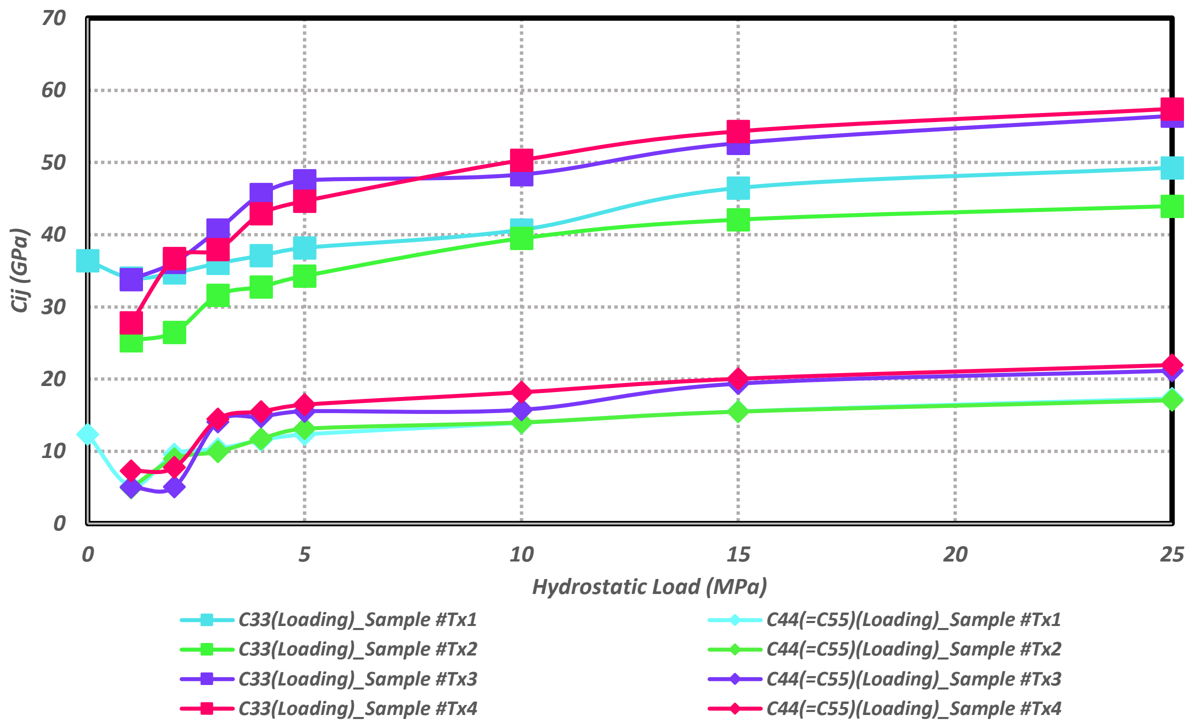

Figure 4-12: Graphical compilation of elastic constants estimated on samples Tx1, Tx2, Tx3 and Tx4 during hydrostatic loading.

4.2.1.2 Horizontal Sample

To measure velocities of a horizontal sample under hydrostatic loading, the same procedures as the vertical samples was utilized. Measured velocities during hydrostatic loading from 0 to 25 MPa are presented in Figure 4-13. Horizontal S-wave velocity show a trend of increasing velocity with increasing hydrostatic stress the same as vertical velocities, with stress sensitivity being greatest at low stress (below approximately 5MPa). However, horizontal P-wave shows less sensitivity to increase in hydrostatic stress.

Estimated elastic constants for the horizontal sample are shown in Figure 4-14. Elastic constants show exactly the same trend as velocities. Off-diagonal elastic stiffness parameters (C_{12} and C_{13}) are estimated based on the equation 3.1 and are presented in Figure 4-15

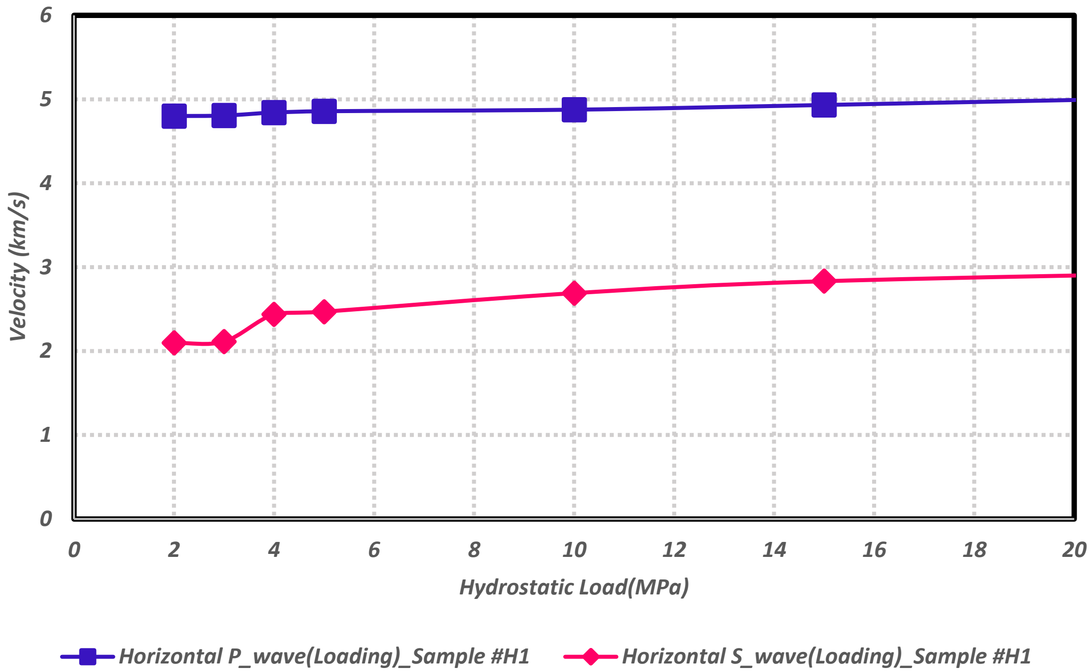

Figure 4-13: Graphical compilation of horizontal velocities measured on #H1, during hydrostatic loading.

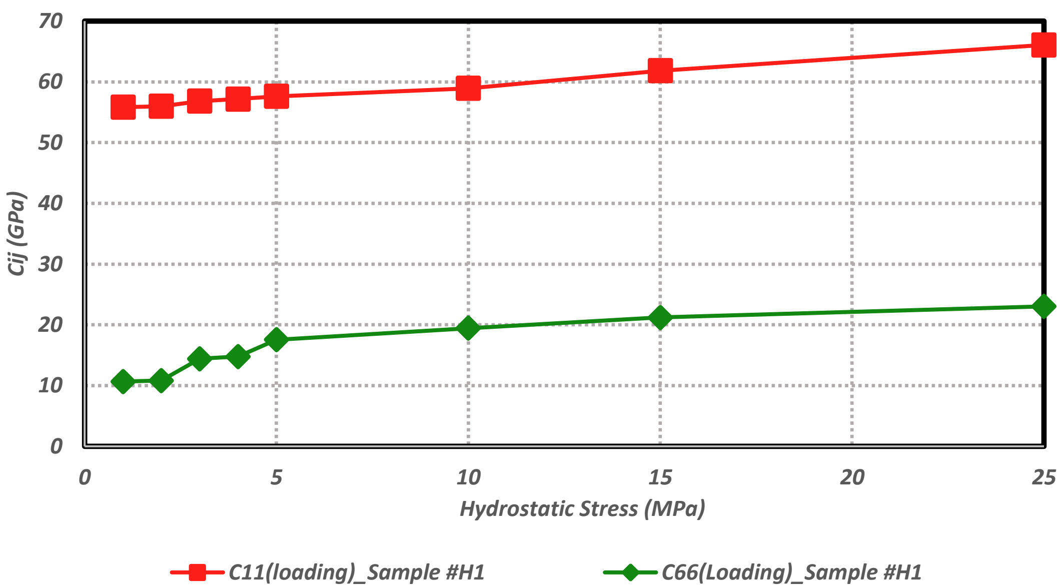

Figure 4-14: Graphical compilation of elastic constants estimated on sample #H1, during hydrostatic loading.

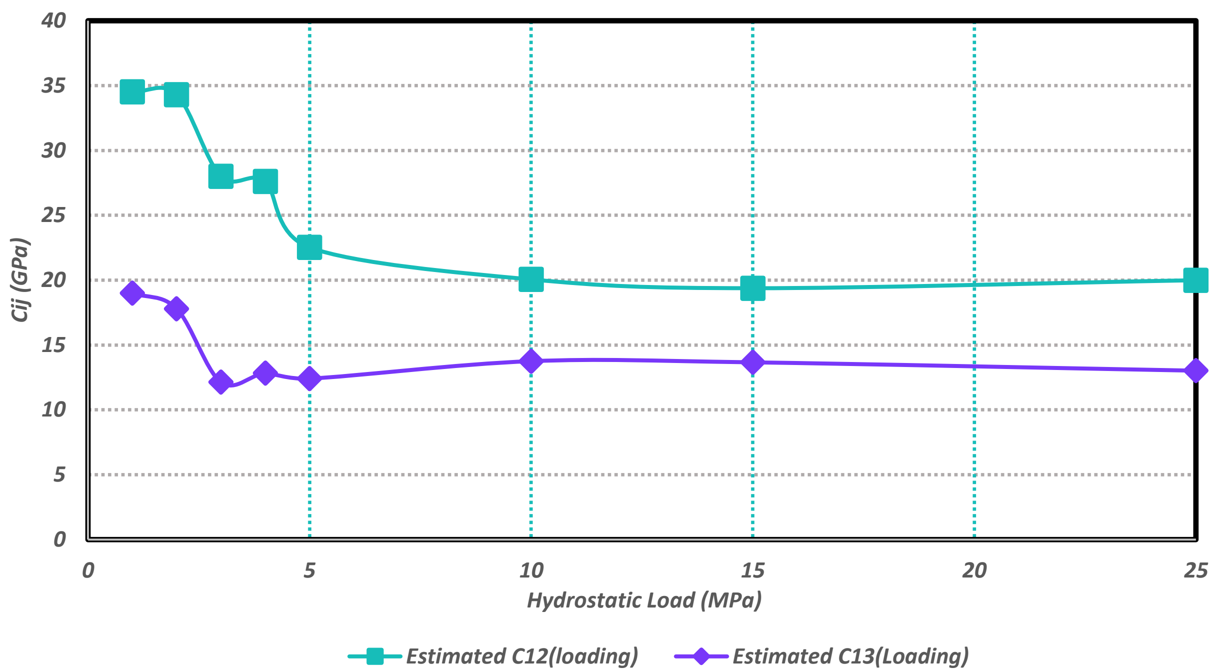

Figure 4-15: Graphical compilation of estimated off-diagonal elastic constants, during hydrostatic loading.

4.2.1.3 Relationship Between Dynamic Elastic Constants and Hydrostatic Stress

The same scenario as mentioned in section 4.1.1.4 was used to describe the dependence of the effective stiffness tensor as a function of a 3D stress field in intrinsically anisotropic formations, as an input for the dynamic analysis in COMSOL.

To predict the stress dependency of all five elastic medium parameters comprising the transversely isotropic stiffness tensor, the lab data at lower hydrostatic stress (P< 3 MPa) was ignored to eliminate the role of microcracks in the derived relationships. The same assumption as section 4.1.1.4 was utilized to define the relation between applied stresses and effective elastic stiffness constants, as follows:

$$C_{ij} = a_{1_{ij}}(\sigma_1 + \sigma_2 + \sigma_3) + a_{2_{ij}} \tag{4.1}$$

Where a_1 and a_2 are constants derived from experimental data. Figure 4-16 shows each elastic constant plotted against mean stress for Aquistore sample, as well as linear trendlines fit through the data points. These trendlines are based on the data for hydrostatic stresses greater than 3 MPa;

i.e., they ignore the data at low stresses, where stress-dependent is more acute and – in some cases- erratic. The average constants based on three hydrostatic experiments are presented in Table 4-4.

Table 4-4: Trendline parameters (see equation 4.1) for the Deadwood Formation during hydrostatic loading.

	$\mathbf{a}_{1_{Dyn}}$(-)	$\mathbf{a}_{2_{Dyn}}$(GPa)
$\mathbf{C}_{11_{Dyn}}$	422.73	55.37
$\mathbf{C}_{33_{Dyn}}$	651.58	37.06
$\mathbf{C}_{44_{Dyn}}(= \mathbf{C}_{55_{Dyn}})$	306.65	12.24
$\mathbf{C}_{66_{Dyn}}$	383.00	14.45
$\mathbf{C}_{12_{Dyn}}(= \mathbf{C}_{21_{Dyn}})$	0	22.93
$\mathbf{C}_{13_{Dyn}}(= \mathbf{C}_{23_{Dyn}})$	0	20.95

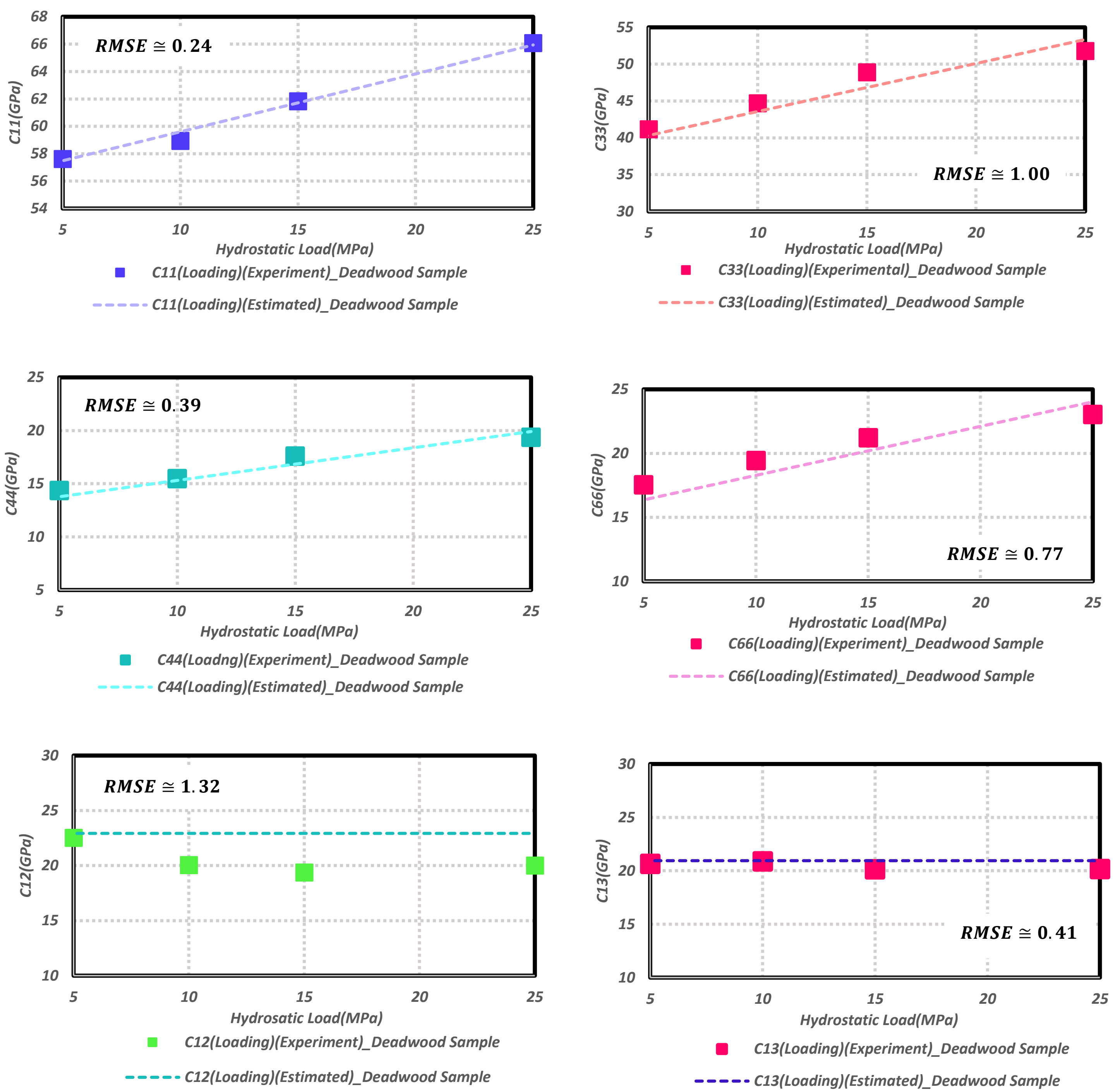

Figure 4-16: Dynamic elastic constants and linear trendlines plotted versus hydrostatic stress for Deadwood Formation samples. *RMSE* denotes root mean square error, in GPa.

4.2.2 Experimental Data for Static Analysis (Deadwood Samples)

Strain measurements were conducted to enable the interpretation of selected elastic properties. By applying load parallel to the bedding (on sample H1), Young's modulus parallel to the bedding (E_1) and Poisson's ratio relating contraction parallel to the bedding and parallel to the axis of symmetry expansion parallel to the bedding (ϑ_{13}) were interpreted. By applying load in the direction perpendicular to the bedding on vertical samples ($Tx1, Tx2$), Young's modulus in the direction perpendicular to the bedding (E_3) and Poisson's ratio relating contraction parallel to the axis of symmetry and expansion parallel to the bedding (ϑ_{31}) were interpreted. Bulk modulus was measured during hydrostatic loading. The static elastic properties interpreted from the three aforementioned loading configurations are presented in Figures 4-17, 4-18 and 4-19. As expected, with increasing hydrostatic stress the static elastic properties increase, and Young's modulus parallel to bedding is greater than Young's modulus perpendicular to bedding.

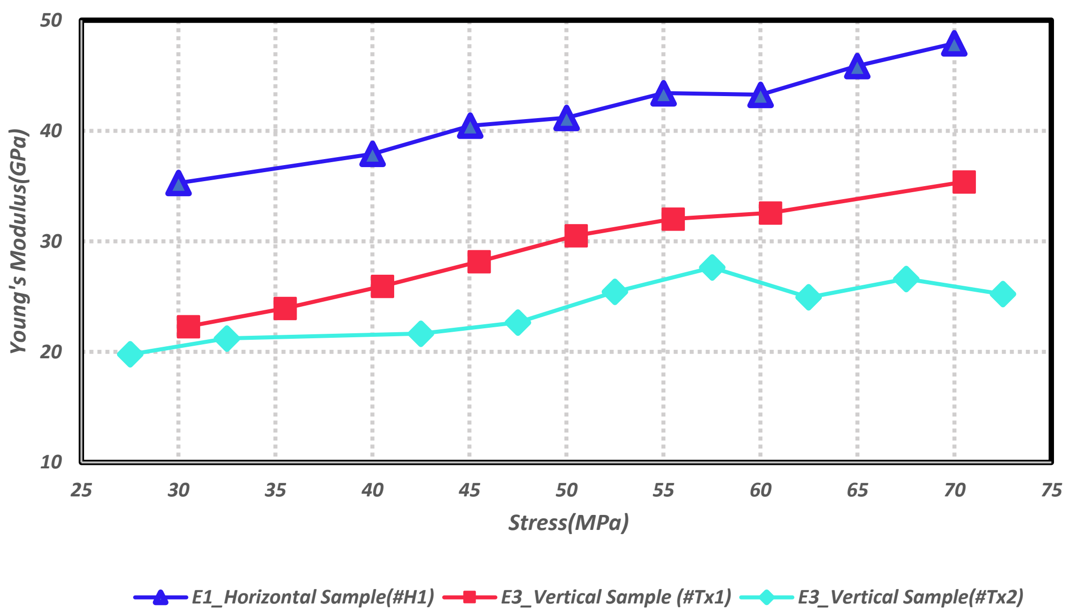

Figure 4-17: Graph of static Young's moduli calculated for one horizontal and two vertical samples from the Deadwood Formation .

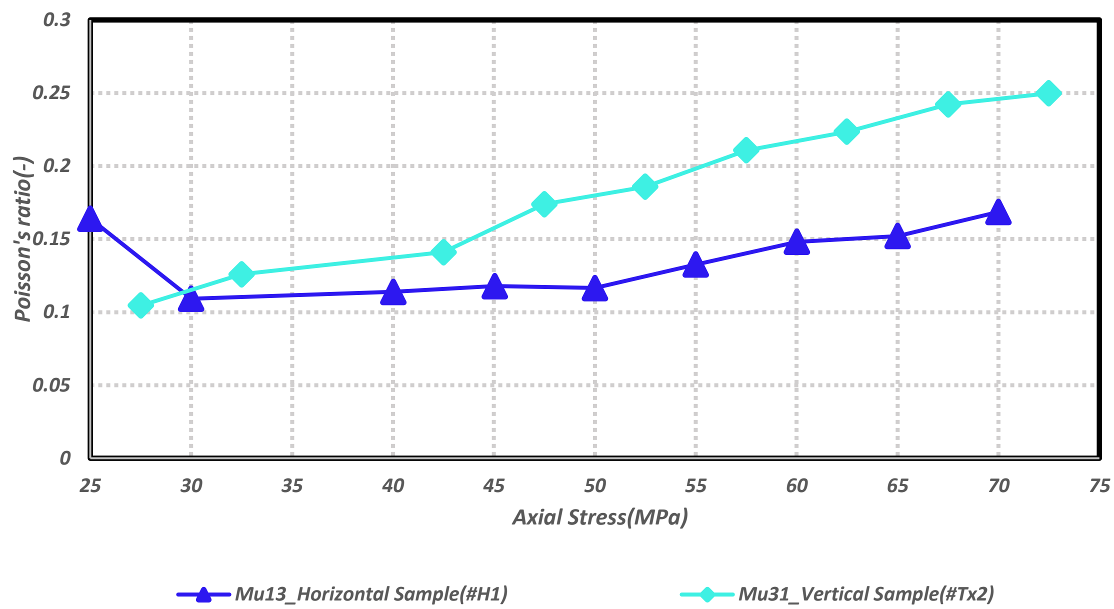

Figure 4-18: Graph of static Poisson's ratios calculated for one horizontal and two vertical samples of Deadwood Formation (Aquistore site).

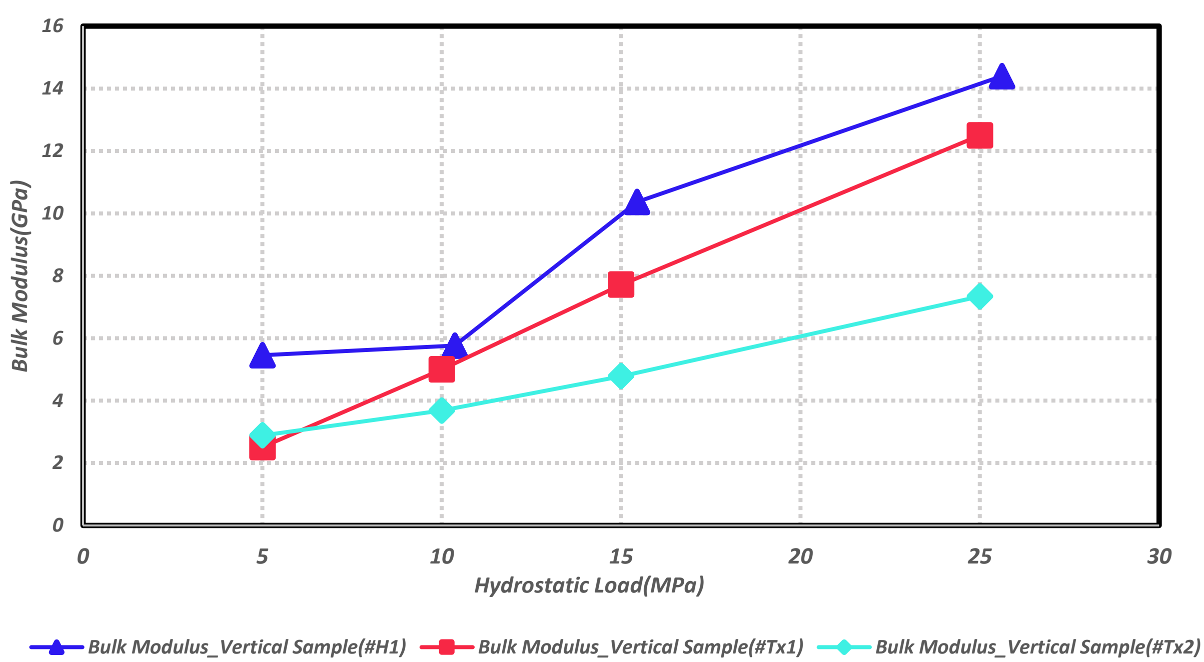

Figure 4-19: Graph of static bulk moduli calculated for one horizontal and two vertical samples from the Deadwood Formation.

To fully characterize the static elastic properties, the equations presented in section 3.1.3 (equations 3.22, 3.23, 3.30) were used to calculate the $\vartheta_{12,} G_{12}$ and G_{23}.

4.2.3 Static-Dynamic Property Constants

The same procedures as section 4.1.3 were used to define effective static elastic stiffness constants as a function of stress. A linear relationship between effective static and dynamic elastic properties was assumed, as follows:

$$C_{ij_{Static}} = a_{ij}\left(C_{ij_{Dynamic}}\right) + b_{ij} \tag{4.3}$$

By correlating static elastic stiffness constants with dynamic elastic stiffness constants, as shown in Figure 4-20, the average values for a_{ij} and b_{ij} were determined (see Table 4-5). Based on these correlations, constants were obtained to define static elastic stiffness constants as functions of stress (see Table 4-6).

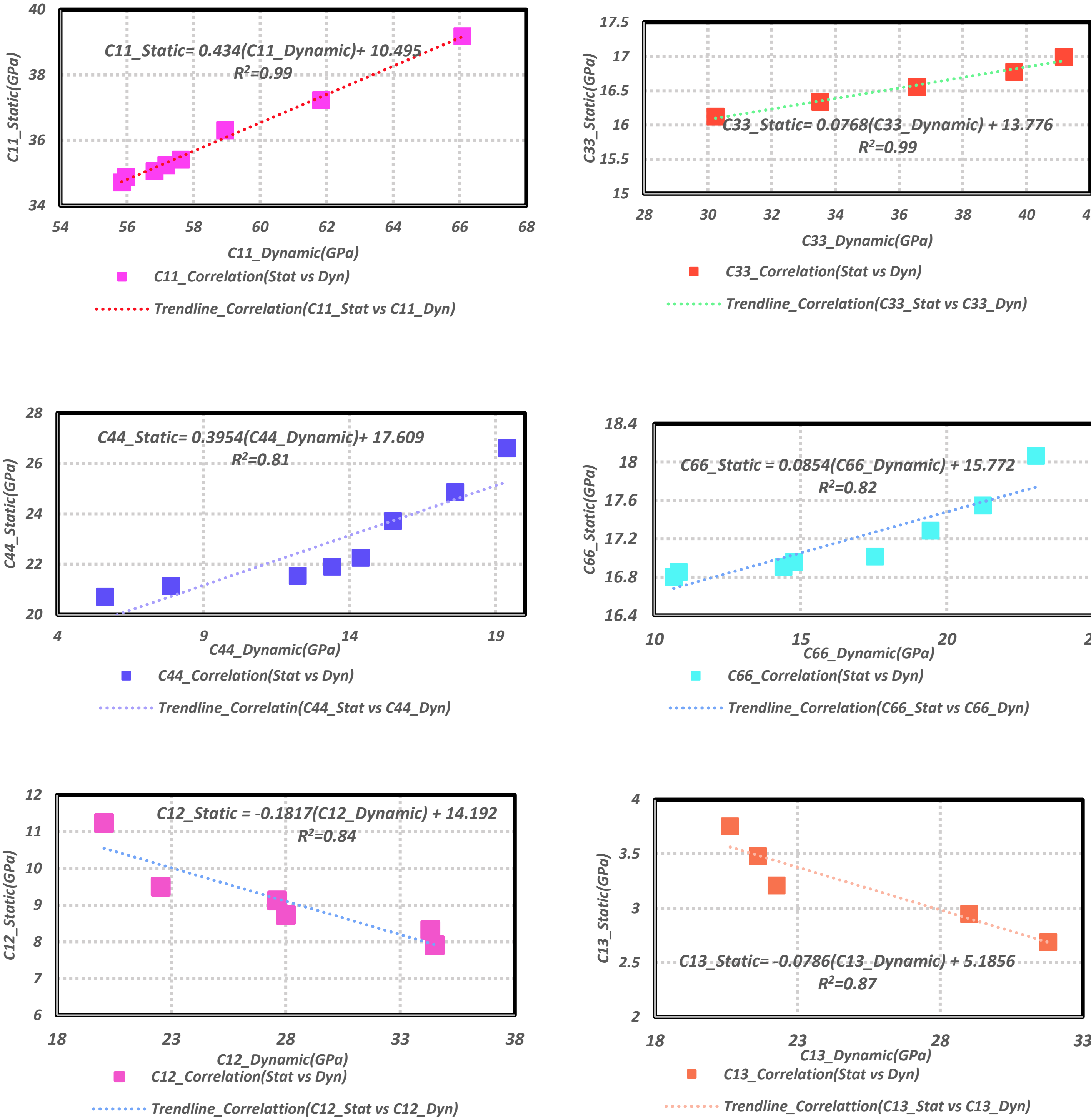

Figure 4-20: Correlation between static and dynamic elastic stiffness constants for Deadwood Formation samples. For simplicity, linear correlations were assumed for all parameters; investigation of non-linear correlations, as suggested by the data for C_{44} and C_{66}, is a recommended topic of future research.

Table 4-5: Averaged values of linear trendline coefficients, relating effective static and dynamic elastic stiffness constants (Deadwood Formation).
$(C_{ij} = a_{1_{ij}}(\sigma_1 + \sigma_2 + \sigma_3) + a_{2_{ij}})$

$a_{ij}(-)$		$b_{ij}(GPa)$	
a_{11}	0.44	b_{11}	10.50
a_{33}	0.08	b_{33}	13.80
a_{44}	0.40	b_{44}	17.61
a_{66}	0.09	b_{66}	15.77
a_{12}	-0.19	b_{12}	14.20
a_{13}	-0.08	b_{13}	5.20

Table 4-6: Derived trendline parameter for stress-dependent static elastic stiffness constants of the Deadwood Formation.

	$\mathbf{a_{1_{Stat}}}$**(-)**	$\mathbf{a_{2_{Stat}}}$**(GPa)**
$\boldsymbol{C_{11_{Stat}}}$	148.11	34.53
$\boldsymbol{C_{33_{Stat}}}$	50.04	16.62
$\boldsymbol{C_{44_{Stat}}(= C_{55_{Stat}})}$	121.25	22.45
$\boldsymbol{C_{66_{Stat}}}$	32.71	17.01
$\boldsymbol{C_{12_{Stat}}(= C_{21_{Stat}})}$	0	10.02
$\boldsymbol{C_{13_{Stat}}(= C_{23_{Stat}})}$	0	6.54

4.3 Numerical Modelling

As previously mentioned, when a borehole is drilled in a rock subjected to an applied stress, the local stress field around the borehole is changed. Formation elastic properties near a borehole may be altered from their original state due to the stress concentration around the borehole, which is known as the stress-induced anisotropy.

Quantification of this stress induced anisotropy and its effect on sonic logging tools requires laboratory data that characterize stress-dependent elastic properties (static and dynamic), and numerical modelling tools to characterize static stress state in the rock formation around a borehole and dynamic wave propagation through this formation. Theses modelling tools are explained in sections 4.3.1 and 4.3.2.

4.3.1 Static Stress Analysis

4.3.1.1 Assessment of Numerical Simulation by Comparison with Analytical Solution

Figure 4-21 summarizes the results of the borehole stresses around the borehole wall for the three chosen scenarios described in section 3.2.3.1. The agreement between the two solutions is observed to be excellent ($RMSE$ < 1 MPa in all cases), which suggests that the numerical model is reliable.

4.3.1.2 Static Stress Analysis (Montney Formation)

Figures 4-22 to 4-29 show the modeled local stress fields around the vertical and horizontal borehole scenarios considered for the Montney Formation at Farrell Creek. The following is presented in each Figure:

- Figure 4-22 shows the variation of radial stresses around the vertical borehole. The maximum radial stress is in direction of maximum horizontal stress.
- Figure 4-23 shows the variation of tangential stresses around the vertical borehole. The maximum tangential stress is in direction of minimum horizontal stress.
- Figures 4-24 to 4-25 present the axial (z-direction) and mean stresses around the vertical borehole, respectively.
- Figure 4-26 shows the variation of radial stresses around the horizontal borehole. The maximum radial stress is in direction of vertical stress.
- Figure 4-27 shows the variation of tangential stress around the horizontal borehole drilled. The maximum tangential stress is in direction of minimum horizontal stress.

- Figures 4-28 to 4-29 present the axial and mean stresses around the horizontal borehole, respectively.

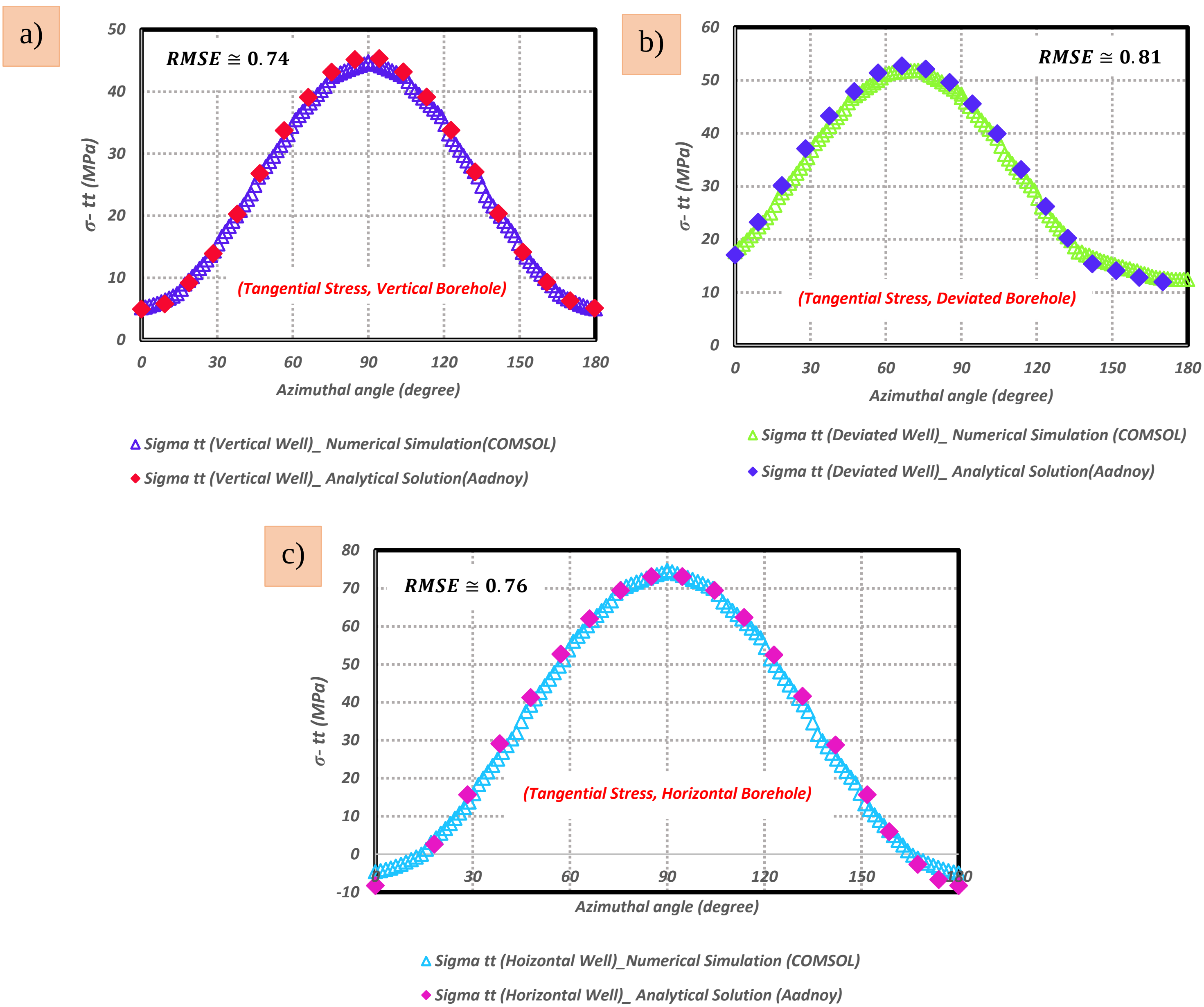

Figure 4-21: Comparison of numerical solution against analytical solution for static borehole stresses for three different scenarios. a) Vertical borehole (drilled parallel to the axis symmetry); b) deviated borehole (drilled 45° apart from axis of symmetry); c) horizontal borehole (drilled 90° from the axis of symmetry). *RMSE* denotes root mean square error, in MPa.

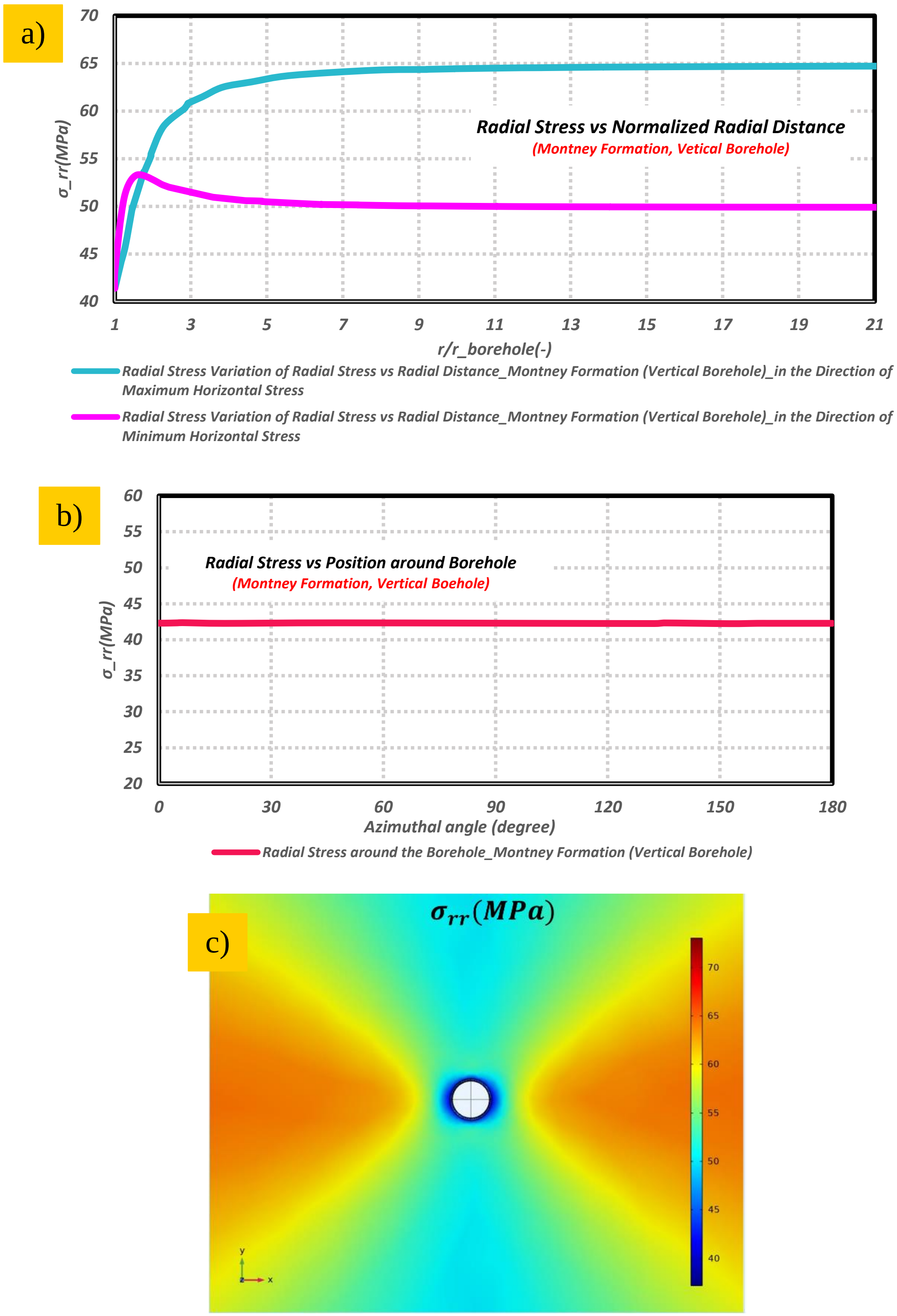

Figure 4-22: Radial stress distributions modeled using COMSOL for a vertical borehole in the Montney Formation: a) Radial stress versus normalized radial distance; b) radial stress around the perimeter of the borehole (angle=0° corresponds to the direction parallel to the maximum horizontal stress(oriented parallel to the x-axis); c) contour plot of radial stress in the plane normal to the borehole axis.

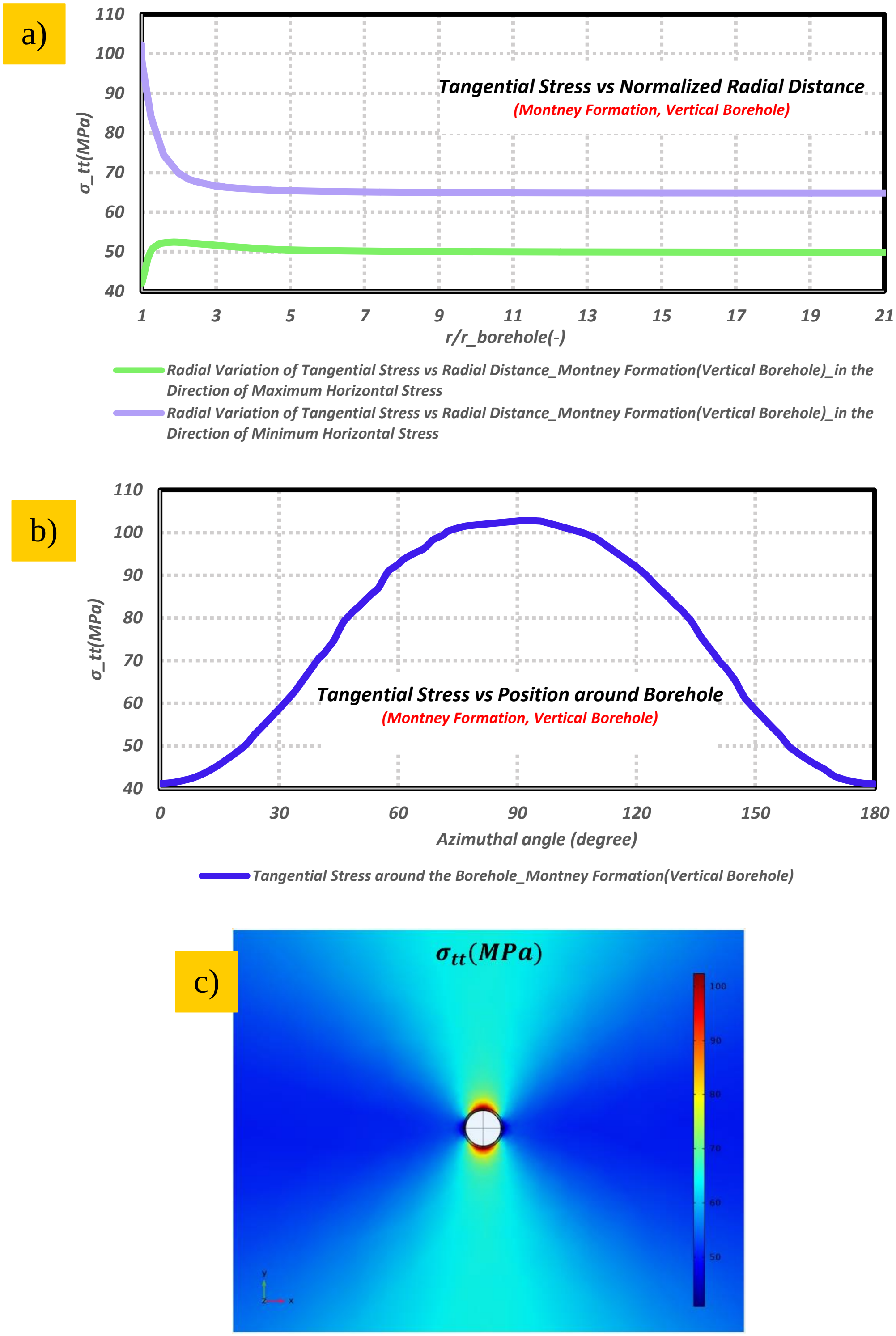

Figure 4-23: Tangential stress distributions modeled using COMSOL for a vertical borehole in the Montney Formation: a) Tangential stress versus normalized radial distance; b) tangential stress around the perimeter of the borehole (azimuthal angle=0° corresponds to the direction parallel to the maximum horizontal stress(oriented parallel to the x-axis); c) contour plot of tangential stress in the plane normal to the borehole axis.

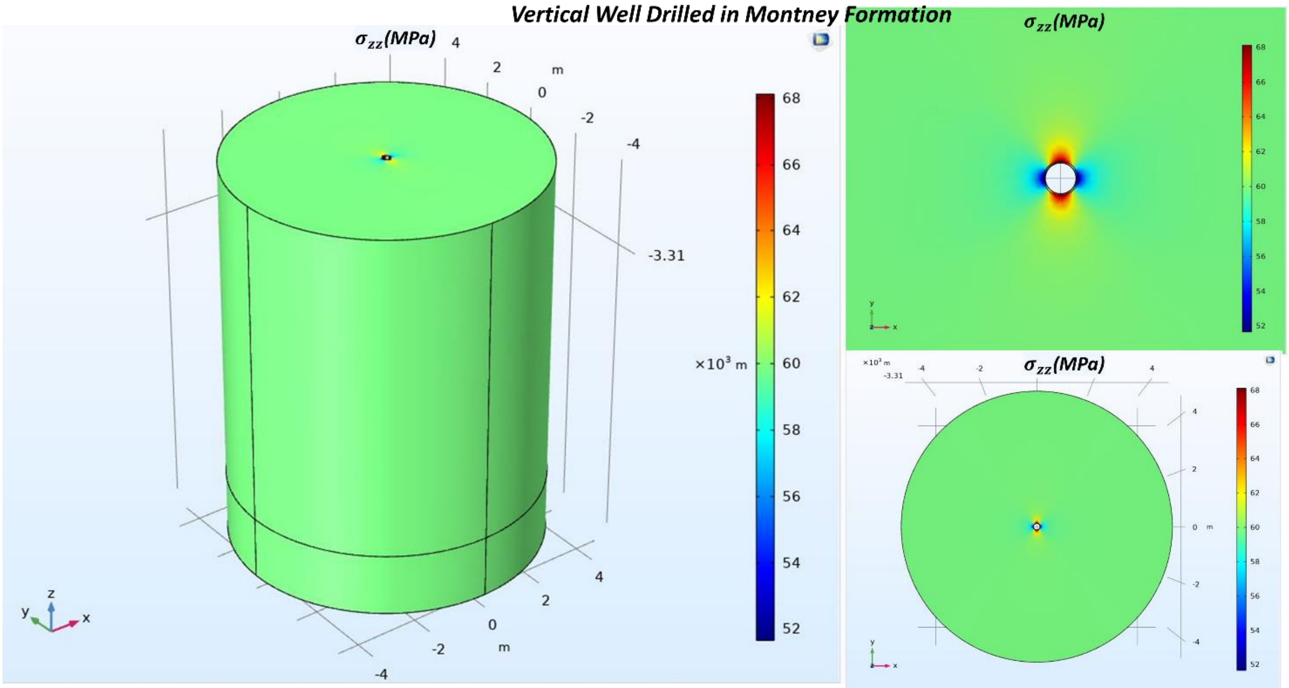

Figure 4-24: Modeled distribution of stress in the z-direction around a vertical borehole in the Montney Formation.

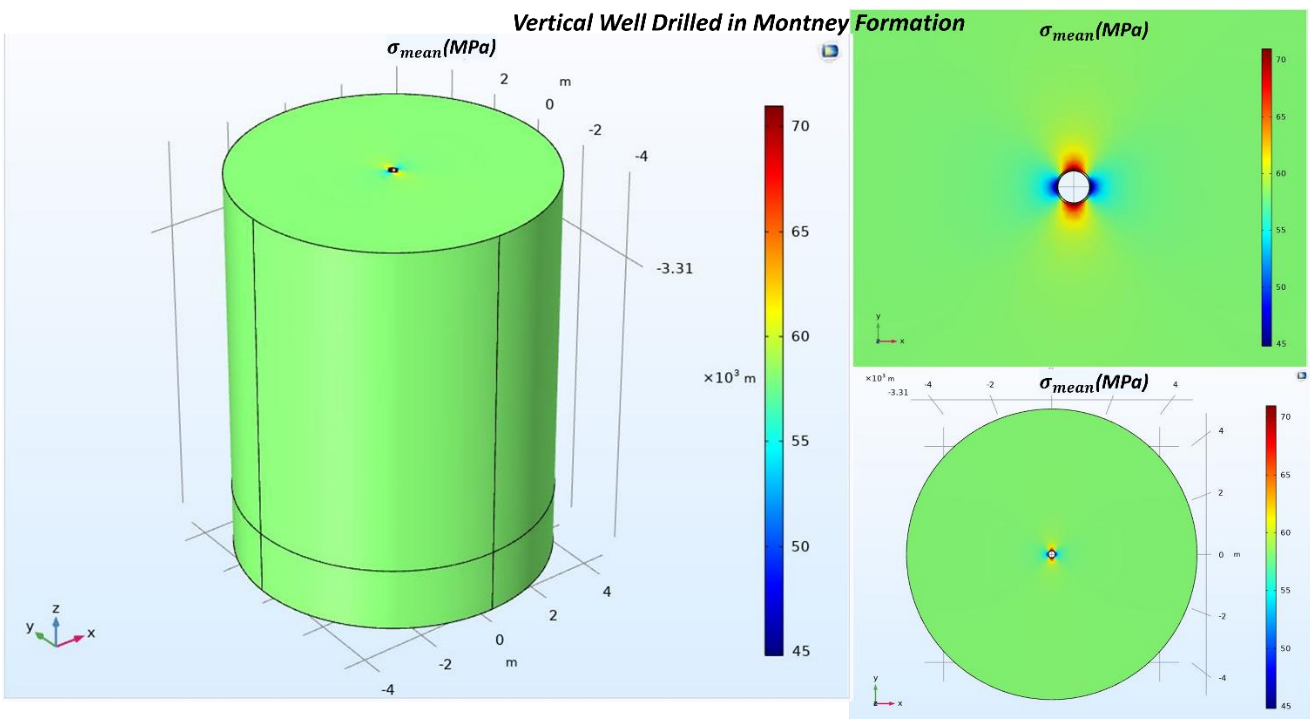

Figure 4-25: Modeled distribution of mean stress around a vertical borehole in the Montney Formation.

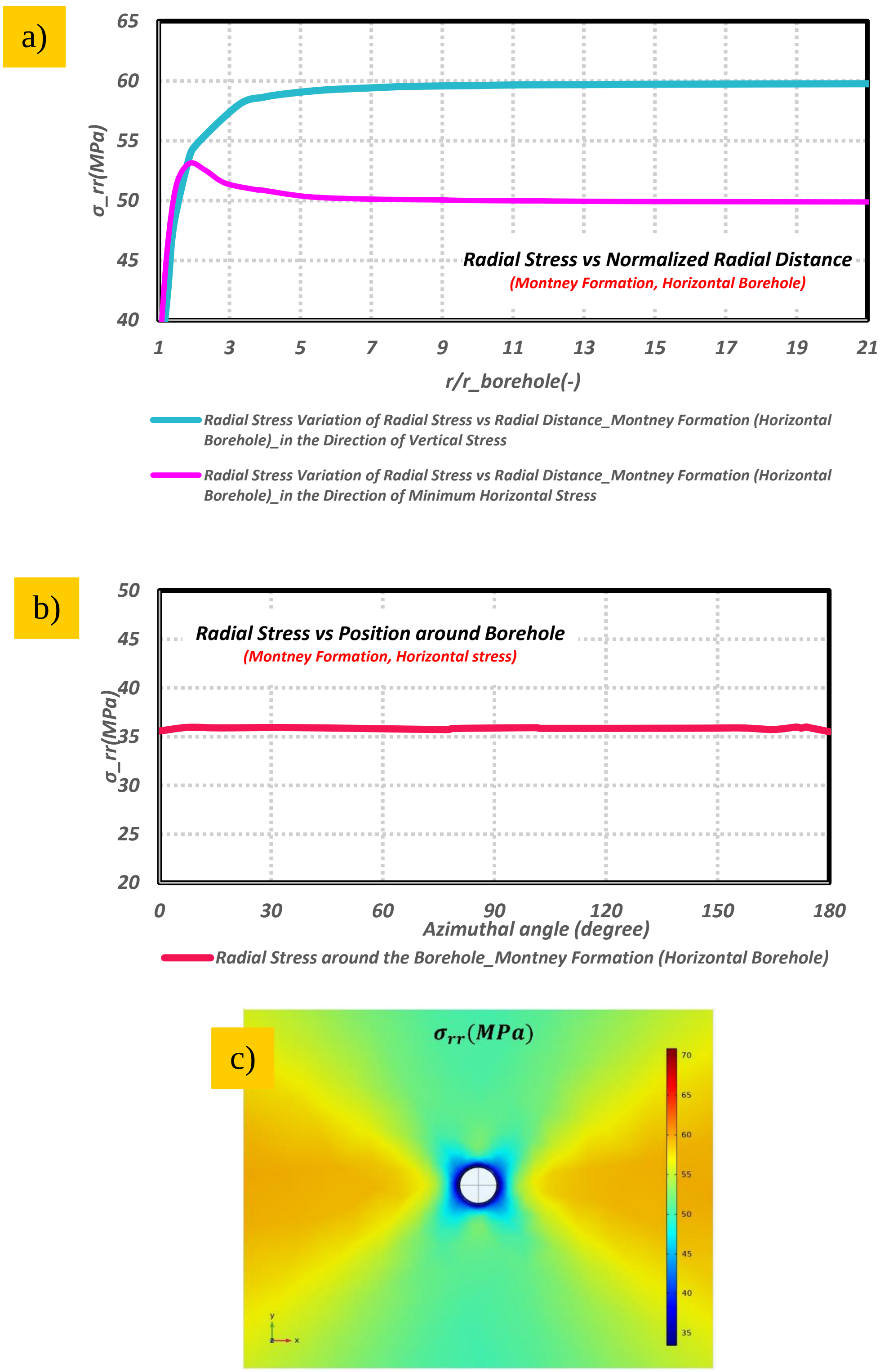

Figure 4-26: Radial stress distributions modeled using COMSOL for a horizontal borehole in the Montney Formation: a) Radial stress versus normalized radial distance; b) radial stress around the perimeter of the borehole (azimuthal angle=0° corresponds to the direction parallel to the vertical stress(oriented parallel to the x-axis); c) contour plot of radial stress in the plane normal to the borehole axis.

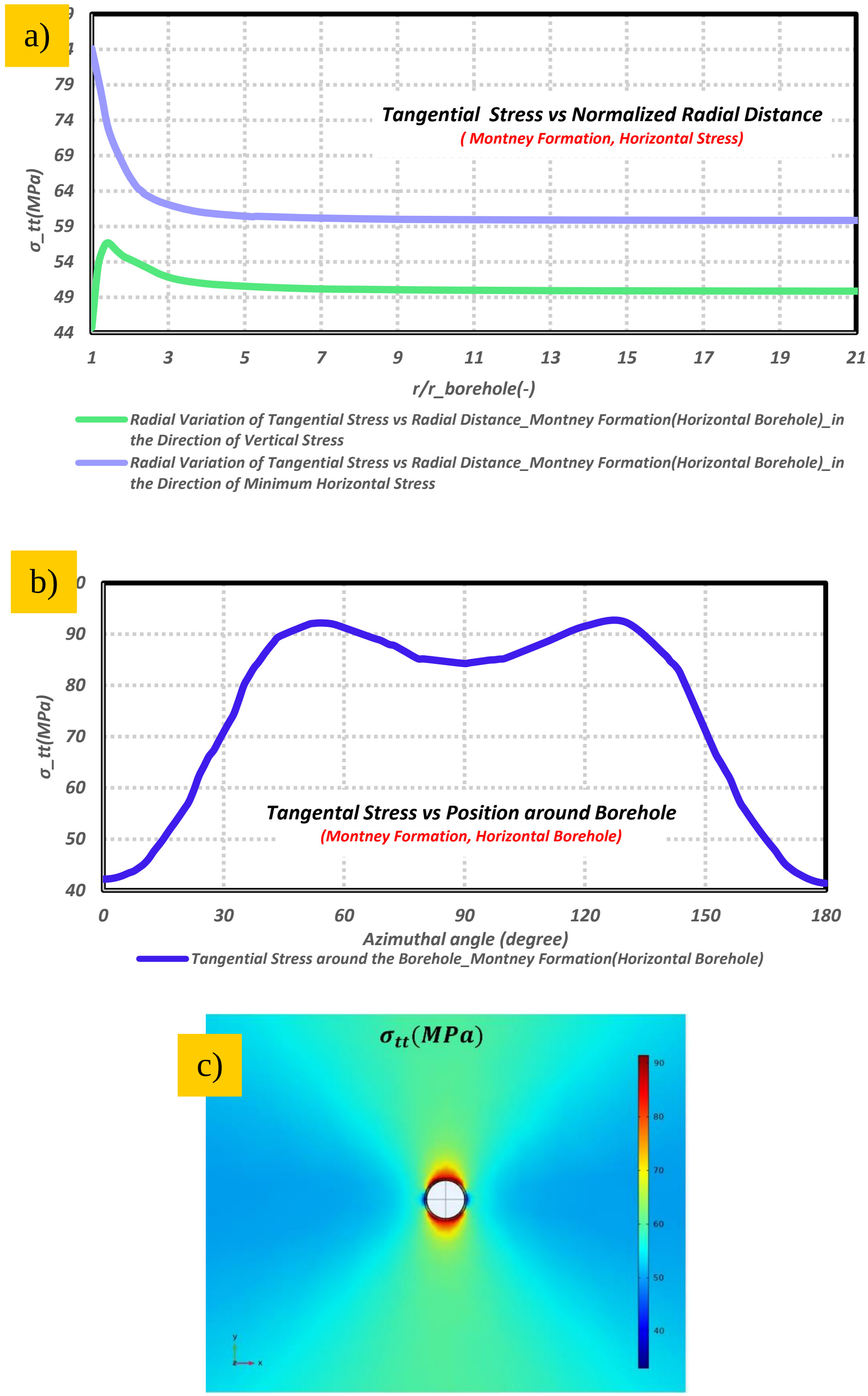

Figure 4-27: Tangential stress distributions modeled using COMSOL for a horizontal borehole in the Montney Formation: a) Tangential stress versus normalized radial distance; b) tangential stress around the perimeter of the borehole (azimuthal angle=0° corresponds to the direction parallel to the vertical stress(oriented parallel to the x-axis); c) contour plot of tangential stress in the plane normal to the borehole axis.

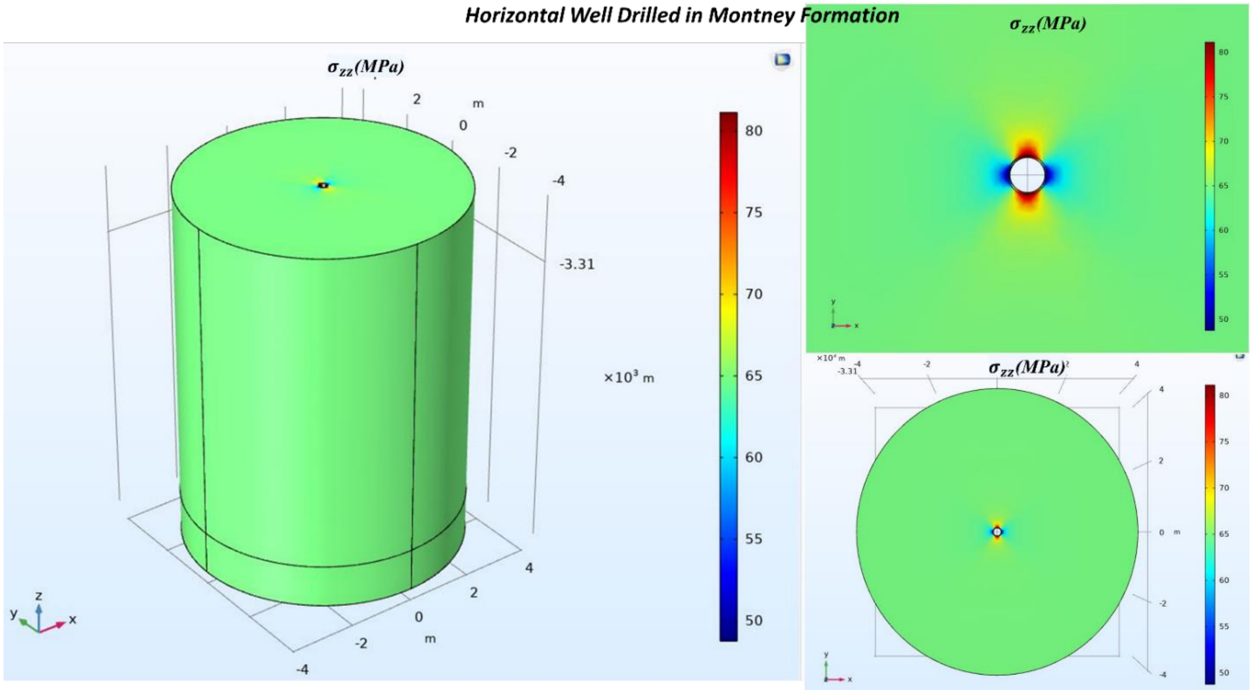

Figure 4-28: Modeled distribution of stress in the z-direction around a horizontal borehole in the Montney Formation.

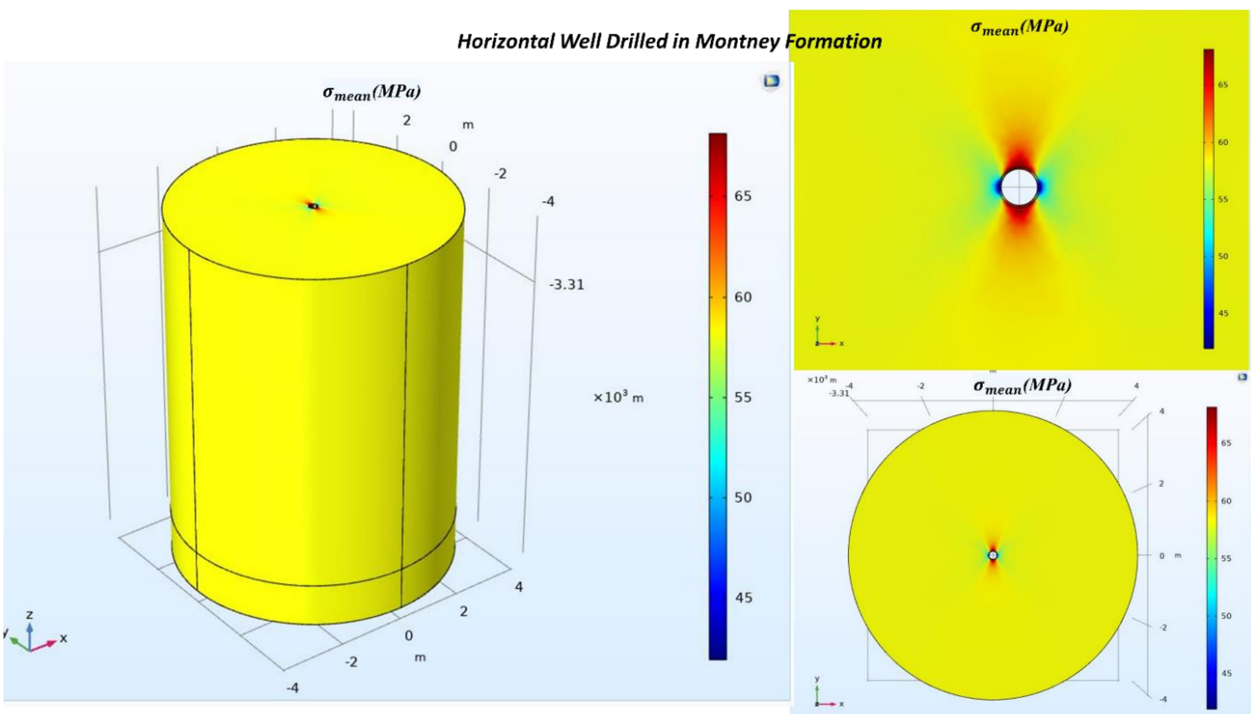

Figure 4-29: Modeled distribution of mean stress in the around a horizontal borehole in the Montney Formation.

4.3.1.3 Static Stress Analysis (Deadwood Formation)

Figures 4-30, 4-31, 4-32 and 4-33 show the modeled local stress fields around the vertical borehole in the Deadwood Formation at the Aquistore site. The following is presented in each Figure:

- Figure 4-30 shows the variation of radial stresses around the vertical borehole. The maximum radial stress is in direction of maximum horizontal stress.
- Figure 4-31 shows the variation of tangential stresses around the vertical borehole. The maximum tangential stress is in direction of minimum horizontal stress.
- Figures 4-32 to 4-33 present the axial and mean stresses around the vertical borehole drilled in Deadwood Formation, respectively.

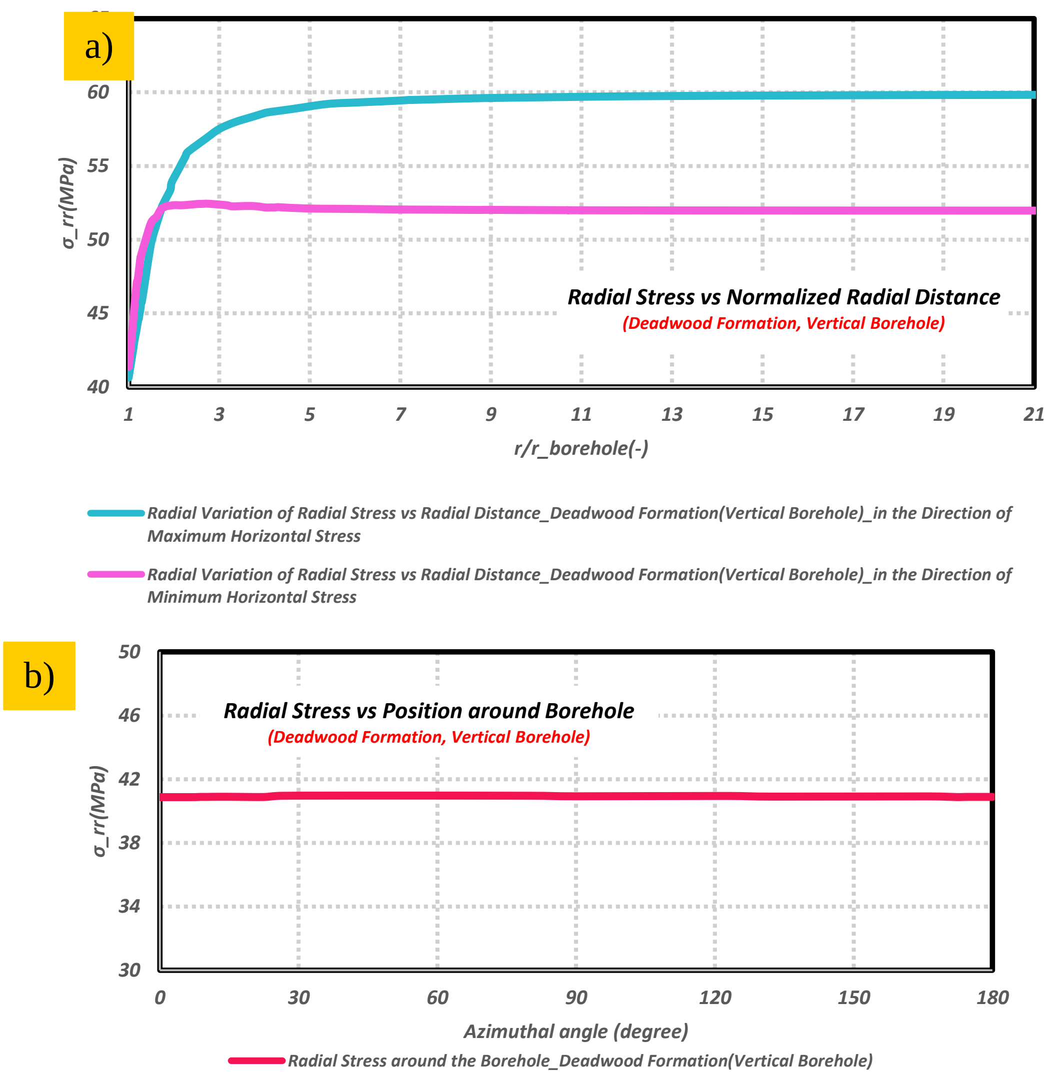

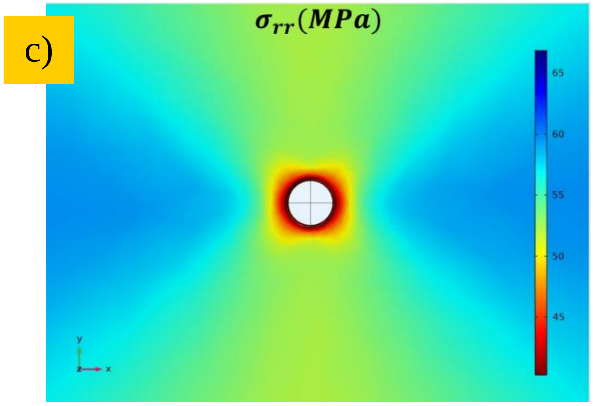

Figure 4-30: Radial stress distributions modeled using COMSOL for a vertical borehole in the Deadwood Formation: a) Radial stress versus normalized radial distance; b) radial stress around the perimeter of the borehole (Azimuthal angle=0° corresponds to the direction parallel to the maximum horizontal stress); c) contour plot of radial stress in the plane normal to the borehole axis.

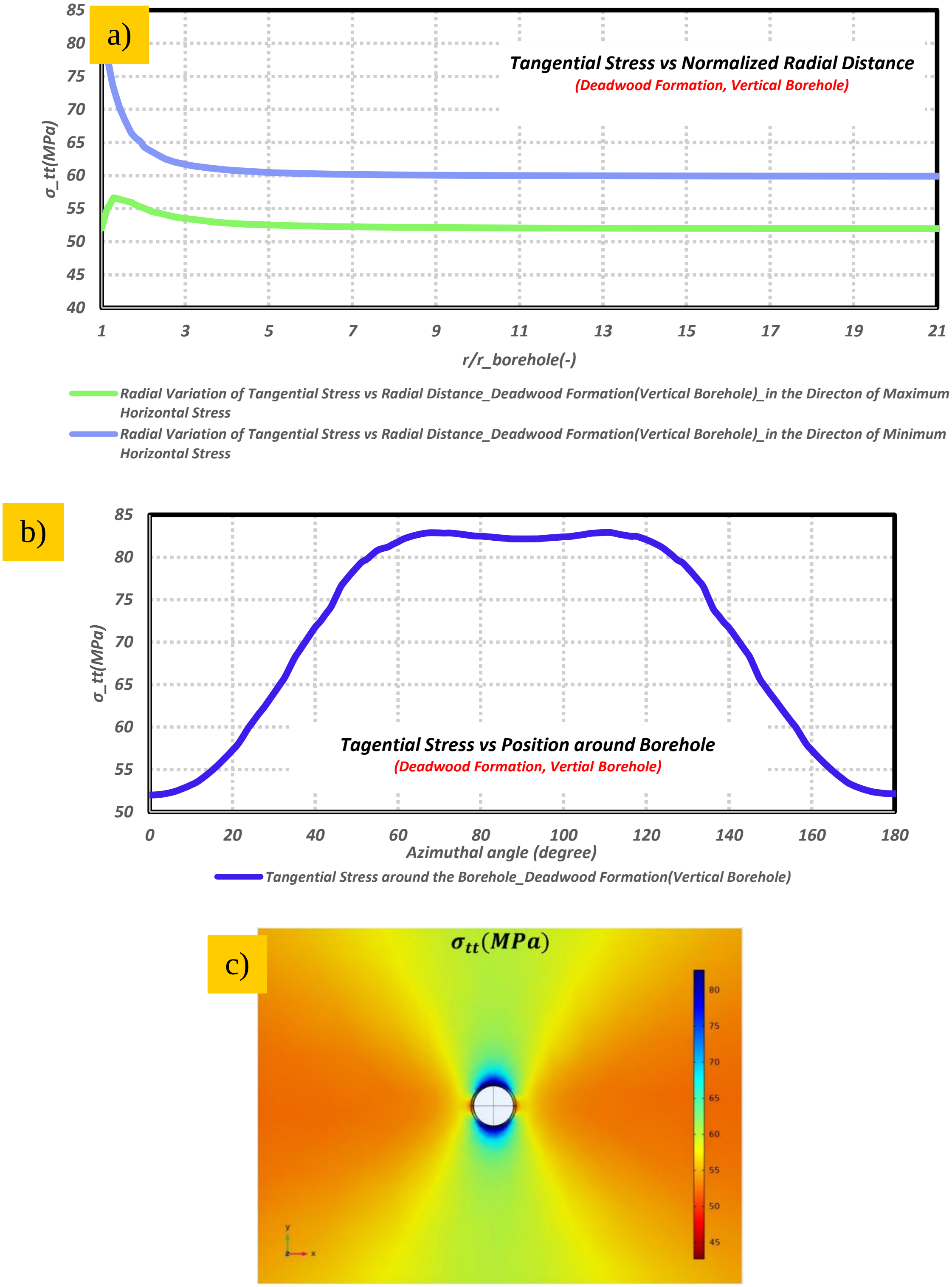

Figure 4-31: Tangential stress distributions modeled using COMSOL for a vertical borehole in the Deadwood Formation: a) Tangential stress versus normalized radial distance; b) tangential stress around the perimeter of the borehole (Azimuthal angle=0° corresponds to the direction parallel to the maximum horizontal stress); c) contour plot of tangential stress in the plane normal to the borehole axis.

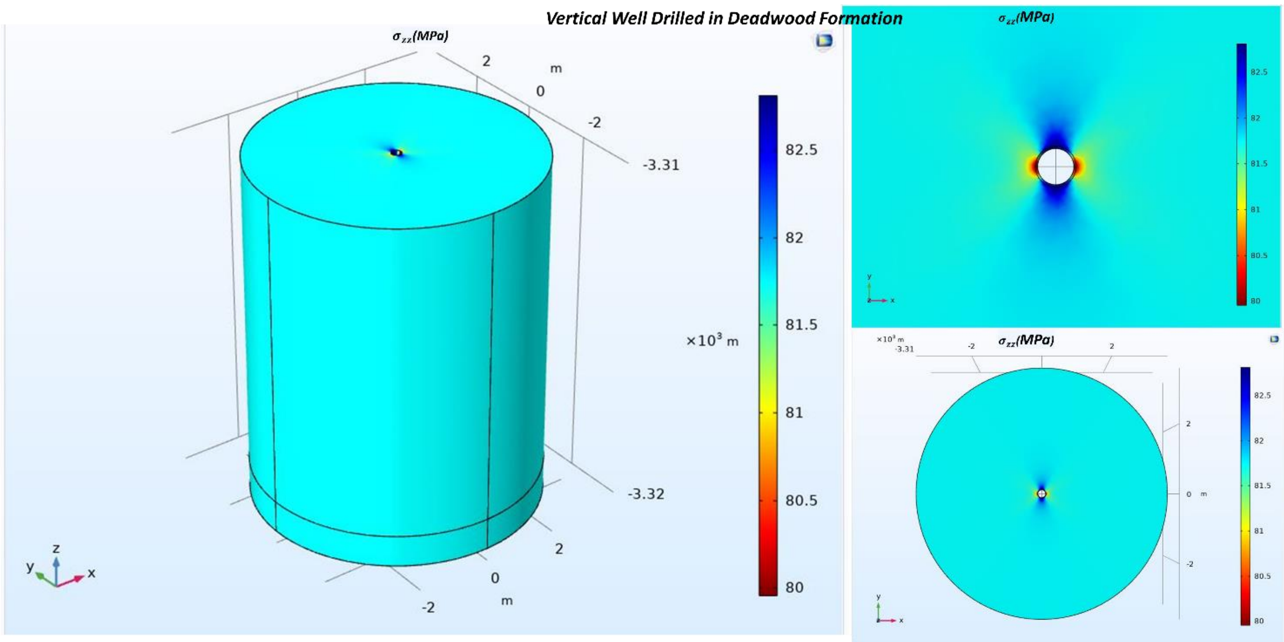

Figure 4-32: Modeled distribution of stress in the z-direction around a vertical borehole in the Deadwood Formation.

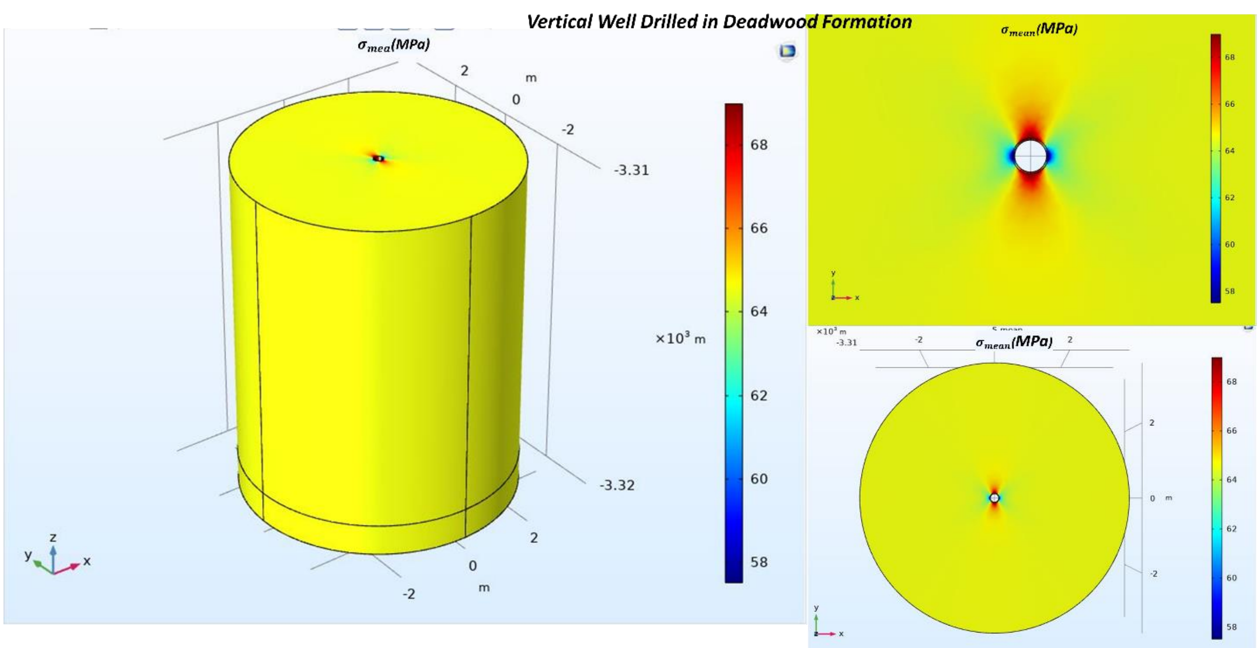

Figure 4-33: Modeled distribution of mean stress in the around a vertical borehole in the Deadwood Formation.

4.3.2 Dynamic Analysis

4.3.2.1 Assessment of Numerical Dynamic Simulation by Comparison with Analytical Solution

Model assessment results for the Ricker wavelet are presented in Figure 4-34. In order to compare the simulation results (frequency domain) with the analytical model (time domain), the simulation results were passed through an inverse Fast Fourier Transform (FFT) algorithm. It is observed that the agreement between the two solutions is excellent.

The Ormsby wavelet, in time the domain, is shown in Figure 4-35. As shown in Figure 4-36, in which a published tool frequency sweep is compared to the modeled source wavelet in the frequency domain, a favourable comparison is achieved.

Figures 4-37 and 4-38 compare the results of wave propagation modelling generated by a monopole point source inside the fluid domain, based on the analytical solution presented in section 3.5 and the numerical simulation completed using COMSOL. The agreement between the two solutions is observed to be excellent.

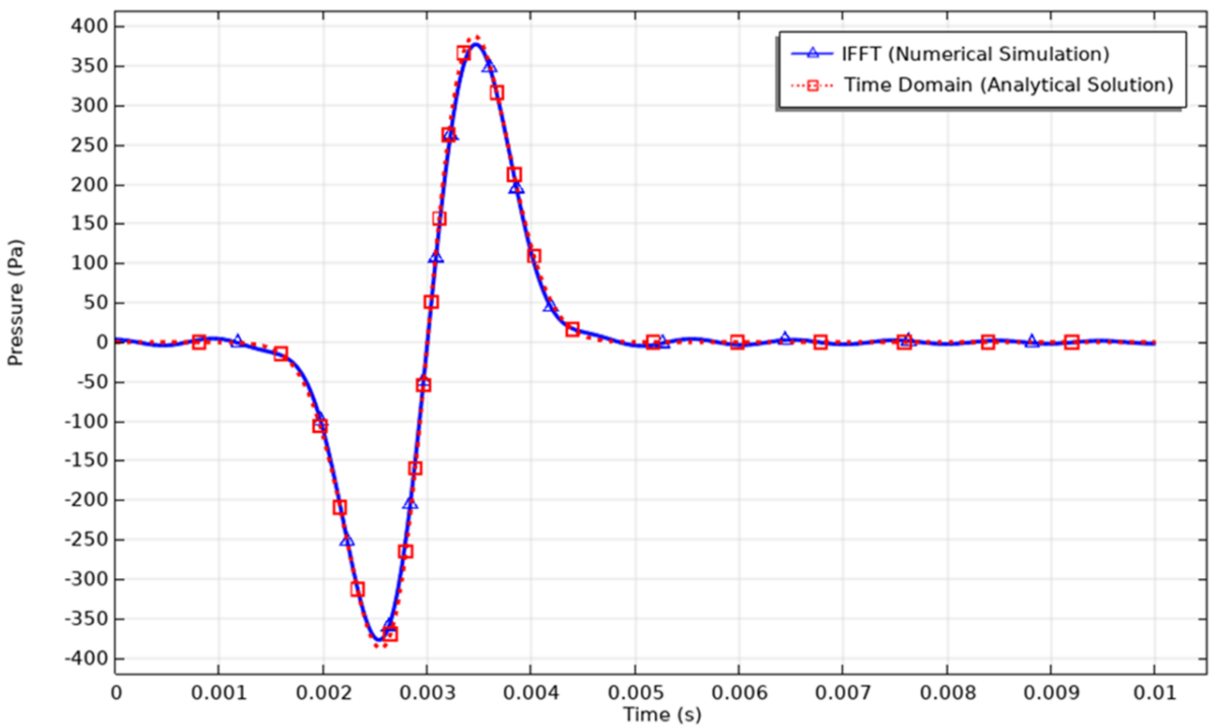

Figure 4-34: Comparison of numerical dynamic solution of the waveform recorded at the transmitter against the waveform predicted by the analytical solution (Ricker Wavelet generated by a monopole point source).

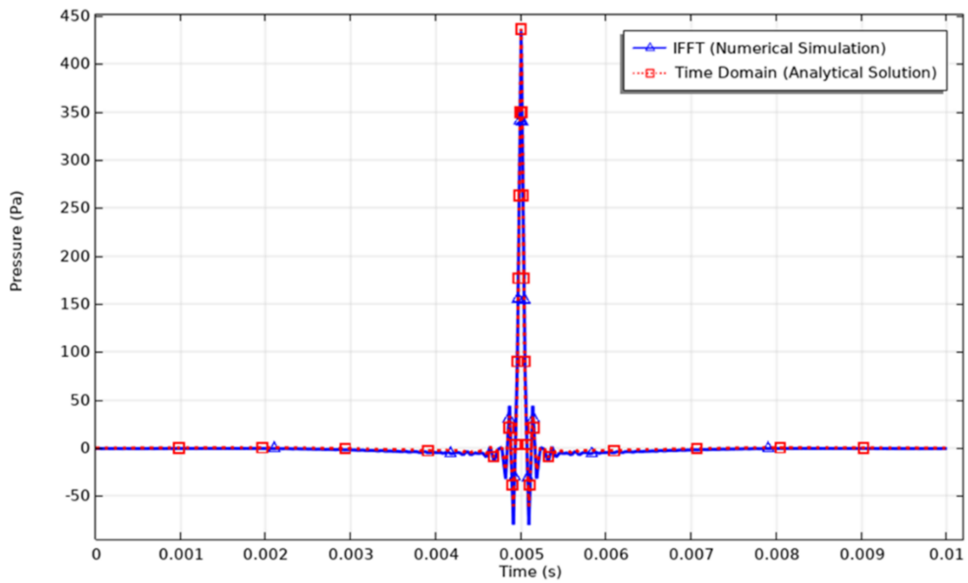

Figure 4-35: Comparison of numerical dynamic solution of the waveform recorded at the transmitter against the waveform predicted by the analytical solution (Ormsby Wavelet generated by a monopole point source).

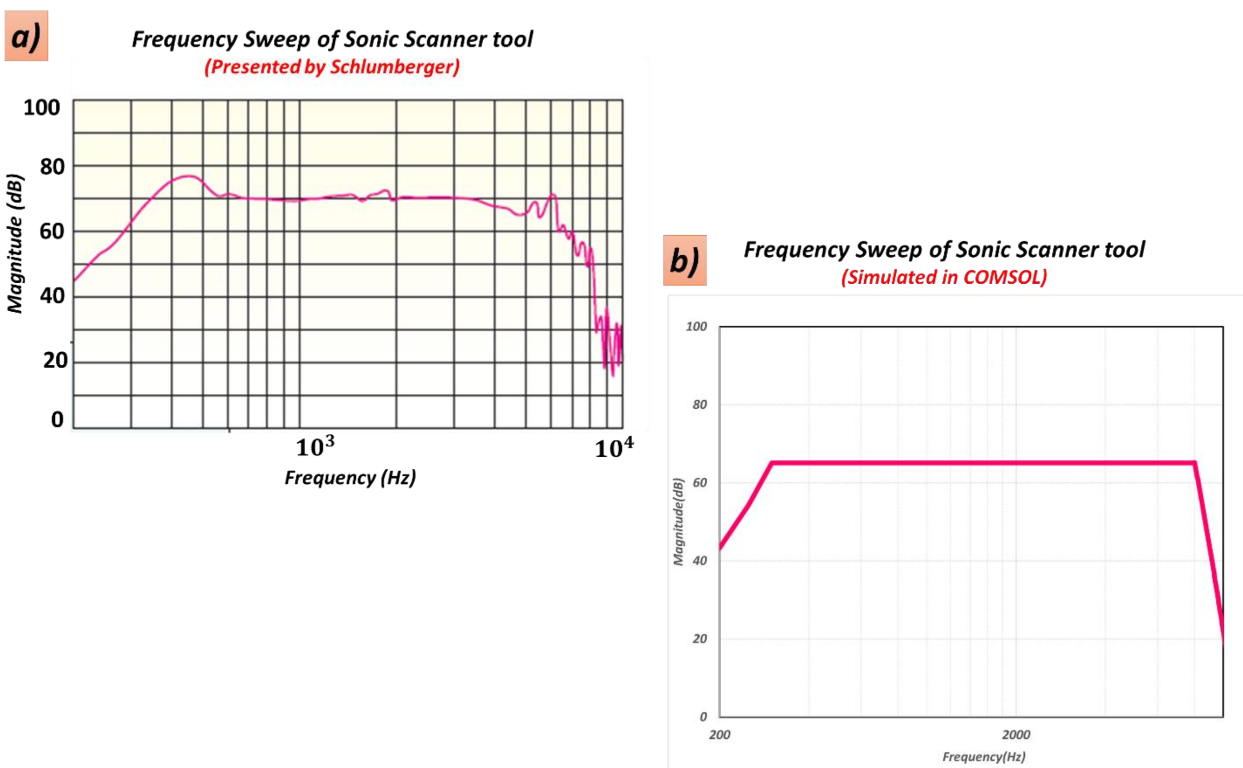

Figure 4-36: Comparison of the frequency sweep used in COMSOL simulations (b) against the frequency sweep presented by Schlumberger (Franco et al., 2006) (a).

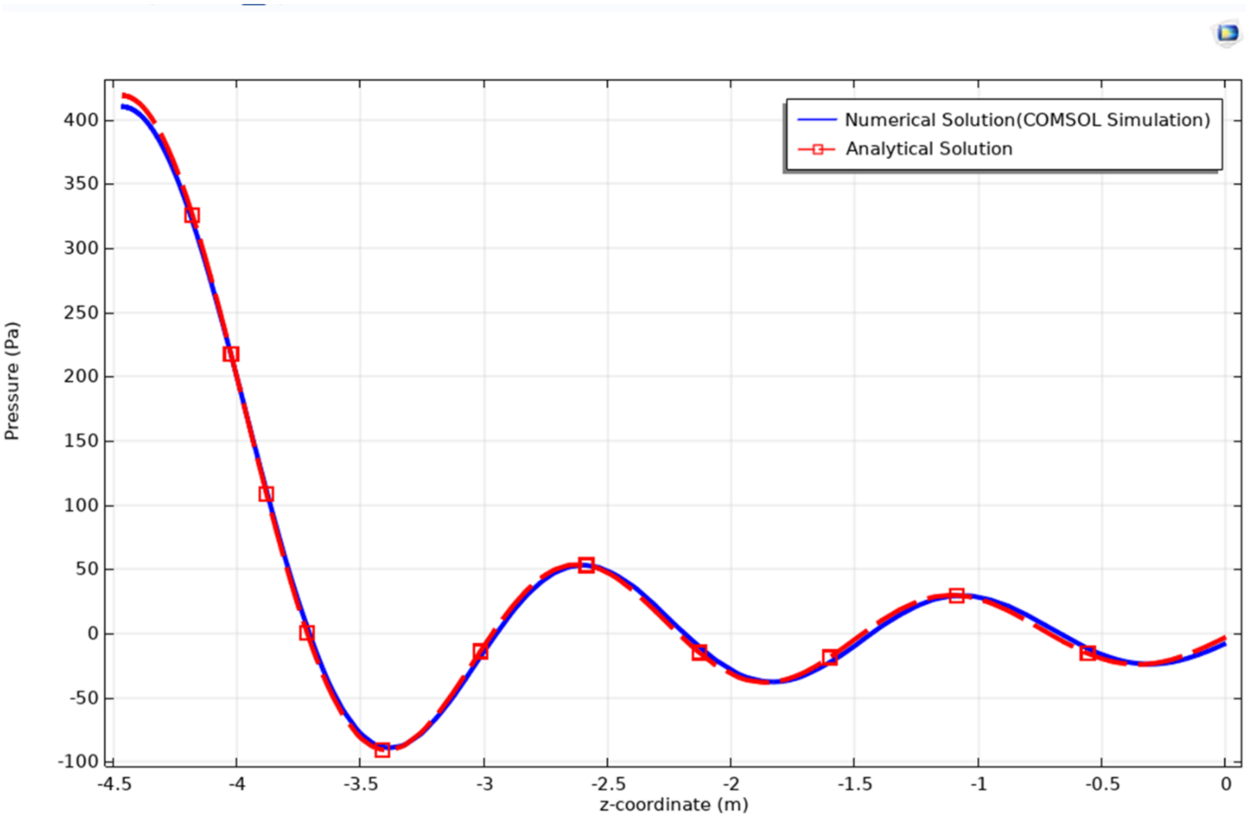

Figure 4-37: Comparison of numerical dynamic solution of pressure recorded inside the borehole against pressure predicted by the analytical solution at a frequency of 1000 Hz (generated by monopole point source).

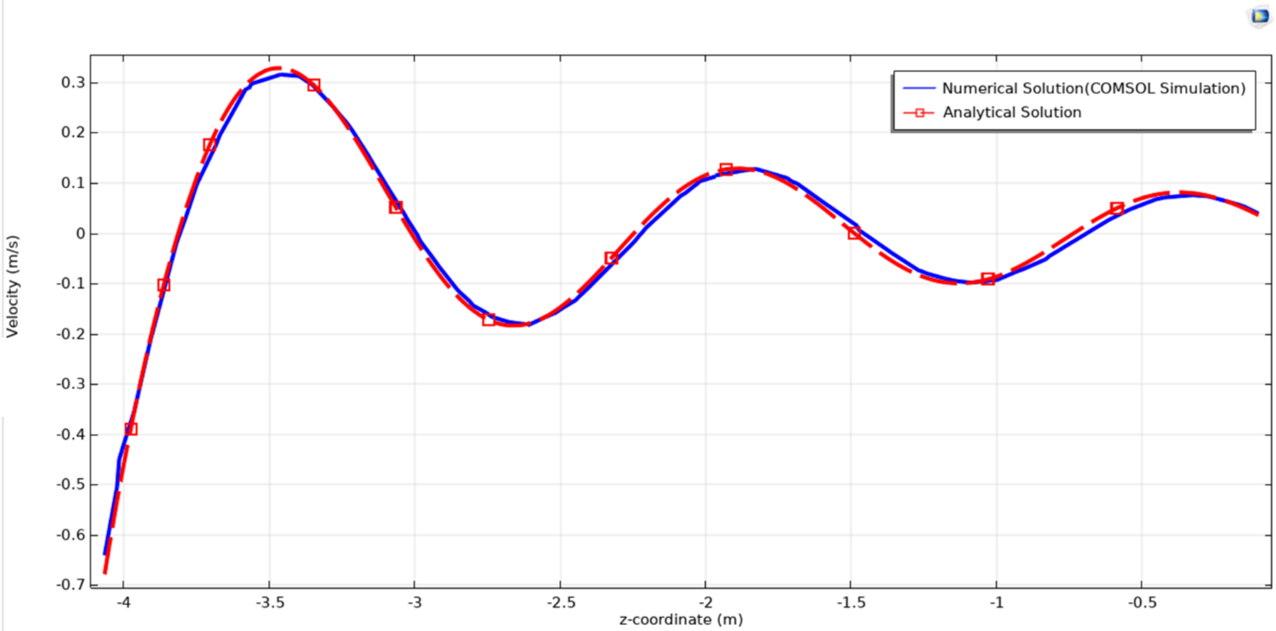

Figure 4-38: Validation of numerical dynamic solution of particle velocity recorded inside the borehole against acoustic velocity predicted by the analytical solution at frequency of 1000 Hz (generated by monopole point source).

4.3.2.2 Dynamic Analysis (Montney Formation)

Figures 4-39, 4-40, 4-41 and 4-42 show the numerical modeling results obtained for the vertical and horizontal borehole scenarios considered for the Montney Formation at Farrell Creek. The following is presented in each figure:

- Figure 4-39 shows the modeled X-X waveforms (i.e., waveforms recorded by dipole receivers oriented parallel to the x-axis after the dipole transmitter oriented parallel to the X-axis had been fired) for the vertical borehole scenario. (Note: The X-axis is parallel to maximum horizontal stress direction.)

- Figure 4-40 shows the Y-Y waveforms for the vertical borehole. (Note: The Y-axis is parallel to minimum horizontal stress direction.)

- Figure 4-41 shows the X-X waveforms for the horizontal borehole. (Note: The X-axis is parallel to vertical stress direction.)

- Figure 4-42 shows the Y-Y waveforms for the horizontal borehole. (Note: The Y-axis is parallel to minimum horizontal stress direction.)

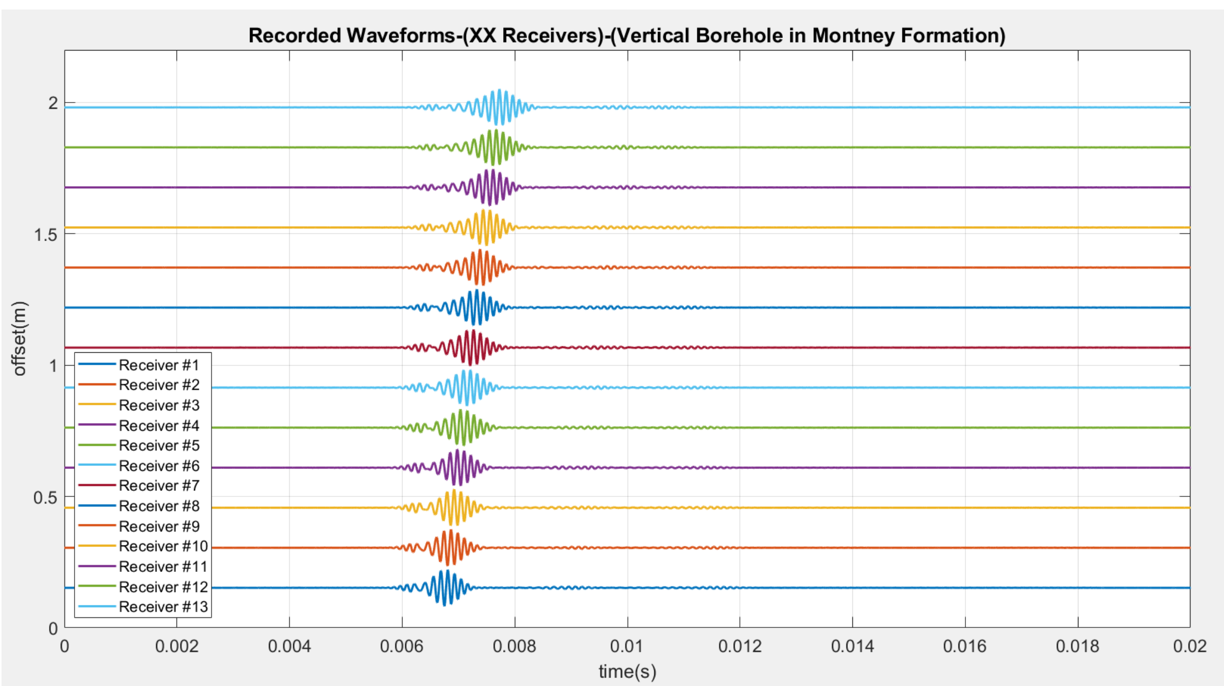

Figure 4-39: Recorded X-X dipole waveforms, vertical borehole in the Montney Formation.

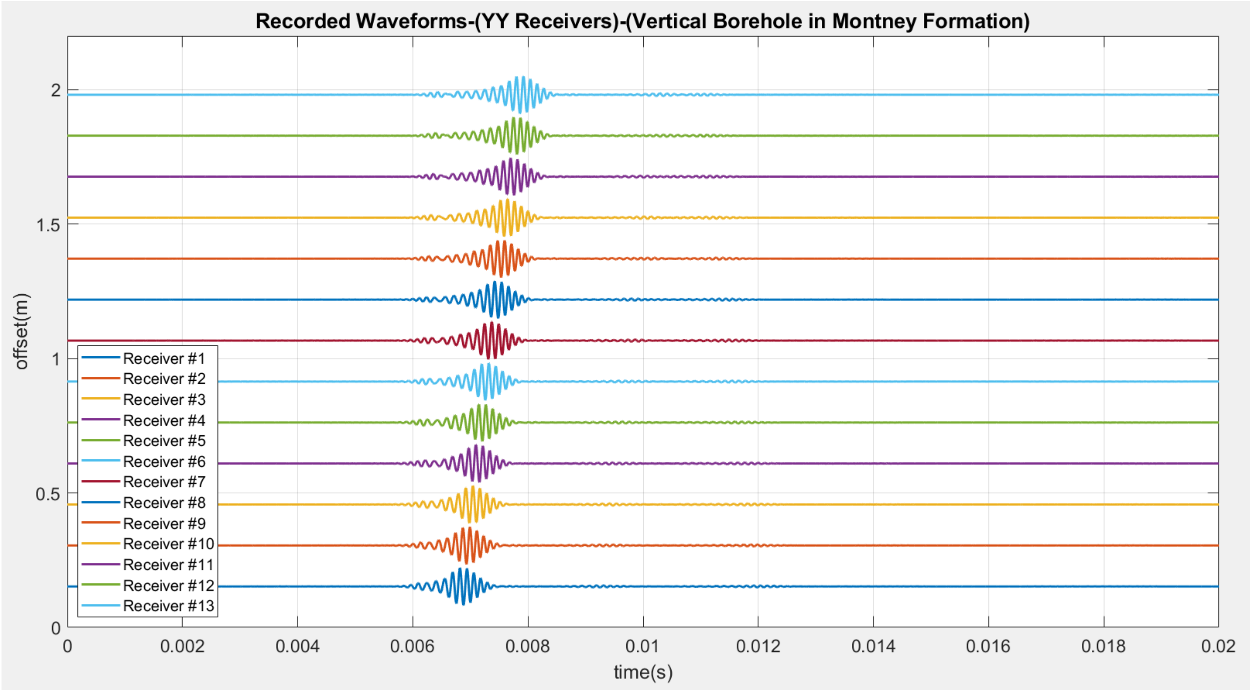

Figure 4-40: Recorded Y-Y dipole waveforms, vertical borehole in the Montney Formation.

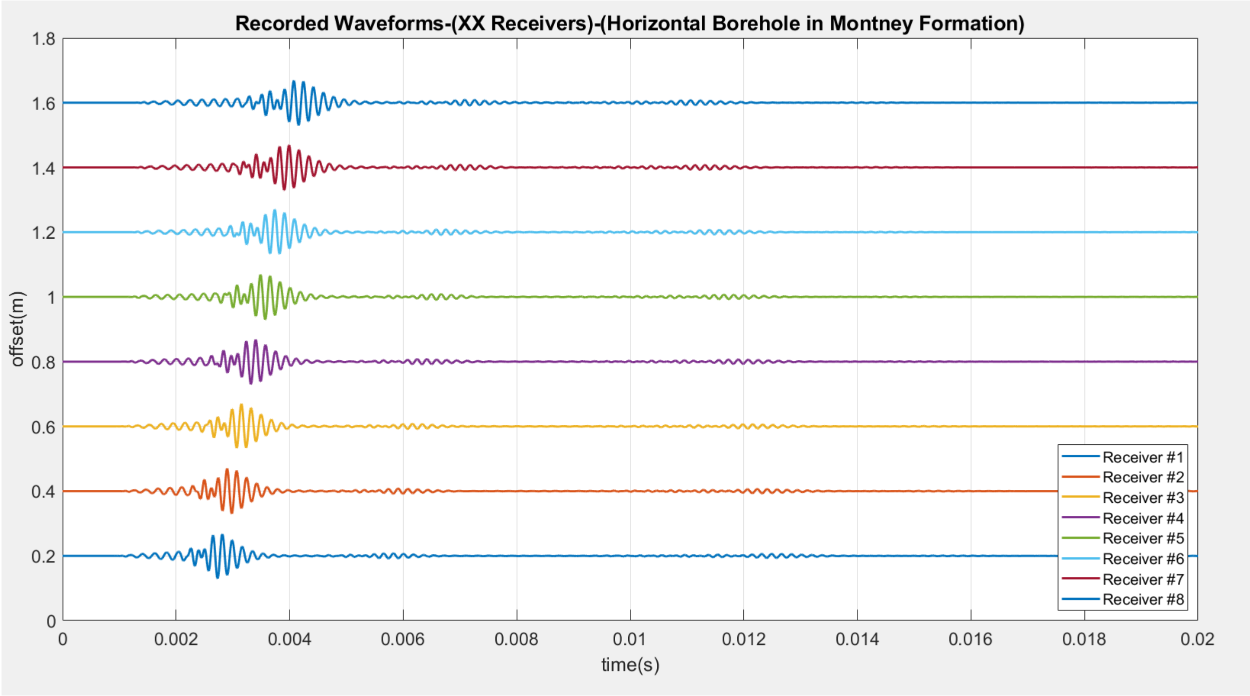

Figure 4-41: Recorded X-X waveforms, horizontal borehole in the Montney Formation.

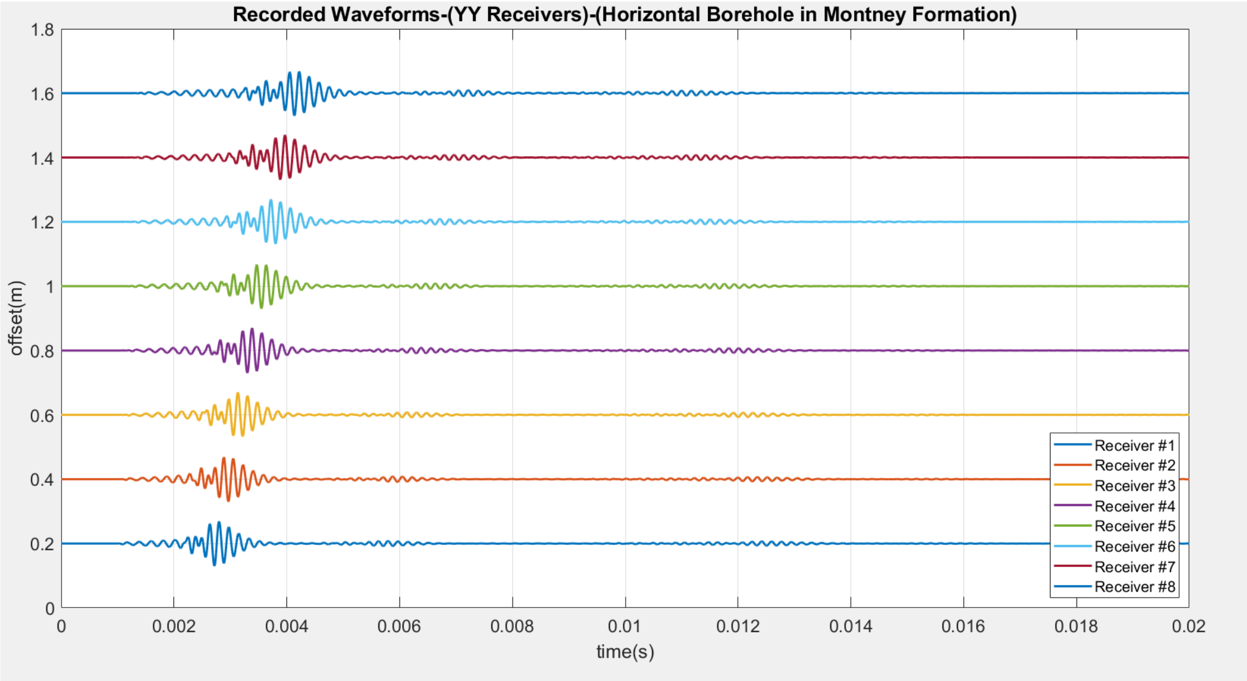

Figure 4-42: Recorded Y-Y dipole waveforms, horizontal borehole in the Montney Formation.

4.3.2.3 Dynamic Analysis (Deadwood)

Figures 4-43 and 4-44 show the numerical modeling results obtained for the vertical borehole in the Deadwood Formation at the Aquistore site. Figure 4-43 shows the X-X waveforms (i.e., in the maximum horizontal in-situ stress direction) and Figure 4-44 shows the Y-Y waveforms (i.e., in the minimum horizontal stress direction). Although the same source type was used in simulation of the vertical borehole in the Montney Formation, there is a difference in appearance of the waveforms. The difference in appearance of the waveforms is because of difference in defined drilling mud velocities as well as differences in compressional and shear velocities of the formation.

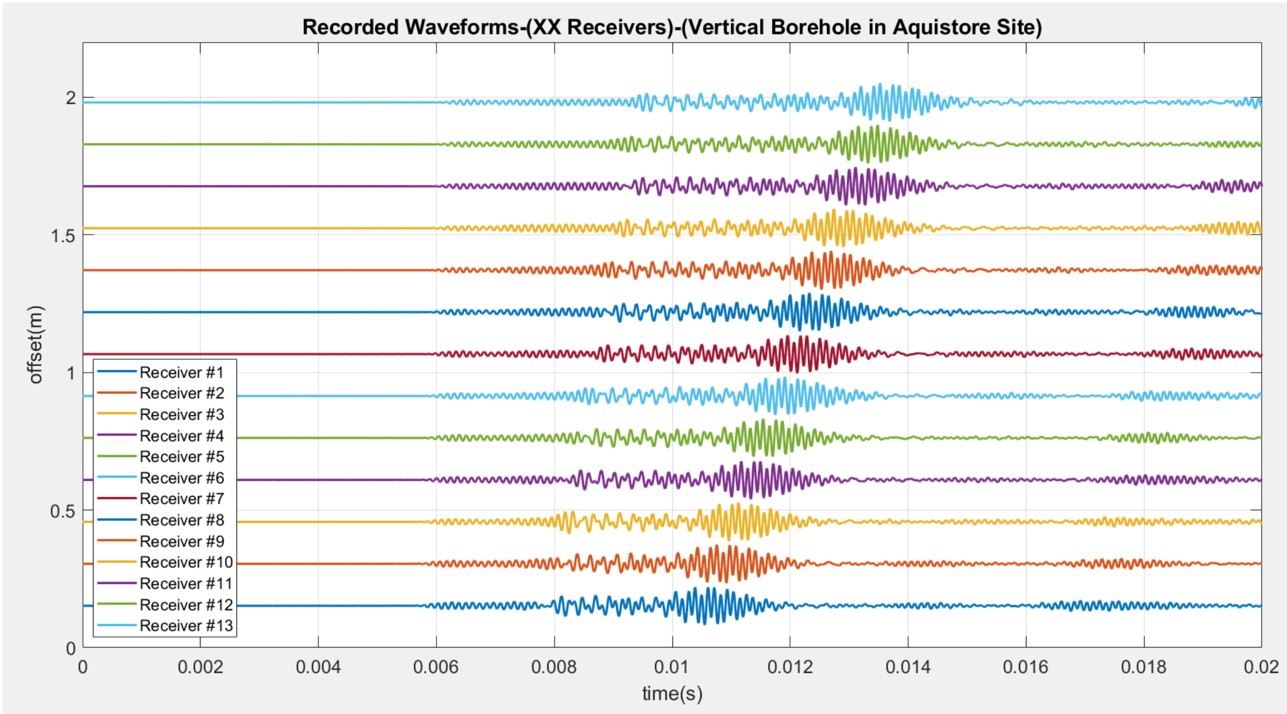

Figure 4-43: Recorded X-X dipole waveforms, vertical borehole in the Deadwood Formation.

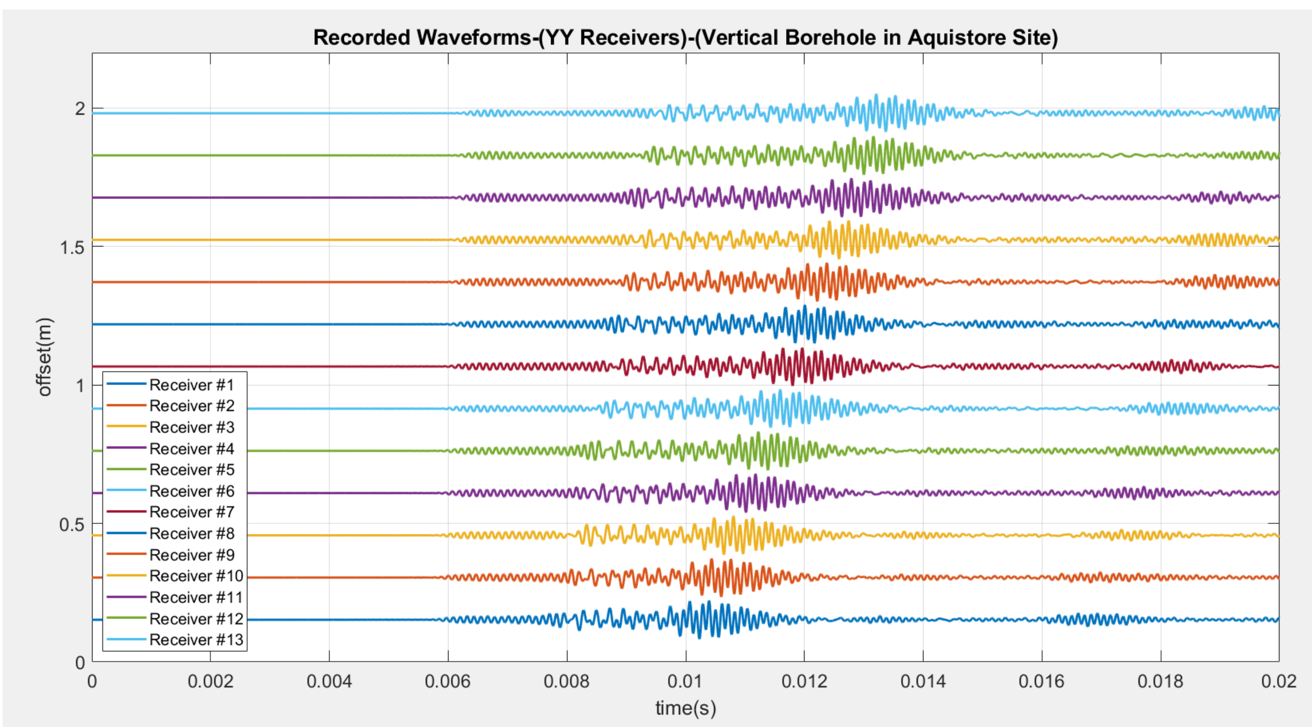

Figure 4-44: Recorded Y-Y waveforms, vertical borehole in the Deadwood Formation.

4.3.3 Dispersion Analysis

4.3.3.1 Dispersion Analysis (Montney Formation)

Figures 4-45 to 4-50 show the dispersion plots generated using two different methods for the vertical and horizontal borehole scenarios considered in the Montney Formation at Farrell Creek. (As noted previously: For the vertical borehole, the X-axis was parallel to the maximum in-situ horizontal stress, and the Y-axis was parallel to the minimum horizontal stress; for the horizontal borehole, the X-axis was parallel to vertical in-situ stress, and the Y-axis was parallel to the minimum horizontal stress.)

- Figure 4-45 shows a dispersion plot for the X-X and Y-Y dipole waveforms in the vertical borehole, based on the Phase Moveout method. The blue dashed line represents slowness obtained directly from velocity measurements conducted in the laboratory testing program, which serves as a comparison against slowness interpreted from the outputs of the modeling workflow, which used elastic properties obtained from the laboratory program as model inputs. (In theory, if the simulation is accurate, the low frequency component of the simulated flexural wave is expected to match the shear wave velocity measured in the laboratory.)

- Figure 4-46 shows a dispersion plot for X-X dipole waveforms in the vertical borehole, based on the DISECA method. In this figure, the areas with maximum coherence of energy (magnitude = 1), which are shown in dark red, represent the predicted flexural wave dispersion curve.

- Figure 4-47 shows a dispersion plot for Y-Y dipole waveforms in the vertical borehole, based on the DISECA method. Similar to Figure 4-46, the predicted dispersion curve tracks the areas of maximum coherence (dark red).

- Figure 4-48 shows a dispersion plot for the X-X and Y-Y dipole waveforms in the horizontal borehole, based on the Phase Moveout method. The blue and red dashed lines were obtained directly from velocity measurements conducted in the laboratory testing program; the low frequency components of the flexural waves are expected to match these shear wave velocities.

- Figure 4-49 shows a dispersion plot for X-X dipole waveforms in the horizontal borehole, based on the DISECA method. The predicted dispersion curve tracks the areas of maximum coherence (dark red).
- Figure 4-50 shows a dispersion plot for Y-Y dipole waveforms in the horizontal borehole, based on the DISECA method. The predicted dispersion curve tracks the areas of maximum coherence (dark red).

A discussion of the form of these curves is given in the following chapter. [*Note: In the dispersion curve plots generated in this work, slowness is presented in* ${}^{\mu s}/_{ft}$ *to be comparable with plots generated using Techlog, and with most of the literature on this subject.*]

The algorithm of the Phase Moveout method is presented by Weatherford for the CXD logging tool, which is different from the Sonic Scanner tool in terms geometry (i.e., transmitter to receiver spacing and spacing between two receivers). In order for this algorithm to be applicable for the Sonic Scanner tool, some corrections were made by the author of this thesis.

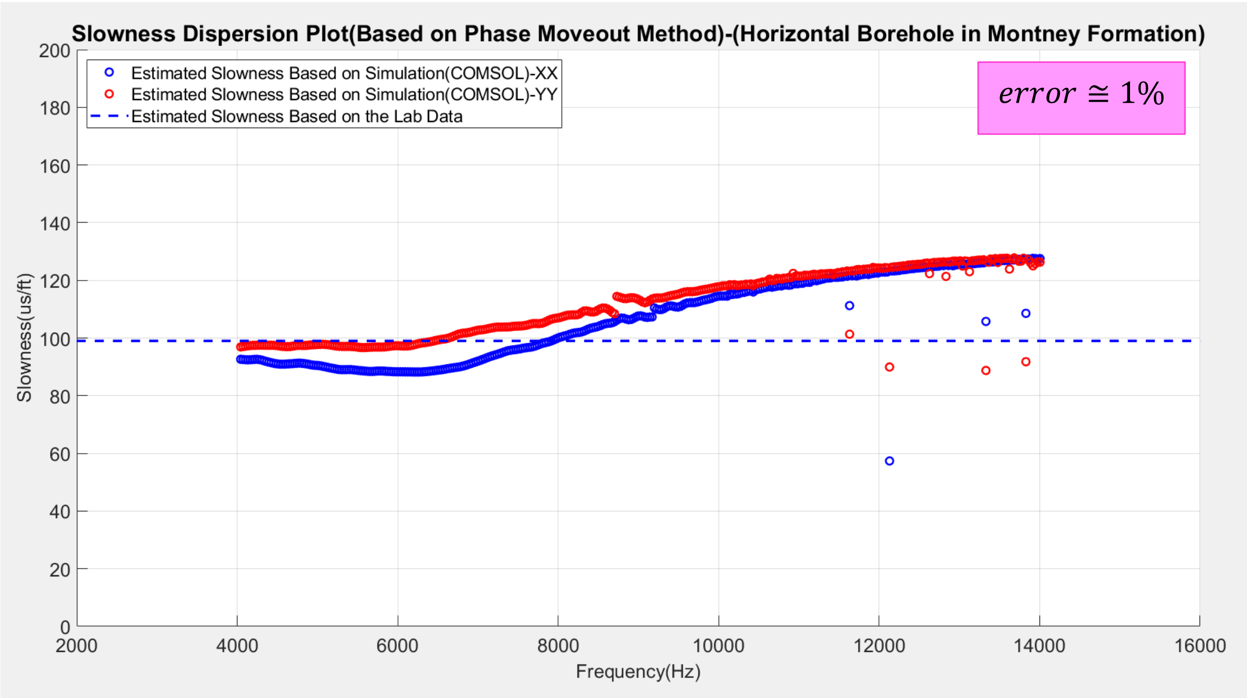

Figure 4-45: Graph showing generated dispersion plots of the modeled X-X and Y-Y waveforms, based on the Phase Moveout method (vertical borehole in the Montney Formation).

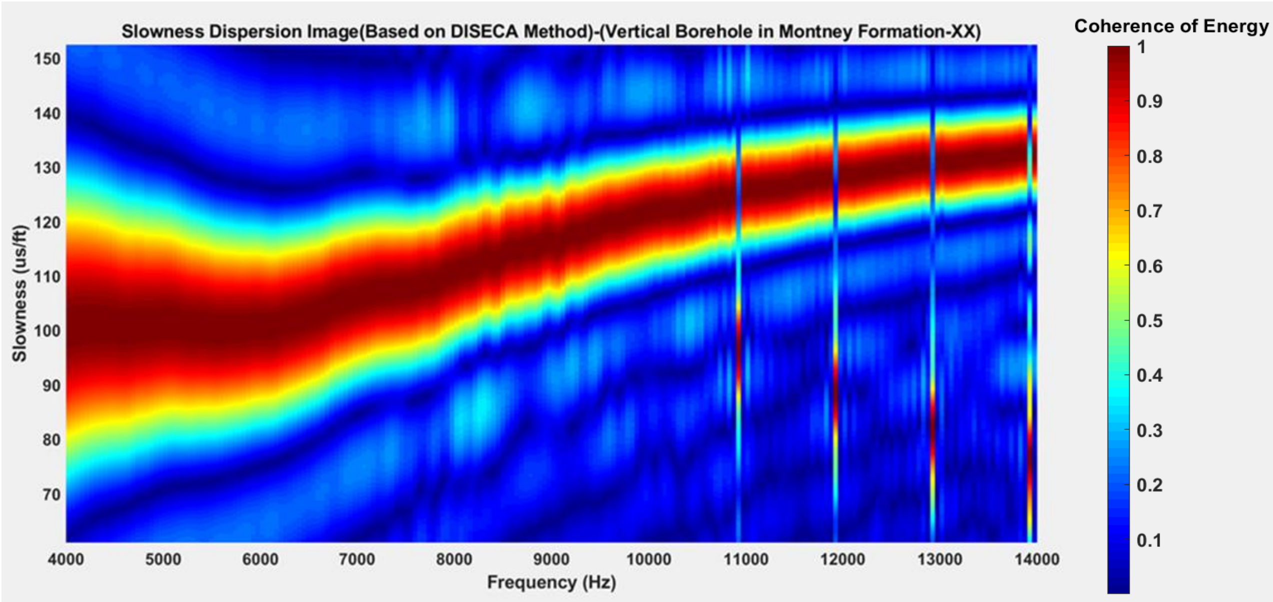

Figure 4-46: Dispersion plot of modeled X-X dipole waveforms, based on the DISECA method (vertical borehole in the Montney Formation).

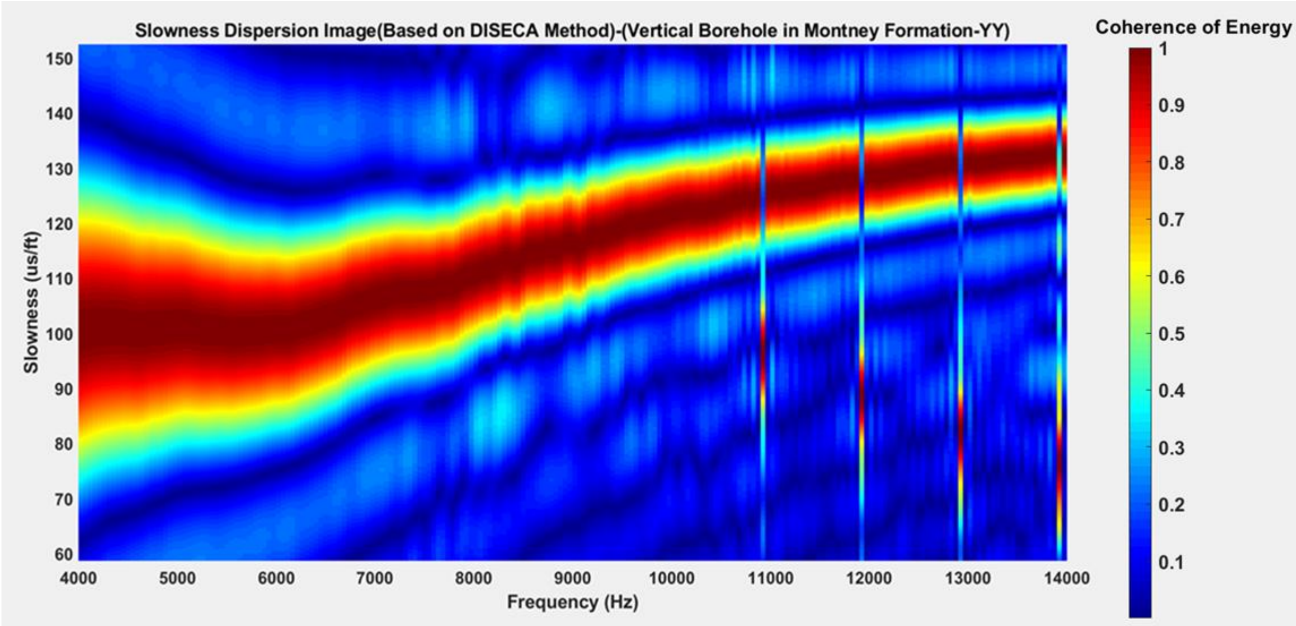

Figure 4-47: Dispersion plot of modeled Y-Y dipole waveforms, based on the DISECA method (vertical borehole in the Montney Formation).

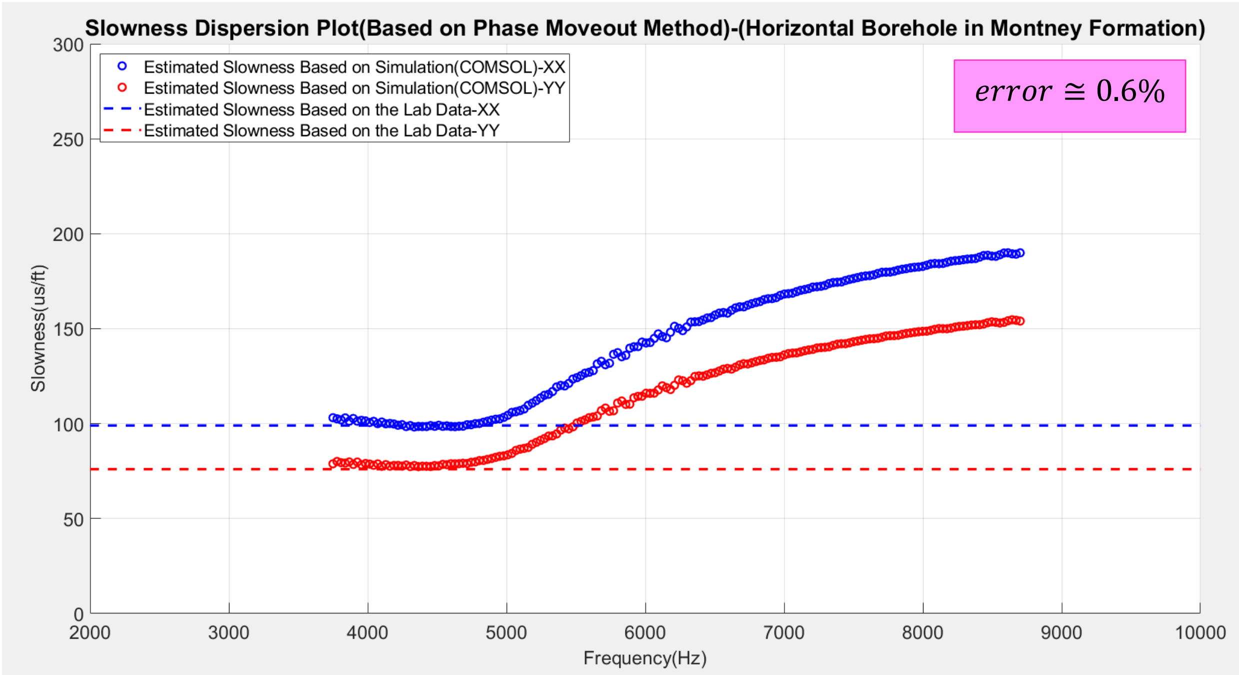

Figure 4-48: Graph showing generated dispersion plots of the modeled X-X and Y-Y waveforms, based on the Phase Moveout method(horizontal borehole in the Montney Formation).

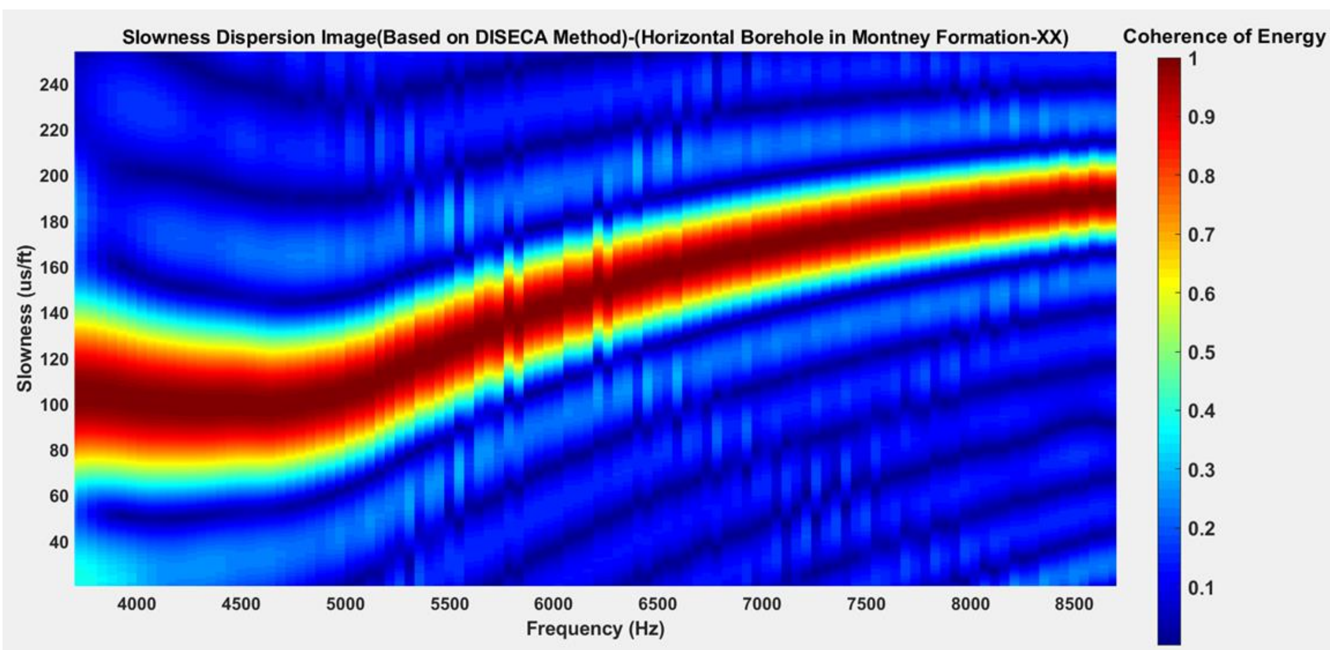

Figure 4-49: Dispersion plot of modeled X-X dipole waveforms, based on the DISECA method (horizontal borehole in the Montney Formation).

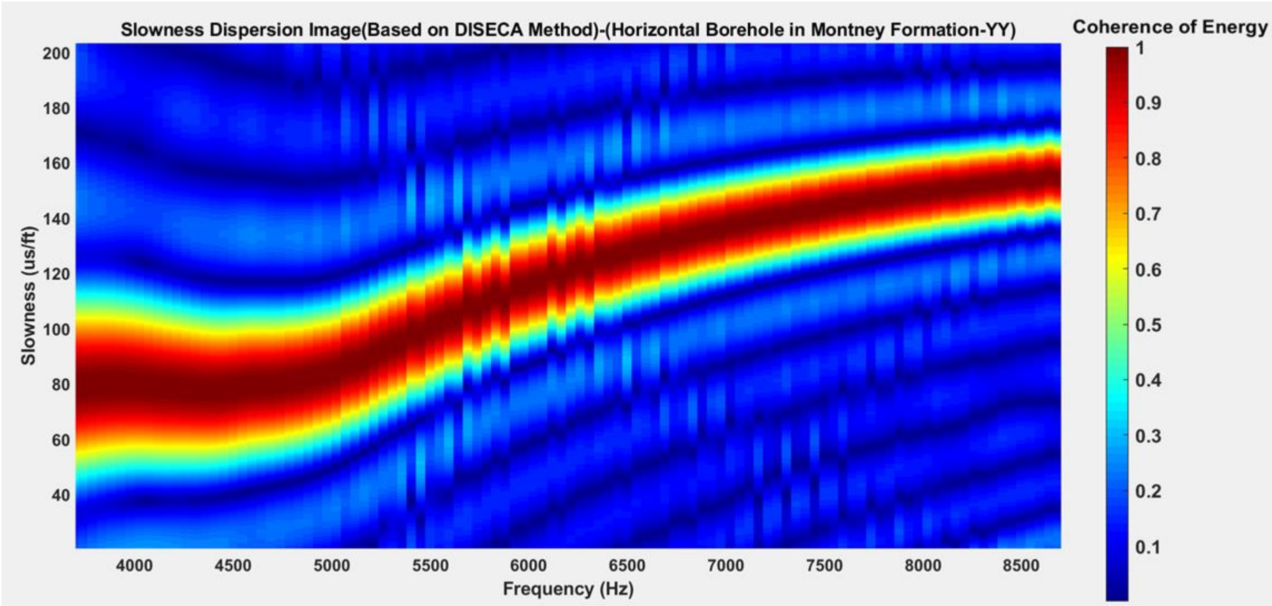

Figure 4-50: Dispersion plot of modeled Y-Y dipole waveforms, based on the DISECA method (horizontal borehole in the Montney Formation).

4.3.3.2 Dispersion Analysis (Deadwood Formation)

Figures 4-51, 4-52 and 4-53 show the dispersion plots generated using based on two different methods for the vertical borehole scenario considered in the Deadwood Formation at the Aquistore site. (As noted previously: For the vertical borehole, the X-direction was parallel to maximum horizontal in-situ stress, and the Y-direction was parallel to the minimum horizontal stress.)

- Figure 4-51 shows a dispersion plot for the X-X and Y-Y dipole waveforms in the vertical borehole, based on the Phase Moveout method. The blue dashed line represents slowness obtained directly from velocity measurements conducted in the laboratory testing program; the low frequency component of the flexural wave is expected to match this shear wave velocity.

- Figure 4-52 shows a dispersion plot for X-X dipole waveforms in the vertical borehole, based on the DISECA method. The predicted dispersion curve tracks the areas of maximum coherence (dark red).

- Figure 4-53 shows a dispersion plot for Y-Y dipole waveforms in the vertical borehole, based on the DISECA method. The predicted dispersion curve tracks the areas of maximum coherence (dark red).

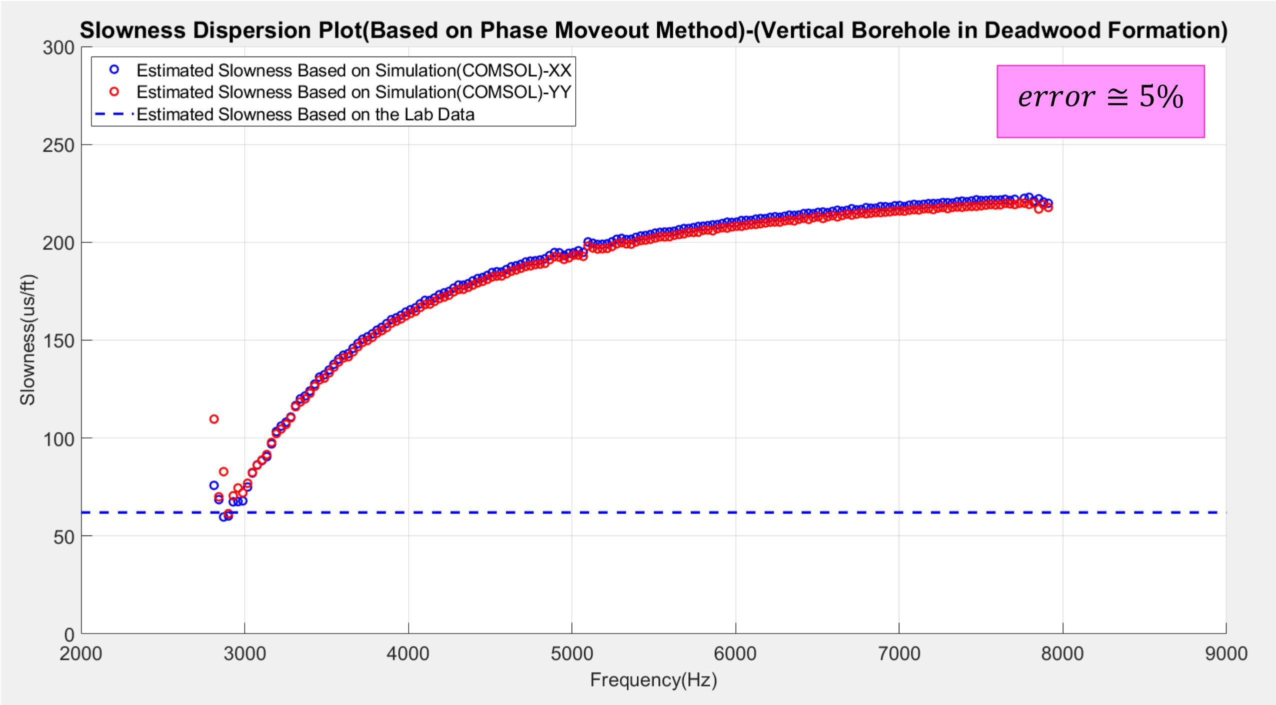

Figure 4-51: Graph showing generated dispersion plots of the modeled X-X and Y-Y waveforms, based on the Phase Moveout method (vertical borehole in the Deadwood Formation).

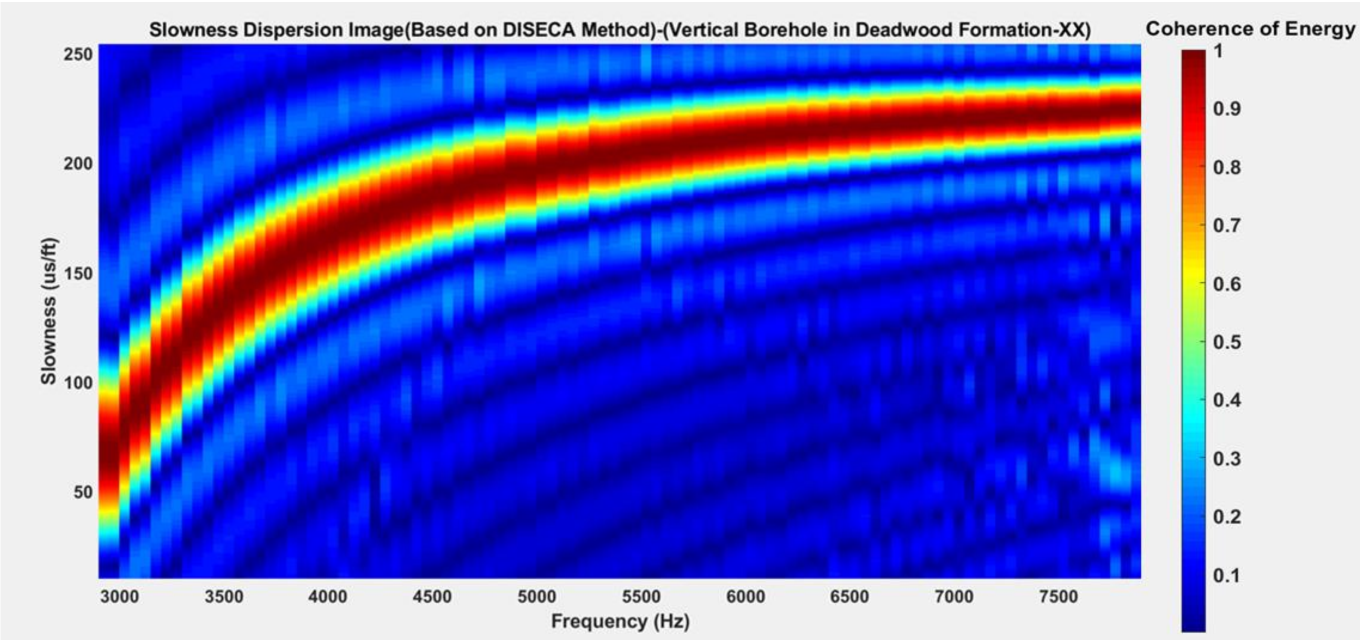

Figure 4-52: Dispersion plot of modeled X-X dipole waveforms, based on the DISECA method (vertical borehole in the Deadwood Formation).

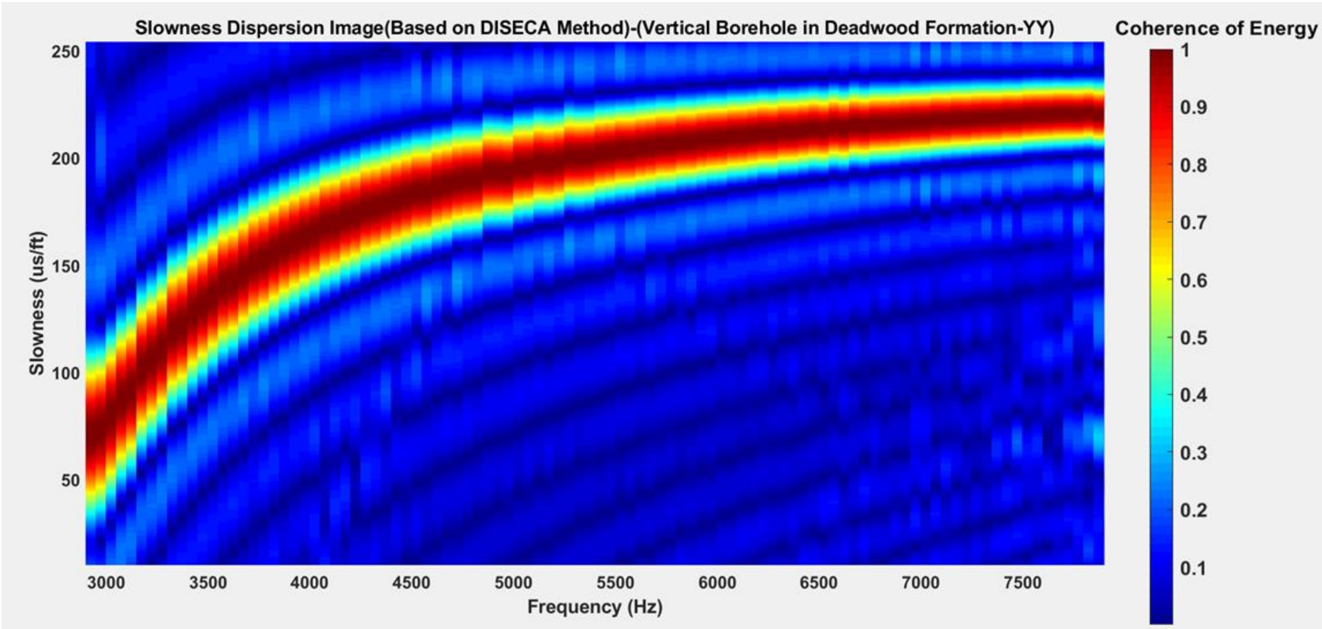

Figure 4-53: Dispersion plot of modeled Y-Y dipole waveforms, based on the DISECA method (vertical borehole in the Deadwood Formation).

5. Comparison of Simulation Results to Field Data

5.1 QC Techniques

In this project, the waveforms and the corresponding dispersion curves were generated at depths corresponding to the average corrected depths of the samples used for lab testing. For quality control, dispersion curves for each scenario modeled were generated using two different methods: the Phase Moveout method and the DISECA method. The consistency between the outputs of two dispersion methods suggests that both methods were coded correctly, and the model results have a form that is consistent with expectations. Most importantly, the shear wave slowness values interpreted from the dispersion curves obtained from the low frequency component of the flexural waves match the values extracted directly from the lab testing.

In this chapter, the simulation results are assessed in more detail, by comparison against real data measured by sonic logging tools in the Montney and Deadwood formations.

5.2 Effect of the Type of Anisotropy on Wave Propagation around a Borehole

Simulation results for the horizontal borehole in the Montney Formation showed parallel dispersion curves (Figure 4-48), which suggests that the dispersive character of wave propagation around the horizontal borehole is dominantly controlled by intrinsic anisotropy (bedding) in this scenario. This is consistent with expectations based on the input values, taken from lab testing. Based on the input values, C_{66} (representing the slow shear wave) was aligned in the X-X direction (or the axis of symmetry) and was smaller than C_{44} (representing the fast shear wave) which was aligned in the Y-Y direction (or parallel to the plane of anisotropy).

As shown in Figure 4-45 and Figure 4-51, dispersion curves for the vertical boreholes showed cross-over. This cross-over results from the fact that dispersive behaviour of wave propagation around the vertical borehole drilled in VTI medium is dominantly controlled by stress-induced anisotropy. As a result of drilling a borehole, the stress concentration around the borehole has a tangential stress which reaches its maximum value in the direction of the minimum horizontal in-situ stress and minimum value in the direction of the maximum horizontal stress. So, near the borehole, the fast shear wave is recorded in the direction of minimum horizontal stress and the slow shear is recorded wave in the direction of maximum horizontal stress. This order is opposite to the fast and slow orientations observed in the far field (as illustrated in Figure 2-20).

5.3 Comparison between Predicted Slowness Based on Logged Data and Simulation Results

In order to compare the predicted slowness based on simulation results with predicted values obtained from real logging data, dispersion curves were generated using Techlog for a vertical borehole in the Montney Formation at Farrell Creek, at a depth corresponding to the simulations and lab testing. Similarly, Techlog was used to generate dispersion curves for the Deadwood Formation at the Aquistore site (Figure 5-1.a and 5-2.a).

In order to compare data-driven results (which tend to be noisy) with model results, it is recommended to fit a continuous curve through the data. A sigmoid-shaped function is generally deemed appropriate for this purpose (Assous & Elkington, 2014). As such, a sigmoid-shaped curve was fitted to dispersion curves based on real field data to get smoother figures for comparison, given that curve-fitting is standard practice. The method used for curve-fitting is presented in Appendix F. A sigmoid- shaped curve was then fitted to these dispersion curves, as shown in Figure 5-1.b and Figure 5-2.b.

By comparison between Figures 5-1.b and 5-2.b with 4-45 and 4-51, it is evident that there is similarity is the general form of the simulated and logged dispersion curves. More specifically, the Montney Formation - vertical borehole scenario shows cross-over both for the simulated results (Figure 4-45) and the field data (Figure 5-1.b). For the Deadwood Formation scenario (vertical borehole), there is a very weak suggestion of cross-over for both for the simulated results (Figure 4-51) and the field data (Figure 5-2.b). However, the absolute values of slowness interpreted from the simulated curves are significantly (20% - 40%) less than the values interpreted from the field data. Since there a favourable comparison was observed between the predicted slowness based on simulation and estimated value taken directly from the experimental results, the difference between simulated and field-based dispersion curves could result from the following reasons:

- In this project, samples were tested at ambient temperature, hence the effect of temperature was ignored. It seems reasonable to expect that the elastic properties of rocks could be functions of temperature in addition to stress.
- The transducers used in the laboratory testing operate at much higher frequencies than sonic logging tools (MHz vs. kHz). Literature has shown that there is a direct relationship between measured velocities and wave frequencies (e.g., Szewczyk et al., 2017). As such,

velocities measured in the laboratory would be expected to be greater than those measured by sonic logging tools (or, equivalently, laboratory slowness values would be less than field-based values).

- The size of tested samples is small compared to compared to the volume of investigation by sonic logging tool, hence the samples do not capture the material property heterogeneity that would exist in-situ.

Subtle differences in the form of the dispersion curves could stem from the fact that dispersion curve modeling of formation flexural slowness is influenced by the following parameters, in addition to compressional and shear wave velocities of the formation:

- Compressional wave velocity and density of drilling mud borehole.
- Diameter of borehole.

No information was provided regarding the compressional velocities of the drilling muds used in the boreholes that were studied. Mud compressional velocities were estimated by the author based on their types (Invert oil-based or Polymer water-based) and volume fractions of the components mentioned in the drilling reports. Although these values were estimated based on the real field condition in terms of pressure and temperature, these estimated values could be slightly different from real ones.

Borehole diameter plays a crucial role in the "airy phase" frequency at which surface waves are created. To be more clear, flexural wave excitation is maximum at the "airy phase" frequency, when the wavelength (λ) is approximately one-half the borehole circumference. Finally, at high frequency, when the wavelength (λ) becomes small compared with borehole size, the flexural wave becomes a surface wave (Vimal et al., 2018).

Unfortunately, the data available for the horizontal borehole in Montney Formation did not include raw data required for generating dispersion curves. For the horizontal borehole the predicted fast and slow shear wave slownesses were compared with the logged values (Figure 5-3). Though the general character of the results are similar (i.e., both results show well-define fast and slow shear waves), the absolute values of the simulation and field-based results are notably different (simulated slownesses 20% - 30% less than field-based values). These differences are likely related to the same factors mentioned above. Further, for this horizontal well scenario, differences could be related heterogeneity; i.e., it is possible that the rock properties in bedding layers in the upper part of the borehole are different from the layers in the lower part.

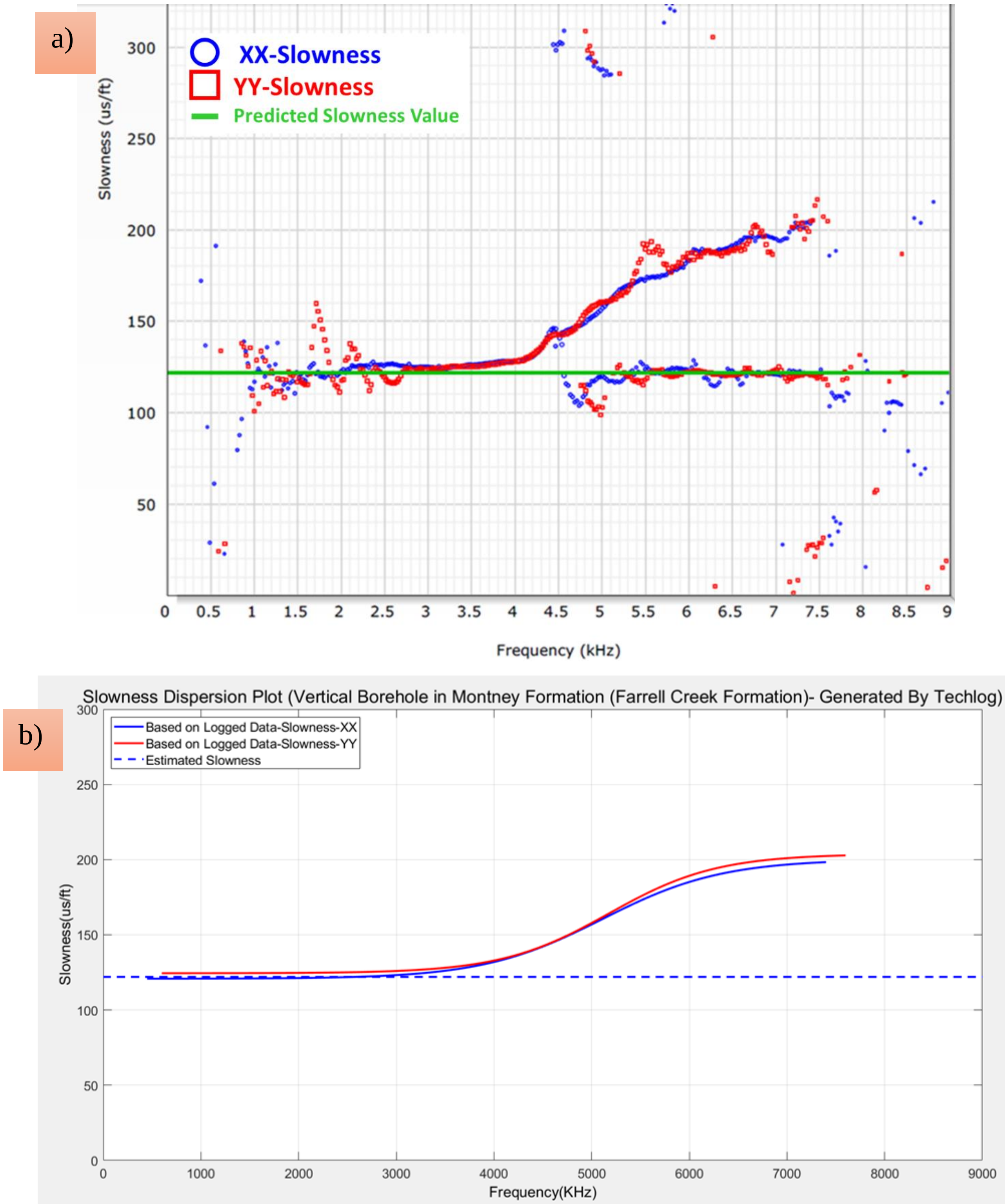

Figure 5-1: a) Dispersion curves generated using Techlog for logging data collected in the vertical borehole in the Montney Formation; and b) Sigmoid-shaped curves fit to these data using Techlog. Note that data points recorded when the monopole transmitter was fired (visible at frequencies greater than 4.5 kHz) were ignored during fitting of the sigmoid curves. The horizontal lines (at ~120 µ/ft) show the shear wave slowness interpreted from this data, based on the low-frequency component of the flexural waves.

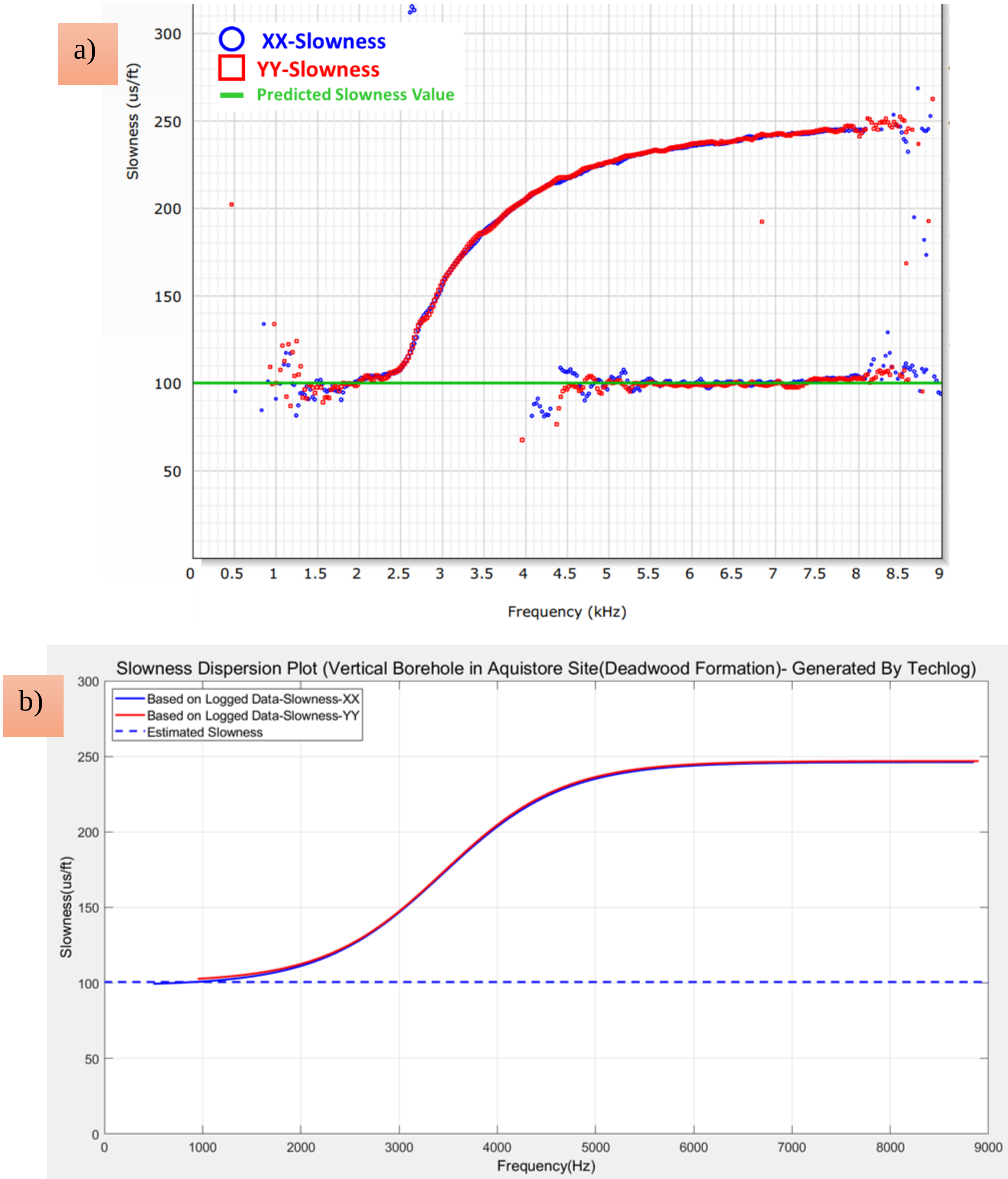

Figure 5-2: a) Dispersion curves generated using Techlog for logging data collected in the vertical borehole in the Deadwood Formation; and b) Sigmoid-shaped curves fit to these data using Techlog. Note that data points recorded when the monopole transmitter was fired (visible at frequencies greater than 4.5 kHz) were ignored during fitting of the sigmoid curves. The horizontal lines (at ~100 µ/ft) show the shear wave slowness interpreted from this data, based on the low-frequency component of the flexural waves.

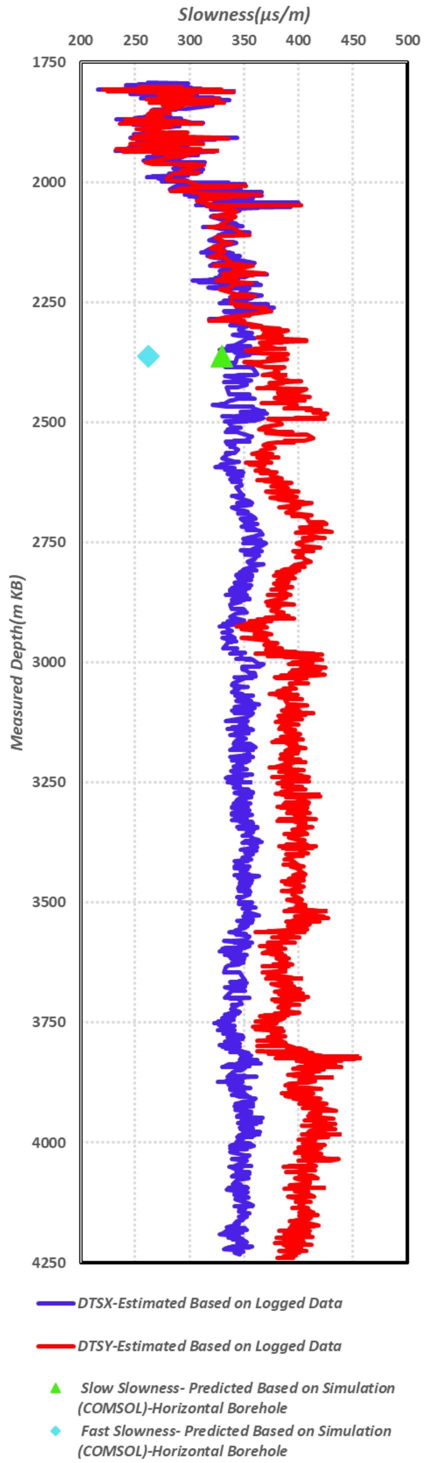

Figure 5-3: Comparison between predicted fast and slow shear wave slownesses based on sonic logging (continuous curves) and simulation results (discrete symbols), for the horizontal borehole in the Montney Formation.

6. Conclusions and Recommendations

6.1 Conclusions

The following is a list of conclusions based on this study:

- A numerical modelling workflow was developed in this research which enables the prediction of intrinsic and stress-induced anisotropy on the response of a cross-dipole sonic logging tool. Workflow comprises two main steps: static and dynamic analysis. In static analysis, static stress-dependent properties (acquired from lab testing results) were utilized to define the static elastic stiffness tensor to predict the stress alteration around the borehole. The results of this static stress analysis were then used in conjunction with dynamic elastic properties (defined as a function of stress) to determine dynamic elastic properties of the rock around the borehole to simulate wave propagation around the borehole.
- Predicted shear slowness based on simulation compare favourably with estimated values based on experimental results. As such, it would be concluded that the workflow is effective and appropriate.
- The results obtained (more specifically, dispersion curves) suggest that model domain size recommended in literature is not sufficiently large. Results obtained using a formation radius of six times the borehole radius resulted in low quality of the low-frequency portion of the dispersion curve. Good results were obtained using a formation radius that was nine times the borehole radius.
- The character of the dispersion curves generated using the new workflow were consistent with expectation. The dispersive behaviour of shear wave slowness around a horizontal borehole in a VTI medium was found to be more affected by intrinsic anisotropy than stress-induced anisotropy. The opposite was observed for a borehole is drilled vertically in a VTI medium.
- Comparison between predicted values based on logged data and simulation results revealed similarity in general character of the output but some differences in an absolute sense. These difference likely stem from differences between lab testing conditions and in-situ conditions such as temperature, frequency, size (dimensions), pore fluid properties, pore pressure, and rock property heterogeneity.

- Comparison between dispersion curves based on logged data and simulation results showed slight differences in the appearance of the curves. This difference could stem from differences in estimated compressional velocity and density of the drilling mud, compressional and shear velocities of formations, and the presence of the logging tool.

6.2 Limitations and Recommendations

Following is a list of key limitations of this research, and recommendations to overcome these limitations in future research:

- For simplicity, the effects of poroelasticity were ignored in this research. Give that pore fluid pressure and type could affect sonic wave propagation, a poroelastic material model should be used in future research.
- Mud penetration into the rock surrounding the borehole was not accounted for in this research. Mud penetration could result in pore pressure change, and change in rock properties due mud-rock interactions (e.g., hydration of clay minerals), both of which could affect elastic properties hence sonic velocities. Future research should include the modeling of mud penetration, and the resulting effects on rock properties.
- A circular borehole in an elastic continuum was assumed in this research; i.e., the effects of yielding (plastic zone development), failure (e.g., tensile fracturing; borehole breakout development), and natural fractures on stresses and wave propagation were neglected. These effects should be considered in future research.
- The laboratory testing conducted for this research was undertaken at ambient temperatures, which are tens of degrees Celsius cooler than in-situ temperatures. Given that elevated temperatures generally reduce rock stiffness and sonic wave velocities, future research should measure rock properties at representative in-situ temperatures (or, at least, use correction factors to ensure that model input parameters are representative of in-situ conditions).
- The effect of frequency difference (i.e., laboratory transducers having significantly higher frequencies that sonic logging tools) was ignored in this research. Given that elevated frequencies generally result in increased stiffness and velocities, future research should use correction factors to ensure that model input parameters are representative of in-situ conditions.

- The size of samples used in the laboratory component of this research was small relative to the volume of rock involved in wave propagation around a borehole, and the number of samples was relatively limited. As such, the effects of heterogeneity were not addressed in this work. These effects could be most important in a horizontal borehole scenario; i.e., for a horizontal borehole in layered sedimentary rocks, it is possible that the rock properties in the upper part of the borehole are different from the rock properties in the lower part. Future research should use a greater number of samples, greater in size (if feasible), and should use a modeling framework that allows for heterogeneous material properties (e.g., discrete layering, geostatistical representation of material property distributions).
- In this study, due to limitations in the number and orientation of strain gauges used in the laboratory testing, some static elastic stiffness constants were estimated based on simplifying assumptions. Future research should include more comprehensive strain measurements, in order to obtain more accurate representation of static elastic property anisotropy.
- This research assumed that elastic properties were controlled solely by mean effective stress, and that linear relations existed between stresses and elastic properties (and between dynamic and static elastic properties). Future laboratory work should be designed to assess the effects of each principal stress component (or some combined representation of deviatoric and mean stress) on material properties, and should investigate possible non-linear relationships between stresses and elastic properties. The models developed in this research are capable of supporting more complex relationships between stresses and elastic properties, but more sophisticated laboratory testing would be required to provide the required input parameters.
- In the horizontal well (Montney Formation) investigated in this research, the samples tested in the laboratory were not taken from the exact depth as the horizontal leg of the borehole that was logged. A closer match between core sampling and logging is recommended for future research.
- The body of the sonic logging tool was not included in the models developed for this research. Given that tool properties can influence wave propagation around the

borehole, the geometry and material properties of the body of the sonic logging tool should be included in future simulations.

Following are additional recommendations for future research on this topic:

- The radius of the modeled formation surrounding a borehole should be chosen based on static stress analysis results, to ensure that the model domain extends beyond the zone of induced stress change.
- If computational facilities of sufficient capability are available, it is recommended that modeling should be conducted in the time domain (to avoid the complexity of working in the frequency domain, which was used in this research).
- Methods to improve the efficiency of the dynamic model should be investigated; computation times and data processing times were substantial in this research (e.g., roughly one-week total for each simulation, using a desktop workstation and with 64 GB of RAM).
- An algorithm that will facilitate the use of this modeling workflow to solve inverse modeling problems should be developed (i.e., to solve for in-situ stress based on logging tool response, when rock elastic properties are known).

References

Aadnoy, B. S. (1987). Continuum mechanics analysis of the stability of inclined boreholes in anisotropic rock formations (Doctoral dissertation, The Norwegian Institute of Technology).

Alford, J., Blyth, M., Tollefsen, E., Crowe, J., Loreto, J., Mohammed, S., & Rodriguez-Herrera, A. (2012). Sonic Logging While Drilling-Shear Answers. Oilfield Review, 24(1), 4-15.

Assous, S., Elkington, P., & Linnett, L. (2014). Phase-based dispersion analysis for acoustic array borehole logging data. The Journal of the Acoustical Society of America, 135(4), 1919-1928.

Ávila-Carrera, R., Spurlin, J. H., & Valle-Molina, C. (2011). Simulating elastic wave propagation in boreholes: Fundamentals of seismic response and quantitative interpretation of well log data. Geofísica internacional, 50(1), 57-76.

Beltran-Mejia, F.(2014, April 16). PML width for longer wavelength. Retrieved from https://www.comsol.com/forum/thread/43219/pml-width-for-longer-wavelength.

Bouchon, M. (2003). A review of the discrete wavenumber method. Seismic Motion, Lithospheric Structures, Earthquake and Volcanic Sources: The Keiiti Aki Volume, 445-465.

Carcione, J. M., & Poletto, F. (2000). Sound velocity of drilling mud saturated with reservoir gas. Geophysics, 65(2), 646-651.

Chan, A. K., & Tsang, L. (1983). Propagation of acoustic waves in a fluid-filled borehole surrounded by a concentrically layered transversely isotropic formation. The Journal of Acoustical Society of America, 74(5), 1605-1606.

Che, X., Zhang, H., Qiao, W., & Ju, X. (2005). Numerical study on scanning radiation acoustic field in formations generated from a borehole. Science in China Series G: Physics Mechanics and Astronomy, 48(2), 247-256.Liu, L., Lin, W., & Zhang, H. (2014). Numerical Study on the Acoustic Field of a Deviated Borehole with 2.5 D Method.

Cheng, N. (1994). Borehole wave propagation in isotropic and anisotropic media: Three-dimensional finite difference approach (Doctoral dissertation, Massachusetts Institute of Technology).

Davey, H. (2012). Geomechanical characterization of the Montney shale, northwest Alberta and northeast British Columbia, Canada (Doctoral dissertation, Colorado School of Mines. Arthur Lakes Library).

Duenas, C. (2014). Understanding rock quality heterogeneity of Montney shale reservoir, Pouce Coupe field, Alberta, Canada (Doctoral dissertation, Colorado School of Mines. Arthur Lakes Library).

Egbobawaye, E. I. (2013). Tight Gas Reservoir Characterization in Montney Formation, Northeastern British Columbia, Western Canada. University of Alberta (Canada).

Eissa, E. A., & Kazi, A. (1988). Relation between static and dynamic Young's moduli of rocks. International Journal of Rock Mechanics and Mining and Geomechanics Abstracts, 25(6).

Fang, X., Fehler, M., Zhu, Z., Chen, T., Brown, S., Cheng, A., & Toksoz, M.N. (2013). An approach for predicting stress-induced anisotropy around borehole. Geophysics, 78(3), D143-D150.

Franco, J. A., Ortiz, M. M., De, G. S., Renlie, L., & Williams, S. (2006). Sonic investigation in and around the borehole. Oilfield Review, 18(1), 14-33.

Frydman, M., & da Fontoura, S. (1997). Numerical modeling of borehole pressurization. International Journal of Rock Mechanics and Mining Sciences, 34(3-4), 82-e1.

Gaede, O., Karpfinger, F., Jocker, J., & Prioul, R. (2012). Comparison between analytical and 3D finite element solutions for borehole stresses in anisotropic elastic rock. International Journal of Rock Mechanics and Mining Sciences, 51, 53-63.

Gaždová, R., & Vilhelm, J. (2011). DISECA–A Matlab code for dispersive waveform calculations. Computers and Geotechnics, 38(4), 526-531.

Haldorsen, J.B.U., Johnson, D.L., & Plona, T., Sinha, B., & Valero, H., & Winkler, K. (2006). Borehole acoustic waves. Oilfield Review, 18(1), 34-43.

Havens, J. (2012). Mechanical properties of the Bakken Formation (Doctoral dissertation, Colorado School of Mines. Arthur Lakes Library).

Hawkes, R. V., Anderson, I., Bachman, R. C., & Settari, A. (2013, February). Interpretation of Closure Pressure in the Unconventional Montney Using PTA Techniques. In 2013 Hydraulic Fracturing Technology Conference, The Woodlands, Texas (pp. 4-6).

Hudson, J. A., & Harrison, J. P. (2000). Engineering rock mechanics: an introduction to the principles. Elsevier.

Ikeda, T., Tsuji, T., Nakatsukasa, M., Ban, H., Kato, A., Worth, K., ... & Roberts, B. (2017). Shallow characterization and monitoring of the Aquistore CO2 storage site from spatially windowed surface-wave analysis with a permanent seismic source. In SEG Technical Program Expanded Abstracts 2017(pp. 5465-5470). Society of Exploration Geophysicists.

Jiang, T., Pekot, L. J., Jin, L., Peck, W. D., Gorecki, C. D., & Worth, K. (2017). Numerical modeling of the Aquistore CO2 storage project. Energy Procedia, 114, 4886-4895.

Karpfinger, F., Prioul, R., Gaede, O., & Jocker, J. (2011). Revisiting borehole stresses in anisotropic elastic media: comparison of analytical versus numerical solutions.

Kendall, D. R. (1999). Sedimentology and stratigraphy of the lower triassic Montney Formation, Peace River basin, subsurface of northwestern Alberta. University of Calgary.

King, M. S. (1983). Static and dynamic elastic properties of igneous and metamorphic rocks from the Canadian shield.

Kurkjian, A. L. (1985). Numerical computation of individual far-field arrivals excited by an acoustic source in a borehole. Geophysics, 50(5), 852-866.

Kurz,M.D., Heebink, L.V., Smith, S.A., & Zacher, E. J. (2014). Petrophysical Evaluation of Core from the Aquistore CO2 Injection Site. North Dakota, USA: Energy & Environmental Research Center.

Lin, W., & Liu, L. (2015). Numerical Study of Mode Waves in a Deviated Borehole Penetrating a Transversely Isotropic Formation. Physics Procedia, 70, 102-105.

Liu, Q. H., & Sinha, B. K. (2000). Multipole acoustic waveforms in fluid-filled boreholes in biaxially stressed formations: A finite-difference method. Geophysics, 65(1), 190-201.

Liu, Q. H., & Sinha, B. K. (2003). A 3D cylindrical PML/FTD method for elastic waves in fluid-filled pressurized boreholes in triaxially stressed formations. Geophysics, 68(5), 1731-1743.

Marcia,K.(2019, May 29). DEEP earth energy Production’s Williston Basin Hot Sedimentary Geothermal Power Project Development. Retrieved from https://wbpc.ca/sessions/deep-earth-energy-productions-williston-basin-hot-sedimentary-geothermal-power-project-development/

Markhasin, B. (1998). Sedimentology and stratigraphy of the Lower Triassic Montney Formation, subsurface of northwestern Alberta. University of Calgary.

Martínez, J. M., & Schmitt, D. R. (2013). Anisotropic elastic moduli of carbonates and evaporites from the Weyburn-Midale reservoir and seal rocks. Geophysical Prospecting, 61(2), 363-379.

Mavko, G., Mukerji, T., & Godfrey, N. (1995). Predicting stress-induced velocity anisotropy in rocks. Geophysics, 60(4), 1081-1087.

McLellan, P., Anderson, I., Wong, J., & Mostafavi, V. (2014). Geomechanical Characterization of the Farrell Creek Montney Reservoir, Northeast British Columbia. CSPG CSEG CWLS GeoConvention.

Melendez Martinez, J. (2014). Elastic properties of sedimentary rocks (Doctoral dissertation, University of Alberta).

Mockovčiaková, A., & Pandula, B. (2003). Study of the relation between the static and dynamic moduli of rocks. Metalurgija, 42(1), 37-39.

Moslow, T. F., & Davies, G. R. (1997). Turbidite reservoir facies in the Lower Triassic Montney Formation, west-central Alberta. Bulletin of Canadian Petroleum Geology, 45(4), 507-536.

Muga, I., Pardo, D., Matuszyk, P. J., & Torres-Verdín, C. (2015). Semi-analytical response of acoustic logging measurements in frequency domain. Computers & Mathematics with Applications, 70(4), 314-329.

NEB., 2013. The ultimate Potential for Unconventional Petroleum from the Montney Formation of British Columbia and Alberta.

Note, E. B. (2013). The Ultimate Potential for Unconventional Petroleum from the Montney Formation of British Columbia and Alberta.

Petrowiki. (2015, June 24). Acoustic Logging Tools. Retrieved June 16,2017, from http://petrowiki.org/Acoustic_logging_tools

Pissarenko, D., Reshetova, G. V., & Tcheverda, V. A. (2009). 3D finite-difference synthetic acoustic logging in cylindrical coordinates. Geophysical Prospecting, 57(3), 367-377.

Prioul, R., Bakulin, A., & Bakulin, V. (2004). Nonlinear rock physics model for estimation of 3D subsurface stress in anisotropic formations: Theory and laboratory verification. Geophysics, 69(2), 415-425.

Reiter, K., Heidbach, O., Schmitt, D., Haug, K., Ziegler, M., & Moeck, I. (2014). A revised crustal stress orientation database for Canada. Tectonophysics, 636, 111-124.

Roever, W. L., Rosenbaum, J. H., & Vining, T. F. (1974). Acoustic waves from an impulsive source in a fluid-filled borehole. The Journal of the Acoustical Society of America, 55(6), 1144-1157.

Rogers, S., McLellan, P., & Webb, G. (2014). Investigation of the Effects of Natural Fractures and Faults on Hydraulic Fracturing in the Montney Formation, Farrell Creek Gas Field, British Columbia. In DFNE Conference Vancouver, Paper ID(Vol. 224).

Rostron, B., White, D., Hawkes, C., & Chalaturnyk, R. (2014). Characterization of the Aquistore CO2 project storage site, Saskatchewan, Canada. Energy Procedia, 63, 2977-2984.

Saskatchewan. Department of Mineral Resources, & Fyson, W. K. (1961). Deadwood and Winnipeg stratigraphy in south-western Saskatchewan. Saskatchewan Department of Mineral Resources, Petroleum and Natural Gas Branch, Geology Division.

Saskatchewan. Petroleum and Natural Gas Branch. Geology Division, & McLean, D. D. (1960). Deadwood and Winnipeg stratigraphy in east-central Saskatchewan. Saskatchewan Department of Mineral Resources, Petroleum and Natrual Gas Branch, Geology Division.

Saxena, Vimal., Krief, Michel., & Adam, Ludmila. (2018). Handbook of borehole acoustics and rock physics for reservoir characterization. Amsterdam, Netherland: Elsevier.

Sayers, C. M. (2010). Geophysics under stress: Geomechanical applications of seismic and borehole acoustic waves. Society of Exploration Geophysicists and European Association of Geoscientists and Engineers.

Schmitt, D. P. (1989). Acoustic multipole logging in transversely isotropic poroelastic formations. The Journal of the Acoustical society of America, 86(6), 2397-2421.

Sinha, B. K., & Zeroug, S. (1999, October). Applications of sonics and ultrasonics in geophysical prospecting. In 1999 IEEE Ultrasonics Symposium. Proceedings. International Symposium (Cat. No. 99CH37027) (Vol. 1, pp. 521-532). IEEE.

Sinha, B. K., Kane, M. R., & Frignet, B. (2000). Dipole dispersion crossover and sonic logs in a limestone reservoir. Geophysics, 65(2), 390-407.

Sinha, B. K., Liu, Q. H., & Kostek, S. (1996). Acoustic waves in pressurized boreholes: A finite difference formulation. Journal of Geophysical Research: Solid Earth, 101(B11), 25173-25180.

Sone, H., & Zoback, M.D. (2013). Mechanical properties of shale-gas reservoir rocks- Part 1: Static and dynamic elastic properties and anisotropy. Geophysics, 78(5), D381-D392.

Song, L., & Hareland, G. (2012, January). Minimum horizontal stress profile from logging data for Montney Formation of North East British Columbia. In SPE Canadian Unconventional Resources Conference. Society of Petroleum Engineers.

Stork, A. L., Nixon, C. G., Hawkes, C. D., Birnie, C., White, D. J., Schmitt, D. R., & Roberts, B. (2018). Is CO 2 injection at Aquistore aseismic? A combined seismological and geomechanical study of early injection operations. International Journal of Greenhouse Gas Control, 75, 107-124.

Sun, H., & Prioul, R. (2010). Relating shear sonic anisotropy directions to stress in deviated wells. Geophysics, 75(5), D57-D67.

Szewczyk, D., Bauer, A., & Holt, R. M. (2017). Stress-dependent elastic properties of shales—laboratory experiments at seismic and ultrasonic frequencies. Geophysical Journal International, 212(1), 189-210.

Tak, H., Choi, J., Jo, S., & Hwang, S. (2017). Stress anisotropy analysis and its effect on unconventional resource development in Montney play, Kakwa, Canada. Journal of Applied Geophysics, 139, 177-187.

Tang, X. M., & Cheng, C. H. A. (2004). Quantitative borehole acoustic methods (Vol. 24). Gulf Professional Publishing.

Walsh, W., Adams, C., Kerr, B., & Korol, J. (2006). Regional “shale gas” potential of the Triassic Doig and Montney formations, northeastern British Columbia. British Columbia Ministry of Energy, Mines and Petroleum Resources, Resource Development and Geoscience Branch, 2006-02.

Wang, Z. (2002). Seismic anisotropy in sedimentary rocks, part 2: Laboratory data. Geophysics, 67(5), 1423-1440.

White, D. J., Hawkes, C. D., & Rostron, B. J. (2016). Geological characterization of the Aquistore CO2 storage site from 3D seismic data. International Journal of Greenhouse Gas Control, 54, 330-344.

Winkler, K. W., Sinha, B. K., & Plona, T. J. (1998). Effects of borehole stress concentrations on dipole anisotropy measurements. Geophysics, 63(1), 11-17.

Xiang, L., Bo, Z., & Gaoyang, L. (2012). Application of SDZS-1 Multipole Array Acoustic Logging Tool in Xifeng Oilfield, 7th PNN & Well Logging Conference, Austria, 13-15 September 2012.

Yang, B. (2018). Geological characteristics and reservoir properties in the unconventional Montney Formation, southwestern Alberta, Canada. Geosciences Journal, 22(2), 313-325.

Yoshida, S. (2018). Wave equations and solutions. Waves: Fundamentals and Dynamics. Morgan & Claypool Publishers, San Rafael, CA.

Zhang, X., Zhang, H., & Wang, X. (2009). Acoustic mode waves and individual arrivals excited by a dipole source in fluid-filled boreholes. Science in China Series G: Physics, Mechanics and Astronomy, 52(6), 822-831.

Zhang, Y. (2011). FD3D-ERL USER MANUAL Finite Difference Modeling of Seismic Wave Propagation in Elastic and Viscoelastic Media with MPI, OpenMP and MPI/OpenMP Hybrid.

Zoback, M. D. (2010). Reservoir geomechanics. Cambridge University Press.

Zoback, M. D., Moos, D., Mastin, L., & Anderson, R. N. (1985). Well bore breakouts and in situ stress. Journal of Geophysical Research: Solid Earth, 90(B7), 5523-5530.

Zonneveld, J. P., Beatty, T. W., MacNaughton, R. B., Pemberton, S. G., Utting, J., & Henderson, C. M. (2010). Sedimentology and ichnology of the Lower Triassic Montney Formation in the Pedigree-Ring/Border-Kahntah River area, northwestern Alberta and northeastern British Columbia. Bulletin of Canadian Petroleum Geology, 58(2), 115-140.

Zou, Y., Taylor, W. E. G., & Heath, D. J. (1996, January). A numerical model for borehole breakouts. In International journal of rock mechanics and mining sciences & geomechanics abstracts (Vol. 33, No. 1, pp. 103-109). Pergamon.

Appendix A - Aadnoy's Analytical Model for Stress Distribution around a Borehole in an Anisotropic Medium

In this section, Aadnoy analytical solution for anisotropic medium is presented as an approach to validate static stress simulation. The strain components are related to the stress components through the constitutive relations of the anisotropic body as follows:

$$\begin{bmatrix} \varepsilon_x \\ \varepsilon_y \\ \varepsilon_z \\ \gamma_{yz} \\ \gamma_{xz} \\ \gamma_{xy} \end{bmatrix} = \begin{bmatrix} a_{11} & a_{12} & a_{13} & a_{14} & a_{15} & a_{16} \\ a_{21} & a_{22} & a_{23} & a_{24} & a_{25} & a_{26} \\ a_{31} & a_{32} & a_{33} & a_{34} & a_{35} & a_{36} \\ a_{41} & a_{42} & a_{43} & a_{44} & a_{45} & a_{46} \\ a_{51} & a_{52} & a_{53} & a_{54} & a_{55} & a_{56} \\ a_{61} & a_{62} & a_{63} & a_{64} & a_{65} & a_{66} \end{bmatrix} \begin{bmatrix} \sigma_x \\ \sigma_y \\ \sigma_z \\ \tau_{yz} \\ \tau_{xz} \\ \tau_{xy} \end{bmatrix} \tag{A-1}$$

Where $a_{ij}$is element of matrix of compliance.

Aadnoy's proposed method is based on the generalized plane strain concept ($\varepsilon_z = 0$) and linear elasticity. Based on these assumptions, the following equation was expressed for the axial stress component:

$$\sigma_z = -\frac{1}{a_{33}} \left(a_{31}\sigma_x + a_{32}\sigma_y + a_{34}\tau_{yz} + a_{35}\tau_{xz} + a_{36}\tau_{xy}\right) \tag{A-2}$$

In order to find relations for principal and shear stresses, two stress functions (F and ψ), strain compatibility and a system of differential equations were introduced. Coupled partial-differential equations were used to determine the parameters of the stress functions.

$$\sigma_x = \frac{\partial^2 F}{\partial y^2} \tag{A-3}$$

$$\sigma_y = \frac{\partial^2 F}{\partial x^2} \tag{A-4}$$

$$\tau_{xy} = \frac{\partial^2 F}{\partial x\, \partial y} \tag{A-5}$$

$$\tau_{xz} = \frac{\partial \psi}{\partial y} \tag{A-6}$$

$$\tau_{yz} = -\frac{\partial \psi}{\partial x} \tag{A-7}$$

Which yields

$$L_4 F + L_3 \psi = 0 \tag{A-8}$$

$$L_3 F + L_2 \psi \tag{A-9}$$

Where $[L]$ is matrix of elastic constants for porous material in rock and is defined as follows:

$$L_2 = \beta_{44} \frac{\partial^2}{\partial x^2} - 2\beta_{45} \frac{\partial^2}{\partial x \partial y} + \beta_{55} \frac{\partial^2}{\partial y^2} \tag{A-11}$$

$$L_3 = -\beta_{24} \frac{\partial^3}{\partial x^3} + (\beta_{25} + \beta_{45}) \frac{\partial^3}{\partial x^2 \partial y} - (\beta_{14} + \beta_{56}) \frac{\partial^3}{\partial x\, \partial y^2} + \beta_{15} \frac{\partial^3}{\partial y^3} \tag{A-12}$$

$$L_4 = \beta_{22} \frac{\partial^4}{\partial x^4} - 2\beta_{26} \frac{\partial^4}{\partial x^3 \partial y} - 2\beta_{16} \frac{\partial^4}{\partial x\, \partial y^3} + (2\beta_{12} + \beta_{66}) \frac{\partial^4}{\partial y^4} \tag{A-13}$$

Where:

$$\beta_{ij} = \alpha_{ij} - \frac{\alpha_{i3}\alpha_{j3}}{\alpha_{33}} (i, j = 1,2,4,5,6) \tag{A-14}$$

It was readily observed that the solution depends on the elements of the constitutive relation matrix of equation A-2. Solved in terms of F, we are left with a sixth-order differential equation:

$$(L_4 L_2 - L_3^2) F = 0 \tag{A-15}$$

Inspection of equations A-8 and A-9 gave some insight into the properties of the solution and it revealed that the anisotropic stress equations are very complicated. Indeed the, the solution to equation A-9 gave complex or imaginary roots. The resultant stress equations are rather lengthy; Aadnoy provided complete expressions. In Aadnoy's model, it was assumed that a general stress field at infinite radius is the outer boundary condition. The following equations are derived to determine stress field in anisotropic medium:

$$\sigma_x = \sigma_{x,0} + 2Re[\mu_1^2 \varphi_1'(z_1) + \mu_2^2 \varphi_2'(z_2) + \lambda_3 \mu_3^2 \varphi_3'(z_3)] \tag{A-16}$$

$$\sigma_y = \sigma_{y,0} + 2Re[\varphi_1'(z_1) + \varphi_2'(z_2) + \lambda_3 \varphi_3'(z_3)] \tag{A-17}$$

$$\tau_{xy} = \tau_{xy,0} - 2Re[\mu_1\varphi_1'(z_1) + \mu_2\varphi_2'(z_2) + \lambda_3\mu_3\varphi_3'(z_3)] \quad \text{(A-18)}$$

$$\tau_{xz} = \tau_{xz,0} + 2Re[\lambda_1\mu_1\varphi_1'(z_1) + \lambda_2\mu_2\varphi_2'(z_2) + \mu_3\varphi_3'(z_3)] \quad \text{(A-19)}$$

$$\tau_{yz} = \tau_{yz,0} + 2Re[\lambda_1\varphi_1'(z_1) + \lambda_2\varphi_2'(z_2) + \varphi_3'(z_3)] \quad \text{(A-20)}$$

Where

λ_i= The three complex numbers($i = 1,2,3$)

Re= The notation for the real part of the complex expressions in the brackets

z_k= The complex variable ($k = 1,2,3$)

φ_k= The three analytic functions ($k = 1,2,3$)

$\sigma_{x,0}$, $\sigma_{y,0}$, $\sigma_{z,0}$, $\tau_{xy,0}$, $\tau_{xz,0}$, and $\tau_{yz,0}$= Virgin in-situ stress field.

(x, y)= The coordinates of the point within the body where stress, strain and displacement components must be determined

Analytical functions were gained from boundary conditions:

$$\varphi_1'(z_1) = \frac{1}{2\Delta(\mu_1\cos\theta - \sin\theta)} \times [D'(\lambda_2\lambda_3 - 1) + E'(\mu_2 - \lambda_2\lambda_3\mu_3) + F'\lambda_3(\mu_3 - \mu_2)] \quad \text{(A-21)}$$

$$\varphi_2'(z_2) = \frac{1}{2\Delta(\mu_2\cos\theta - \sin\theta)} \times [D'(1 - \lambda_1\lambda_3) + E'(\lambda_1\lambda_3\mu_3 - \mu_1) + F'\lambda_3(\mu_1 - \mu_3)] \quad \text{(A-22)}$$

$$\varphi_3'(z_3) = \frac{1}{2\Delta(\mu_3\cos\theta - \sin\theta)} \times [D'(\lambda_1 - \lambda_2) + E'(\lambda_2\mu_1 - \mu_2\lambda_1) + F'\lambda_3(\mu_2 - \mu_1)] \quad \text{(A-23)}$$

Where:

$\Delta = \mu_2 - \mu_1$

$D' = (P_w - \sigma_{x,0})\cos\theta - \tau_{xy,0}\sin\theta - i(P_w - \sigma_{x,0})\sin\theta - i\tau_{xy,0}\cos\theta$

$E' = -(P_w - \sigma_{y,0})\sin\theta - \tau_{xy,0}\cos\theta - i(P_w - \sigma_{y,0})\cos\theta - i\tau_{xy,0}\sin\theta$

$F' = -\tau_{xz,0}\cos\theta - \tau_{xz,0}\sin\theta + i\tau_{xz,0}\sin\theta - i\tau_{yz,0}\, cos\,\theta$

Appendix B - Formulation for Transformation of the Compliance Tensor

For the sake of simplicity, for the computation of the borehole stress concentration, all measurement would be better to obtain in the borehole, so compliance and stress tensors must be rotated on the top of borehole (TOH) frame, which is the aim of this section.

- ***Stress Tensor Rotation***

It is assumed that the vertical stress (σ_v) is always aligned with the vertical (*V*) component of the *NEV* (North-Eat-Vertical) coordinate system. The horizontal stress field could be rotated by an angle γ measured between *N* (north) and σ_H towards *E* (east). In order to rotate the regional stress field into the NEV frame the following coordinate transform is used.

$$\sigma_{NEV} = R_z(\gamma)\,\sigma\,R_z{}'(\gamma) \tag{B.1}$$

Where $R_z(\gamma)$ is a rotation matrix defined as follows:

$$R_z(\gamma) = \begin{pmatrix} \cos\gamma & -\sin\gamma & 0 \\ \sin\gamma & \cos\gamma & 0 \\ 0 & 0 & 1 \end{pmatrix} \tag{B.2}$$

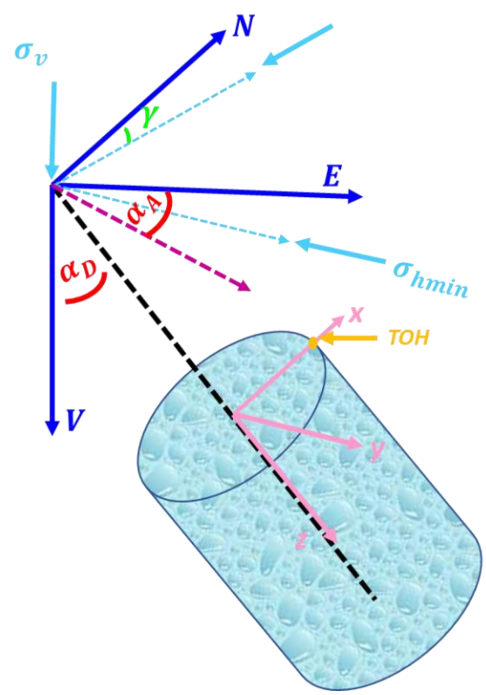

Figure B-1: Schematic of the geographic and borehole reference frames and the principal stress direction.

The coordinate transform of the *NEV* stress tensor σ_{NEV} to the stress tensor in the borehole frame σ_{TOH} is:

$$\sigma_{TOH} = T_t(\alpha_D, \alpha_A)\ \sigma_{NEV}\ T_t{}'(\alpha_D, \alpha_A) \tag{B.3}$$

Here α_D and α_A are the borehole deviation and azimuth respectively. The rotation matrix $T_t(\alpha_D, \alpha_A)$ is defined as follows:

$$T_t(\alpha_D, \alpha_A) = \begin{pmatrix} l_x & m_x & n_x \\ l_y & m_y & n_y \\ l_z & m_z & n_z \end{pmatrix} \tag{B.4}$$

Where the directional cosines are defined as:

$l_x = \cos(\alpha_D)\cos(\alpha_A)$ $\quad m_x = \cos(\alpha_D)\sin(\alpha_A)$ $\quad n_x = -\sin(\alpha_D)$

$l_y = -\sin(\alpha_A)$ $\quad m_x = \cos(\alpha_A)$ $\quad n_y = 0$

$l_Z = \sin(\alpha_D)\cos(\alpha_A)$ $\quad m_z = \sin(\alpha_D)\sin(\alpha_A)$ $\quad n_z = \cos(\alpha_D)$

- ***Compliance tensor rotation***

Compliance tensor rotation (S_{ijkl})is done by applying two bond transformations to the 6×6 Voigt notation compliance matrix s_{ij} giving a_{ij} as follows:

$$a = T_\epsilon T'_\sigma\ s\ T_\sigma T'_\epsilon \tag{B.5}$$

Where T_ϵ and $T_\sigma$are two bond transformation matrices. One of these transformation matrices takes into account the orientation of the material frame which has the form:

$$T_\sigma = \begin{pmatrix} l_s^2 & m_s^2 & n_s^2 & 2m_s n_s & 2n_s l_s & 2m_s l_s \\ l_t^2 & m_t^2 & n_t^2 & 2m_t n_t & 2n_t l_t & 2l_t m_t \\ l_n^2 & m_n^2 & n_n^2 & 2m_n n_n & 2n_n l_n & 2l_n m_n \\ l_t l_n & m_t m_n & n_t n_n & m_t n_n + m_n n_t & n_t l_n + n_n l_t & l_t m_n + l_n m_t \\ l_n l_s & m_n m_s & n_n n_s & m_s n_n + m_n n_s & n_s l_n + n_n l_s & l_s m_n + l_n m_s \\ l_s l_t & m_s m_t & n_s n_t & m_s n_t + m_t n_s & n_s l_t + n_t l_s & l_s m_t + l_t m_s \end{pmatrix} \tag{B.6}$$

The second one takes into account the orientation of the borehole:

$$T_\epsilon = \begin{pmatrix} l_x^2 & m_x^2 & n_x^2 & 2m_x n_x & 2n_x l_x & 2m_x l_x \\ l_y^2 & m_y^2 & n_y^2 & 2m_y n_y & 2n_y l_y & 2l_x m_x \\ l_z^2 & m_z^2 & n_z^2 & 2m_z n_z & 2n_z l_z & 2l_z m_z \\ 2l_y l_z & 2m_y m_z & 2n_y n_z & m_y n_z + m_z n_y & n_y l_z + n_z l_y & l_y m_z + l_z m_y \\ 2l_z l_x & 2m_z m_x & 2n_z n_x & m_x n_z + m_z n_x & n_x l_z + n_z l_x & l_x m_z + l_z m_x \\ 2l_x l_y & 2m_x m_y & 2n_x n_y & m_x n_y + m_y n_x & n_x l_y + n_y l_x & l_x m_y + l_y m_x \end{pmatrix} \tag{B.7}$$

In order to rotate the 6 × 6 Voigt notation elastic matrix into the borehole frame have to define the directional cosine for the material frame:

$$l_s = \cos(\beta_D)\cos(\beta_A) \qquad m_s = \cos(\beta_D)\sin(\beta_A) \qquad n_s = -\sin(\beta_D)$$

$$l_t = -\sin(\beta_A) \qquad m_t = \cos(\beta_A) \qquad n_t = 0$$

$$l_n = \sin(\beta_D)\cos(\beta_A) \qquad m_n = \sin(\beta_D)\sin(\beta_A) \qquad n_n = \cos(\beta_D)$$

Where the β_D is the dip of the transverse isotropy plane and β_A is the dip azimuth, as shown in Figure B-2.

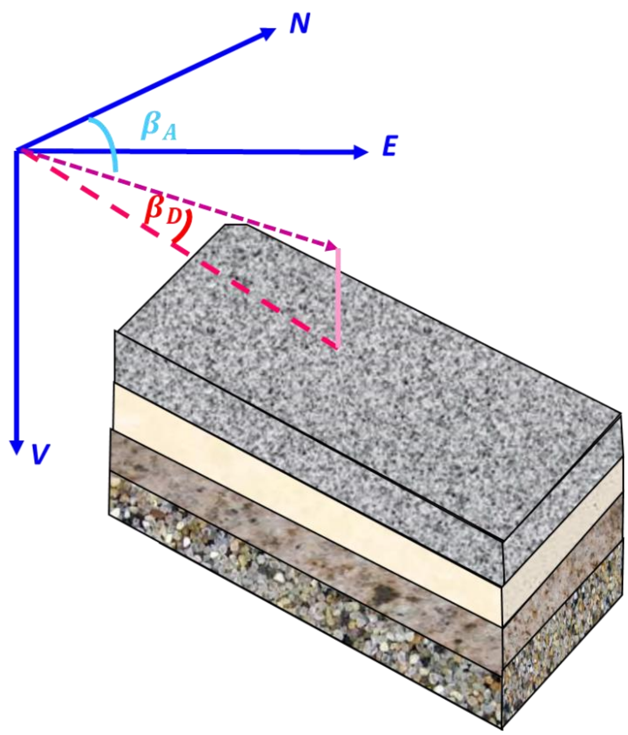

Figure B-2: The material coordinate system for transverse isotropic medium with tilted symmetry axis (Called TTI) where β_D is the dip of the transverse isotropy plane and β_A is the dip azimuth (after Gaede et al., 2012).

Appendix C –Simulation of Sonic Logging using a Monopole Source

The same numerical model described in this thesis for modeling sonic logging using a dipole source can also be used to simulate logging using a monopole source; this simply requires the use of a monopole source function rather than a dipole. To demonstrate monopole modeling capabilities, a vertical borehole scenario (Montney Formation) was run and the results are presented in this appendix.

Material properties and model geometry were defined as described in section 3.2.4.2. This simulation is different from the dipole simulation in terms of frequency and type of generated energy (uniform acoustic pressure rather than directional acoustic pressure). Figure C-1 shows the modeled waveforms recorded by monopole receivers after firing the monopole transmitter. Figure C-2 presents a magnified view of the recorded waveform by receiver #1, which is located 3.5 m above the monopole transmitter. This figure shows each arrival (P-wave, S-wave and mud wave) is clearly visible. The arrival time at each receiver, coupled with knowledge of the vertical position of each receiver, was used to interpret compressional wave (P-wave) and shear wave velocity (effectively, the reciprocal of the slope of the green and purple lines shown in Figure C-1, respectively). As shown in Table C-1, there is a favorable comparison between the velocities interpreted from simulation results, and the velocities taken directly from the experimental results.

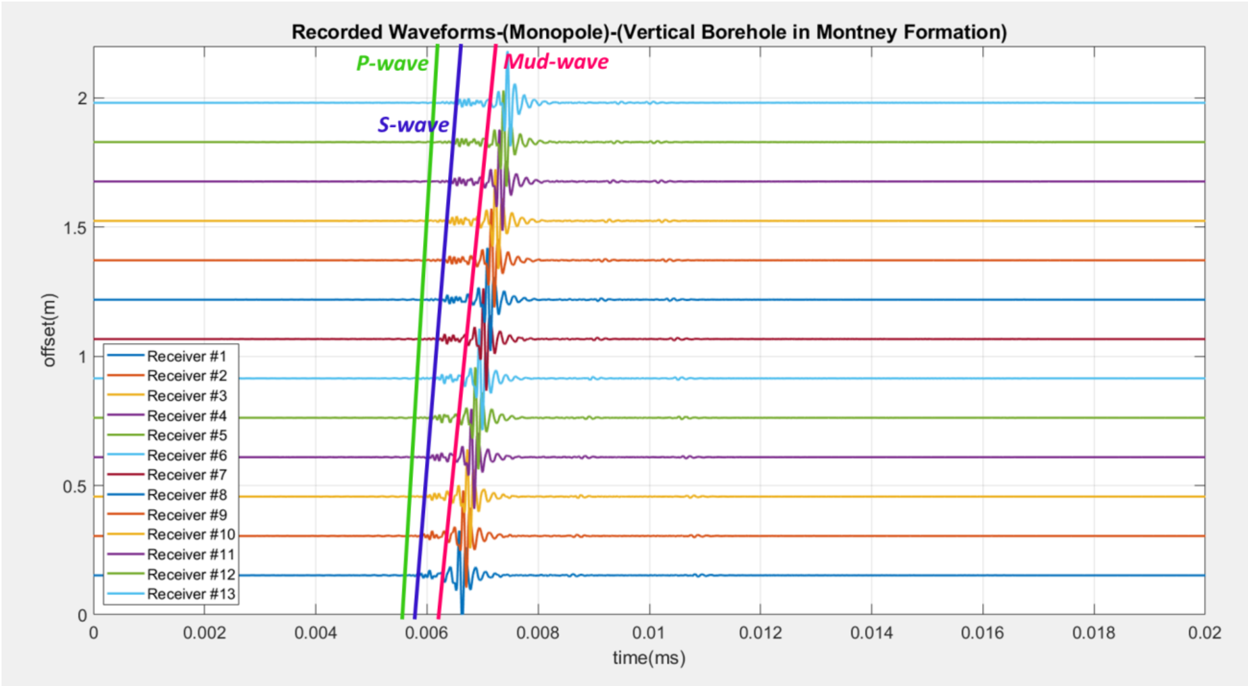

Figure C-1: Recorded monopole waveforms, vertical borehole in the Montney Formation.

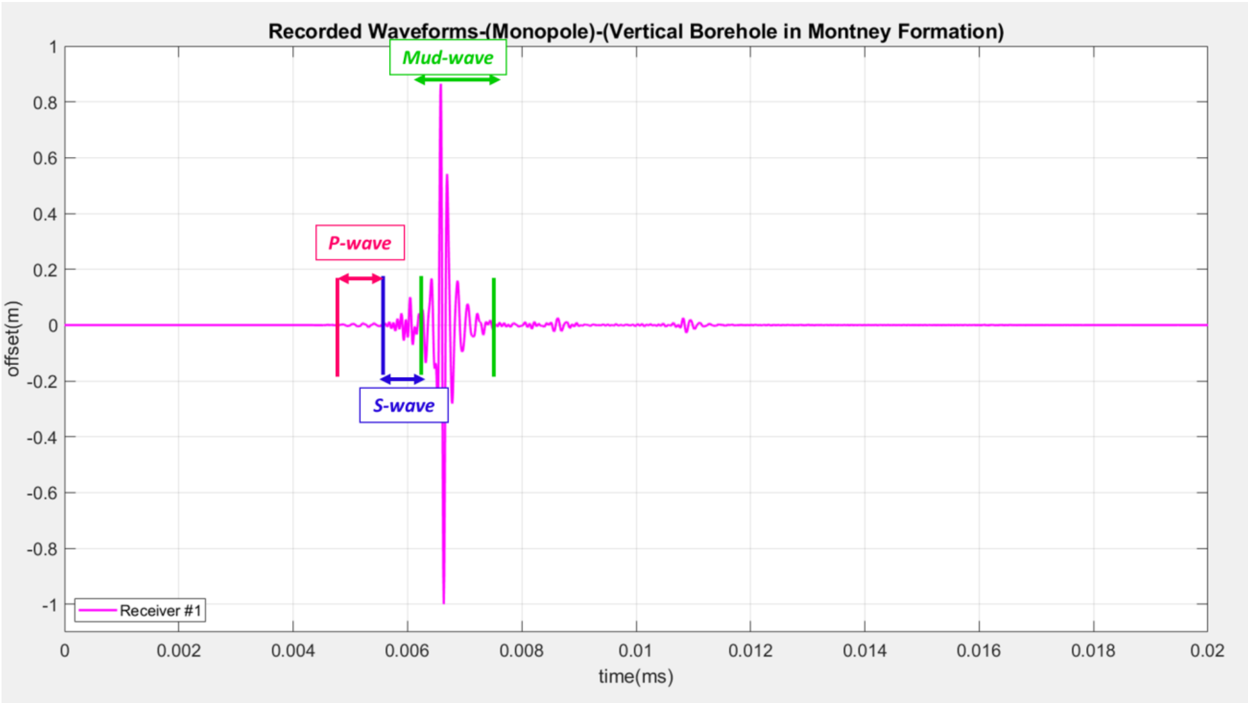

Figure C-2: Recorded monopole waveform by receiver #1, vertical borehole in the Montney Formation.

Table C-1: Comparison between the velocities interpreted from simulation results, and the values taken directly from experimental results

Monopole	***Predicted Velocity (Based on Simulation)***	***Estimated Velocity (Based on Experimental Results)***	***Error***
Compressional Velocity	$5440(^m/_s)$	$5404(^m/_s)$	$\cong 0.66$
Shear Velocity	$3098(^m/_s)$	$3060(^m/_s)$	$\cong 1.24$

Appendix D – Effects of Modeled Formation Radius on Dynamic Simulation Results

In initial simulations, the radius of the formation used for the dynamic simulations was defined as six times the borehole radius, based on the literature (Pissarenko et al., 2009). Dispersion curves generated from these simulations showed low quality at low frequencies, as shown in Figure D-1 through Figure D-9. The low quality of the low-frequency portion of the dispersion curves was interpreted to result from a formation radius that was too small. Further investigation of the results revealed that based on this radius, the entire model domain was affected by drilling-induced stress changes. Based on the static stress analysis and defined elastic stiffness constants, it was determined that the formation radius should be at least nine times the borehole radius (Figure D-10). Thus, all subsequent simulations (e.g., in sections 4.3.2 and 4.3.3) were generated using this bigger formation radius.

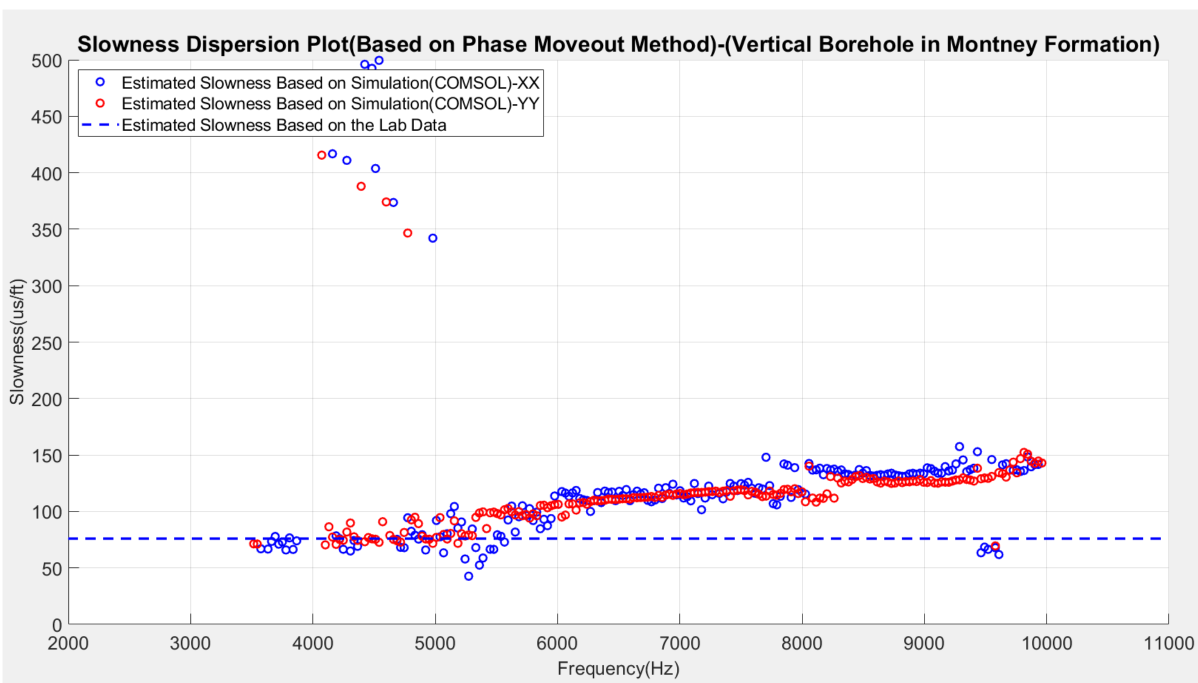

Figure D-1: Graph showing generated dispersion plots of the modeled X-X and Y-Y waveforms (vertical borehole in the Montney Formation).

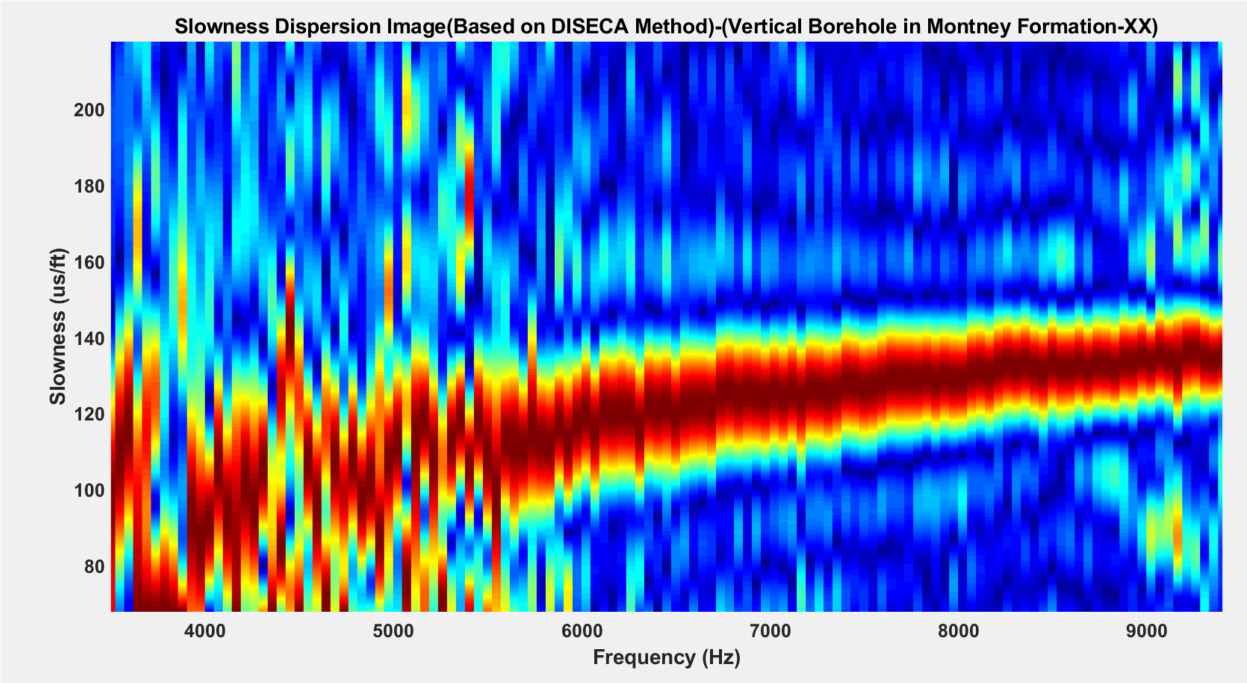

Figure D-2: Dispersion plot of modeled X-X dipole waveforms, based on DISECA method (vertical borehole in the Montney Formation).

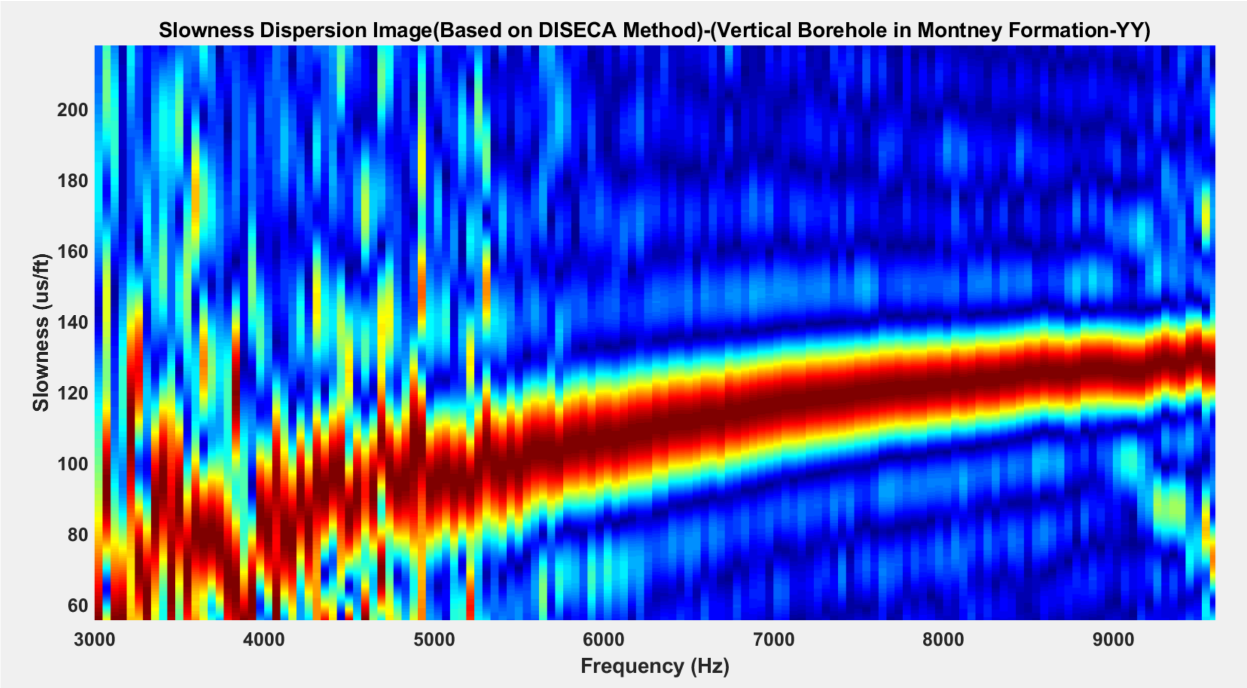

Figure D-3: Dispersion plot of modeled Y-Y dipole waveforms, based on DISECA method (vertical borehole in the Montney Formation).

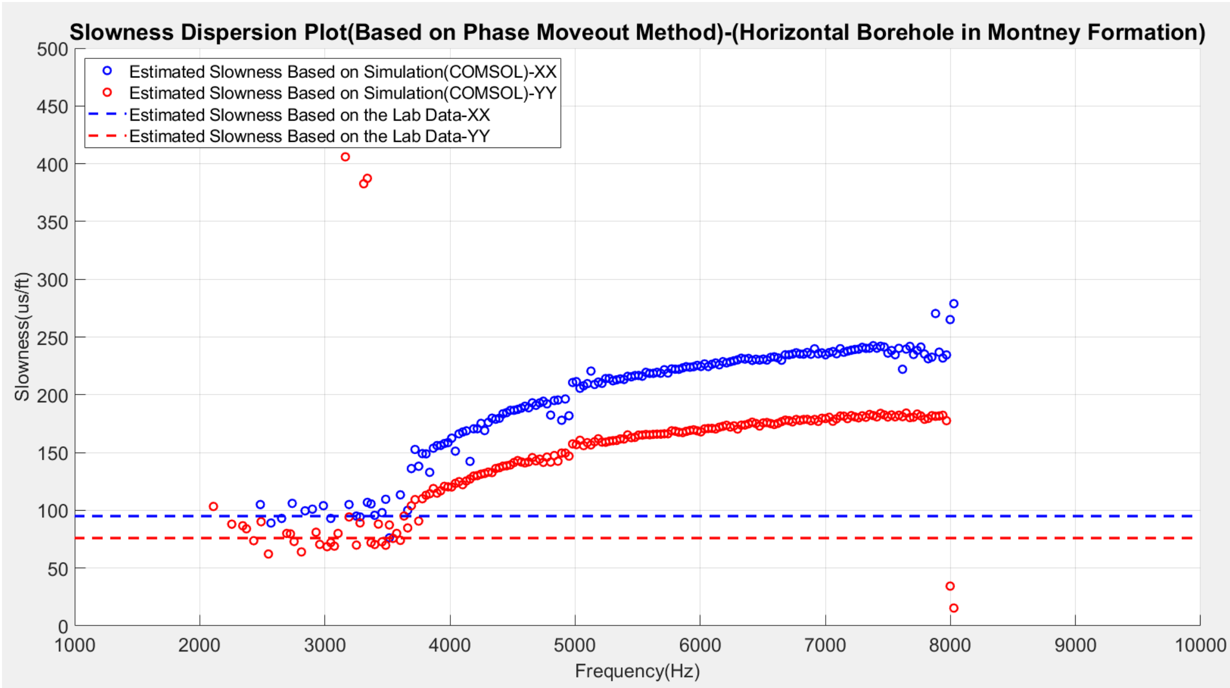

Figure D-4: Graph showing generated dispersion plots of the modeled X-X and Y-Y waveforms (horizontal borehole in the Montney Formation).

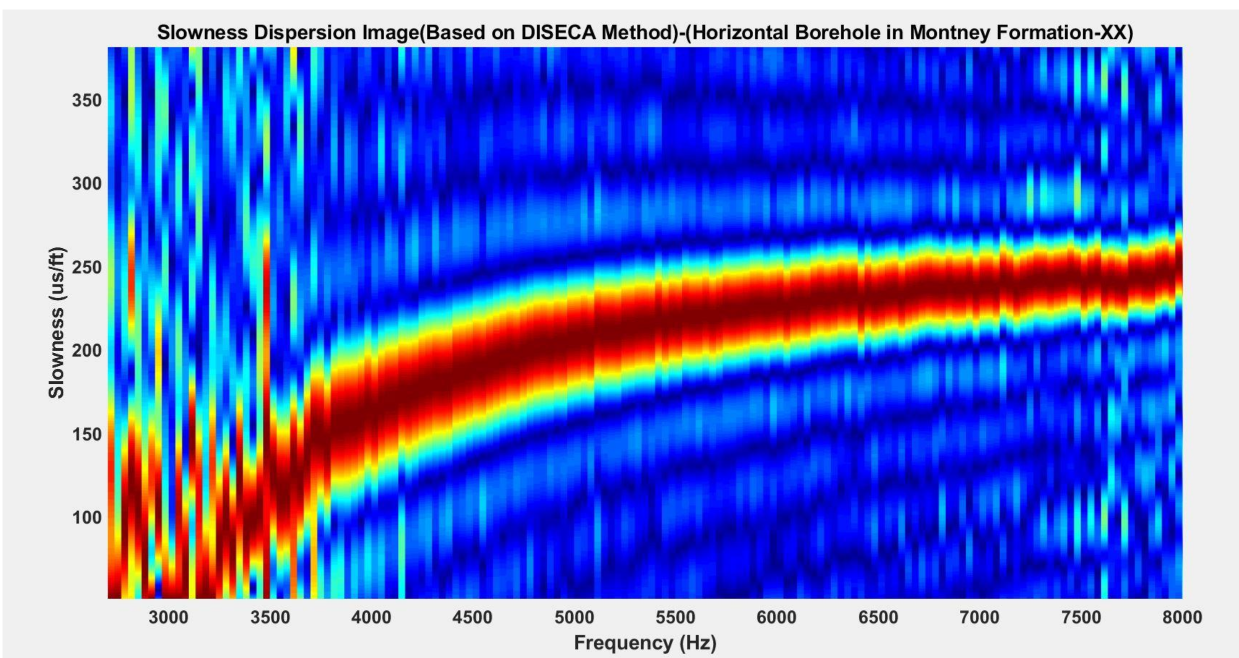

Figure D-5: Dispersion plot of modeled X-X dipole waveforms, based on DISECA method (horizontal borehole in the Montney Formation).

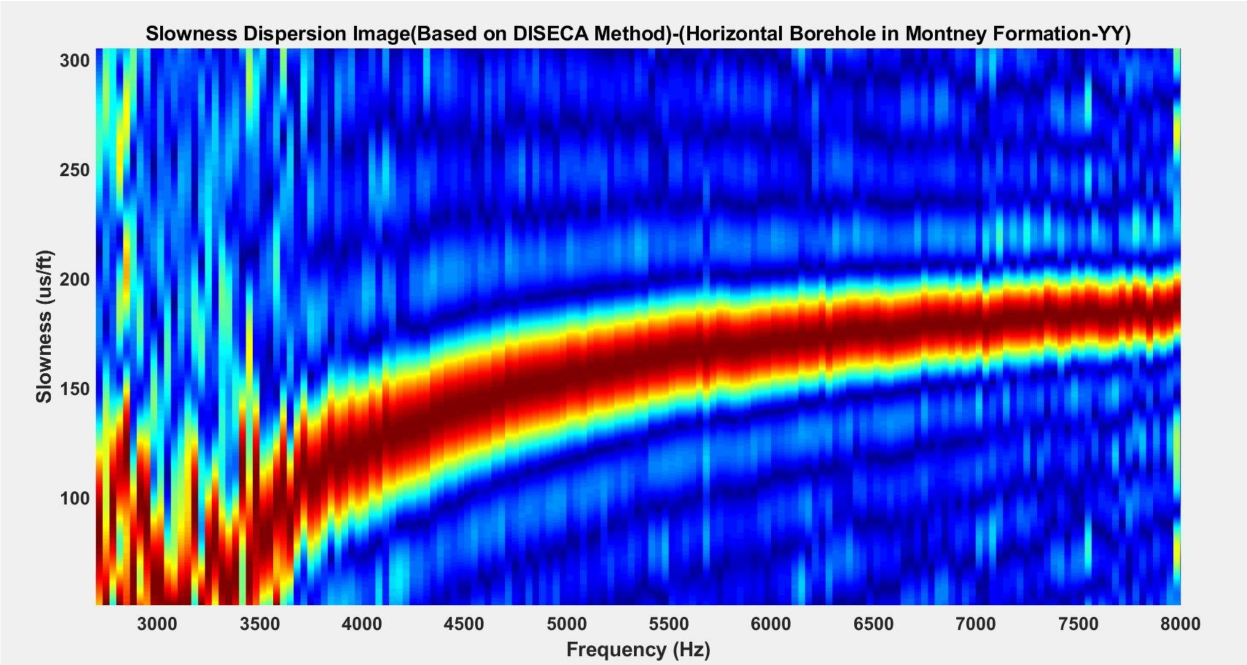

Figure D-6: Dispersion plot of modeled Y-Y dipole waveforms, based on DISECA method (horizontal borehole in the Montney Formation).

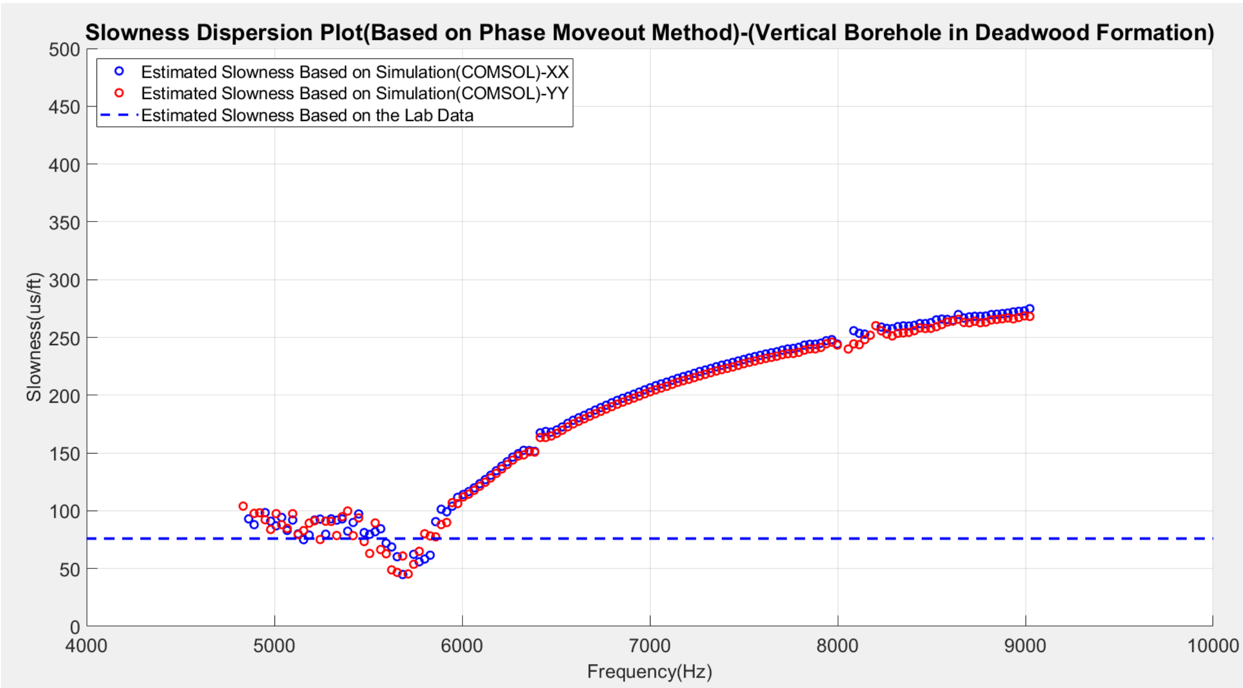

Figure D-7: Graph showing generated dispersion plots of the modeled X-X and Y-Y waveforms (vertical borehole in the Deadwood Formation).

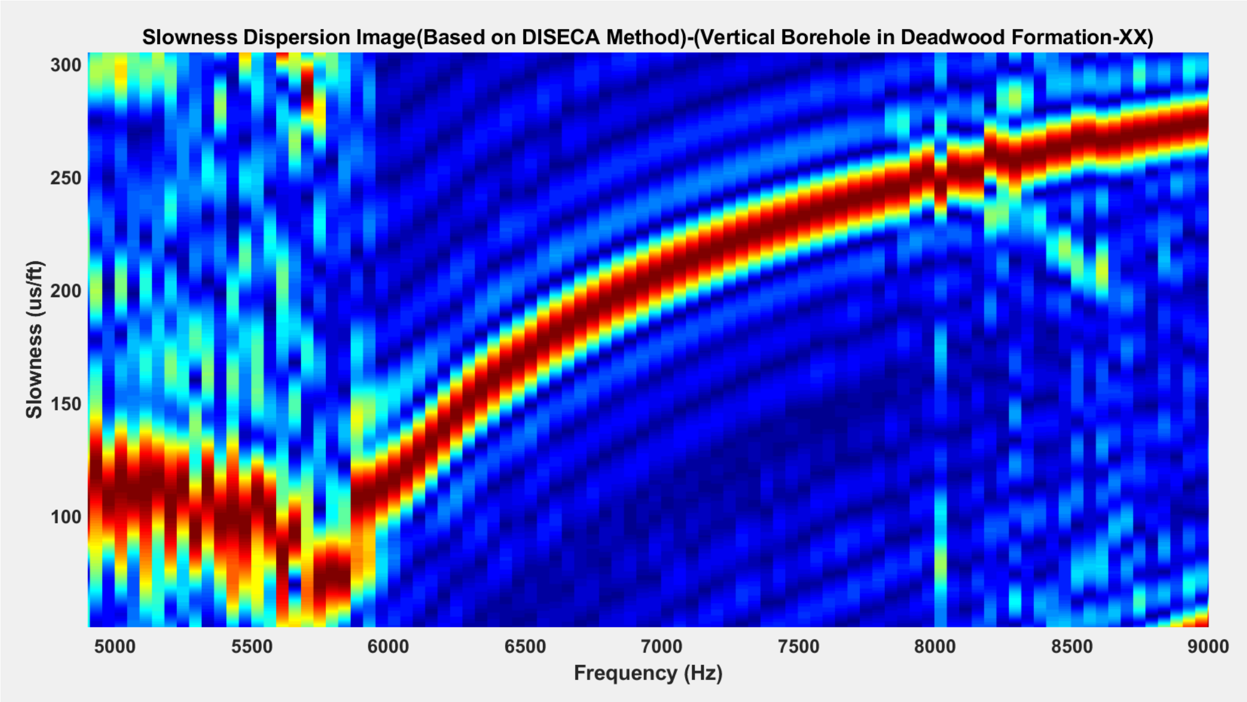

Figure D-8: Dispersion plot of modeled X-X dipole waveforms, based on DISECA method (vertical borehole in the Deadwood Formation).

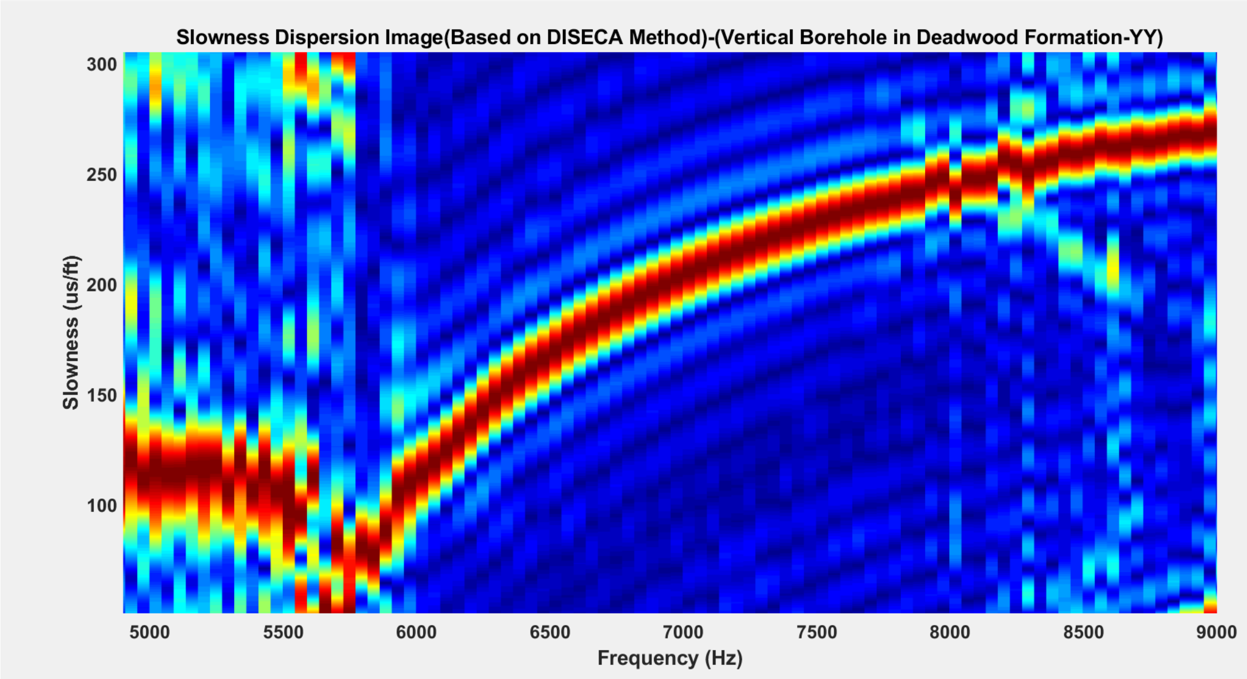

Figure D-9: Dispersion plot of modeled Y-Y dipole waveforms, based on DISECA method (vertical borehole in the Deadwood Formation).

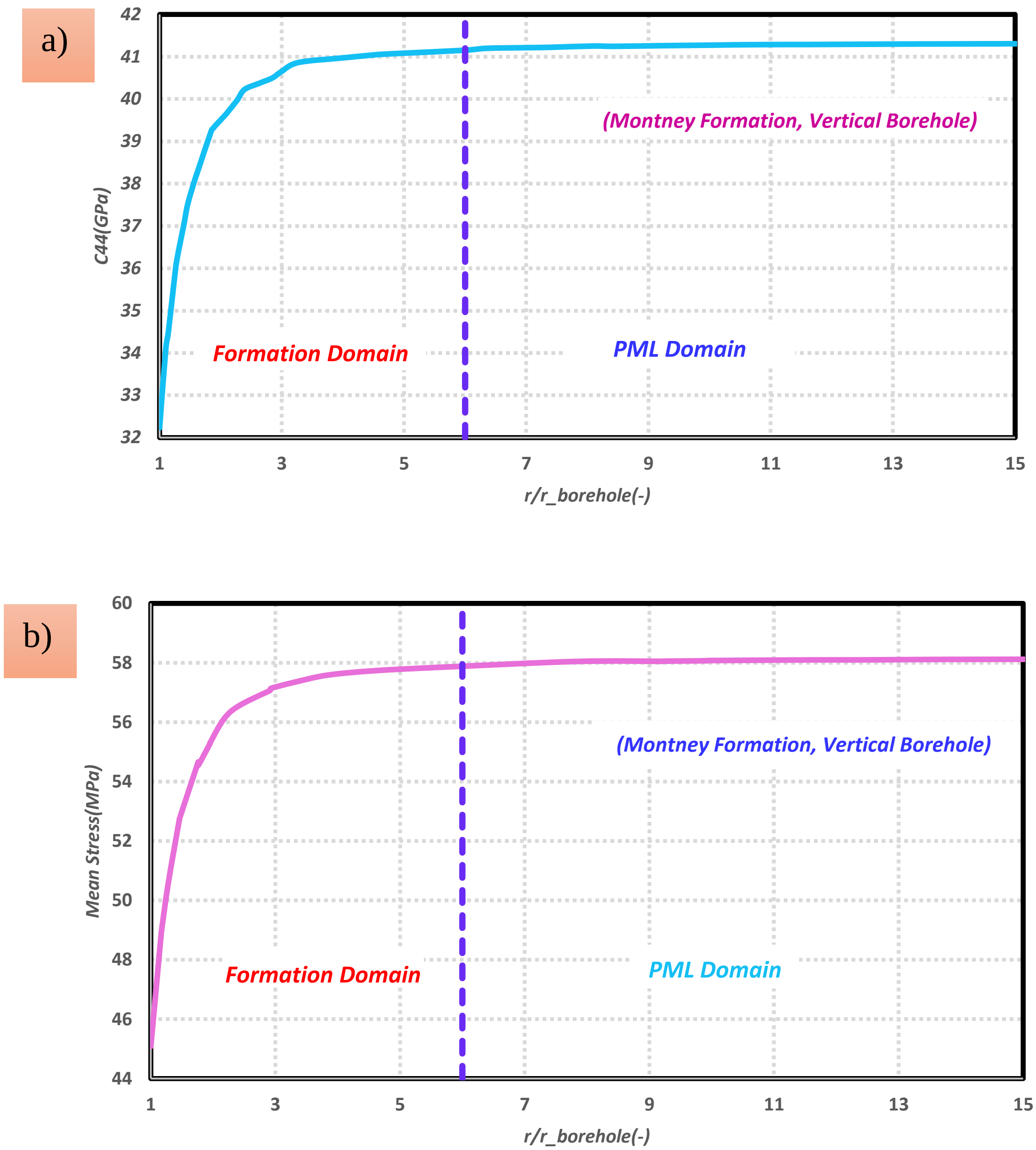

Figure D-10: Altered zone around the borehole, used as a basis to determine the formation radius used for dynamic modeling: a) C_{44} (stress-dependent elastic stiffness constant) versus normalized radial distance; and b) Mean stress versus normalized radial distance (vertical borehole in Montney Formation).

Appendix E - Fast Fourier Transformation Equations

A wavelet is defined as a wave-like oscillation with specific definitions and parameters, which wavelets are intentionally crafted to have a specific property that make them useful for signal processing. The amplitude of a wavelet usually begins at zero, increases, and then decreases back to zero. Generally, wavelets are mathematical functions that cut up data into frequency components. Most basis wavelet functions are presented in time domain.

In COMSOL, depending on the study type (frequency domain or time domain), it is required to define function of amplitude of point source. To derive frequency domain function from time domain function, it is required to apply some mathematical transformation known as Fourier transform. This section is aimed to show how do this transformation for two main type of wavelets, which are frequently used in signal processing: Ricker and Ormsby wavelets.

- **Fourier Transform**

The time and frequency domains are alternative ways of representing signals. The Fourier transform is the mathematical relationship between these two representations. The Fourier transform converts a signal from its original domain (often time domain) to a representation in frequency domain and vice versa by decomposing signals into sinusoids. Given the time domain signal, the process of calculating the frequency domain is called decomposition, analysis, the forward Fourier transform, or simply Fourier transform. If you know the frequency domain, calculation of the time domain is called synthesis, or inverse Fourier transform. The general forms of Fourier transform are as follows:

Forward Fourier transform: Analysis equation

$$X(\omega) = \int_{-\infty}^{+\infty} x(t) e^{-j\omega t} dt \tag{E.1}$$

Inverse Fourie transform: Synthesis equation

$$x(t) = \frac{1}{2\pi} \int_{-\infty}^{+\infty} X(\omega) e^{j\omega t} d\omega \tag{E.2}$$

Where t represents time, $\omega(= 2\pi f)$ stands for angular frequency and f is frequency.

If a signal is modified in one domain, it will also be changed in the other domain, although usually not in the same way. For example, by convolving time domain signals results in their frequency spectra multiplied. Other mathematical operations, such as addition, scaling and shifting, also having matching operations, such as addition, scaling and shifting, also having matching operation in the opposite domain. These relationships are called properties of the Fourier transform, how a mathematical change in one domain results in a mathematical change in the other domain. A brief table of Fourier transform is presented in Table E-1, which makes extremely easier calculation of the transformed function from one domain to the other domain:

Table E-1: Summarize of helpful transformation pairs.

Description	*Function in time domain*	*Transform in frequency domain*
Delta function in time domain (t)	$\delta(t)$	1
Delta function in frequency domain (f)	1	$2\pi\delta(\omega)$
Exponential in time domain (t)	$e^{-a\|t\|}$	$\frac{2a}{a^2+\omega^2}$
Exponential in frequency domain (f)	$\frac{2a}{a^2+t^2}$	$2\pi e^{-a\|\omega\|}$
Gaussian	$e^{-t^2/2}$	$\sqrt{2\pi}e^{-\omega^2/2}$
Derivative in in time domain (t)	$f'(t)$	$i\omega F(\omega)$
Derivative in frequency domain (f)	$xf(t)$	$iF'(\omega)$
Translation in time (t)	$f(t-a)$	$e^{-iaf}F(\omega)$
Translation in frequency domain (f)	$e^{iat}f(t)$	$F(\omega-a)$
Dilation in time domain (t)	$f(at)$	$F(^{\omega}/_{a})/a$

Convolution	$f(t) * g(t)$	$F(\omega)G(\omega)$
Rectangular Function in time domain(t)	$rect(at)$	$\frac{1}{\sqrt{2\pi a^2}} sinc(^{\omega}/_{2\pi a})$
Sinc function in time domain (t)	$sinc(at)$	$\frac{1}{\sqrt{2\pi a^2}} rect(^{\omega}/_{2\pi a})$
Triangular function in time domain (t)	$tri(at)$	$\frac{1}{\sqrt{2\pi a^2}} sinc^2(^{\omega}/_{2})$
Cosine function in time domain (t)	$\cos(\omega_0 t)$	$\pi[\delta(\omega - \omega_0) + \delta(\omega + \omega_0)]$
Sine function in time domain (t)	$\sin(\omega_0 t)$	$^{\pi}/_{j}\, [\delta(\omega - \omega_0) - \delta(\omega + \omega_0)]$

- **Ricker Wavelet**

The Ricker wavelet is a theoretical waveform obtained by solving Stokes differential equation. Mathematically Ricker wavelet is the second derivative of a Gaussian function; therefore, it is symmetric in the time domain. The general time domain form of Ricker wavelet (rw) used in this research is as follows:

$$rw(t) = 2Af_c^2\pi^2(t - t_s)e^{-(f_c^2\pi^2(t-t_s)^2)} \qquad \text{(E.3)}$$

Where

A= amplitude of wavelet

f_c= central frequency

t_s= time shift

It could be understood that equation (E.3) is derivative of one equation:

$$rw(t) = 2Af_c^2\pi^2(t - t_s)e^{-(f_c^2\pi^2(t-t_s)^2)} = -A(e^{-(f_c^2\pi^2(t-t_s)^2)})' \qquad \text{(E.4)}$$

By paying attention on the left-hand side of equation (E.4), the following information could be derived:

- Gaussian function
- Dilation in time
- Translation in time
- Derivative in time

For deriving frequency domain from time domain equation, the following step would be taken.

Step 1: Gaussian in time domain

Time domain		Frequency domain	
$e^{-t^2/2}$	$\Leftrightarrow$	$\sqrt{2\pi}e^{-\omega^2/2}$	(E.5)

Step 2: Dilation in time domain

Time domain		Frequency domain	
$e^{-(\sqrt{2}f_c\pi t)^2/2}$	$\Leftrightarrow$	$\sqrt{2\pi}/\sqrt{2}f_c\pi\; e^{-(\omega/\sqrt{2}f_c\pi)^2/2}$	(E.6)

Step 3: Translation in time domain

Time domain		Frequency domain	
$e^{-(\sqrt{2}f_c\pi(t-t_s))^2/2}$	$\Leftrightarrow$	$e^{(-it_s\omega)}(\sqrt{2\pi}/\sqrt{2}f_c\pi\; e^{-(\omega/\sqrt{2}f_c\pi)^2/2})$	(E.7)

Step 4: Derivative in time domain

Time domain		Frequency domain	
$(e^{-(\sqrt{2}f_c\pi(t-t_s))^2/2})'$	$\Leftrightarrow$	$(i\,\omega/\sqrt{2}f_c\pi)(e^{(-it_s\omega)}(\sqrt{2\pi}/\sqrt{2}f_c\pi\; e^{-(\omega/\sqrt{2}f_c\pi)^2/2}))$	(E.8)

By simplification of equation (E.8), the following equation is derived in frequency domain known as frequency domain version of Ricker wavelet.

$$RW(f) = i\sqrt{\frac{2}{\pi}}\left(\frac{f}{f_c^2}\right)e^{-i(2\pi f t_s)}e^{-(f/f_c)^2} \tag{E.9}$$

- Ormsby Wavelet

Another example of interesting wavelet is called Ormsby wavelet, which features a controllable flat frequency content with formulation (time domain) shown in equation (E.10).

$$Ormsby(t) = A\left(\left(\frac{\pi f_4^2}{f_4 - f_3} sinc^2\big(\pi f_4 (t - ts)\big) - \frac{\pi f_3^2}{f_4 - f_3} sinc^2\big(\pi f_3 (t - ts)\big)\right) - \left(\frac{\pi f_2^2}{f_2 - f_1} sinc^2\big(\pi f_2 (t - ts)\big) - \frac{\pi f_1^2}{f_2 - f_1} sinc^2\big(\pi f_1 (t - ts)\big)\right)\right) \tag{E.10}$$

Where

f_1= low-cut frequency

f_2= low-pass frequency

f_3= high-pass frequency

f_4= high-cut frequency

As it is shown in equation (E.10), Ormsby wavelet is composed of following step:

- $sinc^2(t)$
- Dilation
- Translation

For deriving frequency domain from time domain equation, the following step would be taken.

Step 1: $sinc^2(t)$

Time domain		**Frequency domain**	
$sinc^2(t)$	$\Leftrightarrow$	$tri(f)$	(E.11)

Step 2: Dilation

Time domain		**Frequency domain**	
$(\frac{\pi f_4^2}{f_4 - f_3})(sinc^2(\pi f_4 t))$	$\Leftrightarrow$	$(\frac{\pi f_4^2}{f_4 - f_3})(1/_{\pi f_4})tri(f/_{\pi f_4})$	(E.12)

$$\left(\frac{\pi f_3^2}{f_4 - f_3}\right) sinc^2(\pi f_3 t) \quad \Longleftrightarrow \quad \left(\frac{\pi f_3^2}{f_4 - f_3}\right)\left({}^{1}/_{\pi f_3}\right) tri\left({}^{f}/_{\pi f_3}\right) \tag{E.13}$$

$$\left(\frac{\pi f_2^2}{f_2 - f_1}\right) sinc^2(\pi f_2 t) \quad \Longleftrightarrow \quad \left(\frac{\pi f_2^2}{f_2 - f_1}\right)\left({}^{1}/_{\pi f_2}\right) tri\left({}^{f}/_{\pi f_2}\right) \tag{E.14}$$

$$\left(\frac{\pi f_1^2}{f_2 - f_1}\right) sinc^2(\pi f_1 t) \quad \Longleftrightarrow \quad \left(\frac{\pi f_1^2}{f_2 - f_1}\right)\left({}^{1}/_{\pi f_1}\right) tri\left({}^{f}/_{\pi f_1}\right) \tag{E.15}$$

Step 3: Translation

Time domain **Frequency domain**

$$\left(\frac{\pi f_4^2}{f_4 - f_3}\right) sinc^2(\pi f_4 (t - t_s)) \quad \Longleftrightarrow \quad \left(\frac{\pi f_4^2}{f_4 - f_3}\right)\left({}^{e^{-i\omega t_s}}/_{\pi f_4}\right) tri\left({}^{f}/_{\pi f_4}\right) \tag{E.16}$$

$$\left(\frac{\pi f_3^2}{f_4 - f_3}\right) sinc^2(\pi f_3 (t - t_s)) \quad \Longleftrightarrow \quad \left(\frac{\pi f_3^2}{f_4 - f_3}\right)\left({}^{e^{-i\omega t_s}}/_{\pi f_3}\right) tri\left({}^{f}/_{\pi f_3}\right) \tag{E.17}$$

$$\left(\frac{\pi f_2^2}{f_2 - f_1}\right) sinc^2(\pi f_2 (t - t_s)) \quad \Longleftrightarrow \quad \left(\frac{\pi f_2^2}{f_2 - f_1}\right)\left({}^{e^{-i\omega t_s}}/_{\pi f_2}\right) tri\left({}^{f}/_{\pi f_2}\right) \tag{E.18}$$

$$\left(\frac{\pi f_1^2}{f_2 - f_1}\right) sinc^2(\pi f_1 (t - t_s)) \quad \Longleftrightarrow \quad \left(\frac{\pi f_1^2}{f_2 - f_1}\right)\left({}^{e^{-i\omega t_s}}/_{\pi f_1}\right) tri\left({}^{f}/_{\pi f_1}\right) \tag{E.19}$$

By summation equation from (E.16) to (E.17), the following equation is obtained known as frequency domain type of Ormsby equation.

$$Ormsby(f) = A(e^{-i\omega t_s})\left(\left(\left(\frac{f_4}{f_4 - f_3}\right) tri\left({}^{f}/_{\pi f_4}\right) - \left(\frac{f_3}{f_4 - f_3}\right) tri\left({}^{f}/_{\pi f_3}\right)\right)\right. \tag{E.20}$$

$$\left. - \left(\left(\frac{f_2}{f_2 - f_1}\right) tri\left({}^{f}/_{\pi f_2}\right) - \left(\frac{f_1}{f_2 - f_1}\right) tri\left({}^{f}/_{\pi f_1}\right)\right)\right)$$

Appendix F- Fitting a Sigmoid Curve through Data

A sigmoid function is a mathematical function having a characteristic "S"-shaped curve or sigmoid curve. Although, it has many different applications in science, the main reason of its usage in this research is to compare the logged data with simulation results conveniently by applying this continuous curve on the data. The general form of sigmoid function used in this research is presented in equation F.1:

$$F(x) = \frac{a}{b + c * \exp\left(\left(-d * (x - x0)^{g}\right) + h\right)} \quad \text{(F.1)}$$

Where

a= The curve's maximum value

d= The logistic growth rate or steepness of the curve

$x0$= The x-value of the sigmoid's midpoint

b, c, g, h= Additional curve fitting constants.

In this research, x and $F(x)$ represent frequency and slowness, respectively. Fitting the sigmoid curve involves the following steps:

Step 1: Normalize data between 0 to 1, since the range of change based on the sigmoid function is 1.

$$y_{new} = \frac{y - y_{min}}{y_{max} - y_{min}} \quad \text{(F.2)}$$

Where

y_{min}= Minimum value of available data (in our research is slowness)

y_{max}= Maximum value of available data (in our research is slowness)

y= Available data (in our research is slowness)

y_{new}= New dataset varies between 0 to 1.

Step 2: Fit the function presented in equation E.1 to the new dataset (y_{new}) to find the unknown coefficients (i.e., a, b, c, d, x_0, g, and h).

Step 3: Calculate the new dataset ($\tilde{y}_{new}$) based on the coefficients found in step 2.

Step 4: Return data to the actual range, based on following equation:

$$Fitted\ Curve_{Sigmoid} = \tilde{y}_{new}(y_{max} - y_{min}) + y_{min} \tag{F.3}$$

The curve represented by equation F.3 is the fitted curve on the available data.